UNIVERSIDAD DE CHILE
FACULTAD DE CIENCIAS FÍSICAS Y MATEMÁTICAS
DEPARTAMENTO DE GEOLOGÍA

WESTWARD EXPANSION OF THE ANDEAN OROGENIC WEDGE: TECTONOSTRATIGRAPHY AND ANALOGUE MODELING OF THE WESTERN CORDILLERA OF NORTHERN CHILE

TESIS PARA OPTAR AL GRADO DE
DOCTOR EN CIENCIAS MENCIÓN GEOLOGÍA

SEBASTIÁN SANTIAGO HERRERA ESCOBAR

PROFESORA GUÍA:
LUISA PINTO LINCOÑIR
PROFESOR CO-GUÍA:
MARCELO FARÍAS THIERS

MIEMBROS DE LA COMISIÓN:
MARK T. BRANDON
REYNALDO CHARRIER GONZÁLEZ
PAMELA JARA MUÑOZ

SANTIAGO DE CHILE
2022

RESUMEN DE LA TESIS PARA OPTAR AL GRADO DE
Doctor en Ciencias Mención Geología.
POR: Sebastián Santiago Herrera Escobar
FECHA: 2022
PROFESORA GUÍA: Luisa Pinto Lincoñir
PROFESOR CO-GUÍA: Marcelo Farías Thiers

EXPANSIÓN DE LA CUÑA OROGÉNICA ANDINA AL OESTE: TECTONOESTRATIGRAFÍA Y MODELACIÓN ANALÓGICA DE LA CORDILLERA OCCIDENTAL DEL NORTE DE CHILE

La orogenia en los Andes Centrales es producto de subducción activa bajo el margen occidental de Sudamérica. Junto al magmatismo/volcanismo de arco asociado a la subducción de la placa oceánica, la construcción Cenozoica de la Cordillera Occidental ha sido adjudicada a procesos de subducción intercontinental (o tipo-Ampherer). En las últimas dos décadas, se ha establecido un fuerte debate con respecto a la naturaleza de la subducción intercontinental bajo los Andes Centrales y Andes Centrales del sur. A pesar de la creciente evidencia geológica y geofísica, aún no existe consenso sobre aspectos fundamentales de la orogenia moderna, por ejemplo, la relación entre la estructura moderna, la dirección del transporte tectónico (vergencia) y la dirección de la subducción de basamento. Esto sugiere que es necesario contextualizar la evidencia mencionada en el marco de modelos mecánicos que ilustran los mecanismos de distribución y acomodación de material operando dentro de orígenes convergentes, y su relación con la arquitectura cortical y condiciones de borde.

Este trabajo presenta una aproximación a este problema mediante una combinación de un estudio tectonoestratigráfico de la Cordillera Occidental del norte de Chile (19°15’-19°30’S) y la modelación análoga de cuñas orogénicas doble-vergentes. Los nuevos antecedentes tectonoestratigráficos sugieren que la Cordillera Occidental es subyacida por un “pop-up” de carácter cortical, formado por acortamiento tectónico y consecuente engrosamiento. Edades U-Pb en unidades de roca deformadas sugieren que los eventos de deformación datan de los 49 Ma (Eoceno medio), y que esta fue activa durante gran parte del Neógeno. La sincronicidad entre la deformación en esta región y las Sierras Subandinas sugiere que existe un acople mecánico entre los procesos orogénicos operando en ambos flancos del plateau. Por otro lado, el modelo análogo proporciona una demostración en sección transversal de la distribución y deformación de material incorporado a dos cuñas doble-vergentes por subducción y acreción, bajo condiciones de borde similares a las del prototipo Andino. En un mismo modelo, una cuña y su plano de subducción es análoga a la Cordillera de la Costa y a la placa de Nazca, y una segunda cuña es análoga a la Cordillera Occidental y a la subducción de la placa Sudamericana bajo el orógeno. Un análisis computacional (PIV; *Particle Image Velocimetry*) aplicado al modelo permitió visualizar campos de velocidad, tasa de deformación instantánea y vorticidad cinemática en las cuñas. El movimiento del material dentro de la cuña es predominantemente lateral, con velocidades instantáneas disminuyendo en el mismo sentido que la subducción. La deformación en el modelo tiene una fuerte partición. Por sobre los planos de subducción, se desarrolla una zona de deformación distribuida, análoga a una faja plegada y corrida creciendo hacia el antepaís (pro-lado). Detrás de esta zona (retro-lado) y de manera sincrónica, se desarrolla una zona de deformación focalizada, caracterizada por una sola estructura de alto ángulo y con vergencia solidaria al plano de subducción. Esta zona de deformación trasera comienza a expandirse a medida que la subducción en el pro-lado de la cuña se incrementa, alzándose por sobre una sección plana no-deformada entre las dos cuñas del modelo, que se asemeja al Valle Central de Antearco justo al oeste de los Andes Chilenos.

Considerando las limitaciones del modelo análogo, los resultados son contrastados con la estructura de primer orden de los Andes Centrales. El análisis comparativo muestra las similitudes entre el desarrollo de estructuras del pro-lado de la cuña y la evolución tectónica de las fajas plegadas y corridas en Argentina y Bolivia. Con respecto a los Andes del norte de Chile, la propagación miocena del frente orogénico de la Cordillera Occidental se corresponde con la expansión del retro-lado de la cuña modelada. La similitud entre las características de primer orden del modelo con la estructura cortical observada en el margen permite concluir que la Cordillera Occidental estaría subyacida por una estructura similar a la desarrollada en el lado trasero de este tipo de modelos, creciendo por la acomodación de material por debajo del orógeno desde el este.

ABSTRACT

Orogeny in the Central Andes is the product of active subduction below the western margin of South America. The Cenozoic building of the Western Cordillera has been ascribed to magmatic addition and volcanism associated with subduction of an oceanic plate, but more importantly, to processes related to intracontinental, Ampherer-type, subduction. Despite the increasing geological and geophysical data published in the past ten years, the polarity of this subduction and main direction of tectonic transport (or vergence) are still strongly debated in the case of the Central and Southern Central Andes. This suggests that it is necessary to revisit this evidence in the context of mechanical models that illustrate how orogens "work". These models should include the mechanisms of material distribution and accommodation operating below convergent orogens, and their relationship with crustal-scale structures and boundary conditions (direction of subduction) comparable to those operating below the Andes.

In this work, a combination of tectonostratigraphy and analogue modeling of doubly-vergent subduction wedges is presented to approach the aforementioned problem. The tectonostratigraphy of the Western Cordillera of northern Chile at ~19.5°S suggests that the range is underlain by a crustal-scale pop-up, formed by tectonic shortening and subsequent thickening, in combination with magmatic addition. U-Pb ages in deformed rock units suggest that contraction took place as early as 49 Ma (middle Eocene), and that deformation was active during most of the Neogene. The synchronicity between the deformation in the Western Cordillera and the tectonic events that took place in the Subandean Sierras suggests that they were mechanically coupled. On the other hand, the analogue model provides a cross-sectional demonstration of the distribution and deformation of material accreted into the wedges within a setting similar to the Andean geodynamic scenario. In a single model, one subduction wedge is analogue to the Coastal Cordillera whilst a second subduction wedge is analogue to the Western Cordillera. Each wedge grows above a respective subduction plane, but the wedge analogue to the Western Cordillera grows by accretion of a much thicker section. A PIV (Particle Image Velocimetry) analysis applied to the model allowed the visualization of instantaneous velocity, strain rate and kinematic vorticity of the material inside the wedges. Movements inside the wedges are predominantly lateral, with decreasing velocities in the same sense of subduction. Deformation in the model is partitioned and strongly asymmetrical. Above the subduction plane (AKA pro-side), there is a zone of distributed deformation, analogue to a foreland fold-and-thrust belt. Towards the back (retro-side), a single, high-angle shear zone develops synchronously, thrusting material towards the rear at a slower rate compared to propagation of deformation towards the pro-side. This deformation zone begins to expand towards the rear when cumulative subduction and shortening on the pro-side are high, overriding a flat zone between the two wedges, which in the model resembles the forearc Central Valley of Chile.

Considering all limitations of the analogue model, the results are contrasted with the first-order structure of the Central Andes. The comparative analysis shows similarities between pro-side structure development and the tectonic evolution of fold-and-thrust belts of Argentina and Bolivia. Regarding the Andes of northern Chile, the Miocene propagation of the Western Cordillera monoclines is similar to the rearward propagation of the retro-side of the modeled wedge. The correspondence allows to conclude that the Western Cordillera could be underlain by a westward propagating structure, similar to the one developed in the rear of this type of model, growing by accommodation of material incorporated below the orogen from the east.

AGRADECIMIENTOS

Quisiera agradecer a los miembros de la comisión evaluadora, por su valioso apoyo y retroalimentación recibidos en distintos pasajes de la realización de esta tesis. Agradezco a Luisa Pinto por darme la oportunidad de realizar este doctorado bajo su tutela, por contagiarme con su pasión por la modelación analógica, por siempre motivarme y empujarme a ser mejor, sobre todo en las etapas más tempranas de este proyecto- en especial, cuando trabajamos juntos estudiando la geología del norte de Chile. Agradezco a Marcelo Farías por el apoyo que me brindó cuando necesité de guía adicional, por contagiarme con su interés por la cordillera, los complejos de subducción y por mostrarme la dirección final que este proyecto terminó tomando. Agradezco a Mark Brandon por acogerme como su alumno durante mi pasantía doctoral en Estados Unidos, por darme la confianza para usar su laboratorio y por incluirme en su grupo de trabajo como uno más de los suyos. Agradezco a Pamela Jara y a Reynaldo Charrier por sus cuidadosas revisiones, observaciones y recomendaciones durante la parte final de este proceso.

Quisiera agradecer a mis compañeros del programa de doctorado en la Universidad de Chile dedicados a la geología estructural y a la geodinámica. Agradezco a Andrea Navarro, Camila Arróspide, Marcia Ojeda, Huber Rivera, Mario Pérsico, José Araya, Francisca Sandoval, por los buenos momentos que pasamos siendo ayudantes o trabajando en la sala de postgrado, en el aula y en terreno. De la misma manera agradezco a quienes conocí en la Universidad de Yale durante mi pasantía doctoral, a Lucas Fennell Neta Bar y Drew Syverson.

Agradezco especialmente a los colegas Javier Álvarez, Matías Peña, Ítalo Payacán, Javier Reyes y Sebastián Bascuñán por siempre estar presentes y por siempre proporcionar la cuota de humor necesaria para soportar el mundo de las geociencias. Agradezco de todo corazón a Iván Gómez y a Pablo Molina, por ser los buenos amigos que son, por todos los momentos compartidos en terreno, y por haberme brindado todo su apoyo durante los momentos más difíciles durante la realización de este proyecto.

A Sarah, mi compañera, por haberme acompañado y apoyado durante la etapa de redacción de esta tesis, por creer en mí cuando yo no fui capaz de hacerlo.

Finalmente, agradezco a mi madre, Marta, a mi padre, Miguel, a mi hermano Benjamín y a mi abuela Rosa, por todo el amor que me brindaron y que me siguen brindando. Gracias a ellos terminé este trabajo.

Este trabajo fue financiado por el Ministerio de Educación de Chile, a través de la Beca de Doctorado Nacional CONICYT #21160380.

TABLE OF CONTENT

2. TECTONOSTRATIGRAPHY OF THE NORTERN CHILE WESTERN CORDILLERA: CENTRAL ANDES AT 19°S

FIGURE INDEX

1. INTRODUCTION

1.1. Context, presentation of the scientific problem and working hypotheses

The Central Andes (Fig. 1A) are the archetype of an active subduction-related orogenic system, currently involving the oceanic Nazca plate and the western continental margin of South America (e.g., Isacks, 1988). In this deforming region, ocean-continent subduction has been occurring continuously since Carboniferous times (Mpodozis and Ramos, 1989; Charrier et al., 2007; Oliveros et al., 2019). However, modern Andean orogeny began rather recently in the late Cretaceous and continued throughout the Cenozoic (DeCelles and Horton, 2003; Ramos et al., 2004; McQuarrie et al., 2005; Arriagada et al., 2006; 2008; Bascuñán et al., 2016; Fennell et al., 2017; Boyce et al., 2019). Structural accommodation of tectonic shortening has contributed to a significant fraction of the current thickness of the Andean crust, with estimations ranging from 50% to 100% (e.g., Allmendinger et al., 1990; 1997; Kley and Monaldi, 1998; McQuarrie, 2002). Unravelling the structural evolution of the orogenic crust is then fundamental for the understanding of the first-order tectonic mechanisms operating beneath the Andes.

Geologists and geophysicists have determined the styles of Andean structure, have measured crustal shortening (e.g., Roeder, 1988; Sempere et al. 1990; Sheffels 1990; Baby et al., 1997; Kley and Monaldi, 1998; Kley et al., 1999; 2002; McQuarrie, 2002; Ramos et al., 2004; Pearson et al., 2013; Farías et al., 2010; Giambiagi et al., 2014; Anderson et al., 2017) and have shed light on the current nature of the lithosphere, mantle and crustal seismicity beneath the margin (e.g., Isacks, 1988; Wigger et al., 1994; Yuan et al., 2000; Beck and Zandt, 2002; Chase et al., 2009; Tassara et al., 2006; Farías et al.. 2010; Tassara and Echaurren, 2012; Metcalf and Kapp, 2014; Comte et al., 2019). This large body of data combined with tectonostratigraphic (e.g., Charrier et al., 2007; 2013), thermochronological (e.g., Barnes and Ehlers, 2009; Lossada et al., 2017; Rodríguez et al., 2018) and petrological (e.g., Kay and Coira, 2009; Muñoz et al., 2013) studies have been key to comprehend Andean evolution and its relationship with the dynamics of the governing subduction processes. The tectonostratigraphy of deforming regions -the "vertical and lateral lithological variations resulting from tectonic, magmatic and/or sedimentary processes prior to, or during exhumation or subduction", (Brovarone et al., 2018)- provide insights to the geometry, kinematics and time of crustal deformation. In particular, along the northern Chile Western Cordillera and western Altiplano

(Figure 1), a west-vergent system of monoclinal folds evolved synchronous to the emplacement of the Eastern Cordillera and Subandean Sierras of the eastern Altiplano flank. This synchronicity suggests that there is a mechanical coupling between these morphostructures. However, there is still a lack of consensus on the nature (polarity) of intracontinental subduction and its relationship with the structural evolution at both sides and along the region comprising the wide Altiplano at 15°S-25°S and the narrow Principal Cordillera at 30°S-35°S (e.g., Farías et al., 2005; 2010; Armijo et al., 2010; 2015).

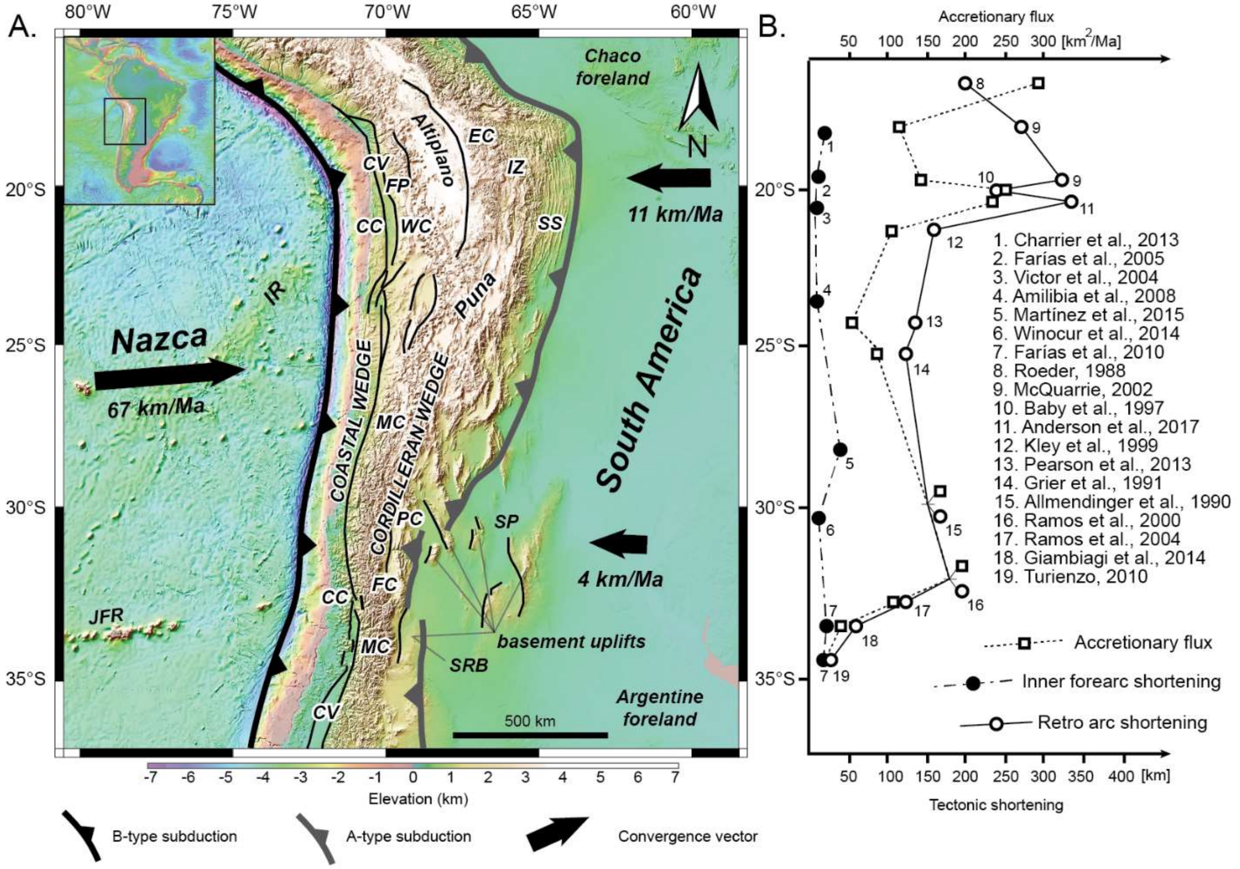

Figure 1. A. Tectonic scenario of western South America above SRTM15+ topography and bathymetry of Tozer et al. (2019) and **B. Shortening estimates along the western (inner forearc) and eastern (retroarc) sides of the Andes**. In A., main morphostructural features and structural boundaries of the Central and Southern Central Andes are shown: CC: Coastal Cordillera; CV: Central Valley; FP: Forearc Precordillera; WC: Western Cordillera; EC: Eastern Cordillera; IZ: Interandean Zone; SS: Subandean Sierras; MC: Main Cordillera; FC: Frontal Cordillera; PC: Precordillera; SP: Sierras Pampeanas; SRB: San Rafael Block; IR: Iquique Ridge; JFR: Juan Fernández Ridge. B- (Benioff) and A- (Ampherer) type subduction boundaries are drawn after Bally (1975). Convergence rates are adjusted to the forearc-fixed reference frame, based on the absolute plate motions of Gripp and Gordon (2002) (Nazca Plate) adjusted to retroarc shortening rates (references in B), in agreement with the continental velocity fields of Brooks et al. (2003; 2011). Estimations of accretionary fluxes in (B) are based on the corresponding shortening rate and depth-to-main detachment of the retroarc thrust system (references in figure). Adapted from Herrera et al. (in prep.).

On the other hand, subduction wedge models for shortening of the lithosphere offer additional insight into the interplay between the structural evolution of mountain belts and deep subduction processes. The application of these models to natural systems is important because they provide proof of concept for underlying assumptions that are essential in understanding the internal mechanics involved in the growth of mountain belts (e.g., Malavieille, 1984; 2010; Willettt et al., 1993; Jamieson and Beaumont, 2013). In other words, subduction wedge models demonstrate how an orogen mechanically "works", illustrating the growth, internal kinematics and deformation of double-sided crustal-scale accretionary wedges above a velocity discontinuity, singularity, or S-point (e.g., Davis et al., 1983; Fig. 2A, Malavieille, 1984; Fig. 2B, Willettt et al., 1993). Growth of these wedges is self-similar, driven by material accretion triggering internal deformation, rotation and strong lateral material displacements, resulting in wedge thickening and asymmetric lateral expansion (Malavieille, 1984; Willettt et al., 1993). The scientific literature is actually rich in publications where these models (e.g., Fig. 2A and 2B) reconcile a diverse array of tectonic and geological features observed in many orogens developed above subduction zones. A few examples are the European Alps (Fig. 2C, e.g., Malavieille; 1984; 2010; Brandon, 2004), Taiwan (Davis et al., 1983; Malavieille et al., 2019), the Eastern Cordillera of Colombia (Nemcok et al., 2013), Zagros (McClay et al., 2004), New Zealand (Koons, 1990; Beaumont et al., 1996) and Cascadia (Fig. 2D, Brandon, 2004). The reason for this strong model-prototype similarity is that these simple models are developed under the same boundary conditions operating upon natural systems: an upper coulomb layer (or layers) analogue to the upper crust, deforming above strong converging rigid plates analogue to the upper mantle.

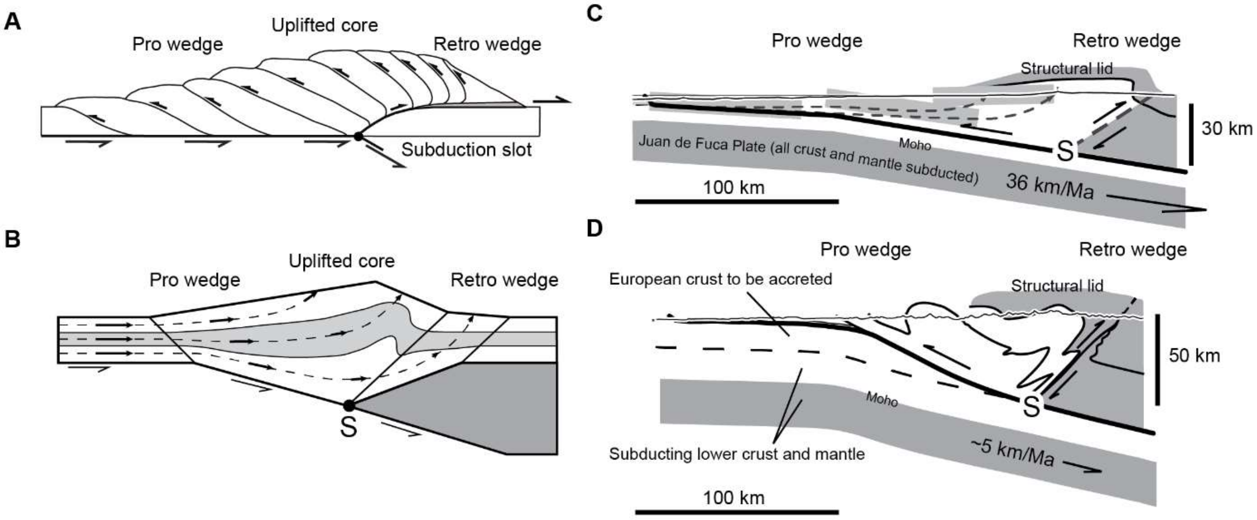

Figure 2. Mechanical models for shortening of the lithosphere and natural examples. **A.** Doubly-vergent sand wedge of Malavieille (1984). **B.** Doubly-vergent numerical wedge considering the effects of isostasy and temperature (adapted from Willettt et al., 1993). **C.** Cross-section of the Cascadia and **D.** European Alps orogenic wedges (adapted from Brandon, 2004).

Despite the fact that the Central Andes are certainly a subduction-related orogenic system, very few studies have analyzed Andean orogenic structure under the scope of mechanical models of lithospheric shortening and thickening (Pope and Willett, 1998; Sobolev and Babeyko, 2004; Babeyko and Sobolev, 2005; Vietor and Oncken; 2005). Lithospheric-scale structures accommodating growth of the high Andes indeed share some fundamental aspects with both models and orogens described above (e.g., Baby et al., 1997; Beck and Zandt, 2002; Ramos et al., 2004; Farías et al., 2010; DeCelles et al., 2014), suggesting that there might be a correspondence between such models and Andean architecture. Certainly, the structure of the Coastal Cordillera of central Chile was explained in terms of a crustal-scale subduction wedge model (Comte et al., 2019) and, as well, Martinod et al. (2020) suggested that the evolution of the Altiplano can be envisioned as a result of growth and expansion of laterally distinct orogen-scale crustal wedges. The cited mechanical models, combined with new specific geological data open new research possibilities, as the application of S-point models to the entire Andean range rises as a tenable approach.

Simple comparisons along the Andes show remarkable east-to-west and north-to-south first-order morphostructural transitions that are useful for validating the application of a subduction wedge model. The entire Andean retro arc (eastern Andean slope) is underlain by east-vergent fold-and-thrust belts grown by accretion of a thick section (up to 50 km; Baby et al., 1997) of Paleozoic and Mesozoic rocks composing the South American basement (Fig. 1 and Fig. 3; e.g., Roeder, 1988; Baby et al., 1997; McQuarrie, 2002; Ramos et al., 2004; Pearson et al., 2013; Giambiagi et al., 2014). Horizontal shortenings below the eastern slope range from c. 70 km in western central Argentina (~33.5°S, Fig. 1B; Giambiagi et al., 2014) increasing northwards, reaching maximum values of c. 330 km at the Altiplano plateau (~19°S, Fig. 1B; McQuarrie, 2002). Orogenic topography as well increases from south to north. At the latitude of Santiago, Chile (33.5°S) Southern Central Andes are a narrow chain with moderate average elevations and crustal thicknesses (e.g., Farías et al., 2010; Giambiagi et al., 2014). In turn, the Central Andes at 19°S are ~600 km wide (Fig. 1), have a very thick crust (~75 km, e.g., Yuan et al., 2000; Beck and Zandt, 2002) and an anomalous high heat flow (Springer and Forster; 1998). On the other hand, the inner forearc (western Andean slope; Fig. 1) is structured by narrow thrust belts that have accommodated relatively low shortenings (<40 km; Fig. 1B) but have contributed significantly to modern Andean uplift (e.g., Charrier et al., 2013; Farías et al., 2005; 2010; Victor et al., 2004; Martínez et al., 2016; Fuentes et al., 2018). Considering the aforementioned structure of the eastern Andean slope, a strong asymmetry from side to side thus characterizes the cross-sectional Andean orogenic structure and morphology.

These across- and along-strike morphostructural transitions works to the advantage of this work, as they would provide of a space-for-time representation for the evolution of the orogenic topography and underlying structure of the range, which is to be explained in terms of a subduction wedge model applied to the orogen. The fundamental hypotheses of this work is that the Southern Central Andes show an “initial” orogenic configuration of the margin, in which two crustal-scale subduction wedges of similar dimensions are separated by a tectonically stable longitudinal central valley: a Coastal wedge to the west, associated with subduction of the oceanic plate beneath the forearc, and a Cordilleran wedge to the east, grown by accretion from the eastern foreland, in association with westward subduction of the South American lithosphere. The rates of retro arc accretion increase northwards, and account for the middle-late Miocene westward expansion of the Central Andes Western Cordillera along the western flank of the Altiplano. A good correspondence between the structure of the Andes and the mechanics observed in model subduction wedges is expected to be found.

1.2. Objectives

General Objective

The general objective of this dissertation is to provide a tenable mechanical subduction wedge model for the tectonic evolution of the Central and Southern Central Andean orogen, particularly, for the Andes of northern Chile. The model should demonstrate proof of concept of underlying assumptions on Andean orogeny, and as well show good correspondence with the geology and structure of the range.

This general objective encompasses the following specific objectives, established to answer the key questions outlined above.

Specific Objectives

1. To illustrate the mechanical behavior and evolution of a crustal orogenic wedge by means of an analogue model for lithospheric shortening and thickening, set up with boundary conditions compatible to the Andean tectonic scenario, providing insight to mechanical processes operating within a subduction wedge.
2. To compare the results to the geology and first order crustal architecture of the Andes of northern Chile, providing insight on mechanisms possibly operating beneath this side of the range.
3. To understand and explain the along-strike morphostructural segmentation and transitions of the Andes at different latitudes in terms of the evolution of the analogue model and other working models for lithospheric shortening.

1.3. Methodologies

To accomplish the general objective, the main methodology implemented in this thesis is the development of an analogue sandbox model, with a setup designed to emulate convergence of lithospheric plates. The setting of the model will be compatible with a subduction advance setting, a situation in which the overriding plate advances towards the subduction zone, that applies to the tectonic configuration of almost the entire Central and Southern Central Andes. To assure the correspondence between model and prototype, an exhaustive bibliographic review on geodynamics of subduction, orogenic evolution and Andean tectonics is conducted.

For specific objective 1, key mechanical aspects (e.g., instantaneous velocity field, strain distribution and kinematic vorticity) of the analogue model will be visualized by means of a Particle Image Velocimetry (PIV) technique. These key aspects, together with broader observations on the model will be extrapolated to the orogenic processes possibly operating underneath the Andes and other orogens.

For the second specific objective, different phases of model evolution will be compared to the main morphology, geology and first-order structure of the Central and Southern Central Andes at different segments of the range. In particular, a detailed tectonostratigraphic study of the Western Cordillera of northern Chile provides details on timing and geometry of this first-order structure. In the discussion, correspondence between model and prototype is addressed.

For specific objective 3, model results and crustal-scale cross-sections of the different segments of the Central and Southern Central Andes will be paralleled with working models for orogenesis and other natural prototypes. Different segments of the Andes will be classified within a Temperature-Magnitude framework for growing orogens.

2. TECTONOSTRATIGRAPHY OF THE NORTERN CHILE WESTERN CORDILLERA AT ~19°S

The Central Andes of northern Chile include the Present western orogenic front adjacent to the Altiplano plateau and have been formed as a result of late Cretaceous-Cenozoic plate reorganizations at the Nazca (and former oceanic plates)-South America plate boundary. At ~19°S, the Andean Precordillera, Western Cordillera and western Altiplano are relatively well accessible and have received attention mainly for its structure, its volcanism, and as a target for the exploration of ore deposits. Several studies carried out along the Chilean flank of the Altiplano have focused on the western monoclines of the Precordillera and on the associated syntectonic deposits that have accumulated adjacent to these structures, allowing a good determination of chronological constraints on structural activity in this part of the Andes (e.g., Pinto et al., 2004; García et al., 2004; Victor et al., 2004; Farías et al., 2005). Seismic surveys have aided this understanding, yielding information on the subsurface structure (e.g., Victor et al., 2004; Farías et al., 2005; Arriagada et al., 2006; Fuentes et al., 2018; Martínez et al., 2021). In turn, to the east, towards the volcanic front and plateau, both stratigraphy and structure are less well documented as they are obscured by recent and widespread volcanic and sedimentary deposits. This said, the tectonostratigraphy of the entire western flank of the Altiplano appears as a key aspect to be unraveled to better constrain the timing and style of the deformation, and its possible synchronicity with other major Andean morphostructures.

In this chapter, new stratigraphic, structural and geochronological data from the Chilean Western Cordillera (Altiplano western flank) is presented. They show that the entire Western Cordillera was uplifted synchronically during most of the Neogene above a doubly-vergent "pop-up" crustal structure, and that tectonic shortening has been occurring as early as the middle Eocene (c. 49 Ma). These results and the timing of deformation in the Eastern Cordillera and Subandean Sierras suggest that both flanks of the plateau have been mechanically coupled in association with the westward subduction of the South American craton.

Andean Geology 44 (2): 87-122. May, 2017 ***Andean Geology***

doi: 10.5027/andgeoV44n2-a01 *www.andeangeology.cl*

Cenozoic tectonostratigraphic evolution and architecture of the Central Andes in northern Chile based on the Aquine region, Western Cordillera (19°-19º30' S)

***Sebastián Herrera[1], Luisa Pinto[1], Katja Deckart[1, 2],**

Javier Cortés[1], Javier Ignacio Valenzuela[1]

[1] *Departamento de Geología, FCFM, Universidad de Chile, Plaza Ercilla 803, Casilla 13518, Correo 21, Santiago, Chile. sebherre@ing.uchile.cl; lpinto@ing.uchile.cl; kdeckart@ing.uchile.cl; jacortes@ing.uchile.cl; valenvolke@gmail.com*

[2] *Advanced Mining Technology Center (AMTC), Universidad de Chile, Tupper 2007, Santiago, Chile.*

**Corresponding author: sebherre@ing.uchile.cl*

ABSTRACT. Crustal thickening by horizontal shortening and associated deformation have been broadly considered as prime mechanisms for mountain building in the Central Andes of western South America. However, timing and structural style of Andean orogeny in northernmost Chile remains to be fully understood. By means of this contribution we attempt to unravel the Cenozoic tectonostratigraphy and structural architecture of a narrow segment within the Western Cordillera (western flank of the Altiplano plateau), based on detailed structural mapping, available and new geochronological data gathered from the Aquine region (~19°15' S). The geology of this area indicates that compressive tectonics dominated for ~21 Myr, between 27 Ma and 6 Ma, and that onset of deformation probably occurred in the middle Eocene (after *ca*. 49 Ma). According to angular unconformities registered throughout the region, three principal compressive episodes have been determined: **(1)** middle Eocene-late Oligocene (*ca*. 49-27 Ma); **(2)** late Oligocene-middle Miocene (*ca*. 27-14 Ma); and **(3)** middle-latest Miocene, 14-6 Ma. Paleogene and Neogene structural development within the Aquine region was concomitant to activity on the bordering West and East Vergent Thrust Systems (WTS and ETS), which controlled uplift of the western Altiplano since the late Oligocene-early Miocene, located at the foot of the Precordillera and within the eastern part of the Western Cordillera, respectively. Major structures in the western segment of the region are high-angle, east-vergent, substratum-involving thrusts that affect late Mesozoic and Cenozoic volcanic and sedimentary intra-arc deposits. Unalike, a west-vergent fold-and-thrust belt is developed in the southeastern segment of the region, involving only Miocene deposits. These contrasting structural styles and opposite vergences indicate a combination of thin- and thick-skinned tectonics in a "*pop-up*" like structural array. Growth strata and sedimentological features in alluvial and fluvial sandstones and conglomerates of the upper Miocene Mauque Formation suggest the occurrence of syntectonic deposition. In addition, gentle angular unconformities within upper Oligocene-upper Miocene arc deposits suggest that sedimentation and volcanism developed synchronic to compressive tectonics throughout the Miocene and coeval to deposition in the active bordering thrust systems (WTS and ETS). The interpreted tectonostratigraphic development of the study area is similar to but slightly diachronic with the Cenozoic evolution in the Belén region (18°-19° S) of northernmost Chile. We interpret that east- and west-vergent thrusts within the Western Cordillera, are deeply rooted in a crustal-scale *"pop-up"* structure that accommodated Cenozoic deformation on the western flank of the Altiplano. Uplift as a consequence of contraction along the Western Cordillera was coeval to late Paleogene block exhumation and subsequent Neogene development of fold-and-thrust belts on the eastern border of the Altiplano. The main structural characteristics within the Aquine region suggest that inversion of an Upper Cretaceous intra-arc basin was of major relevance for the Cenozoic structural development of the Western Cordillera.

Keywords: Central Andes, Structure, Western Cordillera, Western Altiplano, Syntectonic deposits, U-Pb ages.

RESUMEN. Evolución tectonoestratigráfica y arquitectura cenozoica de los Andes Centrales en el norte de Chile, región de Aquine, Cordillera Occidental (19°-19°30' S). La deformación y el engrosamiento cortical por acortamiento horizontal han sido ampliamente considerados como mecanismos primordiales involucrados en la construcción de los Andes Centrales. No obstante, el estilo estructural y la temporalidad de la orogenia Andina en el extremo norte de Chile son aún objeto de debate. Basada en un registro detallado de la geología de la región de Aquine (~19°15' S), nuevas edades U-Pb y la geocronología disponible, por medio de esta contribución intentamos dilucidar la tectonoestratigrafía cenozoica y la arquitectura de un angosto segmento de la Cordillera Occidental (flanco occidental del Altiplano). En esta área, la geología indica que durante ~21 Myr, la región estuvo sometida a condiciones tectónicas compresivas, entre los 27 Ma y 6 Ma. Este régimen contraccional se habría iniciado durante el Eoceno medio (post- ~49 Ma). De acuerdo con las discordancias angulares registradas en la región, tres episodios contraccionales han sido determinados: **(1)** Eoceno medio-Oligoceno tardío (*ca.* 49-27 Ma); **(2)** Oligoceno tardío-Mioceno medio (*ca.* 27-14 Ma); y **(3)** Mioceno medio-tardío 14-6 Ma. El desarrollo estructural Paleógeno y Neógeno asociado fue concomitante con la actividad tectónica en los sistemas regionales de cabalgamientos de vergencia al oeste (WTS) y al este (ETS), situados en los márgenes occidental y oriental de la Cordillera Occidental, respectivamente, y que controlaron el alzamiento tectónico del Altiplano occidental desde el Oligoceno tardío-Mioceno temprano. Las mayores estructuras en el segmento occidental de la región corresponden a fallas inversas de alto ángulo que involucran substrato Mesozoico y afectan a depósitos del Mesozoico tardío y depósitos sedimentarios y volcánicos del intraarco Cenozoico con una vergencia al este. De manera contrastante, una faja plegada y corrida vergente al oeste se desarrolla en el segmento suroriental de la región, deformando solo depósitos miocenos. Las vergencias y estilos contrastantes de las estructuras indican una combinación de tectónica de "piel fina" y "piel gruesa", desarrollada en un arreglo estructural de tipo *pop-up*. Estratos de crecimiento y características sedimentológicas asociadas a depositación sintectónica en areniscas y conglomerados aluviales y fluviales de la Formación Mauque (Mioceno superior), además de suaves discordancias angulares entre depósitos del arco Oligoceno superior-Mioceno sugieren que la sedimentación y el volcanismo ocurrieron sincrónicos a la tectónica compresiva y a la depositación asociada a los sistemas estructurales regionales marginales activos (WTS y ETS). La evolución tectonoestratigráfica interpretada para la región es similar, aunque levemente diacrónica a la evolución cenozoica de la región de Belén (18°-19° S), en el extremo norte de Chile. Interpretamos que las fallas inversas de la Cordillera Occidental, vergentes al este y al oeste, están enraizadas en una estructura tipo *pop-up* de escala cortical que acomodó deformación Cenozoica en el flanco occidental del Altiplano. El alzamiento originado por contracción a lo largo de la Cordillera Occidental fue coetáneo a la exhumación de bloques durante el Paleógeno tardío y al subsecuente desarrollo de fajas plegadas y corridas durante el Neógeno, en el flanco oriental del Altiplano. La estructura de la región de Aquine sugiere que la inversión de la cuenca del intraarco del Cretácico Superior tuvo un control sustancial en el desarrollo estructural del Cenozoico de la Cordillera Occidental.

Palabras clave: Andes centrales, Estructura, Cordillera occidental, Altiplano occidental, Depósitos sintectónicos, Edades U-Pb.

1. Introduction

In a constant attempt to unravel the evolution of Andean uplift, numerous studies have taken place along this long-lived, subduction-related, cordilleran-type mountain belt (*sensu* Dewy and Bird, 1970), of which many have focused on the formation of the Altiplano plateau (*e.g.*, Isacks, 1988; Allmendinger *et al.*, 1997; Lamb *et al.*, 1997; Gregory-Wodzicki, 2000; Elger *et al.*, 2005; McQuarrie *et al.*, 2005; Barnes *et al.*, 2008; Barnes and Ehlers, 2009; Hartley and Evenstar, 2010; Jordan *et al.*, 2010; Charrier *et al.*, 2013; Garzione *et al.*, 2014). Crustal thickening by horizontal shortening and associated deformation has been evoked as a prime mechanism for mountain building throughout the western margin of South America (Isacks, 1988; Allmendinger *et al.*, 1997) and for bending of the Bolivian orocline (*e.g.*, Isacks, 1988; Arriagada *et al.*, 2008). Other factors proposed to have controlled orogeny of the Andes are magmatic addition to the lithosphere, lower-crustal ductile flow (*e.g.*, Isacks, 1988; Allmendinger *et al.*, 1997), lower lithosphere removal or delamination (*e.g.*, Garzione *et al.*, 2006, 2014), orogen-scale westward tilting (*e.g.*, Lamb *et al.*, 1997; Farías *et al.*, 2005; Jordan *et al.*, 2010), isostatic balancing of crustal deformation (*e.g.*, Victor *et al* ., 2004; Farías *et al.*, 2005) and massive surface erosion (*e.g.*, Montgomery *et al.*, 2001).

The structural evolution of the morphostructures east of the Altiplano have been intensively studied (Fig. 1a) and shows the following sequence: deformation and initial block exhumation migrated eastwards through the Eastern Cordillera during the Eocene and early Oligocene (*ca.* 40-30 Ma), across the Interandean Zone during the late Oligocene-

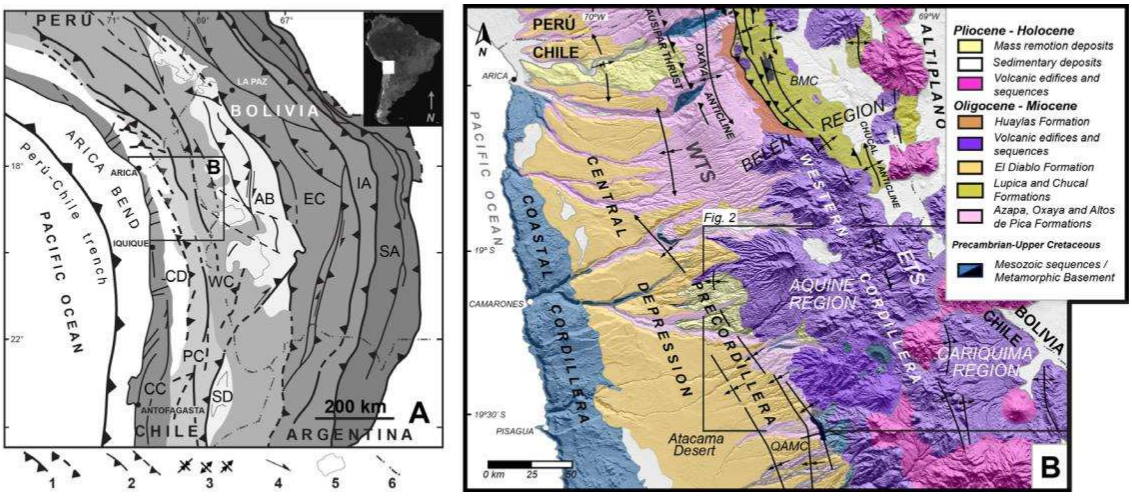

FIG. 1. **A.** Physiography of the Central Andes and thrust systems that define the limits of labeled morphostructural provinces. The Interandean Zone is included as part of the eastern margin of the Eastern Cordillera. **SA:** Subandean ranges; **IA:** Interandean ranges; **EC:** Eastern Cordillera; **AB:** Altiplano Basin; **WC:** Western Cordillera; **PC:** Precordillera; **CD:** Central Depression; Coastal Cordillera; **SD:** Salars Depression; (Modified from Charrier *et al.*, 2013); **B.** Simplified geological map of northernmost Chile (~18°30'-19°30' S) (Modified from García *et al.*, 2004, 2011; Charrier *et al.*, 2007, 2013; Cortés *et al.*, 2012a). **BMC:** Belén Metamorphic Complex; **QAMC:** Quebrada Aroma Metaturbiditic Complex; **WTS:** West Vergent Thrust System; **ETS:** East Vergent Thrust System. Simbology: **1.** Major thrusts; **2.** Secondary faults and structural alignments; **3.** Syncline, anticline and monocline axis; **4.** Strike-slip direction of displacement; **5.** Major lakes and salars; **6.** International border.

Miocene (*ca.* 25-18 Ma), and into the Subandean Sierras during most of the Neogene (*ca.* 20-0 Ma) (McQuarrie *et al*., 2005; Barnes *et al* ., 2012), by means of thick- and thin-skinned, mainly east-vergent, but also doubly-vergent, fold-and-thrust systems.

In contrast, the structural geology of the western border of the Altiplano in Chile, adjacent to Bolivia and northwestern Argentina (Fig. 1), is obscured by widespread Neogene volcanic products of the Andean Central Volcanic Zone, limiting our access and understanding of the Mesozoic, Paleogene and even Neogene Andean structural history in this area. Within this sector, the geology of the Western Cordillera and Precordillera indicates a complex history of long-lived compressive tectonics, which includes middle Eocene deformation (Incaic compressive phase) (*e.g.*, Steinmann, 1929; Cornejo *et al.*, 2003; Charrier *et al.*, 2007; 2009), which has been correlated with a significant increase in the velocity of plate convergence during this epoch (Pardo-Casas and Molnar, 1987), and possibly an Early to Late Cretaceous compressive event (Peruvian phase, *e.g.*, Steinmann, 1929; Jaillard, 1992; Bascuñán *et al.*, 2015) and a Late Cretaceous-early Cenozoic compressive event (K-T phase; Cornejo *et al.*, 2003; Charrier *et al.*, 2007, 2009, 2013).

During the Neogene, the Western Cordillera and its magmatic arc (Fig. 1) developed continuously under a compressive tectonic regime since the late Oligocene - early Miocene, beginning with the Quechua phase of Mégard (1984), which is correlated with another major increase in the velocity of plate convergence at *ca.* 30-20 Ma (Pardo-Casas and Molnar, 1987; Somoza, 1998). Since this time, two deeply-rooted, orogen-scale thrust systems, with opposite vergences and NNW-SSE to N-S trends, developed aligned and along both the Western Cordillera and Precordillera (Charrier *et al*., 2013) (Fig. 2), with the West-Vergent Thrust System (WTS) located within the Precordillera (Muñoz and Charrier, 1996; Victor *et al*., 2004; Farías *et al*., 2005; García and Hérail, 2005; García *et al*., 2011) and the East-Vergent Thrust System (ETS) located within the Western Cordillera, in the present-day arc (Charrier *et al*., 2005; Farías *et al*., 2005; Cortés *et al*., 2012a). These systems controlled the Neogene structural and depositional evolution of this part of the Andes (Charrier *et al*., 2007, 2013;

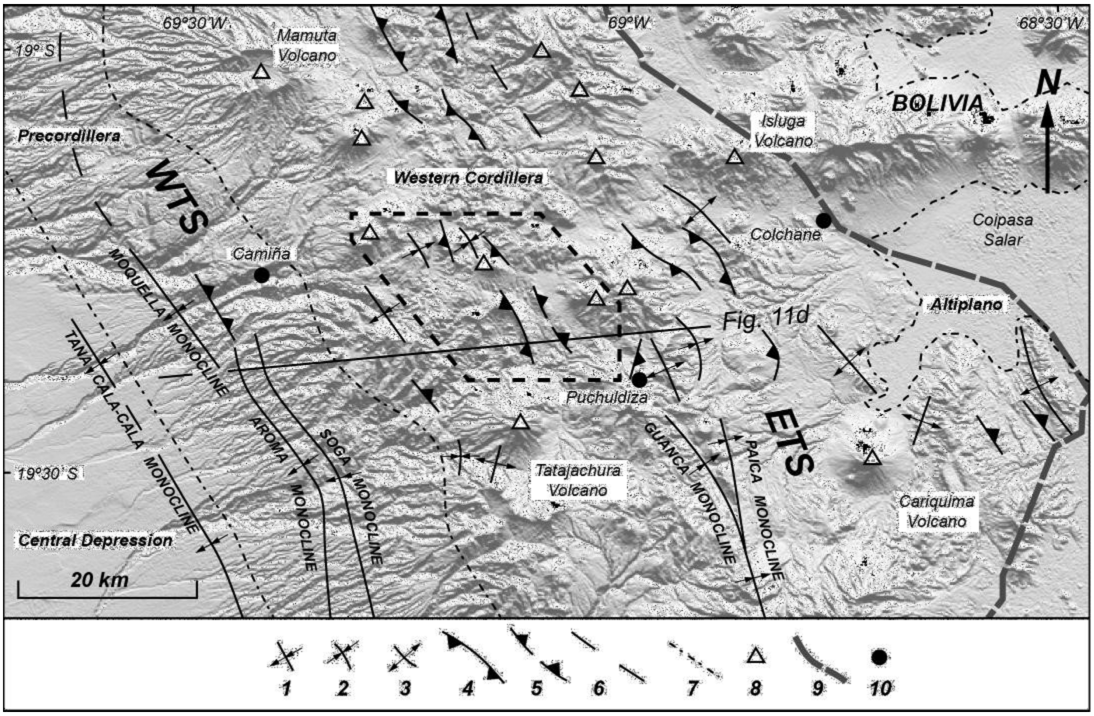

FIG. 2. STRM DEM based shaded relief image for the Western Cordillera, and adjacent Precordillera and Altiplano. Main structures are taken from Pinto *et al.* (2004), Farías *et al.* (2005), Cortés *et al.* (2012a,b), García *et al.* (2013), Herrera *et al.* (2013), Cortés *et al.* (2014), Valenzuela *et al.* (2014), and this study. **WTS:** West Vergent Thrust System; **ETS:** East Vergent Thrust System. Simbology: **1.** Monocline; **2.** Syncline; **3.** Anticline; **4.** Thrust; **5.** Covered thrust; **6.** Inferred structure; **7.** Approximate limits of Andean morphostructures; **8.** Miocene to Holocene volcanic center; **9.** International border; **10.** Town/village. Polygon encloses the geological map for this study, shown in figure 4 and the location of the model cross section in figure 11 is indicated.

García *et al.*, 2011), exerting a substantial role in the construction of the present-day relief of the region (Muñoz and Sepúlveda, 1992; Muñoz and Charrier, 1996; Pinto *et al.*, 2004; Victor *et al.*, 2004; Charrier *et al.*, 2005; Farías *et al.*, 2005; Jordan *et al.,* 2010; Cortés *et al* ., 2012a, b). Nonetheless, the detailed temporal and geometrical interrelationship of these structural systems has not yet been well established, nor the role they have played in controlling the lithostratigraphy and structure of the region lying between them. Understanding the relationship of these two structural systems is crucial for comprehending the Cenozoic structural evolution of the western border of the Altiplano.

We have focused on a region of the Western Cordillera in the Central Andes (the Aquine region; 19°15' S-19°30' S) between the WTS and ETS (Fig. 2), which exhibits a narrow (~25 km) but elongate area in which deformed Mesozoic and Cenozoic volcanic and sedimentary rocks are well exposed. This occurrence has allowed us to carry out an integrated structural, stratigraphical and geochronological analysis of the Western Cordillera. The main objective of this contribution is to elucidate the timing and style of deformation in the Western Cordillera by integrating available and new geochronological data with detailed stratigraphy and structural mapping. Our purpose is to generate a coherent conceptual model for the Cenozoic structural and depositional evolution of the Western Cordillera in order to clarify the relationship between the WTS and ETS.

2. Geological setting

2.1. General geodynamic framework

The tectonic evolution of the western margin of South America has been described as the result of discrete events, or "phases", (*e.g.*, Steinmann, 1929; Mégard, 1984) of intense compressive tectonics, beginning in the Early Cretaceous, in a geodynamic environment characterized by continuous subduction since the Jurassic (Charrier *et al*., 2007). These compressive events include: the Early to Late Cretaceous "Peruvian" phase; the Late Cretaceous-early Cenozoic "K-T" phase; the middle Eocene "Incaic" phase; the late Oligocene-Early Miocene "Quechua" phase, and the late Miocene "Pehuenche" phase (*e.g*., Steinmann, 1929; Mégard, 1984; Jaillard, 1992; Gregory -Wodzicki, 2000; Cornejo *et al* ., 2003; Arriagada *et al*., 2006; Hoke *et al*., 2007; Charrier *et al*., 2007, 2009, 2013; Farías *et al* ., 2010). The phases are interpreted as a product of changing plate convergence conditions through time, and consequent deformation of the leading edge of the continental plate (Charrier *et al*., 2007, 2013). Specifically, the Oligocene- Miocene Quechua event has been correlated with breakup of the Farallon plate into the Nazca plate and an associated increase in the convergence rate (Pardo-Casas and Molnar, 1987; Somoza, 1998; Reutter, 2001). Crustal deformation during this period has been inferred to have been associated with increased ductile thickening and melting of the lower crust, with a consequent influence on late Paleogene and Neogene magmatism, and formation of structural systems along the western flank of the Altiplano during most of the Neogene (*e.g*., Victor *et al*., 2004; Farías *et al*., 2005).

2.2. Geological context: physiography, lithostratigraphy and structure of the Central Andes

The Central Andes, between ~18° and ~22° S, are marked by a series of continental scale, ~N-S trending, morphostructural units of a highly contrasting character. From west to east, at ~19°30' S, these correspond to the Coastal Cordillera, the Central Depression, the Precordillera, the Western Cordillera, and the Altiplano (Fig. 1). The abrupt west to east elevation increase (~1,000 to ~6,500 m a.s.l.) from the Central Depression to the Altiplano has been ascribed to the development of a wide, crustal-scale monocline (Isacks, 1988), or attributed to the development of the structural systems that bound the Western Cordillera to the west (WTS) and east (ETS) (*e.g*., Muñoz and Sepúlveda, 1992; Muñoz and Charrier, 1996; Farías *et al*., 2005; Charrier *et al*., 2005; Jordan *et al*., 2010).

2.2.1. Central Depression and Precordillera

The Central Depression (Figs. 1 and 2) corresponds to a 25-100 km wide, relatively flat surface that shows a gradual eastward increase in altitude from ~1,000 to 1,600 m a.s.l. To the east, the Precordillera (Figs. 1 and 2) appears at the present-day Andean orogenic front as a ~35 km wide slope that separates the Central Depression from the Western Cordillera. The major west to east topographic elevation increase (~1,600 to ~3,500 m a.s.l.) is herein attributed to thrust activity within the WTS (Muñoz and Charrier, 1996; Pinto *et al*., 2004; Victor *et al*., 2004; Farías *et al*., 2005).

The sub-surface of the Central Depression is composed of ~1,100 m of Oligocene-Holocene strata, which overlie a Mesozoic substratum (García *et al*., 2004, 2013; Hartley and Evenstar, 2010). Outcrops of the Paleozoic are restricted to the Precordillera at ~19°30' S, where the Devonian-Carboniferous Quebrada Aroma Metaturbiditic Complex is exposed (Figs. 1b and 3) (Harambour *et al*., 1990; Morandé *et al*., 2015). Mesozoic units mainly include deformed marine and continental sedimentary rocks, volcanic rocks and plutonic rocks, which underlie Cenozoic units in a regional angular unconformity, the "Choja Pediplain" of Galli (1967) (Fig. 3). Cenozoic units include conglomerates of the Azapa Formation (Oligocene), thick ignimbrite sheets of the Oxaya Formation (upper Oligocene-lower Miocene), conglomerates and ignimbrites of the Altos de Pica Formation (upper Oligocene-lower Miocene), conglomerates of the El Diablo Formation (lower-upper Miocene) and, restricted to the easternmost Central Depression, conglomerates and fine lacustrine sedimentary rocks of the Huaylas Formation (upper Miocene) (Figs. 1b and 3) (García *et al*., 2004; Valenzuela *et al*., 2014; Morandé *et al*., 2015). The Oxaya, Altos de Pica and El Diablo Formations exhibit westward-fanning syntectonic growth strata related to the development of the WTS (Pinto *et al*., 2004; Farías *et al*., 2005; Blanco and Tomlinson, 2013). Miocene volcanic deposits and edifices complete the Cenozoic record, covering the Precordillera from the east, of which the Mamuta (middle Miocene) and Tatajachura (upper Miocene) volcanoes are the most striking features in the region (Figs. 1, 2 and 3).

The WTS lies in the Precordillera (Figs. 1 and 2) as an almost continuous (>450 km) N-S trending compressive structural system consisting of several west-vergent, high-angle thrusts and gentle folds with a dominantly monoclinal geometry. These structures

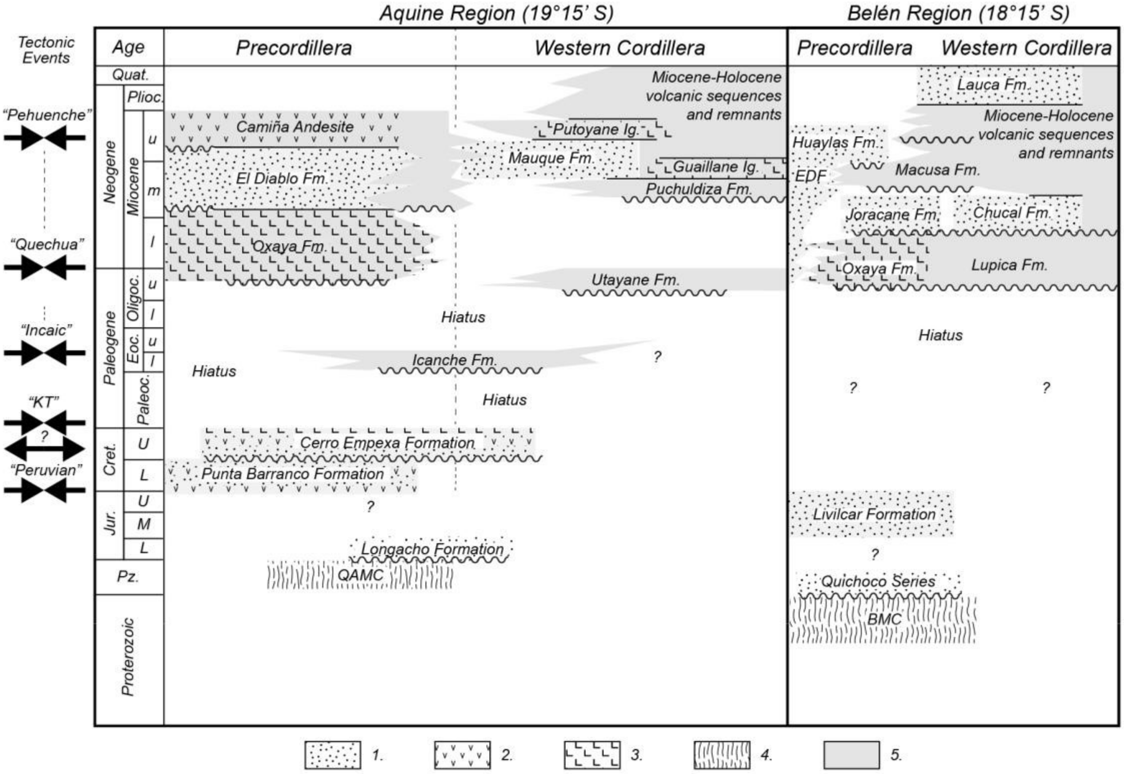

FIG. 3. Chronostratigraphic chart of the western flank of the Altiplano at the Aquine (this study) and Belén (modified from García *et al*., 2004) regions, showing the sequences within the Precordillera and Western Cordillera (segmented line represents the approximate limit). **QAMC:** Quebrada Aroma Metaturbiditic Complex; **BMC:** Belén Metamorphic Complex; **EDF:** El Diablo Formation. Andean tectonic regimes and their inferred duration are indicated: Cretaceous "Peruvian" phase; Cretaceous extensional phase; Cretaceous-Paleogene boundary "K-T" phase; Middle Eocene "Incaic" phase and Oligo-Miocene "Quechua" phase. Simbology: **1.** Sedimentary rocks; **2.** Andesitic lava sequences; **3.** Rhyolitic lithic ignimbrites; **4.** Metamorphic rocks; 5. Ignimbrites and andesitic lava sequences.

present slight variations in displacement magnitudes along-strike (*e.g.*, Pinto *et al*., 2004; Farías *et al*., 2005), and are exposed from southern Perú (~18° S) to the Altos de Pica region (20°-21° S), in northern Chile (Fig. 1; García *et al*., 2004, 2013; Blanco and Tomlinson, 2013; Valenzuela *et al*., 2014; Morandé *et al*., 2015; Tomlinson *et al*., 2015). It is considered to have accommodated major deformation and consequent uplift (>3,000 m) in the Andean forearc and arc during the latest Oligocene-latest Miocene, and to have strongly influenced the middle to late Cenozoic paleogeographic evolution of the area (Muñoz and Charrier, 1996; García, 2002; García *et al*., 2004; Pinto *et al*., 2004; Victor *et al*., 2004; Farías *et al*., 2005; Charrier *et al*., 2007, 2013). The high-angle geometry of thrusts of the system in the Belén region (*e.g.*, Ausipar fault of García *et al*., 2004) suggests that these correspond to re-activated normal faults (Charrier *et al*., 2013). In the Altos de Pica region (20°-21° S), high-angle thrusts are interpreted to be deeply rooted and linked to a regional-scale transpressive fault zone (Victor *et al*., 2004), the Precordilleran Fault System (PFS) (Scheuber and Reutter, 1992; Tomlinson and Blanco, 1997).

2.2.2. Western Cordillera and Altiplano

The Western Cordillera (Figs. 1 and 2) represents the present-day volcanic arc. With an irregular topography that varies between ~3,700 and 4,700 m a.s.l., it is also characterized by high peaks that surpass 5,300 m a.s.l., which correspond to late Neogene and Quaternary volcanoes (*e.g.*, Isluga and Cariquima volcanoes; Fig. 2). Towards the Altiplano, the topography rapidly decreases and becomes relatively smooth, with a mean elevation of ~3,700 m a.s.l. (Horton *et al*., 2001).

At 18°-19° S, the stratigraphy along the Western Cordillera and adjacent Altiplano is mostly composed of Cenozoic deposits (Figs. 1b and 3). In spite of the latter, thrusting of the easternmost features of the WTS has exposed schists and gneisses of the upper Proterozoic-lower Paleozoic Belén Metamorphic Complex (BMC in figures 1b and 3) (Pacci *et al*., 1980; Basei *et al*., 1996; Bahlburg and Hervé, 1997; García, 1996, 2002; García *et al*., 2004; Loewy *et al*., 2004). The majority of the record involves Cenozoic sedimentary and volcanic deposits of the Lupica (upper Oligocene-lower Miocene), Chucal (lower-middle Miocene), Macusa (middle-upper Miocene) and Lauca (Pliocene-Pleistocene) Formations, which are covered by volcanic units of the latest Neogene (Miocene to Holocene) (Figs. 1b and 3) (Riquelme, 1998; García, 2002; García *et al*., 2004; Charrier *et al*., 2005). At ~19°15' S, Cretaceous rocks have been thrust over a series of late Oligocene to Pleistocene sedimentary and volcanic layers that represent correlatives to the units in the Belén area mentioned above (Cortés *et al*., 2012a, b, 2014; Herrera *et al*., 2013; Valenzuela *et al*., 2014). Within Neogene deposits, syntectonic eastward-fanning growth strata and progressive unconformities have been registered in the Chucal anticline (~18°45' S; Fig. 1b) (García *et al*., 2004; Charrier *et al*., 2005) and to the east of the study area, towards the Altiplano (Figs. 1b and 2) (Cariquima Region of Cortés *et al*., 2012a).

The ETS dominates the structure of the easternmost Western Cordillera (Figs. 1b and 2). It is a ~N- S aligned, ~200 km long (18°40'-19°40' S) system of thin- and thick-skinned thrusts and folds that share a mainly east vergence (Figs. 1b and 2). The system is considered active since the early Miocene until the early Pliocene, as a coeval counterpart of the WTS (Charrier *et al*., 2005; Farías *et al*., 2005; Cortés *et al*., 2012a) and responsible for the origin of eastward-fanning growth strata in Miocene units. At ~19°30' S (Cariquima Region) the system it is thought to be mainly controlled by two deeply-rooted, substratum-involving thrusts, with detachment levels that reach ~20 km depth in the Altiplano Low Velocity Zone (ALVZ) (ANCORP, 2003; Cortés *et al*., 2012a). The surface expression of the westernmost of these two thrusts is represented by the Guanca monocline located just to the southeast of the Aquine area (Fig. 2).

3. Geology of the Aquine region

3.1. Stratigraphy

The lithostratigraphy of the Aquine region consists of a Mesozoic substratum composed of Upper Cretaceous volcanic and sedimentary rocks, and a Cenozoic cover consisting of late Oligocene-early Miocene ignimbrites and Neogene sedimentary and volcanic deposits. Geochronological data for the study region is summarized in table 1 and detailed in section 3.2 U- Pb geochronology. The general stratigraphy of the region and correlative units north of the study area are summarized in figure 3.

3.1.1. Mesozoic Substratum

The substratum of the Cenozoic in the region is represented by the Upper Cretaceous Cerro Empexa Formation, which is exposed along the southwestern portion of the study area (Fig. 4). The Cerro Empexa Formation corresponds to a volcanic and sedimentary unit, first defined by Galli and Dingman (1962) and extensively exposed along the Precordillera of northern Chile, from ~19° S to 21° S (Blanco and Tomlinson, 2013; Valenzuela *et al*., 2014; Morandé *et al*., 2015; Tomlinson *et al*., 2015). In the Precordillera, the lower portions of the unit are composed of andesitic lavas, including auto-breccias, overlain by conglomerates and conglomeratic sandstones. The upper portion is mainly composed of poorly sorted sandstones. In the Aquine region, the Cerro Empexa Formation reaches a thickness of ~1,000 m, it is folded and underlies Oligocene and Miocene units in angular unconformity. Eastwards, in the Western Cordillera, the unit shows a predominance of lithic and welded tuffs and subordinate andesites, dacites and sandstones, reaching a thickness of >500 m. The Cerro Empexa Formation underlies the sub-horizontal Icanche Formation (Fig. 4) in angular unconformity along the western portion of the Aquine region, with a gentle dip of ~15° W-NW. Towards the east, along the Putoyane valley, it underlies the Puchuldiza and Mauque formations, upper Miocene andesitic lavas (Fig. 4), and it is thrusted over the Icanche Formation. In the Aroma valley, the Cerro Empexa Formation underlies in strong angular unconformity the Icanche Formation, the upper Miocene andesitic lavas and the Guaillane Ignimbrite (Fig. 4), and it is also thrusted eastwards over the Icanche Formation (Fig. 4). A distal fluvial

TABLE 1. ROCK AGE DATA FOR THE AQUINE REGION.

Sample	Unit	Location (UTM/WGS84) N	E	Method	Sample lithology	Age (Ma)	Reference
CS2-4	Cerro Empexa Formation-CEF	7.865.337	476.728	U-Pb LA-ICP-MS (zircon)	Biotite-bearing dacite	68.5±0.5	this study
HC-07	Icanche Formation-IF	7.854.989	490.455	U-Pb LA-ICP-MS (zircon)	Andesitic lithic lapilli tuff	49.6±0.5	this study
CS3	Utayane Formation-UF	7.861.744	488.572	U-Pb LA-ICP-MS (zircon)	Rhyolitic crystal tuff	26.7±0.3	this study
GPM-84	Puchuldiza Formation-PF2	7.855.620	499.679	K-Ar (whole rock)	Welded glassy ash tuff	14.2±0.5	Ortiz *et al*., 2008
CS2-35	Guaillane Ignimbrite-GI	7.854.319	492.071	U-Pb LA-ICP-MS (zircon)	Andesitic glassy ash tuff	13.9±1.3	this study
CS2-37	Guaillane Ignimbrite-GI	7.851.780	490.316	U-Pb LA-ICP-MS (zircon)	Rhyolitic crystal tuff	13.7±0.3	Valenzuela *et al.*, 2014
CS2-21	Mauque Formation-MF	7.867.924	483.769	U-Pb LA-ICP-MS (detrital zircon)	Lithic sandstone	11.4±0.3	Valenzuela *et al.*, 2014
CP1-5	Mauque Formation-MF	7.872.834	479.160	U-Pb LA-ICP-MS (detrital zircon)	Lithic sandstone	9.7±0.2	Valenzuela *et al.*, 2014
CP1-3	Upper Miocene andesitic lavas-MVS	7.872.734	479.356	U-Pb LA-ICP-MS (zircon)	Andesite	8.7±0.2	Valenzuela *et al.*, 2014
CP1-26	Upper Miocene andesitic lavas-MVS	7.874.081	488.013	U-Pb LA-ICP-MS (zircon)	Andesite	7.7±0.6	Valenzuela *et al.*, 2014
M-1	Putoyane Ignimbrite-PI	7.863.994	489.335	K-Ar (biotite)	Andesitic crystal tuff	6.9±0.3	Argandoña, 1984

environment, accompanied by extrusive andesitic volcanism, is proposed for the origin of the succession in the Precordillera (Valenzuela *et al*., 2014). In the Western Cordillera, explosive volcanism and low-energy sedimentation within restricted intra-montane basins dominate this portion of the Cerro Empexa Formation (Argandoña, 1984; Valenzuela *et al*., 2014). The Cerro Empexa Formation has been interpreted as the result of Upper Cretaceous arc magmatism, and coeval sedimentation, in a complex paleogeographic configuration characterized by intra-arc extension (Blanco and Tomlinson, 2013; García *et al*., 2013; Morandé *et al*., 2015; Valenzuela *et al*., 2014; Tomlinson *et al* ., 2015). Radiometric analyses constrain this unit to the Upper Cretaceous, between 79.4±1.1 Ma and 65.7±1.4 Ma (Zircon U-Pb ages; Tomlinson *et al*., 2015) (*ca.* 79- 66 Ma; Campanian-Maastrichtian). Additionally, a biotite dacite yielded an age of 68.5±0.5 Ma (Zircon U-Pb ages; this study) (Fig. 5a; Table 1), which also dates the unit to the Campanian-Maastrichtian (*ca.* 67 Ma).

3.1.2. Cenozoic cover

The Cenozoic is represented by middle Eocene to Pleistocene sedimentary and volcanic deposits (Figs. 3 and 4). Throughout the central and western segment of the study area, they cover the folded Cerro Empexa Formation. Collectively, Neogene deposits of the Aquine region register the depositional evolution of the middle to upper Miocene intra-arc, mainly represented by ignimbrite sheets, andesitic lavas, and subordinate sedimentary successions.

Lower Eocene deposits are composed of a succession of dacitic to rhyodacitic lithic tuffs of the Icanche Formation (Maksaev, 1978) (Fig. 4). The inferred thickness of the formation in the study area is estimated at ~1000 m (Valenzuela *et al*., 2014). Tuffs within the unit, exposed along the Putoyane

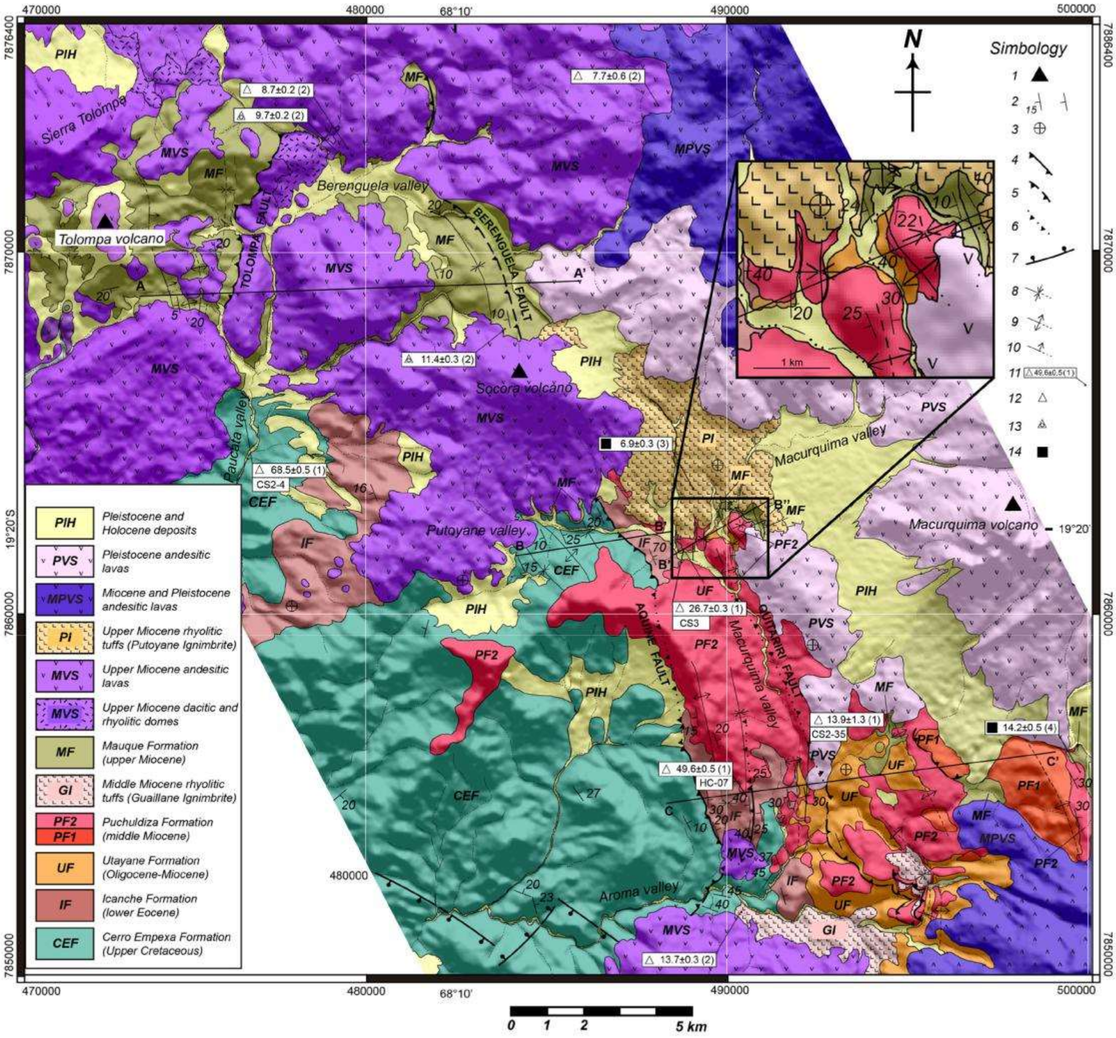

FIG. 4. Detailed geological map of the Aquine region, Western Cordillera (~19°20' S), showing main structural features described in this study (modified from Argandoña, 1984 and Valenzuela *et al*., 2014). A-A', B-B' and C-C′ correspond to structural sections in figure 6. Simbology: **1.** Volcanic center remnant; **2.** Bedding; **3.** Horizontal strata; **4.** Observed thrust; **5.** Photo-interpreted thrust; **6.** Covered thrust; **7.** Observed normal fault; **8.** Observed/inferred syncline; **9.** Observed/inferred anticline; **10.** Observed/ inferred monocline; **11.** Radiometric age; **12.** U-Pb zircon age; **13.** Detrital U-Pb zircon age; **14.** K-Ar biotite age. Source for radiometric ages: this work, Valenzuela *et al*. (2014), Argandoña (1984) and Ortiz *et al*. (2008).

and Macurquima valleys, are rich in plagioclase and quartz and bear subordinate amphibole crystals, as well as pumice, contained in an ash-predominant matrix. The lithics correspond to fragments of reddish and altered andesites. In the Western Cordillera, this unit shows a moderate imprint of propylitic alteration, and it is sub-horizontal in the western portion of the study area along the Paucata valley. Towards the east, it becomes strongly folded, overlying the Cerro Empexa Formation with a strong angular discordance, which is exposed in the Putoyane and Aroma valleys (Figs. 4 and 6a). Along the Macurquima valley, the Icanche Formation is overlain in a strong angular unconformity by tuffs of the Utayane Formation and middle Miocene lavas of the Puchuldiza Formation (Fig. 4). In the Aroma valley it is also overlain in

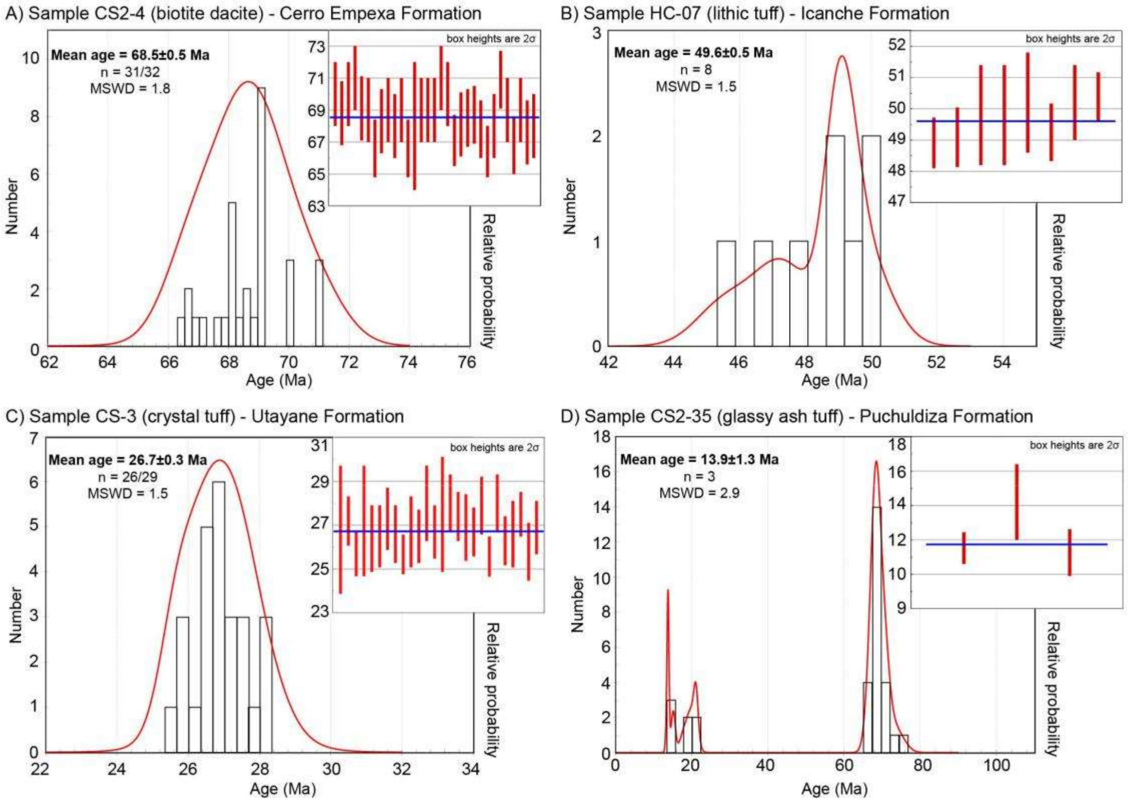

FIG. 5. Geochronological results. U-Pb zircon ages for the: **A.** Cerro Empexa; **B.** Icanche; **C.** Utayane; and **D.** Puchuldiza Formations. The background diagram in each case corresponds to relative probability diagrams (age distributions) and the overlain inset diagram is the weighted mean with error bars for the populations of representative ages of each sample. Sample locations shown in figure 4.

angular unconformity by the Guaillane Ignimbrite (Fig. 4). A lithic tuff yielded an age of 49.6±0.5 Ma (Zircon U-Pb ages; this study) (Fig. 5b; Table 1), which dates the unit to the lower Eocene (*ca.* 49 Ma; Ypresian). This pyroclastic succession represents the scarcely exposed products of the Paleocene-middle Eocene magmatic arc of the N-S trending "Incaic range"; which featured as the primary topographic high during that epoch (Charrier *et al.*, 2009, 2013).

The upper Oligocene to lower Miocene Utayane Formation (Lahsen, 1973[1]; Fig. 4) is composed of volcanic and sedimentary deposits, covering in strong angular unconformity the Icanche Formation along the Putoyane valley, and underlying paraconformably or with gentle angular unconformity the Puchuldiza Formation along the Putoyane and Aroma valleys (Fig. 4). This formation consists of a ~200 m thick succession of strongly welded, lithic lapilli rhyolitic tuffs, with abundant plagioclase, biotite and quartz crystals, which are interbedded with lithic sandstones and conglomerates. In the Aquine region, it is restricted to the Macurquima valley and the southeastern portion of the Aquine region (Fig. 4). Six U-Pb zircon ages of 26.0±0.4 Ma to 19.3±0.3 Ma were reported by Cortés *et al.* (2014), in addition to a zircon U-Pb age of 26.7±0.3 Ma age (this study) (Fig. 5c; Table 1), allows to assign the unit to the upper Oligocene-lower Miocene (*ca.* 27-19 Ma; Chattian-Burdigalian). The Utayane Formation represents pyroclastic flows that covered the proto-Western Cordillera and the adjacent Altiplano, in general, concomitant to the Oxaya Formation in the Precordillera and the upper Azapa Formation in the Central Depression (Figs. 1b and 3).

Covering the Cerro Empexa and Icanche Formations in angular unconformity, and the

---

[1] Lahsen, A. 1973. Geología de Puchuldiza. Informe inédito. CORFO: 49 p. Santiago.

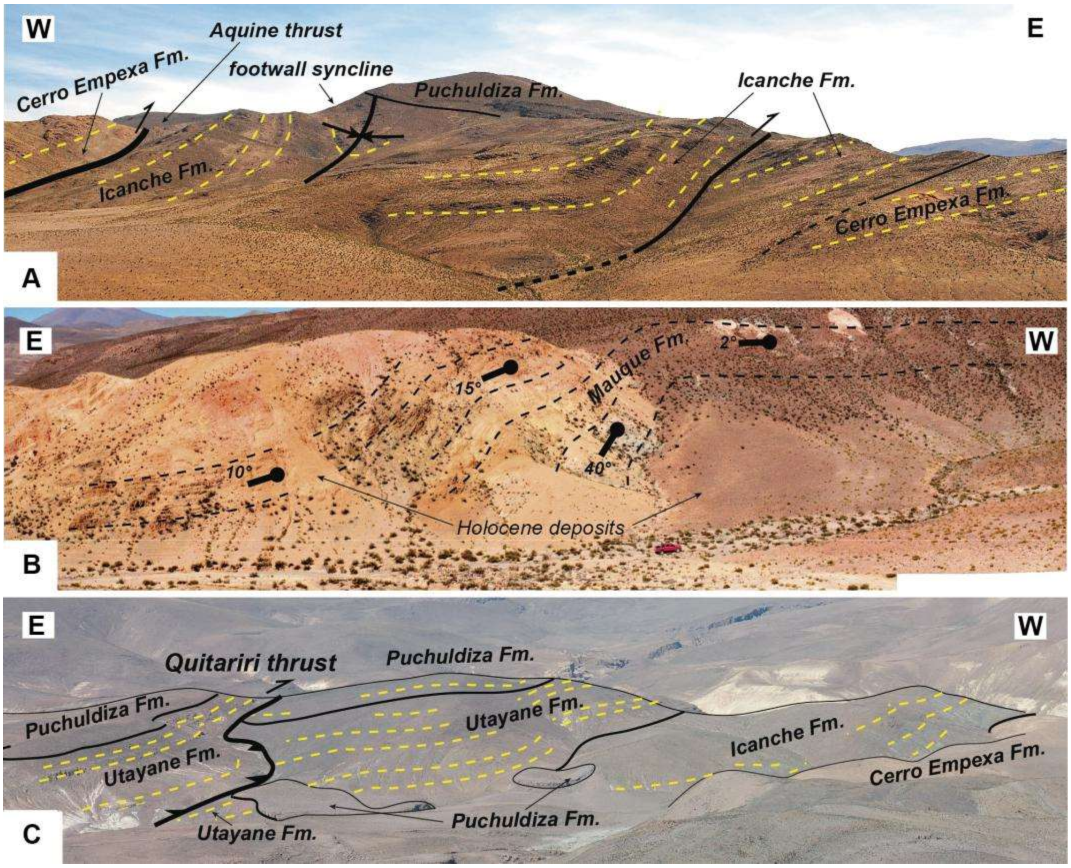

FIG. 6. Structures and deformed units of the Western Cordillera. **A.** A view looking north from the Aroma valley at the Aquine thrust and footwall deformation in the westernmost segment of section CC' in figure 8; **B.** A view looking south at the west-vergent monoclinal fold east of the Tolompa volcano in the westernmost segment of section AA' in figure 8; **C.** A view looking south of the Macurquima valley, where the Quitariri thrust places the Utayane Formation over the Puchuldiza Formation, located immediately south of the central segment of section CC' in figure 8.

Utayane Formation in gentle angular unconformity or paraconformably in the Putoyane valley, the Puchuldiza Formation (Lahsen, 1973) is composed of a ~80 m-thick volcanic sequence in which we differentiated two members (Fig. 4), exposed in the southern portion of the study area and along the Macurquima, Putoyane and Aroma valleys. The Puchuldiza Formation dips gently towards the east in the Aroma and Macurquima valleys, and eastwards it is folded and faulted. However, the unconformity with the Utayane Formation is still gentle even where the unit is most deformed. The Lower Member consists of amphibole-bearing and pyroxene-rich lavas of an andesitic to dacitic affinity (~10 m thick), and to subordinated centimetric (~80-50 cm-thick) block-and-ash deposits with a dominantly andesitic lithic content. The Upper Member corresponds to biotite-rich rhyolitic and dacitic welded tuffs, and subordinate rhyolitic and dacitic lavas, which collectively reach a thickness of ~70 m. A 14.2±0.5 Ma age (K-Ar on biotite) reported by Ortiz *et al*. (2008)[2] (Fig. 4; Table 1), in addition to more recent geochronological results by Cortés *et al*. (2014) that yielded a 13.1±0.4 Ma U-Pb zircon age in the Puchuldiza area (Fig. 2), allows to assign the Puchuldiza Formation to the middle Miocene (*ca*. 14-13 Ma; Langhian-Serravallian). In this study, U-Pb zircon radiometric

---

[2] Ortiz, M.; Achurra, L.; Cortés, R.; Fonseca, A.; Silva, C.; Vivallos, J. 2008. Estudio Geológico, Geofísico e Hidroquímico del Sector de Puchuldiza. Exploración Geológica para el fomento de la Energía Geotérmica (Informe Inédito). Servicio Nacional de Geología y Minería, 168 p., Santiago, Chile.

analyses for a glassy dacitic ash tuff yielded an age of 13.9±1.3 Ma (Fig. 5d) for the Upper Member, consistent with the timespan given by the two ages mentioned above.

The Guaillane Ignimbrite (Fig. 4) overlays with angular unconformity the Cerro Empexa and Icanche Formations, and the Utayane and Puchuldiza Formations in gentle angular discordance, in the southernmost portion of the study area. This ignimbrite is composed of a ~190 m-thick sequence of rhyolitic welded tuffs, which are rich in biotite, pumice, and lithic fragments. Radiometric analyses for the Guaillane Ignimbrite have yielded ages of 13.7±0.3 Ma (U-Pb zircon ages; Valenzuela *et al*., 2014) and 12.7±0.1 Ma (K-Ar on biotite; Argandoña, 1984) (Fig. 4; Table 1), allowing to assign this unit to the middle Miocene (*ca*. 14-13 Ma; Langhian-Serravallian) and indicating, based on the geochronology, that it overlaps, in part, the depositional timespan of the Puchuldiza Formation in the Puchuldiza area.

The Mauque Formation (Cortés *et al*., 2014; Fig. 4), first defined as the "Mauque Series" (Lahsen, 1973), corresponds to a ~200 m-thick predominately sedimentary succession, mainly composed of sandstones, conglomerates and sedimentary breccias, in addition to tuffs in its upper portions (Lahsen, 1973; Ortiz *et al*., 2008; Cortés *et al*., 2014; Valenzuela *et al*., 2014; Herrera *et al*., 2015). The Mauque Formation exhibits strong thickness variations (Figs. 6b and 7), and an imprint of moderate to strong intermediate-argillic alteration throughout the study area. It overlies the Cerro Empexa, Utayane and Puchuldiza Formations in angular unconformity. The deposits of the Mauque Formation predominantly correspond to immature lithic sandstones that are rich in andesite and dacite fragments and show well-defined cross and planar lamination. In its lower portions, the unit is composed of massive sandstones layers, with interbeds of grain-and matrix-supported breccias. The breccias within the unit show inverse-normal and normal grading. Cross-stratification in sandstones is common in metric-scale lenses and paleochannels. The middle portions of the unit show metric-scale (<2 m-thick) layers of laharic breccias interbedded with lithic sandstones. At the Tolompa Volcano, this portion of the succession shows flame and slump structures, and recumbent stratification (Bobadilla, 2015; Herrera *et al*., 2015). Towards its upper portion, the Mauque Formation consists of fine- to medium-grained lithic

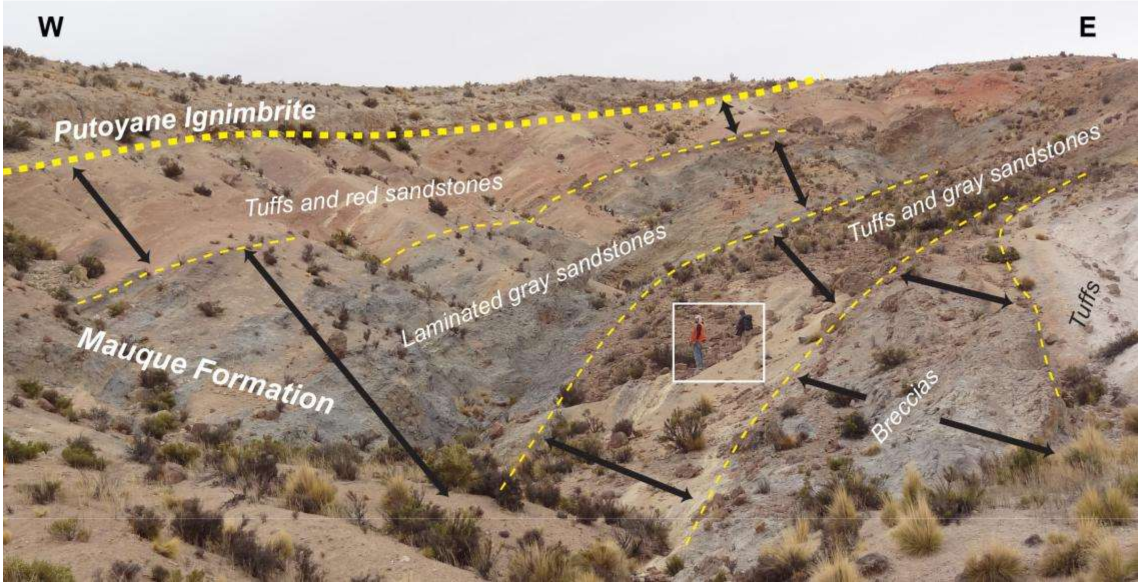

FIG. 7. A view looking north at the overturned western limb of a west-vergent anticline affecting westward-fanning metric-scale growth strata recognized within volcanic and sedimentary layers of the Mauque Formation in the Macurquima valley (Fig. 4). Note the gentle unconformity with the overlying Putoyane Ignimbrite (thick dashed line). Arrow-headed black lines are approximately perpendicular to strata bedding (fine dashed lines), highlighting thickness increases. Geologists stand as scale at the center of the image.

sandstones that show fine parallel lamination, and coarse-grained sandstone layers interbedded with subordinate laminated conglomerates. The unit represents a depositional environment of restricted lakes in a fluvial system with coalescent debris flows within alluvial fans (Bobadilla, 2015; Herrera *et al*., 2015). In the northwestern portion of the study area, immediately east of the Tolompa Volcano (Fig. 4), the Mauque Formation shows a clear thickness increase from ~30-40 m in the west to ~170 m in the east adjacent the Tolompa fault. This trend is also observed in outcrops of the Berenguela valley where the maximum thickness occurs in the vicinity of the Berenguela fault (Bobadilla, 2015; Herrera *et al*., 2015). At the Putoyane valley, westward growth (~5 to 20 m of thickness increase to the west) has been registered in sandstones and breccias (Fig. 7). For the Mauque Formation, in the Berenguela Valley (Fig. 4), U-Pb detrital zircon analyses on two samples yielded maximum depositional ages for the unit of 9.7±0.2 Ma and 11.4±0.3 Ma, which correspond to the mean age of the youngest zircon population in the samples (Table 1) (Valenzuela *et al*., 2014). In addition, its stratigraphic position over the Puchuldiza Formation and the geochronological data for the latter, indicate a maximum deposition age of *ca*. 14 Ma for the Mauque Formation (Cortés *et al*., 2014; Valenzuela *et al*., 2014). The Mauque Formation is also overlain by the Putoyane Ignimbrite (*ca*. 7 Ma; see below) in the Macurquima valley, and by *ca*. 8-7 Ma lavas in the Berenguela valley (Valenzuela *et al*., 2014). Hence, the total possible age range for deposition of the Mauque Formation is *ca*. 14-8 Ma (middle Miocene-upper Miocene; Langhian-Tortonian) (Valenzuela *et al*., 2014). As reported by Valenzuela *et al*. (2014), a strong peak of 14 Ma has been identified in the U-Pb detrital zircon analyses. Moreover, according to the geochemistry and texture of lithic fragments within rocks of the unit, it has been proposed that the sediment source for the formation corresponds to the concomitant Miocene volcanic arc (Bobadilla, 2015; Herrera *et al*., 2015).

Volcanic sequences of the upper Miocene (Fig. 4) are composed of pyroxene-bearing andesites, dacites, basaltic andesites and subordinate lapilli tuffs, and are broadly exposed throughout the northwestern portion of the study area. Included in this unit are dacitic and rhyolitic domes. These lavas overlie in erosive unconformity the Icanche and Cerro Empexa Formations, and cover the Mauque Formation with paraconformity. Andesites and andesitic auto-breccias exposed in the southernmost portion of the study area (Fig. 4) constitute the base of the Tatajachura volcano (Fig. 2), which is assigned to the upper Miocene, based on a 6.0±1.3 Ma whole-rock K-Ar age reported by Morandé *et al*. (2015). Lavas from this volcano cover in angular unconformity the deformed Cerro Empexa and Icanche Formations, as well as the Guaillane Ignimbrite in the Aroma valley. Additionally, U-Pb ages of 8.7±0.2 Ma and 7.7±0.6 Ma in the study area (Fig. 4; Table 1) and reported by Valenzuela *et al*. (2014), allows to assign all sequences of this unit to the upper Miocene (*ca*. 9- 6 Ma; Tortonian-Messinian). The eruptive centers associated with the upper Miocene volcanic sequences correspond to volcanic edifice remnants, located at the northwestern portion of the study area (Fig. 2).

The Putoyane Ignimbrite is exposed in the Putoyane and Macurquima valleys (Fig. 4). This unit is sub-horizontal, and covers the Icanche, Utayane, Puchuldiza and Mauque Formations in angular unconformity and local paraconformities along the Macurquima valley, where these older units are collectively folded (Figs. 4 and 8). It is only overlain in paraconformity by Pleistocene lavas of the Macurquima Volcano (see below) and by Pleistocene and Holocene alluvial fans, also in the Macurquima valley. Towards the west, north of the Putoyane valley, it overlies lavas of the Socora volcano in gentle angular unconformity and paraconformity (Fig. 4). This ~90 m-thick pyroclastic deposit is composed of biotite-rich, amphibole- and pyroxene-bearing crystal and lithic tuffs, of which the main lithic component is andesite rock fragments. A radiometric K-Ar analysis on biotite for the Putoyane Ignimbrite yielded an age of 6.9±0.3 Ma (Argandoña, 1984) (Fig. 4; Table 1), which allows to assign the unit to the upper Miocene (*ca*. 7 Ma; Messinian).

Associated with the remnants of NS-aligned stratovolcanoes (Figs. 2 and 4), lavas composed of amphibole-bearing andesites, interbedded with subordinate lithic tuffs, cover in paraconformity the upper Miocene volcanic sequences from the northeast (Fig. 4). Along the southeastern portion of the study area, amphibole- and biotite-bearing dacites assigned to the same unit cover the Utayane, Puchuldiza and Mauque Formations in angular unconformity, and overlie conformably the Guaillane Ignimbrite. These volcanic sequences are assigned to the upper Miocene-Pliocene (*ca*. 9-3 Ma; Tortonian-Piacenzian;

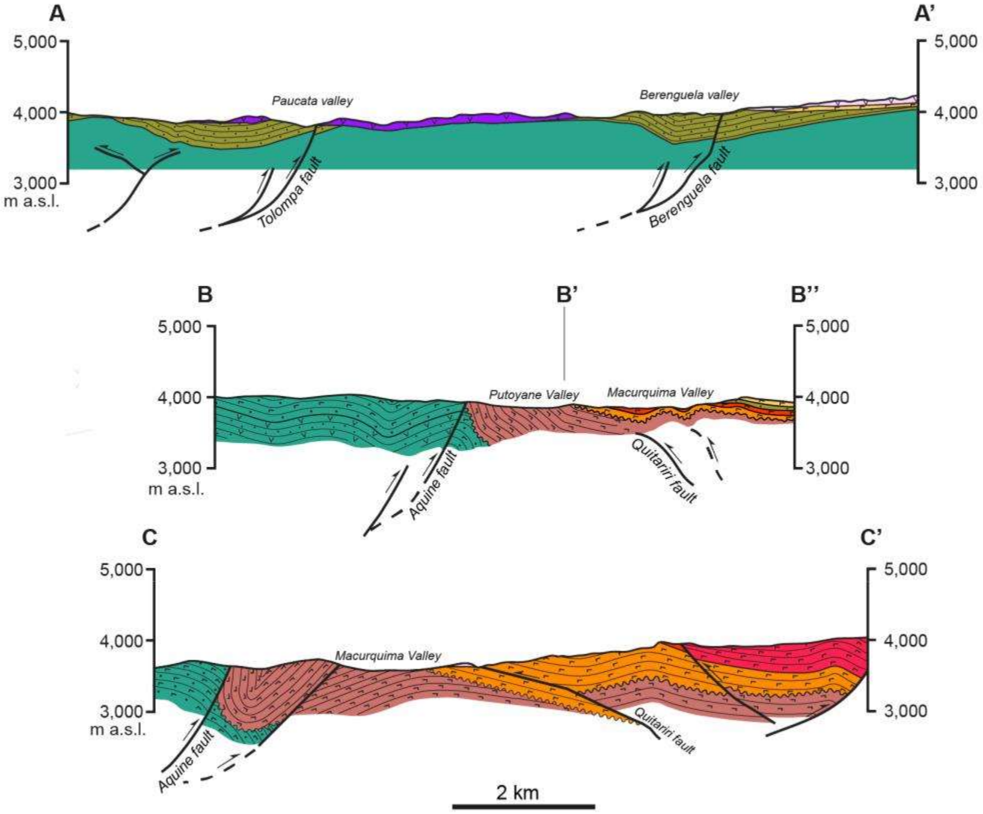

FIG. 8. Schematic structural cross-sections. AA', BB'B''and CC' correspond to the north, central and southern E-W oriented cross sections traced in figure 4, respectively. The unit symbols are the same used in figure 4.

Ortiz *et al*., 2008; Cortés *et al*., 2014; Valenzuela *et al*., 2014).

The youngest volcanic unit of the Aquine region corresponds to Pleistocene volcanic sequences (Fig. 4) composed of amphibole- and pyroxene-bearing andesitic lavas that cover the upper Miocene-Pliocene volcanic sequences and the Putoyane Ignimbrite in paraconformity in the northeast part of the study area. Towards the west and south, these lavas overlie the Utayane, Puchuldiza and Mauque Formations in angular unconformity. These lavas have been assigned to the Pleistocene (*ca*. 2-1 Ma; Gelasian-Calabrian; Ortiz *et al*., 2008; Cortés *et al*., 2014; Valenzuela *et al*., 2014).

3.2. U-Pb Geochronology

Four rock samples from key lithologies (Table 1) have been dated through U-Pb LA-ICP-MS to more accurately time-constrain the lithostratigraphy of the study region (see Appendix for Methodology and Tables). The data of these four samples has been re-interpreted from Valenzuela *et al*. (2014).

Cerro Empexa. A slightly altered biotite dacite sample (CS2-4), characteristic of this formation in the central -west portion of the study area (Fig. 4), yielded an Upper Cretaceous zircon crystallization age of 68.5±0.5 Ma (MSWD=1.8; n=31 grains analyzed) (Fig. 5a). Icanche Formation. The collected lithic tuff (HC-07), crops out mainly in the central-west and -southern portions of the map area (Fig. 4). The U-Pb zircon data (35 analyzes) have a bimodal age population with peaks near 65 and 50 Ma. A single analysis of 10 Ma probably represents a contaminant grain and therefore was rejected for the age calculation. The 65 Ma population is probably derived from the lithics in the tuff, picked up from the Cerro Empexa Formation or its subsurface equivalents. The 50 Ma population is interpreted to be from the magma that gave rise to the pyroclastic deposit and shows evidence for both slight inheritance and lead loss. A coherent subset of 8 out of 35 analyses gives a 206Pb/238U weighted mean age of 49.6±0.5 Ma (MSWD=1.5) which is interpreted to be the depositional age for this formation in the early Eocene (Fig. 5b). Utayane Formation. A weighted mean 206Pb/238U age of 26.7±0.3 Ma (MSWD=1.5; n=26 out of 29 analyses; late Oligocene) (Fig. 5c) was obtained on the crystal tuff (CS-3) belonging to this Oligocene-Miocene unit from the central-southern study area (Fig. 4). Puchuldiza Formation. A U-Pb zircon age was obtained on a glassy ash tuff (CS2 -35) from the central-southeastern part of the study area (Fig. 4). The U-Pb zircon data (35 analyzes) have essentially a bimodal age population with peaks near 68 and 14 Ma, and a single analysis of 485 Ma. The 485 Ma and ca. 68 Ma analyses are interpreted as a zircon population picked up from surrounding rocks at depth during emplacement of the glassy ash tuff. The depositional age for this unit was calculated on the three youngest zircon grains which yield an average age of 13.9±1.3 Ma (MSWD=2.9; n=3; middle Miocene). Age precision is not perfect but it can be excluded that those young ages are related to contamination during analytical work. Youngest ages in general range between 13.6 and 21.1 Ma (Fig. 5d). Methodology for the U-Pb geochronology is detailed in the appendix.

3.3. Structure of the Western Cordillera in the Aquine region

Structures at the northern portion of the study area correspond to east-vergent gentle folds and thrusts (Figs. 4, 6 and 8). The Mauque Formation and volcanic sequences of the Upper Miocene are tectonically affected in this sector, and upper Miocene-Pleistocene lavas and ignimbrites post-date the faulting and folding. Towards the Sierra Tolompa (Fig. 4) from west to east, the Mauque Formation is affected by a ~500 m wavelength, N-S to NNW-SSE trending monocline (Figs. 6b and 8), with dips of ~45° E to 10° E, followed to the east by a ~600 wavelength anticline, with dips of 5° W and 20° E on its western and eastern limbs, respectively (Fig. 8). Eastwards, the Mauque Formation is thrusted over Upper Miocene lavas along the Tolompa fault, a high -angle (~60° W) east-vergent reverse fault, of an N-S trend. This reverse fault folds the Mauque Formation into a N-S trending syncline, immediately west of its surface trace (Figs. 4 and 8). East of the Sierra Tolompa, in the Berenguela valley, the Mauque Formation is also thrusted towards the east, over itself by means of the Berenguela fault, another high-angle reverse fault (30°-40° W), with a NNW- SSE to N-S trend. In the hanging wall of the latter, the Mauque Formation is folded into an asymmetric syncline, with dips of 30° E and ~8° W in its western and eastern limb, respectively (Figs. 4 and 8).

In the central portion of the study area, towards the confluence of the Putoyane and Macurquima valleys (Fig. 4), along the latter, a pair of short-wavelength, NNW-SSE trending anticline and syncline are exposed (Figs. 4 and 8) and affect the Icanche, Utayane, Puchuldiza and Mauque Formations. The fold axes are spaced <800 m apart, are south-plunging and asymmetrical. Growth strata are locally exposed. In particular, an anticline interpreted to be associated to the Quitariri reverse fault (Fig. 8) exhibits westward-fanning growth strata (5 to 20 m thickness increase in 200 m) within sandstones, conglomerates, tuffs and breccias of the Mauque Formation (Fig. 7) along the western, limb of the anticline. Further west, the area is marked by the east-vergent, high-angle (~60° W) Aquine reverse fault, that places the Cerro Empexa Formation over the Icanche Formation, and is overlain by Miocene lavas of the Socora volcano (Figs. 4, 6a and 8). Within the hanging wall of the reverse fault, along the Putoyane valley, three NNW-SSE trending folds affect the Cerro Empexa Formation but not the unconformably overlying Puchuldiza and Mauque Formations. Wavelengths of the folds reach 1,000 to 1,500 m, and dips throughout their limbs reach ~45° ENE and ~25° WSW near the core of the easternmost syncline (Fig. 8).

In the southern part of the Aquine study area, exposed along the Aroma valley (Fig. 4), a tight, north-plunging, symmetrical syncline affects the Icanche Formation in the footwall of the Aquine fault, and, as well, is thrusted in its eastern limb (Figs. 4, 6a and 8). This footwall syncline shows maximum dips of ~80° W and ~45° W in its western and eastern limbs, respectively. The fault plane within the east limb of the footwall syncline dips ~40° W, and its displacement is towards the east (Figs. 6a and 8). In between the Putoyane and Aroma valleys, the upper member of the Puchuldiza Formation overlies the Cerro Empexa and Icanche Formations and partially covers the trace of the Aquine fault (Fig. 4). East of the Aquine fault the Puchuldiza Formation is gently folded into a N- S trending open asymmetric anticline followed to the east by an open symmetric syncline, with ~2 km wavelength (Fig. 4). Like the Aquine fault, the anticline is east-vergent. A minimum throw for the Aquine fault has been estimated at ~200-300 m, based on the topography of the erosive unconformity between the Puchuldiza Formation and Cerro Empexa and Icanche formations. Westwards, across the Aroma Valley, Argandoña (1984) reported the occurrence of NW-SE to SW-NE trending normal faults within the Cerro Empexa Formation.

The structures exposed in the southeastern portion of the Aquine study area, east of the Aquine fault (Fig. 4), are of contrasting character in that they have an opposite structural vergences forming a triangular zone. A west-vergent structure in this area is the NNW-SSE trending west-vergent Quitariri reverse fault (Figs. 4, 6c and 8). The Quitariri fault directly affects the Utayane and Puchuldiza Formations and the Guaillane Ignimbrite in the southernmost sector of the study area, and can be projected to the north, to the Macurquima valley, where it is interpreted to be a blind thrust responsible for formation of the west-vergent anticline with westward-fanning growth strata in the Mauque Formation described above (Figs. 4 and 7). At the confluence of the Aroma and Macurquima valleys, the Quitariri fault cuts the Miocene units by means of a low-angle (<30° ENE) ramp, above which the Utayane Formation is folded into a gentle symmetrical anticline. Further east, the Lower Member of the Puchuldiza Formation is thrusted above its Upper Member by means of a higher angle (*ca.* 40° E) dipping fault. These structures probably involve the Icanche Formation in depth (Fig. 8). Because of the growth strata relations observed in the Macurquima valley, in the central portion of the study area, we infer that deposition of the Mauque Formation is involved in this thrust system. In the hanging wall of the easternmost thrust,

a syncline-anticline fold pair is developed, affecting both members of the Puchuldiza Formation at the surface (Figs. 4 and 8). Development of the fold pair is thought to be controlled by an east-dipping ramp at depth (Fig. 8).

4. Discussion

Interpretation of new field and geochronologic data have allowed us to reconstruct the history of deformation and deposition within the Western Cordillera, and relate the history to the tectonic and stratigraphic evolution of the adjacent WTS and ETS in northernmost Chile (~18°30-19°30' S). The structural and stratigraphic analysis allows to establish three contractional deformation episodes in the Aquine region during the Cenozoic (Figs. 9, 10 and 11), and a preceding extensional phase during the Late Cretaceous is inferred. Constraints have been established by the structural features and the relationships between lithostratigraphic units involved explained above.

4.1. First episode (49-27 Ma)

The Cerro Empexa Formation has been interpreted to have developed in an extensional arc setting towards the south (19°30-21° S; *e.g.*, Charrier *et al.*, 2007, 2009; Blanco and Tomlinson, 2013; Gallardo *et al.*, 2013; Morandé *et al.*, 2015; Tomlinson *et al.*, 2015), as well as the Mesozoic formations that comprise the substratum in the Precordillera towards the north (18°-19°30' S; *e.g.*, García, 2002; García *et al.*, 2004; Charrier *et al* ., 2007, 2013). Normal faults described within the Cerro Empexa Formation in the southernmost portion of the Aquine region, in the hanging wall of the Aquine reverse fault, may be from this period, although a younger age cannot be excluded (Fig. 10). The high-angle character of the Cenozoic substratum- involving thrusts is unlikely to be a consequence of purely compressive tectonics (*e.g.*, Marques and Nogueira, 2008; Bonini *et al.*, 2012), and suggests that these structures likely correspond to reversely reactivated normal faults that participated in the development of the Jurassic and Early Cretaceous backarc basins (*e.g.*, Charrier *et al.*, 2007). Evidence for a post-Cretaceous, pre-Early Eocene deformation, before deposition of the Icanche volcanics, is given by the angular discordance between the Cerro Empexa and Icanche Formations (Figs. 9a; 11a). The folding of the Cerro Empexa Formation can be correlated to the Cretaceous-Paleogene boundary compressive event ("K-T" phase; Cornejo *et al.*, 2003) broadly recognized in northern Chile for the latest Cretaceous and early Paleocene (*e.g.*, Amilibia *et al.*, 2008;

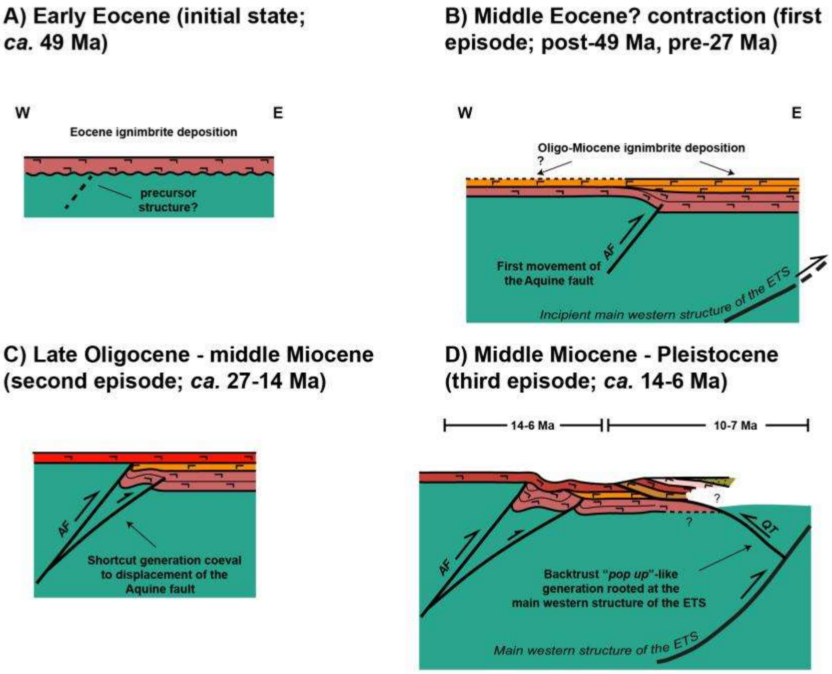

FIG. 9. Simplified structural model for development of the Aquine thrust and associated deposits in the Macurquima valley area for the **A.** Early Eocene; **B.** Middle Eocene-Upper Oligocene; **C.** Upper Oligocene-Middle Miocene; and **D.** Middle Miocene-Pleistocene (Present-day configuration). The east-vergent thrust in which the Quitariri fault (**QT**) is rooted has been traced following Cortés *et al*. (2012a). **AF:** Aquine fault; **ETS:** East Vergent Thrust System.

Blanco *et al*., 2012[3]; Charrier *et al*., 2007, 2009, 2013; Martínez *et al*., 2013).

The deformed volcanic deposits of the Icanche Formation, also unconformably overlying Miocene Utayane Formation indicate that after explosive early Eocene volcanism (Fig. 9a), a contractional event, most likely related to the middle Eocene Incaic phase, affected this segment of the arc between *ca*. 49 and 27 Ma (Fig. 10). Deformation was accomplished by high-angle substratum-involving thrusts, including the east-vergent Aquine reverse fault (Fig. 9b). This proposed situation for the region is simplified in figure 11a. Additionally, paleocurrent and clastic provenance data for Paleogene units in the Altiplano basin indicate the formation of an uplifted area west of the basin, which has been explained in terms of the development of a fold-and-thrust belt in the present-day Western Cordillera (Horton *et al*., 2001, 2002). Protracted Paleogene uplift may explain the lack of Eocene equivalents towards the north, in the Belén region, where a hiatus separates the Middle Jurassic from the Oligocene-Miocene sequences (García *et al*., 2004).

As the Mesozoic substratum is directly involved in the deformation, the style was thick-skinned. The angular unconformity between the Utayane and Icanche Formations, in the vicinity of the Aquine fault which affects the Eocene Icanche Formation, indicates that this structure was active prior to the latest Oligocene (*ca*. >27 Ma). Although the constraints on the timing are broad, post 49 Ma and pre 27 Ma, the deformation is likely related to the middle Eocene Incaic phase. In the Precordillera, Paleogene contraction and consequent erosion and denudation gave rise to the regionally flat, erosive, Choja Pediplain unconformity (Galli, 1967). Block exhumation in the Eastern Cordillera was triggered during the late Eocene-early Oligocene (36-27 Ma) (Barnes *et al*., 2012), synchronic to or slightly later than this first period of contraction in the western Altiplano.

---

[3] Blanco, N.; Vásquez, P.; Sepúlveda, F.; Tomlinson, A.; Quezada, A.; Ladino, M. 2012. Levantamiento geológico para el fomento de la exploración de recursos minerales e hídricos de la Cordillera de la Costa, Depresión Central y Precordillera de la Región de Tarapacá (20°-21°S). Informe Registrado IR-12-50, Servicio Nacional de Geología y Minería, Subdirección Nacional de Geología: 246 p. Santiago.

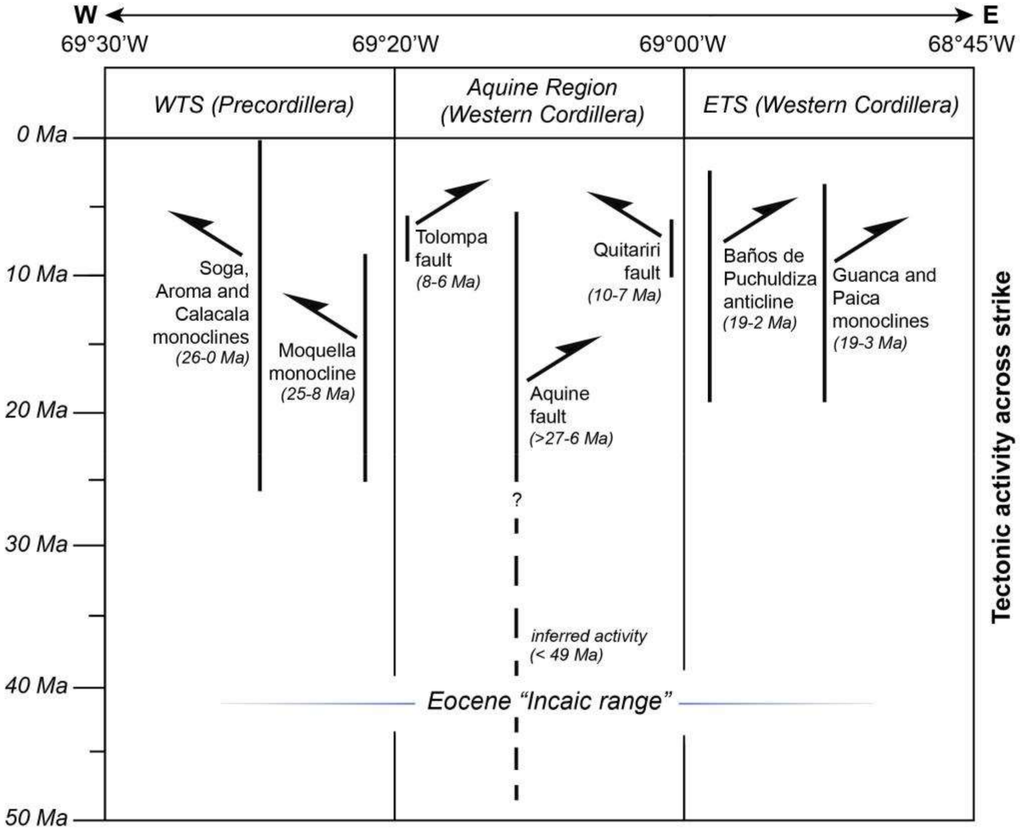

FIG. 10. Correlation of Cenozoic tectonic activity across the Precordillera and Western Cordillera at ~19°15' S. Timing of deformation at the Precordillera (WTS) is depicted after Pinto *et al.* (2004) and Farías *et al.* (2005). Timing of deformation at the Western Cordillera (ETS) is depicted after Cortés *et al.* (2012a, 2014).

4.2. Second episode (27-14 Ma)

Regarding the early Neogene structural evolution of the Western Cordillera, the unconformity between the Utayane and Puchuldiza Formations indicates a second period of contraction during the late Oligocene-middle Miocene (*ca.* 27-14 Ma) (Figs. 9c and 11b), in which the Utayane Formation was tilted towards the east, above the already deformed Icanche Formation. This second period is synchronic to the initial development of the Interandean Zone and Subandean Sierras, east of the Altiplano (McQuarrie *et al.*, 2005; Barnes *et al.*, 2012).

An Oligocene volcanic lull lasted until the late Oligocene-early Miocene (Trumbull *et al.*, 2006), when regional-scale explosive volcanism gave origin to the Utayane and Oxaya Formations (Figs. 9b and 11b) concomitant to a strong peak in plate convergence rates at *ca.* 25 Ma (Somoza, 1998). As the Oxaya Formation lies at the eastern margin of the Precordillera, and it is not exposed in the Western Cordillera (*e.g.*, García *et al.*, 2004; Valenzuela *et al.*, 2014; this study), and considering that the Utayane Formation only outcrops east of the Aquine fault at the southeastern portion of the Aquine region, we attribute this absence of pyroclastic deposits of this age (west and north of the Aquine fault in the study area) to the occurrence of a positive relief, uplifted by substratum-involving faults (Fig. 9b). A gradual eastward thickening of the Utayane Formation has also been registered east and south of the Aquine region, where this unit reaches a ~200 to 600-1,000 m thickness increase, suggesting that deposition of the former developed at the Western Cordillera but concentrated towards the east, in the westernmost Altiplano basin (Cortés *et al.*, 2014; Sellés *et al.*,

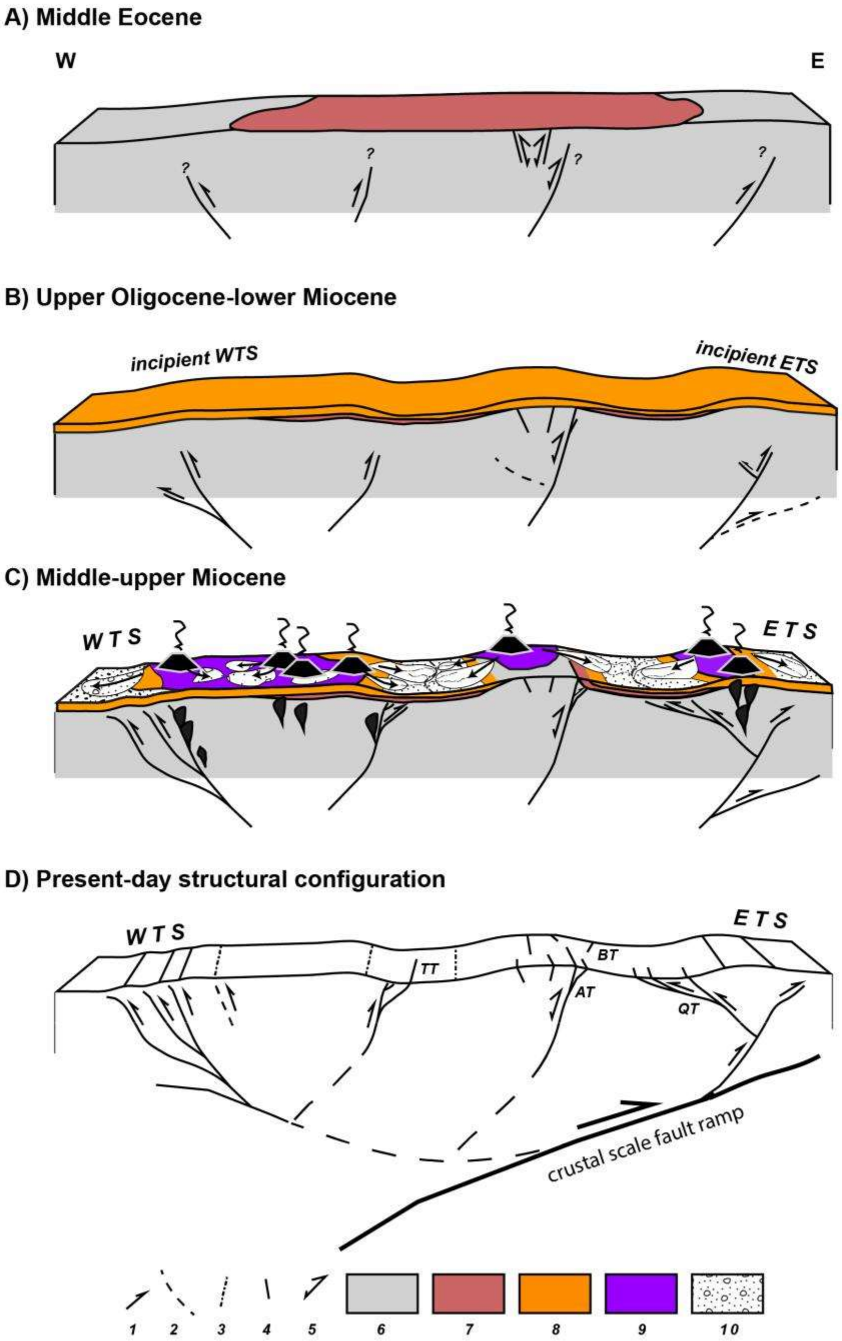

FIG. 11. Integrated model for the Cenozoic structural and depositional evolution of the Western Cordillera at ~19°20’ S. Approximate trace of the present-day structural configuration is shown in figure 2. The deep structure of the WTS and ETS are schematically drawn from Farías *et al*. (2005) and Cortés *et al*. (2012a), respectively. The crustal scale fault bend fold is drawn from Farías *et al*. (2005). Schematic development of the Aquine and Quitariri thrusts is explained in figure 9. Simbology: **1.** Reverse fault; **2.** Inferred in-depth structure; **3.** Inferred superficial trace of structure; **4.** Surface fault and fold traces; **5.** Inversely reactivated normal fault; **6.** Deformed Mesozoic substratum; **7.** Eocene ignimbrites (Icanche Formation); **8.** Oligocene-Miocene ignimbrites (Oxaya and Utayane Formations); **9.** Miocene andesitic lavas and volcanic sequences; **10.** Miocene sedimentary rocks. **TT:** Tolompa fault; **BT:** Berenguela fault; **AT:** Aquine fault; **QT:** Quitariri fault.

in press). The positive relief in the Aquine region would have restricted deposition of pyroclastic flows to depressed areas or prompted erosion of the deposits from topographic highs. In the Western Cordillera of the Belén Region, the Oligocene-Miocene explosive volcanic event is registered in the Lupica Formation (García *et al*., 2004; Charrier *et al*., 2005, 2007, 2013), which exhibits growth strata probably associated with normal faulting near the Oligocene-Miocene boundary, suggesting the existence of calderas along the present-day Precordillera and Western Cordillera (Charrier *et al* ., 2013), likely to be the source of the pyroclastic deposits in the Oxaya and Utayane Formations.

4.3. Third episode (14-6 Ma)

East-vergent folds within the Puchuldiza Formation were developed adjacent to the Aquine reverse fault. As the Aquine fault is sealed by upper Miocene volcanic sequences of the Tatajachura volcano at the Aroma valley, the youngest movement along the reverse fault is prior to *ca*. 6 Ma (lavas of the Tatajachura volcano; Morandé *et al*., 2014), which indicates a third period of compressive deformation during the middle-latest Miocene (*ca*. 14-6 Ma) (Figs. 9d and 11c). The Tolompa fault and associated east-vergent folds, as well as the Berenguela fault and adjacent syncline, in the northern portion of the study area, also developed during this time span, most likely during the latest Miocene.

Volcanism during the middle Miocene, represented by the Puchuldiza Formation and the Guaillane Ignimbrite was more or less concomitant to the latest stages of deposition of the sedimentary Chucal Formation and the volcanic and sedimentary Macusa Formation in the Belén region (Fig. 3, García *et al*., 2004; Charrier *et al* ., 2005, 2013). In the Aquine region, the Miocene Mauque Formation represents the occurrence of humid alluvial fans and associated braided rivers throughout their middle and distal portions, developed in exoreic intramontane basins (Argandoña, 1984; Cortés *et al*., 2014; Valenzuela *et al*., 2014; Bobadilla, 2015; Herrera *et al*., 2015), adjacent to Middle and Upper Miocene volcanic edifices (Fig. 11c), which are still partially conserved in the study area and its surroundings. Given the geochemical and lithological affinity of Miocene volcanic products and clastic content of the Mauque Formation (Bobadilla, 2015), in addition to the fact that detrital U-Pb zircon analyses for the Mauque Formation yielded strong middle-Miocene peaks, we argue that products of the erosion of middle Miocene volcanoes would be the main source of the successions clastic content. Specifically, geochronological analyses for lavas of the Mamuta volcano, which yielded ages of *ca*. 14 Ma (Seguel *et al*., 1991; Valenzuela *et al*., 2014), in addition to ages yielded from U-Pb zircon and K-Ar on biotite analyses carried out for the underlying Puchuldiza Formation (*ca*. 14 Ma; Ortiz *et al*., 2008; Cortés *et al*., 2014; Valenzuela *et al*., 2014), indicate that these units would likely correspond to the predominant detrital source for the Mauque Formation.

As the Mauque Formation (*ca*. 14-8 Ma) is in part synchronic to and involved in the thrust system controlled by the Quitariri fault within the southeastern portion of the study area, deformation can be constrained by the age of the Putoyane Ignimbrite (7 Ma) which covers and seals folds related to the fault in the Macurquima valley. Hence, overlapping the third period, compressive deformation took place during the late Miocene (*ca*. 10- 7 Ma) (Figs. 9d and 11c). Style of deformation in the southeastern portion of the study area is west-vergent and thin-skinned at the surface, although substratum-rooting of thrusts at depth cannot be discarded (Fig. 9d). Movement along the Quitariri and related thrusts is likely to be a result of late Miocene back-thrusting related to activity of a deeply rooted west-dipping thrust of the ETS; which probably corresponds to the westernmost strand of the system in the Cariquima region which passes through the Puchuldiza area (Figs. 9d and 11c) (Cortés *et al*., 2012a). There is no evidence for neotectonic deformation in the study area, nor post-7 Ma deformation.

Growth strata relations observed in the Macurquima valley (Fig. 7), and synsedimentary structures, such as slumping and recumbent stratification, within sandstone layers, suggests a syntectonic interpretation for the development of the Mauque Formation in the Aquine region (*e.g* ., Bobadilla, 2015; Herrera *et al*., 2015). Although the structural style is clear for deformation during the Miocene in the Western Cordillera, the tectonic regime in which the Mauque Formation accumulated, compressional or extensional, is subject of debate (Bobadilla, 2015; Herrera *et al*., 2015). In the Belén region, the Chucal Formation registers a similar syntectonic development of deposition. Lacustrine sedimentation was followed by fluvial sedimentation during the lower to middle Miocene, with concomitant alluvial fans which are represented by a coarsening-up sedimentary sequence that exhibits eastward-fanning growth strata (Charrier *et al*., 2005). These growth strata and progressive unconformities within the formation are associated with the growth of the Chucal anticline, which is inferred to be related to a blind thrust (García *et al*., 2004; Charrier *et al*., 2005). In spite of the diachronic lapses of deposition for the Chucal and Mauque Formations, the observed growth strata relations in the overturned limb of the west-vergent anticline in the Macurquima valley indicate that the Mauque Formation also accumulated under compressive tectonic conditions during the middle to late Miocene. Moreover, the syntectonic deposition of the El Diablo Formation (*ca.* 16 -8 Ma) in the Precordillera at ~19°15' S, directly related to the development of the WTS (Pinto *et al*., 2004; Farías *et al*., 2005), and roughly coeval to the deposition of the Mauque Formation, suggests that sedimentation and volcanism developed throughout the Precordillera and Western Cordillera under active compressive tectonic conditions (Figs. 10 and 11c).

Upper Miocene volcanism continued in the Western Cordillera until present without major interruptions, generating andesitic lava sequences and pyroclastic flow deposits (upper Miocene, Pliocene, Pleistocene and Quaternary volcanic sequences).

4.4. Relationship with the WTS and ETS

With respect to the bordering structural systems, deformation along the WTS occurred at: 21 Ma at ~19°15' S (Pinto *et al*., 2004), 26 Ma at ~19°20' S (Farías *et al*., 2005), and 30 Ma at 18° -19° S (García, 2002) and 20°-21° S (Victor *et al*., 2004). Meanwhile, deformation on the ETS commenced at 21 Ma at ~18°40' S (Charrier *et al*., 2005), and at *ca.* 23 Ma at ~19°30' S (Cortés *et al*., 2012a) (Fig. 10). Neogene activity of the WTS in the Precordillera is considered to be continuous, although at varying deformation rates during the Miocene (*e.g.*, Pinto *et al*., 2004; Victor *et al*., 2004; Farías *et al*., 2005). Peaks of increased deformation have been identified in the Precordillera at ~20°-21° S during *ca.* 25 Ma and *ca.* 12-10 Ma (Victor *et al*., 2004), and roughly coincide with the second and third episodes of contraction registered in the Aquine region. Rapid relative uplift along the WTS has been tracked for most of the Miocene (*ca.* 26-8 Ma; Farías *et al*., 2005), concomitant to Neogene deformation at the Aquine region (Fig. 10) . In regards to the ETS, Neogene activity is also considered to be continuous for most of the period, in a ~18 Myr timespan between *ca.* 21-3 Ma, in which at least four compressive events took place in the Western Cordillera through east-vergent thin-skinned thrusts and folds at ~18°40'S (Jaropilla thrust and Chucal anticline; García *et al*., 2004; Charrier *et al*., 2005). At ~19°15' S, activity of the ETS is constrained to a timespan concomitant to the WTS at the same latitudes, restricted to the Miocene epoch (lower-upper Miocene), rather synchronous to the evolution of the ETS towards the north (Fig. 10) (Cortés *et al*., 2012a, 2014). We relate the third episode of deformation identified at the Aroma region to backthrusting of the ETS during the latest Miocene.

With relation to the present-day structural configuration of the Western Cordillera (Fig. 11d), the geology outlined indicates the occurrence of oppositely verging thrust faults that limit and uplift crustal blocks that effectively define *pop-up* structures on the margins and interior of the Precordillera and Western Cordillera. The westernmost *pop-up* structure is inferred to link the structures of the WTS to the east-vergent thrusts of the Aquine region (Tolompa and Aquine reverse faults). Within the hypothetical *pop-up*, strike-slip motion has been proposed for the easternmost part of WTS at 20°-21° S (*e.g.*, Victor *et al*., 2004). Plate convergence obliquity variations that enhanced dextral along-strike displacements in the Precordillera at 19°30' S within the WTS (Soga and Aroma flexures; Farías *et al*., 2005) are proposed for the present-day geodynamic setting of the arc (Farías *et al*., 2005). However, no direct evidence has been registered in the Aquine region for transpressive tectonics and hence, we consider that strike-slip motions in our study area appear doubtful. The easternmost *pop-up* structure is more evident, and defined by the west-vergent Quitariri fault, which roots into the westernmost thrust of the ETS in the Cariquima Region (Fig. 11d), which, in turn, is proposed to be rooted in the crustal-scale fault ramp of Farías *et al.* (2005) (Cortés *et al*., 2012a). This easternmost *pop-up* can be qualitatively compared to a *pop-up* structure generated as a back thrust associated to a positively reactivated normal thrust (*e.g.*, Bonini *et al*., 2012).

This *pop-up* array structural style proposed for the Western Cordillera was previously advanced by Farías *et al.* (2005), Charrier *et al.* (2007, 2013) and Cortés *et al.* (2012a), and has also been demonstrated for the structure of the Eastern Cordillera in Bolivia (McQuarrie *et al.*, 2005). Towards the ETS and below the Western Cordillera, the crustal-scale fault ramp within the rigid forearc is inferred to flatten towards the Altiplano where it corresponds to the ALVZ (Altiplano Low Velocity Zone in ANCORP, 2003; Farías *et al.*, 2005; Cortés *et al.*, 2012a). We note that this structural style is consistent with the upper crust structure of the Western Cordillera at the study region (Farías *et al.*, 2005; Cortés *et al.*, 2012a), and that similarly, it develops in the local (singular structure), regional (several structures) and crustal (bordering thrust systems) scale. Analogue experiments for compressive systems (Venegas and Nalpas, 2005) indicate that *pop-up* structures and deformation distributed over large zones is favored where the compressive belt has not undergone massive surface erosion during its development, such as the Western Cordillera (García *et al.*, 2011).

Hypothetically, the structure of the Western Cordillera is linked at depth with the WTS and ETS by means of the crustal-scale west-dipping fault ramp of Farías *et al.* (2005) (Fig. 11d). The schematic geometry of our conceptual model (Fig. 11d) is qualitatively comparable to the crustal-scale architecture proposed for the Principal Cordillera of the Andes in Central Chile (~33° S) (Farías *et al.*, 2010).

In regards to the overall timing of deformation, the unconformities exposed amongst the Neogene formations, particularly in the Macurquima valley, suggest the repeated occurrence of contraction during this period in the Western Cordillera, at least for the time span between deposition of the Utayane Formation and the Putoyane Ignimbrite (*ca.* 27-7 Ma), meaning the tectonic activity may have spanned as much as *ca.* 20 Myr. This lapse was preceded by a middle to late Paleogene compressive phase of an undetermined duration. The present- day Western Cordillera appears to be situated in a structural block that absorbed deformation through most of the Cenozoic (Fig. 10), which corresponds to the "Incaic relief" of Charrier *et al.* (2007, 2013). This relief has marked the drainage divide between the Altiplano basin and the Central Depression basin since at least the Eocene (Charrier *et al.*, 2013). As onset and development of deformation in the Aquine region was concomitant to uplift within the eastern Altiplano (Barnes *et al.*, 2012), we interpret that contraction in the study area has contributed to uplift of the western flank of the Andean plateau as part of a long-lived compressive structural system comprised by the WTS, the ETS and the intervening structure of the Western Cordillera.

5. Concluding remarks

The Western Cordillera (WC) in the Aquine region experienced contractional deformation in the middle or late Paleogene, concomitant with uplift in the Eastern Cordillera of Bolivia, and was afterwards characterized by a compressive tectonic regime throughout most of the Neogene, in the *ca.* 27-7 Ma time span, concomitant to deformation in the Interandean Zone and the Subandean Sierras of Bolivia.

During the Neogene, the WC experienced three main episodes of contraction: a middle Eocene-late Oligocene (*ca.* 49-27 Ma) episode, a late Oligocene-middle Miocene (*ca.* 27- 14 Ma) episode, and a middle to latest Miocene episode (*ca.* 14-6 Ma). Synchronically, sedimentation and volcanism developed throughout the Precordillera and Western Cordillera under active compressive tectonic conditions, resembling the tectonostratigraphic evolution of the WC at 18°-19° S.

Deformation was accomplished by means of NNW to SSE striking, high-angle, substratum-involving, thrusts and associated folds, in addition to a low-angle fold-and-thrust belt that constitute a doubly vergent structural domain located between the West Vergent Thrust System, located at the foot of the Precordillera, and the East Vergent Thrust System located within the WC, immediately east of the Aquine region. The structural style within the WC indicates a combination of thin- and thick-skinned deformation. This character is also exhibited by the West Vergent Thrust System in the Precordillera and inferred for the East Vergent Thrust System towards the westernmost Altiplano. Together with the bordering thrust systems, the overall structure of the WC resembles a crustal-scale "*pop-up*" structure.

The high-angle character of substratum-involving thrusts in the WC suggests an inheritance of pre-Cenozoic extensional structures within the Mesozoic substratum that underwent positive inversion during the Cenozoic, highlighting the importance of extensional structural inheritance in the construction of the uppermost crust of the present-day Andes of northernmost Chile.

Acknowledgements.

This study is part of the 1:100.000-scale basic geology mapping project encompassed in the Plan Nacional de Geología of the Servicio Nacional de Geología y Minería (SERNAGEOMIN, Chile). We specially thank reviewers A.J. Tomlinson (SERNAGEOMIN) for a thorough first revision of this manuscript that led to a major improvement of the text and figures, and Professor R. Charrier (Universidad de Chile) for providing constructive comments and suggestions that greatly enhanced our contribution. The authors also thank I. del Real (University of British Columbia) for fieldwork and structural interpretations at an early stage of this study; P. Bobadilla (Universidad de Chile) for fieldwork and for sharing the detailed sedimentology and stratigraphy of the Mauque Formation from his thesis project; J. Vargas and R. Valles (Universidad de Chile) for zircon sample preparation; L. Solari (UNAM) for the U-Pb LA-ICP-MS analyses; and S. Bascuñán and P. Molina (Universidad de Chile) for helpful discussions on the structural and stratigraphical approaches as well as geochronological aspects addressed in the paper.

References

Allmendinger, R.; Jordan, T.; Kay, S.M.; Isacks, B. 1997. The evolution of the Altiplano-Puna plateau of the Central Andes. Annual Reviews of Earth and Planetary Sciences 25: 139-174.

Amilibia, A.; Sàbat, F.; McClay, K.R.; Muñoz, J.A.; Roca, E.; Chong, G. 2008. The role of inherited tectono-sedimentary architecture in the development of the central Andean mountain belt: Insights from the Cordillera de Domeyko. Journal of Structural Geology 30: 1520-1539.

ANCORP Working group. 2003. Seismic imaging of a convergent continental margin and plateau in the central Andes (Andean Continental Research Project 1996 (ANCORP'96)). Journal of Geophysical Research 108 (B7), 2328: 1-25

Argandoña, R. 1984. Geología del cuadrángulo Cerro Socora y características generales del área geotermal de Puchuldiza. Memoria de Título (Unpublished), Universidad de Chile, Departamento de Geología: 166 p.

Arriagada, C.; Cobbold, P.R.; Roperch, P. 2006. Salar de Atacama basin: A record of compressional tectonics in the central Andes since the mid-Cretaceous. Tectonics 25, TC1008: 1-19.

Arriagada, C.; Roperch, P.; Mpodozis, C.; Cobbold, P.R. 2008. Paleogene building of the Bolivian Orocline: Tectonic restoration of the central Andes in 2-D map view. Tectonics 27, TC6014: 1-14.

Bahlburg, H.; Hervé, F. 1997. Geodynamic evolution and tectonostratigraphic terranes of northwestern Argentina and northern Chile. Geological Society of America Bulletin 7: 869-884.

Barnes, J.B.; Ehlers, T.A. 2009. End member models for Andean Plateau uplift. Earth-Science Reviews 97: 117-144.

Barnes, J.B.; Ehlers, T.A.; McQuarrie, N.; O'Sullivan, P.B.; Tawackoli, S. 2008. Thermochronometer record of central Andean plateau growth, Bolivia (19.5°). Tectonics 27, TC3003: 1-25.

Barnes, J.B.; Ehlers, T.A.; Insel, N.; McQuarrie, N.; Poulsen, C.J. 2012. Linking orography, climate, and exhumation across the central Andes. Geology 40 (12): 1135. doi: 10.1130/G33229.1.

Bascuñán, S.; Arriagada, C.; Le Roux, J.; Deckart, K. 2015. Unravelling the Peruvian Phase of the Central Andes: stratigraphy, sedimentology and geochronology of the Salar de Atacama Basin (22°30'-23°S), northern Chile. Basin Research 2015: 1-28.

Basei, M.A.; Charrier, R.; Hervé, F. 1996. New ages (U-Pb, Rb-Sr, $_{39}$K-$_{40}$Ar) from supposed Precambrian units in Chile: some geotectonic implications. *In* Proceedings of the International Symposium on Andean Geodynamics, No 3, editorial ORSTOM: 763-766. Saint Malo.

Blanco, N.; Tomlinson, A. 2013. Carta Guatacondo, Región de Tarapacá. Servicio Nacional de Geología y Minería, Carta Geológica de Chile, Serie Geología Básica 156, 1 mapa escala 1:100.000. Santiago.

Bobadilla, P. 2015. Análisis del ambiente tectonosedimentario de la Formación Mauque y su implicancia durante el Mioceno tardío, Región de Tarapacá (19°15'S/69º15'W). Memoria de Título (Unpublished), Departamento de Geología, Universidad de Chile. 116 p.

Bonini, M.; Sani, F.; Antonielli, B. 2012. Basin inversion and contractional reactivation of inherited normal faults: A review based on previous and new experimental models. Tectonophysics 522-523: 55-88.

Charrier, R.; Chávez, A.; Elgueta, S.; Hérail, G.; Flynn, J.; Croft, D.; Wyss, A.; Riquelme, R.; García, M. 2005. Rapid tectonic and paleogeographic evolution associated with the development of the Chucal anticline and the Chucal-Lauca Basin in the Altiplano of Arica, northern Chile. Journal of South American Earth Sciences 19: 35-54.

Charrier, R.; Pinto, L.; Rodríguez, M.P. 2007. Tectonostrati-graphic evolution of the Andean Orogen in Chile. *In* The Geology of Chile (Gibbons W., Moreno, T.; editors). The Geological Society, Special Publication: 21-116. London.

Charrier, R.; Farías, M.; Maksaev, V. 2009. Evolución tectónica, paleogeográfica y metalogénica durante el Cenozoico en los Andes de Chile norte y central e implicaciones para las regiones adyacentes de Bolivia y Argentina. Revista de la Asociación Geológica Argentina 65: 5-35.

Charrier, R.; Hérail, G.; Pinto, L.; García, M.; Riquelme, R.; Farías, M.; Muñoz, N. 2013. Cenozoic tectonic evolution in the Central Andes in northern Chile and west central Bolivia: Implications for paleogeographic, magmatic and mountain building evolution. International Journal of Earth Sciences 102: 235-264.

Cornejo, P.; Matthews, S.; Pérez de Arce, C. 2003. The "K-T" compressive deformation event in northern Chile (24-27ºS). *In* Congreso Geológico Chileno No. 10, Resumen Extendido, CD-ROM. Concepción.

Cortés, J.; Farías, M.; Comte, D.; Charrier, R. 2012a. Estructuras y depósitos neógenos de la región de Cariquima (Altiplano chileno): Implicancias en el origen de la Cordillera Occidental a los 19°30'S. *In* Congreso Geológico Chileno, No. 13, Actas: 229-231. Antofagasta.

Cortés, J.; Del Real, I.; Pinto, L.; Farías, M.; Herrera, S.; Castruccio, A. 2012b. Primeros resultados de la Geología y Estructura de la Precordillera y Cordillera Occidental entre los 19°15' y 19°30'S (I Región de Tarapacá, Chile). *In* Congreso Geológico Chileno No. 13, Actas: 229-231. Antofagasta.

Cortés, J.; Cascante, M.; Zavala, V. 2014. Geología de las Áreas Isluga y Sierra de Huaillas, Región de Tarapacá. Servicio Nacional de Geología y Minería, Carta Geológica de Chile, Serie Geología Básica 172-173, 1 mapa escala 1:100.000.

Dewey, J.F.; Bird, J.M. 1970. Mountain belts and the new global tectonics. Journal of Geophysical Research 75: 2625-2647.

Elger, K.; Oncken, O.; Glodny, J. 2005. Plateau-style accumulation of deformation, southern Altiplano. Tectonics 24, TC4020: 1-19.

Farías, M.; Charrier, R.; Comte, D.; Martinod, J.; Hérail, G. 2005. Late Cenozoic deformation and uplift of the western flank of the Altiplano: Evidence from the depositional, tectonic, and geomorphologic evolution and shallow seismic activity (northern Chile at 19°30'S). Tectonics 24, TC4001: 1-27.

Farías, M.; Comte, D.; Charrier, R.; Martinod, J.; David, C.; Tassara, A.; Tapia, F.; Fock, A. 2010. Crustal-scale structural architecture in Central Chile based on seismicity and surface geology: implications for Andean mountain building. Tectonics 29, TC3006: 1-22.

Gallardo, F.; Farías, M.; Morandé, J. 2013. Tracking Mesozoic tectonics in the western slope of the Altiplano in northern Chile and the onset of contractional deformation: evidence from the Tarapacá valley at 19°45'S. Bollettino di Geofisica 54 suppl. 2. *In* GeoSur 2013, Resúmenes: 55-56. Viña del Mar.

Galli, C. 1967. Pediplain in northern Chile and the Andean uplift. Science 158: 653-655.

Galli, C.; Dingman, R.J. 1962. Cuadrángulo Pica, Alca, Matilla y Chacarilla con un estudio sobre los recursos de agua subterránea, Provincia de Tarapacá. Instituto de Investigaciones Geológicas, Carta Geológica de Chile. Serie Geología Básica 7-10: 125 p. Santiago.

García, M. 1996. Geología y estructura del borde del Altiplano occidental, en el área de Belén (Chile). Memoria de Título y Tesis de Grado de Magíster en Ciencias mención Geología (Unpublished), Departamento de Geología, Universidad de Chile: 111 p.

García, M. 2002. Évolution oligo-néogene del'Altiplano Occidental (Arc et Avant-Arc du Nord du Chili, Arica): Tectonique, volcanisme, sédimentation, géomorphologie et bilan érosion-sédimentation. Tesis de Doctorado (Unpublished), Université Joseph Fourier, Grenoble: 117 p. Francia.

García, M.; Hérail, G. 2005. Fault-related folding, drainage network evolution and valley incision during the Neogene in the Andean Precordillera of Northern Chile. Geomorphology 65: 279-300.

García, M.; Gardeweg, M.; Clavero, J.; Hérail, G. 2004. Hoja Arica, Región de Tarapacá. Servicio Nacional de Geología y Minería, Carta Geológica de Chile, Serie Geología Básica 84: 150 p., 1 mapa escala 1:250.000.

García, M.; Riquelme, R.; Farías, M.; Hérail, G.; Charrier, R. 2011. Late Miocene-Holocene canyon incision in the western Altiplano, northern Chile; tectonic or climatic forcing? Bulletin of the Geological Society of London 168: 1047-1070.

García, M.; Fuentes, G.; Riquelme, F. 2013. Carta Miñimiñi, Regiones de Arica y Parinacota y de Tarapacá. Servicio Nacional de Geología y Minería, Carta Geológica de Chile, Serie Geología Básica 157: 49 p., 1 mapa escala 1:100.000.

Garzione, C.N.; Molnar, P.; Libarkin, J.C.; MacFadden, B.

2006. Rapid late Miocene rise of the Andean plateau: evidence for removal of mantle lithosphere. Earth and Planetary Science Letters 241: 543-556.

Garzione, C.N.; Auerbach, D.J.; Smith, J.J.; Rosario, J.J.; Passey, B.H.; Jordan, T.E.; Eiler, J.M. 2014. Clumped isotope evidence for diachronous surface cooling of the Altiplano and pulsed surface uplift of the Central Andes. Earth and Planetary Science Letters 393: 173-181.

Gregory-Wodzicki, K. 2000. Uplift history of central and northern Andes: A review, Geological Society of America Bulletin 112: 1091-1105.

Harambour, S. 1990. Geología pre-Cenozoica de la Cordillera de Los Andes entre las Quebradas Aroma y Juan de Morales, I Región. Memoria de Título (Unpublished), Universidad de Chile: 228 p. Santiago.

Hartley, A.J.; Evenstar, L. 2010. Cenozoic stratigraphic development in the northern Chilean forearc: Implications for basin development and uplift history of the Central Andean margin. Tectonophysics 495: 67-77.

Herrera, S.; Pinto, L.; Valenzuela, J.I.; Cortés, J. 2013. Cenozoic tectonostratigraphy of the Western Cordillera: a conceptual model for its origin and evolution (northern Chile at ~19°20' S). Bollettino di Geofisica, 54 suppl. 2. *In* GeoSur 2013, Resúmenes: p. 69. Viña del Mar.

Herrera, S.; Bobadilla, P.; Pinto, L. 2015. Sedimentación y deformación de la Formación Mauque durante el Mioceno: Implicancias tectónicas (Cordillera Occidental; norte de Chile a los 19°15'S). *In* Congreso Geológico Chileno No. 14, Actas: 4 p. La Serena.

Hoke, G.D.; Isacks, B.L.; Jordan, T.E.; Blanco, N.; Tomlinson, A.J.; Ramezani, J. 2007. Geomorphic evidence for post-10 Ma uplift of the western flank of the central Andes 18°30'-22°S. Tectonics 26, TC5021: 1-17.

Horton, B.K.; Hampton, B.A.; Waanders, G.L. 2001. Paleogene synorogenic sedimentation in the Altiplano plateau and implications for initial mountain building in the central Andes. Geological Society of America Bulletin 113 (11): 1387-1400.

Horton, B.K.; Hampton, B.A.; Lareau, B.N.; Baldellón, E. 2002. Tertiary provenance history of the northern and central Altiplano (Central Andes, Bolivia): A detrital record of plateau-margin tectonics. Journal of Sedimentary Research 72 (5): 711-726.

Isacks, B.L.1988. Uplift of the central Andean plateau and bending of the Bolivian Orocline, Journal of Geophysical Research 93: 3211-3231.

Jaillard, E. 1992. La Fase Peruana en la Margen Peruana (Cretáceo Superior). Boletín de la Sociedad Geológica del Perú 83: 81-87.

Jordan, T.E.; Nester, P.L.; Blanco, N.; Hoke, G.D.; Dávila, F.; Tomlinson, A.J. 2010. Uplift of the Altiplano-Puna plateau: A view from the west. Tectonics 29, TC5007: 1-31.

Lahsen, A.; Sepúlveda, F.; Rojas, J.; Palacios, C. 2005. Present Status of Geothermal Exploration in Chile. *In* World Geothermal Congress 2005: 24-29. Antalya.

Lamb, S.; Hoke, L.; Kennan, L.; Dewey, J. 1997. Cenozoic evolution of the Central Andes in Bolivia and northern Chile. *In* Orogeny Through Time (Burg, J.P.; Ford, M.; editors), Geological Society Special Publication 121: 237-264.

Loewy, S.L.; Connelly, J.N.; Dalziel, I.W.D. 2004. An orphaned basement block: The Arequipa-Antofalla Basement of the central Andean margin of South America. Geological Society of America Bulletin 116: 171-187.

Ludwig, K.R. 2008. Isoplot 3.7. Berkeley Geochronology Center, Special publication 4: 1-77.

Maksaev, V. 1978. Cuadrángulo Chitigua y sector oriental del Cuadrángulo Cerro Palpana, Región de Antofa-gasta, Escala 1:50.000. Instituto de Investigaciones Geológicas, Carta Geológica de Chile 31: 55 p. Santiago.

Marques, F.O.; Nogueira, C.R. 2008. Normal fault inversion by orthogonal compression: Sandbox experiments with weak faults. Journal of Structural Geology 30: 761-766.

Martínez, F.; Arriagada, C.; Peña, M.; Del Real, I.; Deckart, K. 2013. The structure of the Chañarcillo Basin: An example of tectonic inversion in the Atacama region, northern Chile. Journal of South American Earth Sciences 42: 1-16.

McQuarrie, N.; Horton, B.K.; Zandt, G.; Beck, S.; De Celles, P.G. 2005. Lithospheric evolution of the Andean fold-thrust belt, Bolivia, and the origin of the central Andean plateau. Tectonophysics 399: 15-37.

Mégard, F. 1984. The Andean orogenic period and its major structures in central and northern Peru. Journal of the Geological Society of London 141: 893-900.

Montgomery, D.R.; Balco, G.; Willettt, S.D. 2001. Climate, tectonics, and the morphology of the Andes. Geology 29: 579-582.

Morandé, J.; Gallardo, F.; Farías, M. 2015. Carta Guaviña, Región de Tarapacá. Servicio Nacional de Geología y Minería, Carta Geológica de Chile, Serie Geología Básica 177. 1 mapa escala 1:100.000.

Muñoz, N.; Sepúlveda, P. 1992. Estructuras compresivas con vergencia al oeste en el borde oriental de la Depresión Central, norte de Chile (19°15'S). Revista Geológica de Chile 19 (2): 241-247. doi: 10.5027/andgeoV19n2-a07.

Muñoz, N.; Charrier, R. 1996. Uplift of the western border of the Altiplano on a west-vergent thrust system, northern Chile. Journal of South American Earth Sciences 9: 171-181.

Pacci, D.; Hervé, F.; Munizaga, F.; Kawashita, K.; Cordani, U. 1980. Acerca de la edad Rb-Sr precámbrica de rocas de la Formación Esquistos e Belén, Departamento de Parinacota, Chile. Revista Geológica de Chile 11: 43-50. doi: 10.5027/andgeoV7n3-a03.

Pardo-Casas, F.; Molnar, P. 1987. Relative motion of the Nazca (Farallon) and South American plates since Late Cretaceous times. Tectonics 6: 233-248.

Paton, C.; Woodhead, J.D.; Hellstrom, J.C.; Hergt, J.M.; Greig, A.; Maas R. 2010. Improved laser ablation U-Pb zircon geochronology through robust downhole fractionation correction. Geochemistry, Geophysics Geosystems 11: 1525-2027.

Petrus, J.A.; Kamber, B.S. 2012. VizualAge: A novel approach to laser ablation ICP-MS U-Pb geochronology data reduction. Geostandards and Geoanalytical Research 36: 247-270.

Pinto, L.; Hérail, G.; Charrier, R. 2004. Sedimentación sintectónica asociada a las estructuras Neógenas en la Precordillera de la zona de Moquella (19°15'S, norte de Chile). Revista Geológica de Chile 31 (1): 19-44. doi: 10.5027/andgeoV31n1-a02.

Reutter, K.J. 2001. Le Ande centrali: elemento di un'orogenesi di margine continentale attivo. Acta Naturalia de l'Ateneo Parmense 37: 5-37.

Riquelme, R. 1998. Estratigrafía y deformación de las unidades cenozoicas del borde altiplánico chileno (18°35'-19°00'S/69° 00'-69°30'W). Memoria de Título y Tesis de Grado de Magíster en Ciencias, mención Geología (Unpublished), Departamento de Geología, Universidad de Chile: 124 p.

Scheuber, E.; Reutter, K.J. 1992. Magmatic arc tectonics in the central Andes between 21° and 25°. Tectonophysics 205: 127-140.

Seguel, J.E.; Lahsen, A.; Vergara, M. 1991. Contribución al conocimiento del Complejo Volcánico Mamuta-Guaichane, Pre-Cordillera de Iquique, Región de Tarapacá: un Complejo Volcánico del Mioceno Medio a superior. *In* Congreso Geológico Chileno No. 6, Actas 1: 368-372. Viña del Mar.

Sellés. D.; Gardeweg, M.; Garibaldi, N. 2016. Geología del Área Pampa Lirima-Cancosa, Región de Tarapacá. Servicio Nacional de Geología y Minería, Carta Geológica de Chile, Serie Geología Básica 182, 1 mapa escala 1:100.000. Santiago.

Sláma, J.; Košler, J.; Condon, D.; Crowley, J.L.; Gerdes, A.; Hanchar, J.M.; Horstwood, M.; Morris, G.; Nasdala, L.; Norberg, N.; Schaltegger, U.; Schoene, B.; Tubrett, M.; Whitehouse, M. 2008. Plesovice zircon-A new natural reference material for U-Pb and Hf isotopic microanalysis. Chemical Geology 249: 1-35.

Solari, L.A.; Gómez-Tuena, A.; Bernal, J.P.; Pérez-Arvizu, O.; Tanner, M. 2010. U-Pb zircon geochronology by an integrated LA-ICPMS microanalytical work-station: achievements in precision and accuracy. Geostandards and Geoanalytical Research 34-1: 5-18.

Steinmann, G.1929. Geologie von Peru. Carl Winters Universitats-Buchhandlung: 448 p.

Somoza, R. 1998. Updated Nazca (Farallon)-South America relative motions during the last 40 My: Implications for mountain building in the central Andean region. Journal of South American Earth Sciences 11: 211-215.

Tomlinson, A.J.; Blanco, N. 1997. Structural evolution and displacement history of the West Fault system, Precordillera, Chile: part II, Postmineral history. *In* Congreso Geológico Chileno No. 8, Actas 3.

Tomlinson, A.; Blanco, N.; Ladino, M. 2015. Carta Mamiña, Región de Tarapacá. Servicio Nacional de Geología y Minería, Carta Geológica de Chile, Serie Geología Básica 174 p., 1 mapa escala 1:100.000. Santiago.

Trumbull, R.B.; Riller, U.; Oncken, O.; Scheuber, E.; Munier, K.; Hongn, F. 2006. The time-space distribution of Cenozoic volcanism in the South-Central Andes: a new data compilation and some tectonic implications. *In* The Andes. Springer Berlin Heidelberg: 29-43.

Valenzuela, J.I.; Herrera, S.; Pinto, L; Del Real, I. 2014. Carta Camiña, regiones de Arica-Parinacota y Tarapacá. Servicio Nacional de Geología y Minería, Carta Geológica de Chile, Serie Geología Básica 170: 97 p., 1 mapa escala 1:100.000.

Venegas, C.; Nalpas, T. 2005. Erosion influence on the evolution of compressive systems constrained by analogue modelling. *In* International Symposium on Andean Geodynamics (ISAG 2005), No. 6, Extended Abstracts: 779-782.

Victor, P.; Oncken, O.; Glodny, J. 2004. Uplift of the western Altiplano plateau: Evidence from the Precordillera between 20° and 21°S (northern Chile). Tectonics 23, TC4004: 1-24.

Wiedenbeck, M.; Alle, P.; Corfu, F.; Griffin, W.L.; Meier, M.; Oberli, F.; von Quadt, A.; Roddick, J.C.; Spiegel, W. 1995. 3 natural zircon standards for U-Th-Pb, Lu-Hf, trace-element and REE analyses. Geostandards Newsletter 19: 1-23.

Manuscript received: December 09, 2015; revised/accepted: February 22, 2017; available online: February 22, 2017.

Appendix

Methodology for U-Pb LA-ICPMS geochronology

Zircon separates from one dacite and three tuff samples have been prepared under standard separation methods at the Geology Department, Universidad de Chile, using the Gemini table, Frantz magnetic separator and heavy liquid procedures. Final grain selection was undertaken by hand, using a binocular. Mineral separates were sent for analyses to the Laboratorio de Estudios Isotópicos (LEI), Geoscience Center, Universidad Nacional Autónoma de México (UNAM), Mexico.

The analytical work was undertaken by using a "Resonetics Resolution M50" 193 nm laser "Excimer of ArF" connected to a "Thermo Xii Series Quadrupole Mass Spectrometer" following analytical procedures and technical details after Solari *et al.* (2010). Selected zircon minerals were mounted in epoxy and polished. Employed laser diameter for ablation was between 24 to 34 mm and reached ablation depth was about 15-25 mm. The Plesovice (337 Ma; Sláma *et al.*, 2008) and 91500 (1065 Ma; Wiedenbeck *et al.*, 1995) international reference zircons were analyzed during age acquisition of the unknown samples. Average ages were calculated and respective plots were obtained using "Isoplot v. 3.7" (Ludwig, 2008). For zircon grains with ages below 1,000 Ma, the $_{206}$Pb/$_{283}$U ages were considered meaningful as best ages.

CS2-4				**CORRECTED AGES[2] (Ma)**						
spots	**U[1] (ppm)**	**Th[1] (ppm)**	**Th/U**	**^{206}Pb/^{238}U**	**±2σ**	**^{207}Pb/^{235}U**	**±2σ**	**^{207}Pb/^{206}Pb**	**±2σ**	**Rho**
16	404	136	0.29	70.0	2.0	74	10	312	244	0.47
17	399	328	0.71	68.8	2.0	72	12	259	324	0.18
18	186	76	0.35	70.0	2.0	76	10	294	266	0.40
19	231	145	0.55	71.0	2.0	83	10	563	240	-0.03
20	311	266	0.74	69.1	2.0	82	16	473	362	0.37
21	356	131	0.32	69.0	2.0	74	8	236	230	0.47
22	329	204	0.54	66.6	1.8	71	12	227	298	0.57
23	410	216	0.46	68.3	2.0	72	8	299	220	0.76
24	203	129	0.55	69.0	2.0	76	10	333	262	0.16
25	450	212	0.41	68.0	2.0	77	10	412	254	0.08
26	259	138	0.47	69.0	2.0	76	12	363	306	0.21
27	754	312	0.37	66.6	1.8	72	8	312	218	0.17
29	256	243	0.85	68.0	4.0	93	46	792	928	0.79
30	364	177	0.44	69.0	2.0	77	12	379	284	0.40
31	425	281	0.60	69.0	2.0	74	8	329	238	0.01
32	327	232	0.64	69.0	2.0	71	6	181	182	0.18
33	511	370	0.65	71.0	2.0	120	24	1269	322	0.91
34	185	125	0.61	70.0	2.0	70	14	58	346	0.26
35	578	214	0.33	67.1	1.6	69	6	148	164	0.61
36	318	300	0.84	68.1	2.0	70	6	263	212	0.09
37	420	215	0.45	68.5	1.8	72	6	223	188	0.46
38	391	330	0.74	68.7	1.8	71	6	236	154	0.59
39	455	237	0.46	67.8	1.8	70	6	204	172	0.38
40	429	148	0.30	66.4	1.6	74	12	327	328	0.35
42	428	156	0.32	68.0	2.0	72	6	303	172	0.50
43	429	298	0.61	70.9	1.8	71	6	124	164	0.64
44	194	129	0.58	69.0	2.0	76	12	350	292	0.38
45	589	265	0.40	~65.1	1.4	71	8	262	212	0.53
47	264	203	0.68	66.8	1.8	79	8	488	170	0.41
48	293	161	0.49	69.0	2.0	77	8	294	220	0.46
49	618	393	0.56	67.6	2.0	87	20	652	410	0.75
50	374	138	0.33	68.0	2.0	76	8	303	196	0.54

[1] U and Th concentrations are calculated employing an external standard zircon as in Paton *et al.*, 2010, G3.

[2] 2σ uncertainties propagated according to Paton *et al.*, 2010, Geochemistry, Geophysics, Geosystems.
^{207}Pb/^{206}Pb ratios, ages and errors are calculated according to Petrus and Kamber (2012), Geostandards Geoanalyt Res.
Analyzed spots were 23 micrometers, using an analytical protocol modified from Solari *et al.* (2010), Geostandards Geoanalyt Res.
Data measured employing a Thermo Xseries QICPMS coupled to a Resonetics, Resolution M050 excimer laser workstation.
~ Spot not included in mean age calculation.

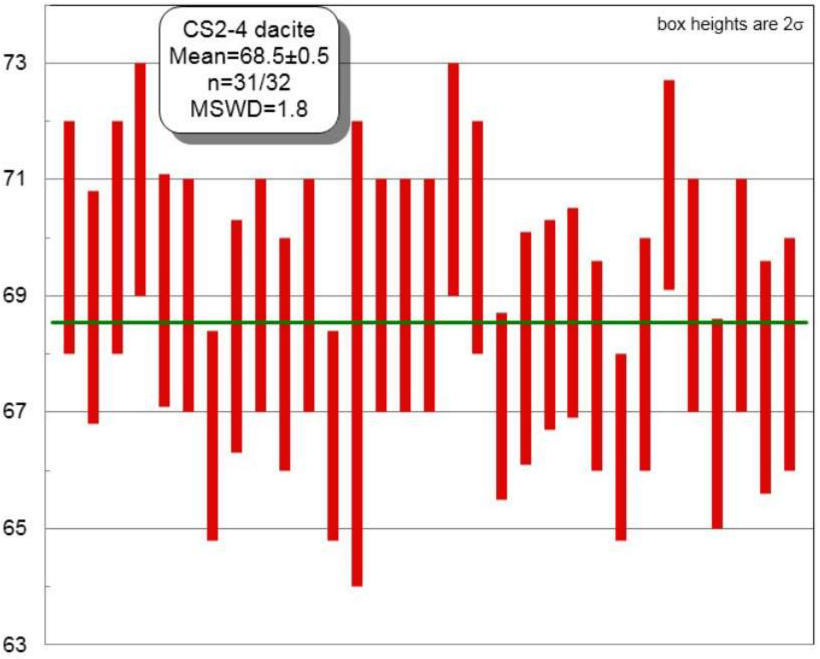
CS2-4 dacite
Mean=68.5±0.5
n=31/32
MSWD=1.8
box heights are 2σ
73
71
69
67
65
63

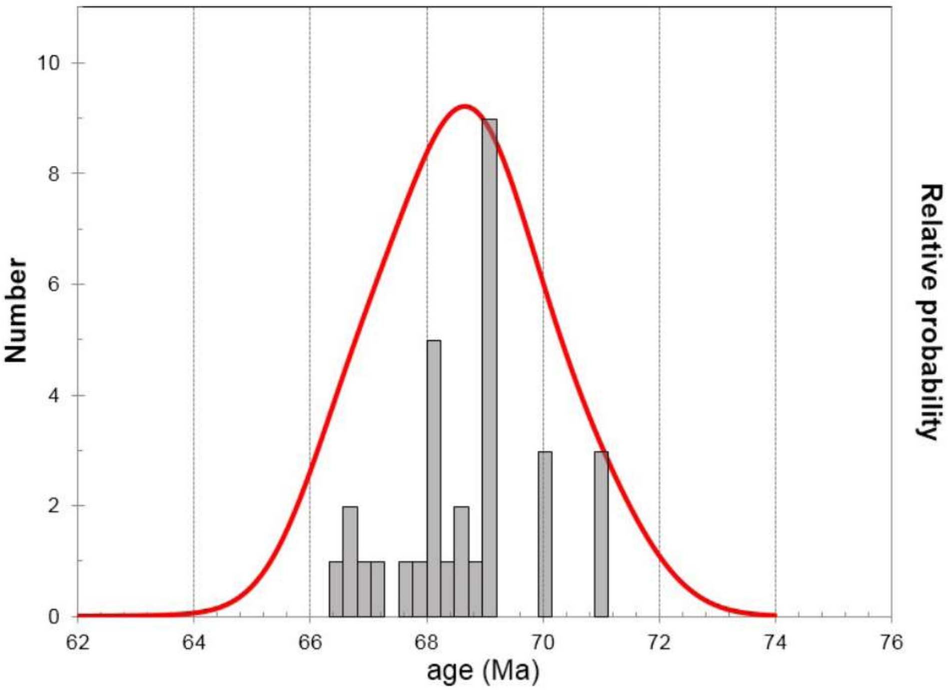
Number
Relative probability
age (Ma)
0
2
4
6
8
10
62
64
66
68
70
72
74
76

CS2-35				CORRECTED AGES[2] (Ma)						
spots	**U[1] (ppm)**	**Th[1] (ppm)**	**Th/U**	**^{206}Pb/^{238}U**	**±2σ**	**^{207}Pb/^{235}U**	**±2σ**	**^{207}Pb/^{206}Pb**	**±2σ**	**Rho**
1	297	169	0.57	71.0	2.0	109.0	10.0	930	140	0.28
2	527	289	0.55	68.0	1.7	69.2	6.7	303	78	0.24
3	140	74	0.53	73.0	3.0	116.0	24.0	1,310	220	0.20
4	386	179	0.46	69.0	2.1	99.5	9.9	970	130	0.29
5	381	261	0.69	69.4	2.1	74.3	9.6	450	110	0.23
6	584	278	0.48	67.1	1.6	71.9	8.1	441	89	0.20
7	306	155	0.51	69.7	2.1	79.0	10.0	690	110	0.22
8	464	190	0.41	68.4	1.9	73.7	7.5	410	85	0.26
9	177	131	0.74	21.1	1.1	75.0	12.0	2,820	190	0.31
10	860	392	0.46	68.4	1.7	71.5	6.2	328	96	0.28
11	339	167	0.49	69.8	3.3	73.5	8.6	410	110	0.39
12	799	360	0.45	68.4	1.9	81.3	6.3	458	87	0.35
13	523	1,017	1.94	485	9.8	484.0	18.0	496	36	0.46
15	490	348	0.71	66.5	2.5	92.0	13.0	930	170	0.26
16	316	303	0.96	*15.1	1.1	16.4	8.3	710	320	0.15
17	511	302	0.59	68.3	2.9	145.0	13.0	1,680	120	0.43
18	141	98	0.69	74.9	3.7	103.0	23.0	980	400	0.21
20	282	232	0.82	66.6	2.2	68.3	7.8	650	150	0.28
21	126	60	0.47	20.7	2.0	129.0	39.0	3,370	370	0.33
22	377	204	0.54	69.4	2.8	77.0	13.0	610	180	0.23
23	433	198	0.46	68.7	2.1	75.4	8.5	460	120	0.26
24	367	246	0.67	67.4	2.4	100.0	14.0	1,160	220	0.24
25	1,230	1,543	1.25	*13.8	0.5	14.1	2.7	610	200	0.17
26	214	102	0.48	71.5	2.5	102.0	13.0	880	170	0.27
27	114	59	0.52	19.6	1.9	112.0	22.0	3,070	160	0.45
28	364	209	0.57	70.8	2.4	76.2	8.2	424	85	0.30
29	279	95	0.34	69.4	2.4	75.5	9.8	470	110	0.27
30	683	738	1.08	*13.6	0.7	19.0	4.9	1,130	180	0.20
31	427	290	0.68	67.9	2.8	76.0	8.1	350	130	0.38
33	268	130	0.49	67.7	2.5	81.0	11.0	790	160	0.26
34	218	174	0.80	69.2	3.0	138.0	23.0	1,550	210	0.25
35	192	190	0.99	18.0	2.2	61.0	15.0	2,650	310	0.51

[1] U and Th concentrations are calculated employing an external standard zircon as in Paton *et al*., 2010, G3.

[2] 2σ uncertainties propagated according to Paton *et al.*, 2010, Geochemistry, Geophysics, Geosystems.
^{207}Pb/^{206}Pb ratios, ages and errors are calculated according to Petrus and Kamber (2012), Geostandards Geoanalyt Res.
Analyzed spots were 23 micrometers, using an analytical protocol modified from Solari *et al*. (2010), Geostandards Geoanalyt Res.
Data measured employing a Thermo Xseries QICPMS coupled to a Resonetics, Resolution M050 excimer laser workstation.
* Spots included in mean age calculation.

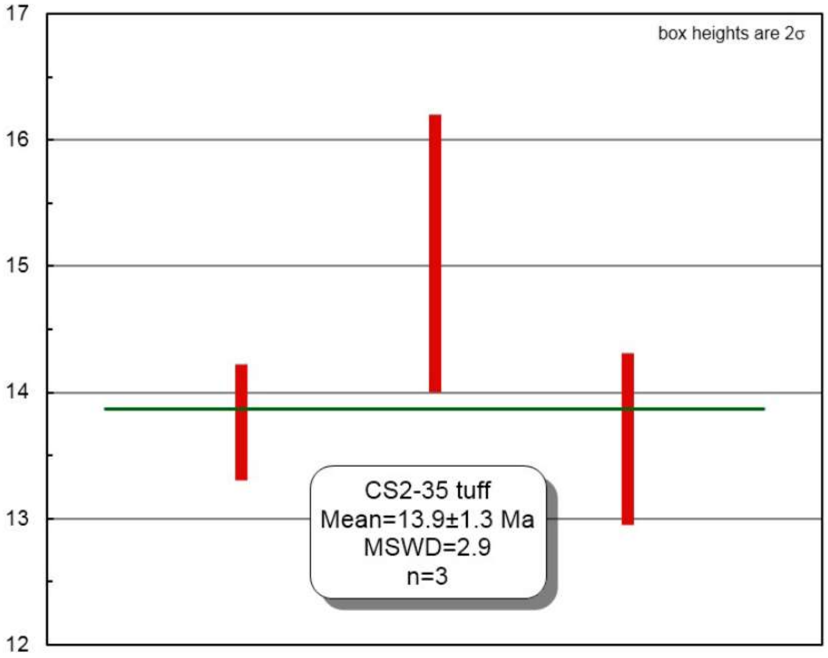
box heights are 2σ
17
16
15
14
13
12
CS2-35 tuff
Mean=13.9±1.3 Ma
MSWD=2.9
n=3

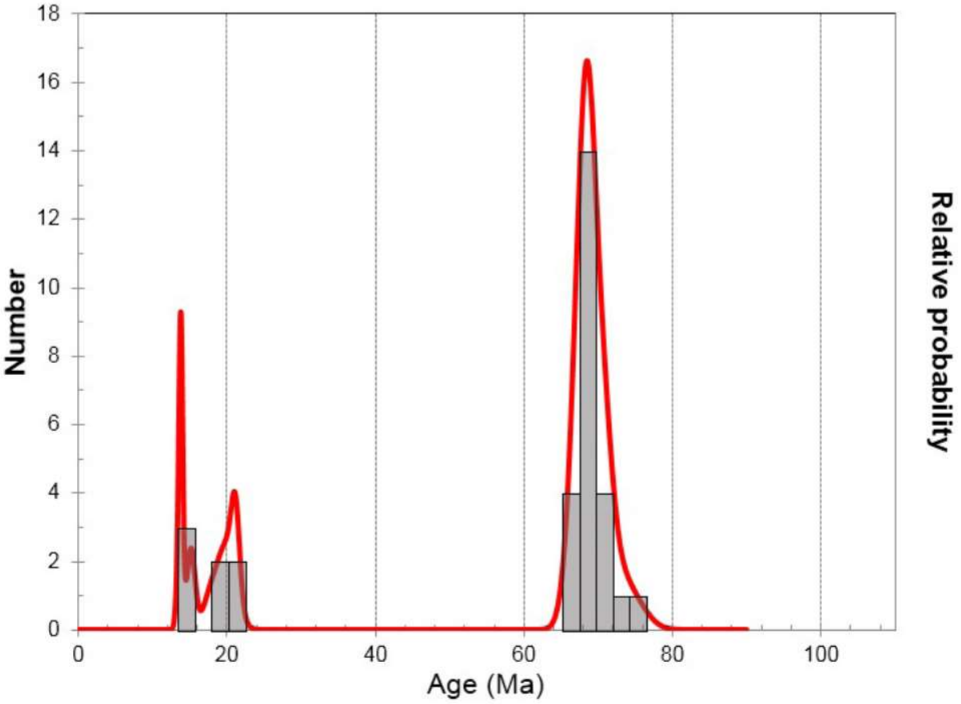
18
16
14
12
10
8
6
4
2
0
Number
Relative probability
0
20
40
60
80
100
Age (Ma)

CS-3 spots	U[1] (ppm)	Th[1] (ppm)	Th/U	CORRECTED AGES[2] (Ma) ^{206}Pb/^{238}U	±2σ	^{207}Pb/^{235}U	±2σ	^{207}Pb/^{206}Pb	±2σ	Rho
71	274	260	0.95	*26.8	2.9	45.0	37.0	1,180	370	0.11
72	278	526	1.89	*27.2	1.1	44.4	5.0	1,310	120	0.35
74	237	470	1.99	*25.7	1.0	32.9	4.6	780	150	0.28
75	149	139	0.93	29.3	1.6	86.0	19.0	2,080	210	0.38
76	203	385	1.90	*27.2	2.5	48.0	33.0	1,340	230	0.11
77	65	76	1.18	*26.4	1.5	54.0	11.0	1,280	210	0.01
78	145	168	1.16	*26.5	1.4	54.0	12.0	1,550	200	0.20
79	157	218	1.39	*27.3	1.4	48.0	11.0	1,270	190	0.50
80	258	529	2.05	24.8	1.1	32.8	4.7	1,060	130	0.30
81	115	156	1.35	*26.6	1.3	45.8	7.6	1,170	150	0.32
82	276	408	1.48	*25.7	0.9	28.5	4.6	760	120	0.21
83	216	460	2.13	*26.7	1.6	53.3	8.8	1,290	190	0.35
84	139	216	1.56	*26.5	1.2	33.6	5.8	890	130	0.17
86	43	62	1.43	*28.0	1.7	71.0	16.0	2,080	240	0.23
87	214	274	1.29	*26.7	1.2	60.1	5.9	1,720	110	0.49
88	280	368	1.31	*27.5	2.6	36.0	42.0	810	360	0.49
89	254	376	1.48	24.7	1.3	41.0	13.0	970	270	0.16
91	102	137	1.34	*28	1.3	37.9	7.0	1,090	210	0.24
92	137	154	1.12	*27.4	1.1	31.0	6.7	670	250	0.04
93	133	195	1.47	*26.9	1.5	39.1	6.9	1,110	170	0.30
94	151	258	1.71	*26.7	1.1	57.7	7.1	1,490	140	0.26
96	201	352	1.75	*27.9	1.3	52.0	11.0	1,550	190	0.31
97	895	1,899	2.12	*25.6	0.9	28.2	5.1	440	190	0.05
98	249	496	1.99	*28.0	1.3	85.5	8.2	2,191	94	0.68
101	184	381	2.07	*26.3	1.1	46.1	4.9	1,470	110	0.40
102	108	104	0.97	*26.6	1.5	34.0	12.0	1,320	240	0.17
103	165	260	1.57	*27.5	1.0	30.9	5.6	750	170	0.20
104	122	109	0.89	*25.8	1.3	37.9	7.3	1,080	160	0.43
105	166	340	2.05	*26.9	1.2	45.0	10.0	1,380	210	0.00

[1] U and Th concentrations are calculated employing an external standard zircon as in Paton *et al*., 2010, G3.

[2] 2σ uncertainties propagated according to Paton *et al.*, 2010, Geochemistry, Geophysics, Geosystems.

^{207}Pb/^{206}Pb ratios, ages and errors are calculated according to Petrus and Kamber (2012), Geostandards Geoanalyt Res.

Analyzed spots were 23 micrometers, using an analytical protocol modified from Solari *et al*. (2010), Geostandards Geoanalyt Res.

Data measured employing a Thermo Xseries QICPMS coupled to a Resonetics, Resolution M050 excimer laser workstation.

* Spots included in mean age calculation.

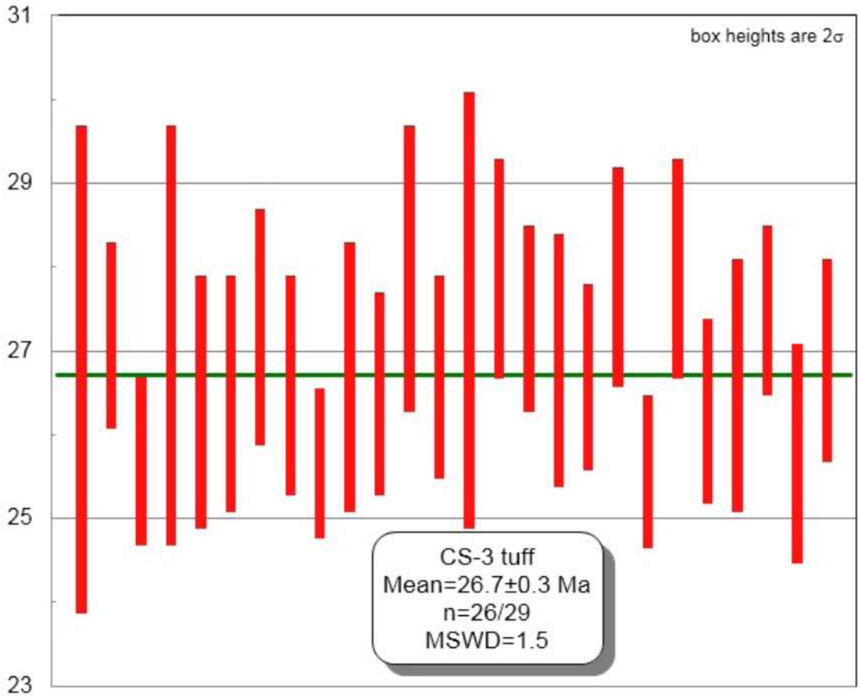
box heights are 2σ
31
29
27
25
23
CS-3 tuff
Mean=26.7±0.3 Ma
n=26/29
MSWD=1.5

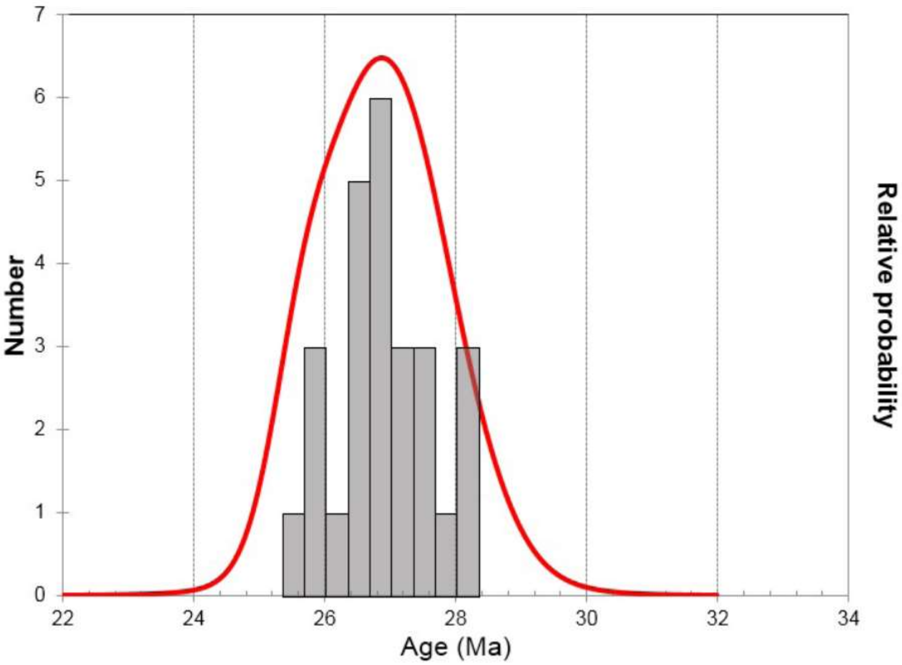
Number
Relative probability
Age (Ma)
0
1
2
3
4
5
6
7
22
24
26
28
30
32
34

HC-07				**CORRECTED AGES[2] (Ma)**						
spots	**U[1] (ppm)**	**Th[1] (ppm)**	**Th/U**	**^{206}Pb/^{238}U**	**±2σ**	**^{207}Pb/^{235}U**	**±2σ**	**^{207}Pb/^{206}Pb**	**±2σ**	**Rho**
71	263	152	0.58	68.7	1.4	85.9	6.5	690	120	0.26
72	315	185	0.59	64.6	1.2	77.0	6.4	585	97	0.22
73	240	123	0.51	50.4	0.8	52.3	5.8	340	150	0.13
74	424	151	0.36	65.6	1.0	77.6	4.2	521	54	0.28
75	210	162	0.77	54.1	1.3	121	13.0	1,700	150	0.21
76	192	105	0.55	53.3	1.3	94.9	5.3	1,341	66	0.43
77	611	130	0.21	68.9	1.0	91.1	6.0	712	82	0.22
78	235	168	0.71	50.2	1.2	57.3	8.6	740	170	0.15
79	197	218	1.11	*46.9	1.6	72.0	16.0	1,070	210	0.14
80	485	201	0.41	63.3	1.3	65.1	5.6	420	95	0.23
81	102	79	0.77	51.7	1.9	125	22.0	2,110	170	0.20
83	621	340	0.55	65.1	1.0	70.8	3.5	322	54	0.29
85	397	256	0.64	*48.9	0.8	49.0	3.2	357	78	0.25
86	594	238	0.40	*49.3	0.9	62.6	4.8	560	110	0.23
87	218	148	0.68	65.2	1.8	90.0	13.0	920	160	0.18
88	229	106	0.46	66.9	1.4	84.5	8.5	610	140	0.20
89	244	148	0.60	50.7	1.4	81.0	15.0	1,190	180	0.14
90	356	142	0.40	65.2	1.4	66.3	5.4	225	93	0.25
91	497	300	0.60	59.6	2.2	82.2	7.3	870	100	0.39
93	444	240	0.54	64.4	1.4	80.6	3.7	618	50	0.44
94	197	174	0.88	65.5	1.4	70.8	7.0	490	130	0.21
95	318	264	0.83	*49.1	1.0	51.2	3.5	339	86	0.27
96	247	246	1.00	*45.5	1.7	74.0	15.0	1,210	220	0.17
97	352	248	0.70	64.9	1.3	66.0	13.0	410	210	0.10
98	198	103	0.52	50.2	1.6	75.2	9.2	1,050	140	0.25
99	340	211	0.62	67.6	1.3	99.0	7.4	957	93	0.24
100	850	394	0.46	62.9	1.2	82.3	3.8	703	39	0.40
102	117	107	0.91	*47.6	1.5	92.0	16.0	1,530	170	0.17
104	185	137	0.74	*49.8	1.6	70.4	8.0	940	150	0.27
105	204	256	1.25	*49.8	1.6	77.0	14.0	1,130	190	0.17

[1] U and Th concentrations are calculated employing an external standard zircon as in Paton *et al.*, 2010, G3.

[2] 2σ uncertainties propagated according to Paton *et al.*, 2010, Geochemistry, Geophysics, Geosystems.

^{207}Pb/^{206}Pb ratios, ages and errors are calculated according to Petrus and Kamber (2012), Geostandards Geoanalyt Res.

Analyzed spots were 23 micrometers, using an analytical protocol modified from Solari *et al.* (2010), Geostandards Geoanalyt Res.

Data measured employing a Thermo Xseries QICPMS coupled to a Resonetics, Resolution M050 excimer laser workstation.

* Spots included in mean age calculation.

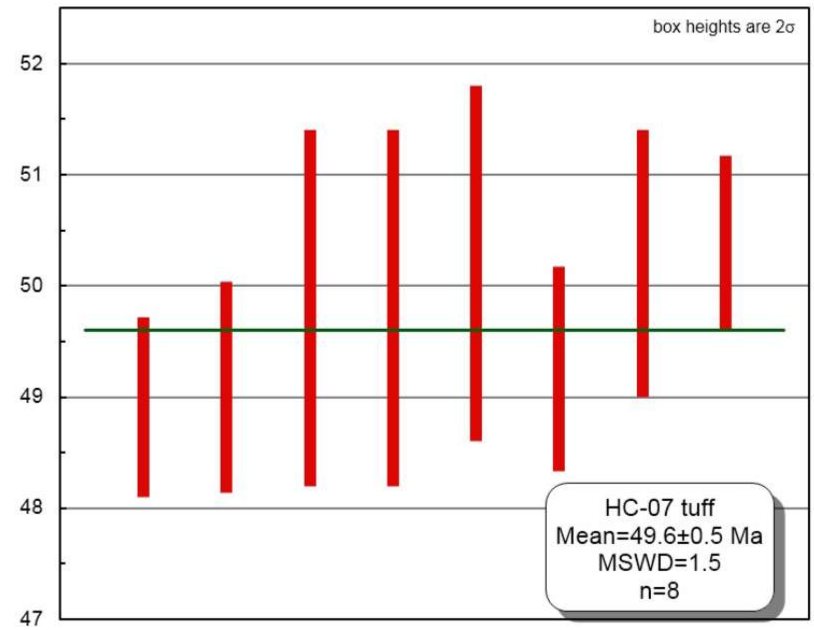
box heights are 2σ
52
51
50
49
48
47
HC-07 tuff
Mean=49.6±0.5 Ma
MSWD=1.5
n=8

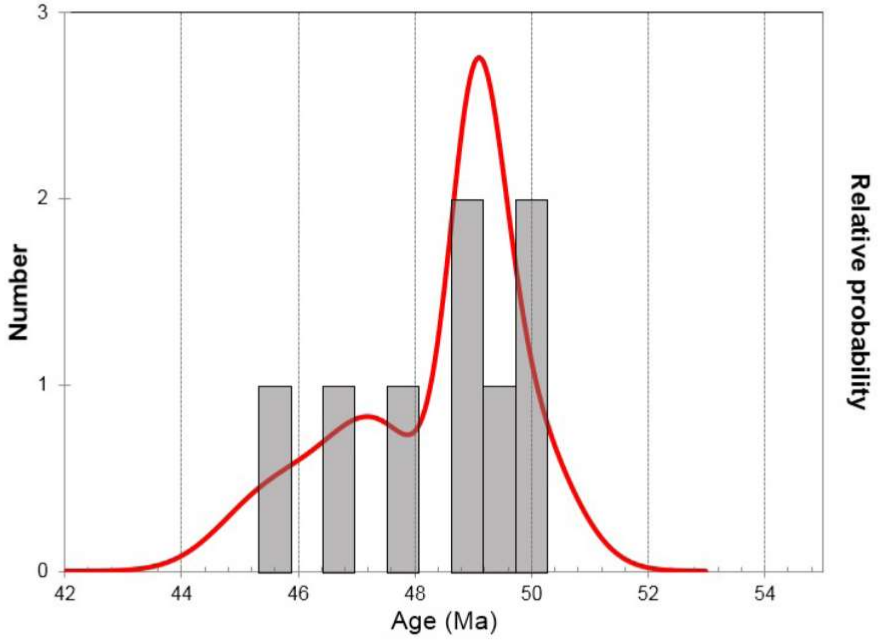
3
2
1
0
Number
Relative probability
42
44
46
48
50
52
54
Age (Ma)

3. ANALOGUE MODELING: UNDERLYING ASSUMPTIONS, SUBDUCTION WEDGE MODELS, METHODOLOGY AND MAIN RESULTS

The basic underlying assumption in the study of orogenesis is that the tectonic evolution of an orogen is the expression of lithospheric-scale plate convergence that initiates at subduction zones or formerly transcurrent plate boundaries (e.g., Jamieson and Beaumont, 2013). The study of these deforming regions has been historically approximated by analogue models that tested similar boundary conditions coupled with analytical approaches (e.g., Davis et al., 1983; Malavieille, 1984; 2010; McClay et al., 2004). By means of such models, it has been recognized that the mechanical (structural) response of the crust to the subduction-collision processes is determined by temperature-dependent material properties, in particular, by rheological properties (e.g., brittle rheology of the uppermost crust).

These studies, complemented by seismological surveys and imaging, lead to the discovery that in subduction environments, the mechanical response of the crust to the resultant tectonic regime was to attain a wedge-shape structural profile in cross-section, consistent with an overall Coulomb rheology for the upper crust. The structure of the lithosphere in ocean-continent and intra-continental subduction environments can then be approximated by means of subduction wedge models, which provide of a first-order approximation to the structure of orogens developed along subduction zones (see Jamieson and Beaumont, 2013 for a thorough review).

In this chapter, I shortly review subduction wedge models on the tectonic evolution of mountain belts originated by shortening of the lithosphere in convergent environments, including the one presented in this thesis. These provide of an explanation on the mechanical behavior of the lithosphere when shortened in response to tensile stresses generated in a convergent geodynamic setting. If specific boundary conditions are correspondent with specific geodynamic scenarios, then local comparisons can be established between models and prototype. The aim of this chapter is to provide a conceptual framework on such mechanical models and to present in this context the main results of this work.

3.1. Subduction wedge models

The primary ideas in which subduction wedge models are based upon arose in the late 70's (Chapple, 1978) and were further developed during the 80's in the works of Davis et al. (1983) and Dahlen et al. (1984), with the aim of understanding the mechanics of hydrocarbon-bearing fold-and-thrust belts developing along deforming regions. In these works, the structure and mechanics of accretionary complexes was approximated to that of a wedge of soil or snow in front of a moving plow (by push from the rear or pull from below with a conveyor belt (e.g., Fig. 1, Fig. 2A and 2B), in which gravitational and frictional forces would compete to achieve balance. Analytical approaches coupled with physical modelling were implemented to provide proof of concept.

A fundamental discovery of these works was that the material within the wedge would deform until it attained a critical taper, after which it would slide stably without major changes in shape, continuing to grow at a constant taper as additional material was encountered at the wedge toe (Fig. 1). The critical taper is the shape (defined by an angle between basal and surface slope) in which the wedge is at the verge of failure under sub-horizontal compression everywhere. Thus, a wedge of less than a critical taper will not slide above the basal thrust and will thicken by internal deformation to increase the taper until it is critical (Fig. 1).

Particularly, Davis et al. (1983) developed a simple analytical theory (critical wedge theory) that related the critical taper for subaerial and submarine subduction Coulomb wedges to the parameters of stress involved in wedge deformation (e.g., basal dip, internal coefficient of friction). They demonstrated that wedges developed in sandbox experiments (one-sided subduction wedges) matched the theory, and so did natural prototypes considering specific parameters included in the analytical procedure.

In summary, Critical Taper Theory states that the structural evolution of an orogenic wedge obeys simple deformation mechanisms that can be compared to the formation of a wedge of sand moving in front of a bulldozed (Fig. 1A). This wedge deforms by sliding along a basal detachment until it develops a triangular shape characterized by a constant angle between the surface slope (α) and the basal detachment (β). The opening angle ($\alpha + \beta$) is called *critical taper* and its magnitude depends on the frictional and pore fluid pressure properties within the wedge and basal detachment (Davis et al., 1983; Fig. 1B). Dahlen et al. (1984) enhanced Davis et al.'s work by providing an exact solution to the relationship between surface and basal slopes of a wedge, and the angles of principal stresses acting withing the wedge (Fig. 1B). The critical taper is then determined as follows:

$$\alpha + \beta = \frac{(1 - \sin\varphi)}{(1 + \sin\varphi)} \cdot (\mu_b + \beta) \tag{1}$$

where μ_b is the coefficient of basal friction and φ is the angle of internal friction of the material of the wedge. Critical wedge theory assumes that the wedge is at the verge of failure everywhere.

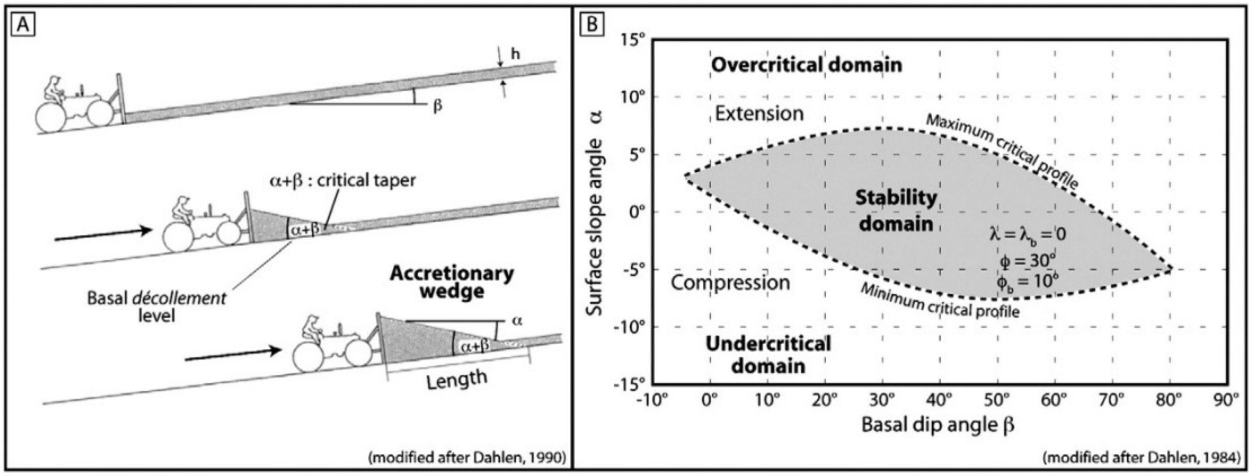

(modified after Dahlen, 1990)

(modified after Dahlen, 1984)

Figure 1. Basic scheme for the critical taper theory (modified after Dahlen et al., 1994 in Graveleau et al., 2012). **A)** Analogy between the formation of an accretionary wedge with a sand or snow wedge moving in front of a plow pushed by a bulldozer. The plow scrapes off a layer of sediment of thickness **h**, overlying a surface tilted at an angle $\boldsymbol{\beta}$. A triangular accretionary wedge forms with a surface slope $\boldsymbol{\alpha}$ by sliding above the detachment and incorporating material by accretion at its toe. A dynamic steady state is reached at a constant taper $\boldsymbol{\alpha + \beta}$. In **B)**, equation (1) is plotted to show a stability domain for a wedge with a coefficient of internal friction $\boldsymbol{\varphi = 30°}$ and basal dip $\boldsymbol{\beta = 10°}$. The area inside the "eye-shaped" represents the domain of stability, in which the wedge will not deform. The envelope of the shaded region represents critical conditions and self-similar growth at constant critical taper. Outside the shaded region compressive or extensional deformation modes are favored in order to restore the critical taper.

Following critical taper theory, the tectonic regime governing the accretionary wedge can be deduced independent of its internal geometry (e.g., Fig. 1B). The critical taper theory equations (eq. 1 for a simplification) are solved under a series of assumptions to determine the orientation of principal stresses affecting the wedge. These assumptions are: 1) there is negligible cohesion; 2) the wedge is internally homogeneous; 3) the basal detachment is homogeneous. A stability diagram can be drawn in function of the basal dip and surface slope angles. For instance, a dry sand wedge (no pore fluid pressure, angle of internal friction of 30° and negligible cohesion) yields the eye-shaped shaded region in Fig. 1B. When taper angle is in the shaded region, no deformation occurs, and the wedge is able to slide above the basal detachment. If the taper is at the dotted envelope (stability domain), the wedge is under critical conditions and grows self similarly by internal deformation, maintaining its taper. Finally, outside the stability domain, the wedge is at an instability state, and will deform according to the taper. For example, if the taper is too high, the wedge will deform to reduce taper under extension. On the contrary, if the wedge is too slender and taper too low, the wedge will deform to increase taper under compression. The mechanism of deformation by which the wedge will adjust taper can likely be frontal accretion, basal accretion, back thrusting, out of sequence thrusting, duplexing or normal faulting (see Section 2.5. Growth sequence within an orogenic wedge).

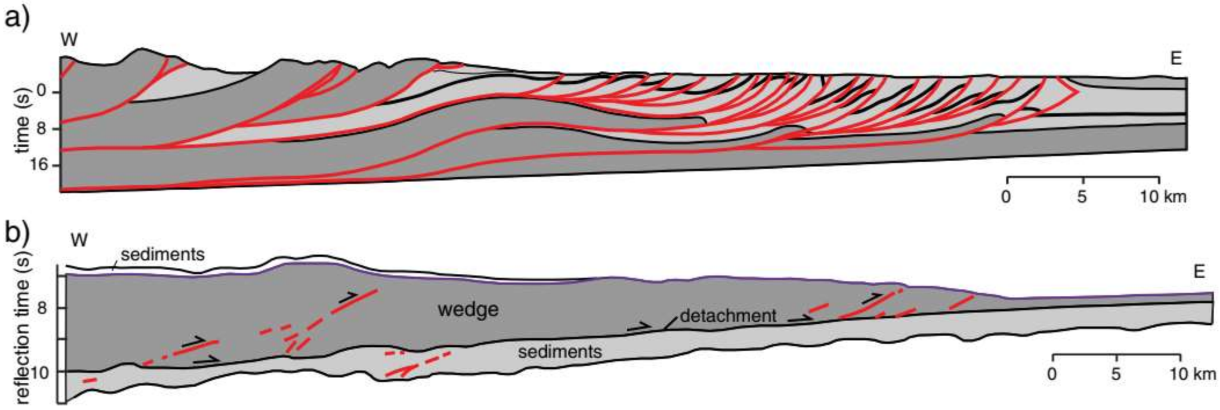

Figure 2. a) Cross-section through the Canadian Rocky Mountains fold-and-thrust belt, redrawn from Bally et al. (1966) in Buiter (2012). b) Cross-section through the Lesser Antilles accretionary wedge, redrawn from Westbrook et al. (1982) in Buiter (2012).

The basic connection of the theory with orogen prototypes (e.g., the Canadian Rockies fold-and-thrust belt and the Lesser Antilles accretionary wedge, Fig. 2) resided in that common silicate sediments and rocks in the upper 10-15 km of the crust have pressure-dependent brittle compressive strengths, which can be approximately represented by empirical Coulomb failure criterion. Geoscientists showed how the theory did not apply if the wedge or decollement exhibited pressure-dependent plastic behavior because of temperature or rock type (Davis et al., 1983). Such behavior, expected in depths of c. 15 km or predicted depths of the brittle-ductile transition for typical geothermal gradients, allowed to restrict the application of the theory for crustal domains above this boundary.

The most important conclusions of Davis et al. (1983) were that "*fold-and-thrust belts and accretionary wedges have the mechanics of bulldozer wedges in compression, they grow in self-similar fashion at a critical taper*" and that "*normal laboratory fracture and frictional strengths are appropriate to mountain-building processes in the upper crust, above the brittle-ductile transition.*"

Although capable of explaining the first-order geometry of fold-and-thrust belts, a fundamental issue that came up with the application of the critical wedge theory was that it was hard to identify the equivalent of a backstop, or bulldozer, in the overriding plate of natural prototypes. While some authors used the relative strengths of deforming rock bodies to define what corresponded to the backstop region of a wedge, in many cases this region could be demonstrated to be deforming together with the accreted material in front of it, contradicting the basic conception of the backstop, considered to be a rigid part of the wedge.

A solution to this issue was brought by Malavieille (1984) by means of an analogue model (Fig. 3C) implemented to understand the overall tectonic evolution of the European Alps (Fig. 4). In his work, a flat-lying backstop was located beneath the layer representing the overriding plate, instead of a vertical rigid backstop above the singularity (compare A and B to C in Fig. 3).

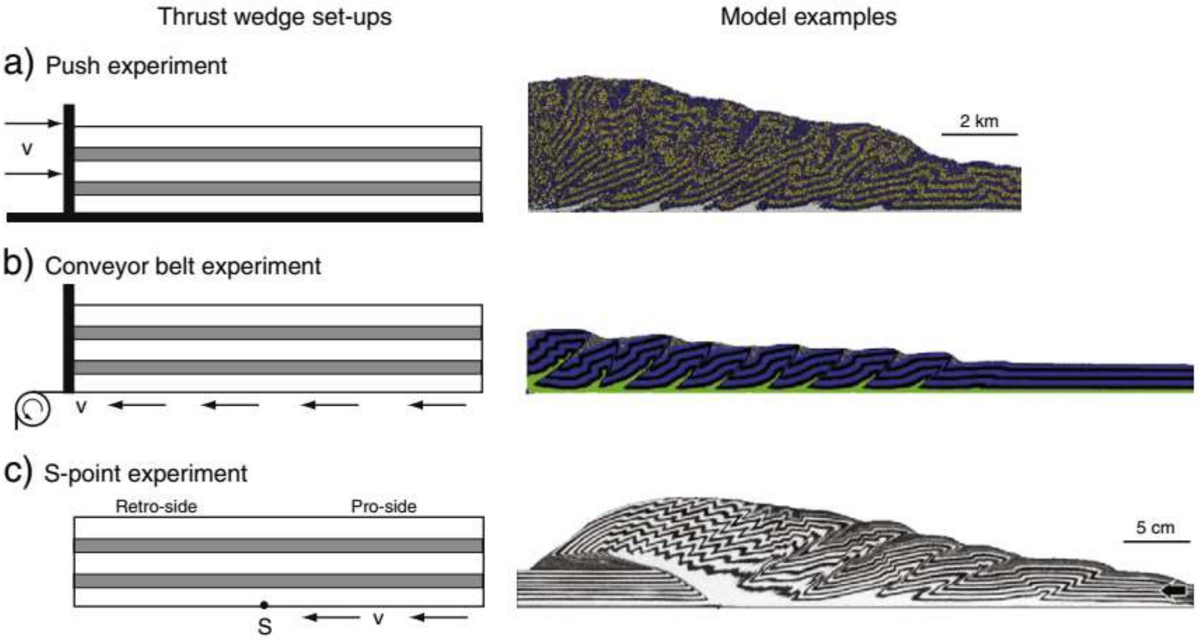

Figure 3. Examples of setups used in subduction wedge models. Schematic set-ups in the left column, examples of model studies in the right column. **a)** In a push-type experiment, a mobile wall is moved into the model domain. **b)** In a conveyor belt experiment, material is pulled towards the backstop. **c)** In an S-point experiment, material is pulled towards a basal discontinuity (the S-point). Examples modified from Buiter (2012).

The work of Malavieille (1984) led to the recognition that:

1. Convergent orogens consist of two tapered wedges, one below each slope of the range, arranged back-to-back. Above the subduction zone, the lithosphere deforms into a double-sided wedge. Deformation is rooted at a basal velocity discontinuity, singularity, subduction point, or S-point.

2. The overriding plate actually corresponds to a deformable backstop with same rheology than the accreted materials.

3. The two sides of an orogenic wedge are limited by respective crustal-scale shears, rooted at the S-point, one corresponding to the subduction thrust, and the other one corresponding to a first order conjugate. The initial deformation is fundamentally asymmetric, but as convergence increases it develops with a distinct asymmetry.

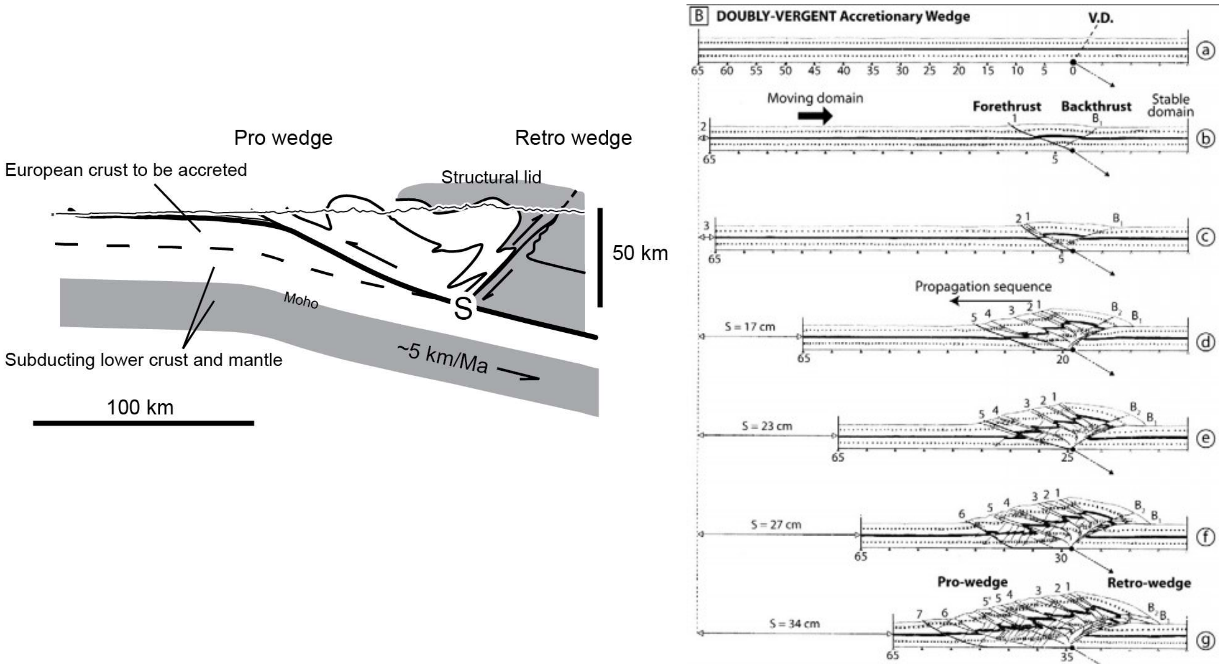

Figure 4. Left panel: Simplified cross section of the European Alps (adapted from Brandon, 2004). Note that thrust systems bound the wedge, rising from the singularity and crustal-scale detachments. Lower panel: Doubly-vergent subduction wedge sandbox experiment (modified from Malavieille, 1984 in Graveleau et al., 2012) showing sequence of deformation at different stages of shortening. Note the initial symmetry above the singularity (VD: Velocity Discontinuity) and similarity in the first order Alpine structure and lower panel (g).

The double-sided wedge idea of Malavieille (1984) increased research possibilities, inspiring the numerical modelling of subduction wedges under the same boundary conditions (Fig. 5). The additional advantage of the numerical approach is that their is option of incorporating additional conditions to the model, in order to offer a more complex, yet more realistic approximation to the mechanical evolution of orogens. For example, Willettt et al. (1993) not only incorporated isostatic effects to the growth of a numerical doubly vergent wedge, but also the effects of erosion and sedimentation, heat transfer and mass transport in orogenesis. The numerical approach also demonstrated proof of concept to the critical wedge theory, it expanded the range of results to a wider variety of orogen prototypes including the development of a viscous orogenic root and formation of plateaus (Fig. 4) and demonstrated reproducibility of the sandbox S-point model (compare Fig. 3C with Fig. 5B).

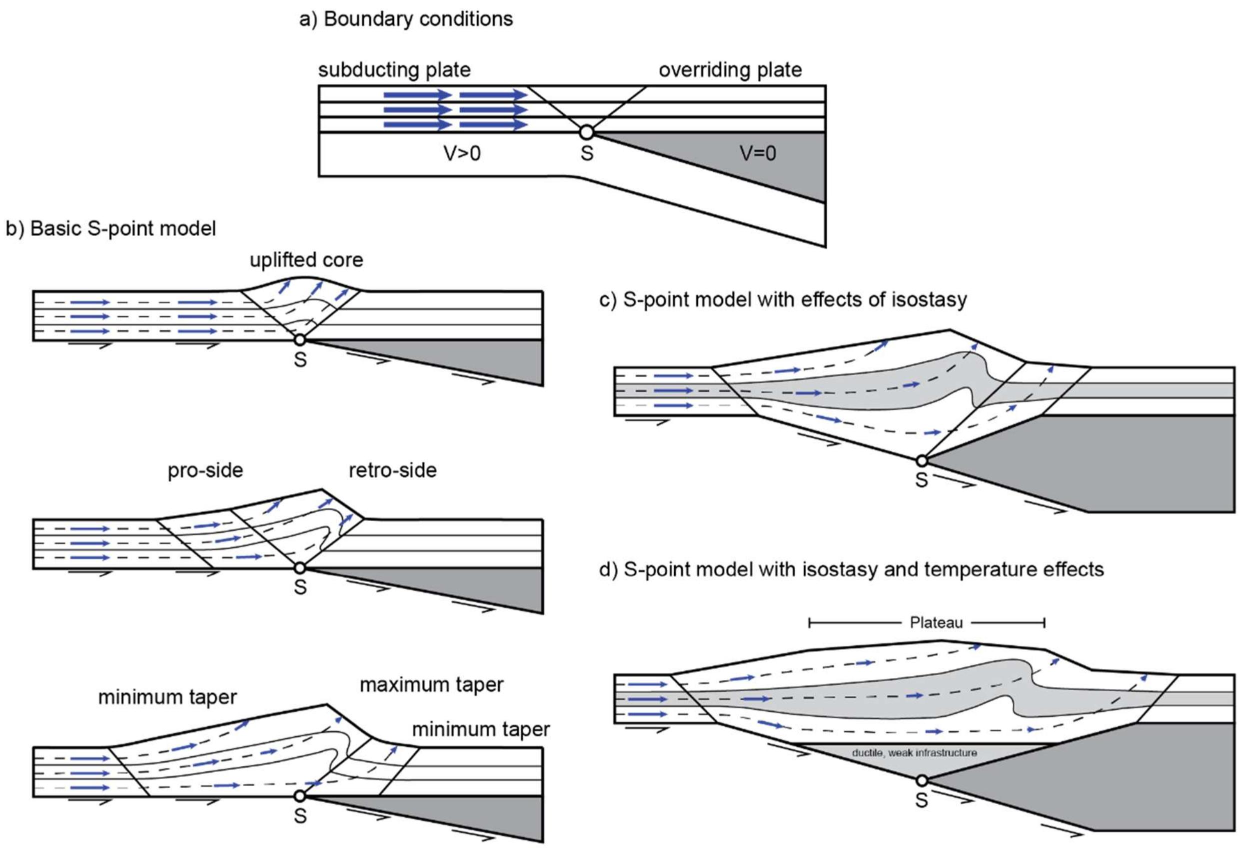

Figure 5. Numerical, doubly-vergent subduction wedge (S-point) models (modified from Willettt et al., 1993). **a)** Initial conditions of the model are the same as in the analogue experiment of Malavieille (1984). **b)** Basic S-point models equivalent to sandbox experiments as the deformable layer has a Coulomb rheology. Dashed lines are instantaneous flow lines, not particle trajectories. Note the development of a pro- and a retro-side in the subducting and overriding plate, respectively with increased convergence. In the latest stage of the model (last row), the retro-side expands towards the rear and a break in slope is generated. **c)** S-point model including the effects of isostasy. **d)** With the inclusion of temperature, there is a decrease in basal shear strength, creating a plateau bounded by frictional-based pro- and retro-sides.

The works of Malavieille (1984) and Willettt et al. (1993) were fundamental in the study of mountain belts, as their template was applicable to the structure of orogens as a whole (from side to side). These works also conciliated the governing mechanics (critical taper theory) with the doubly-vergent nature of a convergent zone, and provided of a solution to the backstop problem, in that the upper plate rocks were incorporated to the actively deforming portion of the entire wedge.

Particularly, Willettt et al. (1993) provided of the terminology used in this thesis regarding the components of a doubly-vergent wedge (Fig. 5). A subduction wedge is composed of:

1. A pro-side or pro-wedge in which the down going or subducting plate is included.

2. A retro-side or retro-wedge in which the upper or overriding plate is included.
3. A central uplifted block in between the two sides.

Above each plate (pro and retro wedge), oppositely-verging thrust belts are developed to accommodate plate convergence by tectonic shortening and thickening (e.g., Fig. 4). Hence it is accurate to use the term “doubly” vergent orogen to refer to orogenic wedges developed in convergent plate boundaries. The identification of the distinctive parts of a subduction wedge is important because it facilitates the comparison between model and prototype as well as between prototypes.

3.2. A “faultless” accretionary wedge: analogue modeling methodology and results

In this thesis, an analogue model for shortening of the lithosphere is presented to establish a comparison with the Central and Southern Central Andes (more details of the modeling device and methodology are presented in Chapter 3; Herrera et al. [in prep]). The standard model illustrates the growth of a brittle subduction wedge based on simple mechanical models of shortening of the lithosphere. The initial conditions are those of the subduction slot model of Malavieille (1984) (Fig. 3C and Fig. 4), or the basic S-point model with Coulomb rheology (discarding isostatic effects) of Willettt et al. (1993) (Fig. 4B). The upper crust was modeled using quartz sand, which has a linear Coulomb behavior.

Quartz sand mixes have been widely used to simulate the brittle behavior of the upper crust in subduction wedge and fold-and-thrust belt experiments aforementioned in the prior paragraphs. The scaling used in this particular experiment was of $L^*=10^{-5}$, meaning that 1 cm in the model represents 1 km in nature. Additional constraints included in the boundary conditions, in order to match the geodynamic setting of the Central Andes are included in the model presented in Chapter 3 (Herrera et al., in prep). The boundary conditions (Fig. 6A) account for a one-layer crust (homogeneous sand pack) overlying strong mantle lithosphere which is fully subducted (Mylar sheet) above a fully accreted upper crustal layer with Coulomb rheology. Visualization of the results was achieved by the implementation of a Particle Image Velocimetry (PIV) software developed by authors Keith Ma and Mark Brandon, Yale University. Instantaneous velocities strain and kinematic vorticity were derived using the PIV software to visualize the mechanical character of the deformation. Chapter 3 addresses the details on this technique.

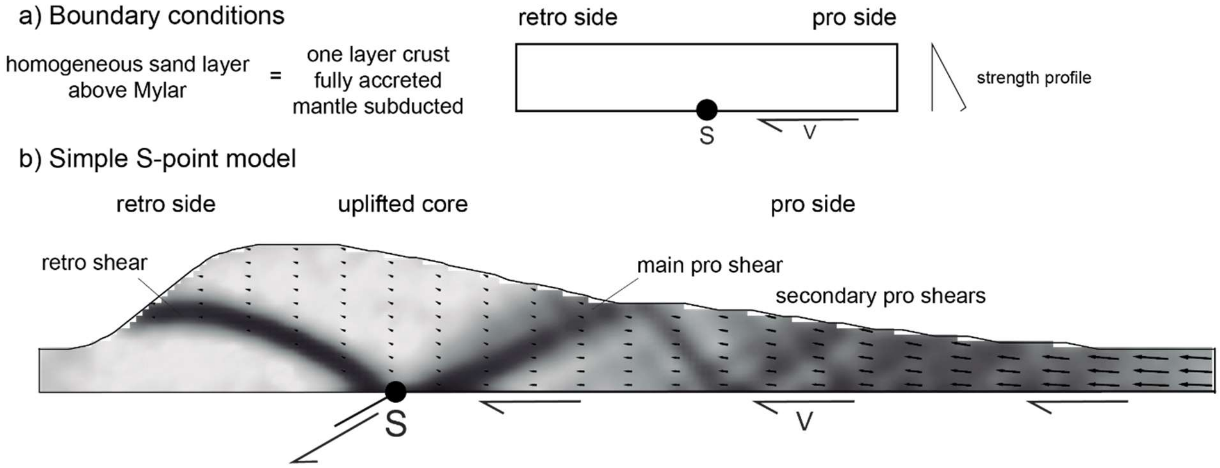

Figure 6. a) Boundary conditions and assumptions for analogue S-point model presented in this thesis. Thickness of the initial layer is of 4 cm. b) Doubly-vergent subduction wedge generated after 25 cm of convergence towards S-point. Normalized instantaneous velocities (arrows) are plotted above instantaneous strain rate (dark tones correspond to high strain rates). Note the main shear bands nucleated at S-point, and secondary pro-shears and conjugates across the pro-side. Length of the wedge is of 60 cm.

While most previous sandbox models (e.g., Malavielle, 1984; 2010; Storti et al., 2000; McClay et al., 2004) yield localization of deformation in form of faulting, the mechanical model presented in Chapter 3 (Herrera et al. in prep.) yielded continuous deformation, and shear bands were generated instead of discrete faults (Fig. 6; hence the term *faultless*). This important aspect of the model was achieved by the handling technique implemented to conform the modeling sand layer. Cohesion in the modeling material (medium sized quartz sand) was removed when passing from the hopper to the modeling surface. The sand pack is entirely faulted in this process of transfer and a peak strength is already achieved. The sand softens during this process and remains loose. The solid line of Figure 6 illustrates the stress-strain curve for the process of decompaction, whilst the dotted line shows how loose sand reaches a dynamic stable strength without strain softening (i.e., faulting). The removal of cohesion is important because critical taper theory requires cohesion to be negligible to be applied (Davis et al., 1983). The wedge experiment of Chapter 3 then appears to account for this theory, and, considering all limitations of the model, would be reflecting the macro-scale deformation of fold-and-thrust belts, showing how deformation tends towards on average in associative flow.

In most sandbox experiments, the material is sieved or poured into the modeling surface, which adds an apparent cohesion to the sand. In presence of apparent cohesion and subject to tensile stresses at the base, the sand must reach a peak strength before a dynamic stable strength is established after softening and faulting (Fig. 7; Lohrman et al., 2003 and Vermeer, 1990 in Buiter, 2012). In absence of cohesion, there is no strain softening of the layer when subject to basal pull and the dynamic strength (throughout the entire model layer) is immediately achieved after stress is applied (Fig. 7).

The fact that deformation is continuum is of major relevance as it reconciles analogue sandboxes with numerical approaches. Numerical experiments with same initial boundary conditions (Fig. 6A) exhibit the same initial failure and subsequent asymmetric development of a pro- and a retro-side (e.g., Fig. 5B; Willettt et al., 1993). The similarity with previous sandbox experiments is clear (Fig. 3C and Fig. 2) and the main difference resides in the mode of deformation, which is explained in the previous paragraph.

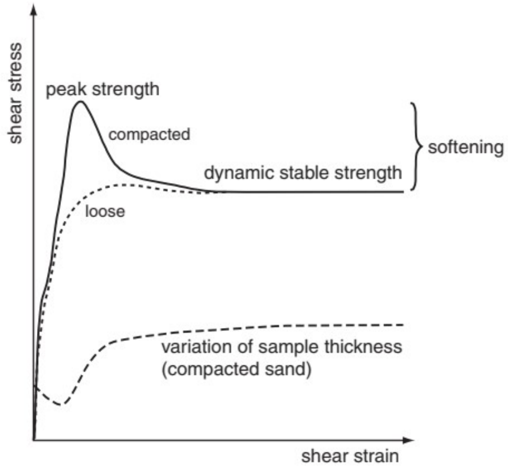

Figure 7. Stress-strain curves for dense and loose granular materials. Curves illustrate strength variations. Note how loose sands by-pass peak strength before reaching a dynamic stable strength. Modified from Buiter (2012) after Vermeer (1990), Lohrman et al. (2003).

Immediately after convergence initiates towards the S-point (Fig. 6B), deformation occurs simultaneously in associative compressive flow and is accretion-driven, as depicted by instantaneous strain rates and velocities in the model layer. The stress singularity S leads to failure of the sand layer and the formation of two pairs of conjugate slip lines or shear bands (Fig. 6B). As material is accreted from the pro side, the shear bands rotate outward bounding a central region that becomes uplifted. Accretion at the pro side occurs simultaneously at the toe and at the base (the entire layer is involved) and leads to growth of the wedge by internal deformation to maintain a critical shape.

The evolution of deformation in the model of Chapter 3, Herrera et al. (in prep), is briefly summarized as follows. Shortly after the initial symmetric phase of deformation, this begins to propagate beyond the initial shear band towards the pro-side, as the layer begins to shear on multiple secondary shears or detachments developing upon the base of the converging (subducting) plate (Fig. 6B; Video DR1 in Herrera et al. [in prep]). In this phase, the wedge is distinctively asymmetric, material is flowing from the pro wedges into the central core region that is translated up the hanging wall of the retro shear band. At this moment and on, material is accreted at the base of the retro wedge, which also grows at critical taper. The instantaneous strain rates at the pro and retro shear bands have equal magnitudes. However, the cumulative deformation is highly asymmetric because of the accumulation of material at the retro wedge after being transported across the pro side. So are the instantaneous velocities which decrease progressively from left to right (Fig. 6B). The high cumulative strain in the retro shear zones contrasts with the resulting distributed finite strain in the pro wedges and uplifted cores (Fig. 6B). At advanced stages of wedge development (high amounts of accretion), the entire wedge is no longer capable of accommodating displacements and expands towards its rear by detachment of the retro side from its base (Willettt et al., 1993). This situation is shown in detail further below in Fig. 12. Deformation throughout the experiment is stick-slip, as shown by instantaneous displacement rates. A stress buildup is required then to thicken the wedge: after each stress-buildup pulse (stick event), the height of the wedge increases to remain stable during the next stress buildup. This close relationship between pulsating deformation and wedge thickening is illustrated by Fig. 7. The evolution of wedge height follows a tendency to increase proportional to $x^{\frac{1}{2}}$ (being x the accreted material) as predicted analytically by Dahlen and Suppe (1988) for non-erosive wedges, and consistent with numerical results of simple doubly-vergent wedges of Naylor et al. (2005) and with the results of Storti et al. (2000) for analogical sand wedges.

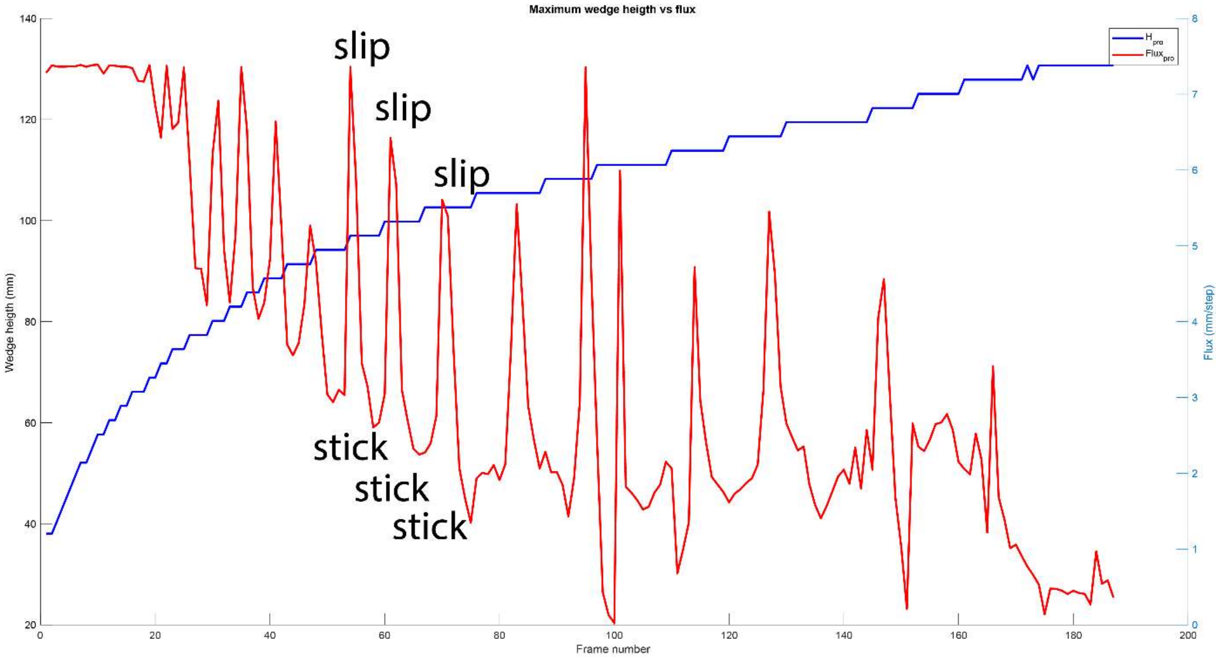

Figure 7. Instantaneous particle displacements (red curve) and thickness (blue curve) of the subduction wedge. Note that for each slip event there is an event of wedge thickening.

Another key aspect shown in Chapter 3 (Herrera et al., in prep.) was the kinematic vorticity of the deforming material. This parameter shows the nature of the rotational component of the velocity field, or its curl. Without going into further detail on the kinematic vorticity number (details in Means et al., 1980; Feehan and Brandon, 1999), the results of Herrera et al. (in prep) show that within a deforming brittle wedge, a partition of solid body rotations occur within the subduction wedge. Figure 8 shows how at the retro sides and central region, material is accommodated by a combination of localized retro-thrusting, uplift and counter-clockwise rotations of the wedge core above the retro shear band. The rotations indicate a right-hand rule relative to the sense of subduction. The sub-horizontal extension directions of the deformation ellipses (Fig. 8) indicate shear stretching at the core of both wedges. On the other hand, subvertical directions dominate the pro and retro sides, indicating shear shortening in association with vertical thickening (Fig. 8). The importance of this parameter is that it shows how the retro side and uplifted core rotate in contrary direction relative to the pro-side and the sense of subduction, and that coaxial deformation occur in the shear bands.

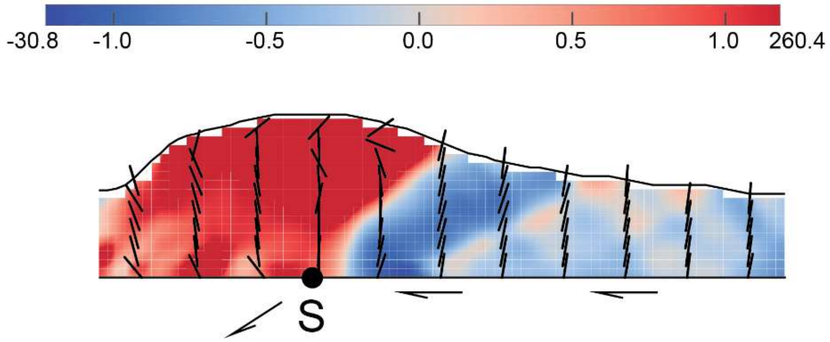

Figure 8. Maximum extension directions of strain ellipses superimposed on kinematic vorticity number field in a doubly-vergent subduction wedge model (modified from Herrera et al., in prep). Length of the shown section is of 20 cm. Blue values represent clockwise solid body rotations. Red values represent counterclockwise solid body rotations.

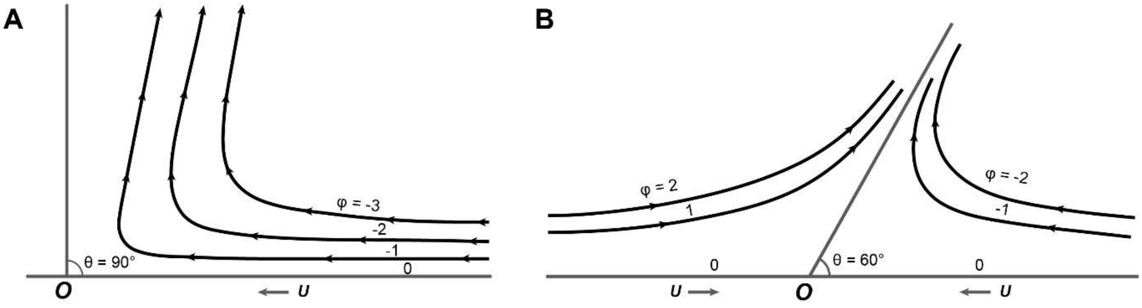

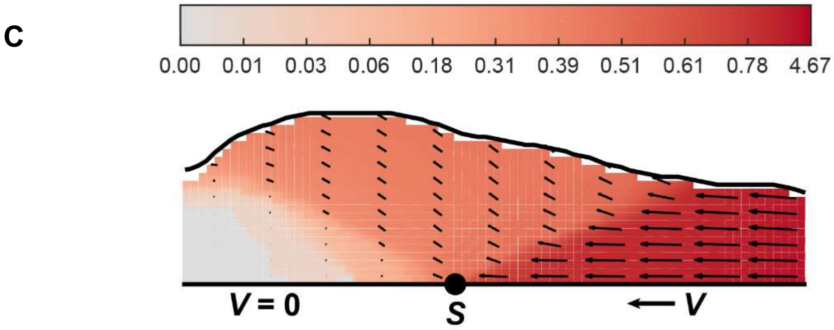

Figure 9. Theoretical solutions for low-Reynolds number flows against corners with a straight angle (A) and non-straight angles (120° and 60°, B). C) Closeup of the standard model of this work, showing the pattern of flow as indicated by instantaneous velocity field (unitary vectors and tones of red; the stronger the red, the higher the velocities and vice-versa).

The significant rearward and upward motions observed in the cores and retro side of the faultless wedge are similar to the theoretical solutions for low-Reynolds number flows against a corner with a given angle (Fig. 9A and B; Batchelor, 1967). This similarity is based upon the fact that long-term behavior of granular materials under tensile stresses is analogue to the long-term behavior of the deforming upper-crust, which can be approximated by the flow of a very viscous fluid (low-Reynolds number). In the sand wedge, the retro-shear band act as a rigid boundary, above which the material flows upward and rearward towards the surface (compare figures 9A and 9B with Fig. 9C). The result is similar to that of the model accretionary wedge of Cowan and Silling (1978), with the distinction that the backstop in this model is not predefined, and its shape is given by the internal friction of sand. As inertia forces are considered negligible for highly viscous media, and as the motions in the model are induced by traction of the underlying plate, the kinematic and boundary conditions accounted in the approach of Batchelor (1967) are the same as those in the experiment presented in this work. The pattern of flow in this model is thus analogous to the overall mass transport within accretionary prisms and fold-and-thrust belts (Cowan and Silling, 1978; Willettt et al., 1993).

The model velocity field is then of major importance as it provides hints into the way materials move inside natural systems. We therefore suggest that in natural subduction wedges operating under equivalent boundary conditions, the transport of crustal material of the distinctive tectonic units (e.g., structural lid, fold-and-thrust belt or accretionary complex) follow a similar trend. Horizontal displacements diminish and and vertical displacements increase from pro to retro side). There is a partition in solid body rotation polarity inside the wedge that has as well been observed in natural systems (Fig. 8, e.g., Feehan and Brandon, 2004; Comte et al., 2009). Cross-sectional material flow patterns such as the one illustrated in Fig. 9 have been proposed for the Cascadia subduction wedge (e.g., Brandon, 2004), the European Alps (Escher and

Beaumont, 1997; Brandon, 2004; Bonnet et al., 2007) the Pyrenees (Beaumont et al., 2000; Storti et al., 2000), Taiwan (Fuller et al., 2006; Malavieille et al., 2019) and observed in numerical experiments (Willettt et al., 1993; Escher and Beaumont, 1997). Some of these examples are addressed in more detail below.

3.3. Comparison with prototypes

The evolution of several orogens has been understood under the scope of subduction wedge models (e.g., Malavieille, 1984; Willettt et al., 1993; Jamieson and Beaumont, 2013). Of course, each prototype has its own peculiarities that will govern the dominant structural style. These peculiarities might depend on the combination of numerous local factors (e.g., the geodynamic setting; the tectonic history of the pre-orogenic crust; magnitudes of convergence; the effects of climate and sedimentation; mechanical stratigraphy; basal friction of the subduction thrust; fluid pore pressure; among others). Despite these differentiating factors, natural orogens do share common characteristics, and hence, it has been possible to model the evolution of several prototypes within the same experimental framework and boundary conditions. In fact, numerical models based on the S-point model (e.g., Fig. 5), capable of incorporating rheological constraints to reproduce deformation at both upper and lower crust, have successfully reproduced the main features of several collisional orogens with a remarkable similarity (e.g., Jamieson and Beaumont, 2013).

The connection between model and prototype can be established by simple comparison. Figure 10 compiles four examples of orogens developed along convergent zones, which first-order structure can be compared with S-point models. Common features are recognized among different orogens. As mentioned in section 2.1., one of the main characteristics of subduction orogens is that they are typically doubly-vergent (e.g., Argand, 1916), this is, that the tectonic transport in the thrust belts developed at both sides is opposite and outwards. As well, both sides of an orogen will exhibit different properties as the governing process (subduction) is intrinsically asymmetric.

Within the pro-side is an accretionary complex, commonly consisting of a fold-and-thrust belt developed above the subducting plate (Fig. 10; compare to Fig. 3C, Fig. 4 and Fig. 6). This part of the orogen will accommodate most of the convergence and therefore, tectonic shortening will be higher in this part. Within the retro-side, an asymmetric counterpart is developed, typically narrower than the fold-and-thrust belt of the pro-side. This counterpart is called structural lid, which is the portion of the upper plate that gets shouldered aside to the rear of the wedge. The distinction between pro-side and structural lid is that the structural lid originated as part of the retro-side, whereas most, if not all, of the accretionary complex in the pro-side is derived by accretion of materials carried by the subducting plate (Brandon, 2004).

Despite of the prevalence of material motions within the pro-side, the role of the retro-side is fundamental as *retrocharriage* (to "carry back" in French; Waschbusch and Beaumont, 1996; Brandon, 2004) of accreted materials allows the generation of space to accommodate the material accreting at the pro-side (Fig. 10; compare to Fig. 3C, Fig. 4 and Fig. 6). Compare the rearward sense of displacements shown in Figure 10C with the instantaneous velocities in Figure 9. Silver and Reed (1988) highlighted the importance of this rearward transport within a subduction wedge in order to explain the occurrence of significant back-thrusting among convergent orogens.

Because thrust belts develop above both plates of a wedge system, corresponding crustal detachments must underlie both sides of the orogen. Hence, subduction orogens are built upon crustal-scale shear zones at the base of each side, limiting the deformation inside the subduction wedge. The main subduction thrust is the pro-shear zone, and below the retro-side thrust belt or structural lid, a retro-shear zone will as well be rooted at a velocity discontinuity. The base of the orogen will then be marked by the velocity discontinuity from which the shear zones arise, corresponding to the s-point in the subduction wedge models.

Only a few examples of natural prototypes of orogenic wedges are Taiwan (Malavieille and Trullenque, 2009; Malavieille et al., 2019; Fig. 10A), the Pyrenees (e.g., Beaumont et al., 2000; Fig. 10B), Cascadia (Brandon, 2004, Fig. 10C) and the European Alps (Malavieille, 1984; 2010; Brandon, 2004; Fig. 10D). These orogens have been included in this section because modeling approaches to explain their tectonic evolution (e.g., references cited just above) provide insights to the evolution of the hypothetical crustal wedges that underlie the Cordilleras of the Central and Southern Central Andes.

These prototypes share aforementioned characteristics in common, but they have been formed under quite different geodynamic settings and have grown from the convergence of lithospheres with contrasting histories. For example, the European Alps (Fig. 10D) have formed after initial inversion of oceanic basins, in a continent-ocean-continent subduction zone (Escher and Beaumont, 1997). In fact, initial Alpine evolution is thought to include subduction of oceanic crust followed by ~300 km of subduction of marginal continental crust in the later stages. The transport of crustal material is mainly lateral, but displacements have a strong vertical component, to which emplacement of tectonic nappes, initial burial and their posterior uplift and exhumation are ascribed (Escher and Beaumont, 1997). A similar evolution has been proposed for the Pyrenees (Fig. 10B), involving the initial inversion of Mesozoic rift basins, and subsequent ocean-continent subduction, leading to the incorporation of marginal oceanic basins and continental crust into an orogenic wedge (Beaumont et al., 2000).

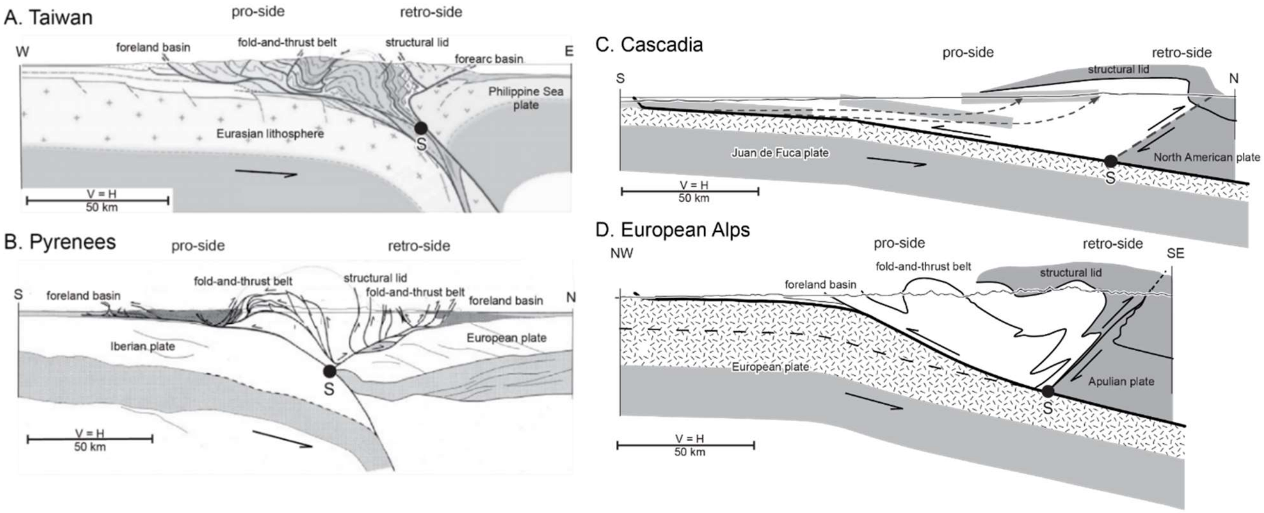

Figure 10. Cross-sections of doubly-vergent subduction wedges. **A)** Taiwan orogen. Schematic structure of the wedge is outlined. Note that the structural lid corresponds to the portion of the upper plate shouldered aside towards the rear of the wedge. Modified after Mallavieille and Trullenque (2009). **B)** the Pyrenees. Schematic structure illustrates the two thrust belts at the pro and retro sides. Flexural foreland basins have developed at the orogen margins. Modified after Beaumont et al. (2000). **C)** the Cascadia margin. The gray bands illustrate the displacement history of sediments presently exposed in the western Olympics, which were accreted at the front of the wedge at 22 Ma and then moved rearward through the wedge, reaching the west side of the Olympics at Present. **D)** the European Alps. Solid line within the wedge represents the schematic structure. Modified after Brandon (2004).

Contrastingly, the Cascadia wedge (Fig. 10C) has formed exclusively under an ocean-continent subduction regime, and the concomitant evolution of a magmatic arc. Here, lateral motions have been equally important, but material has reached shallower depths and minor metamorphism. Early Miocene turbidites, incorporated to the wedge leading edge of the Cascadia wedge at 22 Ma, are now emplaced at the wedge core and exposed subaerially (Fig. 8. Brandon, 2004). The case of Taiwan (Fig. 10A) involves not only continent-continent subduction and the accretion of materials into an orogenic wedge, but also a discrete episode of wedge growth because of coalescence of an initial orogenic wedge into a wedge-shaped, extinct volcanic arc edifice (Malavieille and Trulenque, 2009).

The Central and Southern Central Andes share some of the basic features involved in the tectonic evolution of the aforementioned prototypes. Indeed, the Present-day structure of the leading edge of the South American continent along central Chile (~30°S) has been compared to that of a crustal-scale subduction wedge complex. Based on seismic tomography, a retro-shear zone has been identified above the down-dip limit of frictional detachment (the S-point) to intersect with the surface at the eastern border of the Coastal Cordillera. The pro-shear zone then corresponds to the subduction mega-thrust (Comte et al., 2019). Similar observations at northern Chile (~19°S–23°S; Comte et al., 2016) suggest that this architecture may apply as well for such segment. The configuration is roughly comparable with that of the

Cascadia margin, although geological evidence suggests a protracted and much longer tectonic history of the Andean margin.

Regarding the inner cordilleras of the Andes, modern orogenesis has been related to the westward drift of the South America following spreading of the Atlantic, resulting in continental shortening at the retro-arc (e.g., Russo and Silver, 1996). The pre-orogenic history of the retro-arc region includes the formation of back arc rift basins that developed under extensional conditions, in similarity to that of the Alpine and Pyrenean histories (e.g., Allmendinger and Gubbels, 1996; Charrier et al., 2007). The pre-orogenic crust must have been thinned before the onset of contractional conditions, with an imprint of inherited extensional structures. Structural reconstructions, in fact, illustrate the importance of the latter in the Main Cordillera of Central Chile (e.g., Mescua and Giambiagi, 2012; Giambiagi et al., 2014). Comte et al. (2019) already postulated that seismic tomography show a suspect retro-shear zone corresponding to an hypothetical retro-Cordilleran wedge. In Chapter 3, the doubly-vergent nature of the inner Andean Cordillera and the applicability of the subduction wedge model for the Central and Southern Central Andes is addressed.

3.4. Accretionary flux and material distribution in a subduction wedge

The accretion of materials has a strong influence on the deformation of the overriding plate and of the entire wedge itself. In fact, deformation in subduction wedges is mostly accretion-driven, meaning that there is a dependency between deformation and material influx (e.g., Willettt et al., 1993). The accretionary flux entering a subduction wedge is then of major relevance in its evolution. This parameter provides of a first order estimate of the cross-sectional area of material added to the wedge per unit of time (km^2/Myr), and it determines the rate at which a subduction wedge grows (Brandon, 2004). The depth to the main detachment will define the thickness of the crust to be accreted and the portion of the crust that will be subducted (Fig. 10C and 10D). Convergence velocity, by the other hand, will provide the rate at which material enters the wedge. Because of the dependency between the accretion of material and wedge deformation, the accretionary flux corresponds to the most relevant factor controlling the deformation rates within a subduction wedge, while erosional fluxes modulate growth and the distribution of material until the system reaches a steady state (e.g., Willett and Brandon, 2003). This conclusion runs counter to the widely held idea that deformation rates scale with convergence velocities.

A few examples illustrate the importance of the accretionary flux in growth of a wedge. In Cascadia, thickness of materials accreted into the wedge (Fig. 10C) is of c. 2 km at a convergence velocity of c. 36 km/Myr, yielding an accretionary flux of 72 km^2/Myr. In comparison, the thickness of materials accreted into the wedge underlying the European Alps (Fig. 10D) is of c. 15 km at a convergence velocity of c. 5

km/Myr, yielding an accretionary flux of 75 km^2/Myr. The convergence velocities are quite different, but the fluxes are similar. Both wedges have similar dimensions and similar structural styles. They both have a structural lid and an underlying accretionary complex. Both wedges are doubly-vergent, with a pro-shear zone, marked by the subduction thrust, and a more slowly deforming retro-shear zone defining the back of the wedge. The main difference is that the entire Alpine wedge has been subject to subaerial erosion, whilst only the forearc high portion of the Cascadia wedge has been eroded. As a result, the time to steady state is much longer for the Cascadia wedge, and accreted materials are subject to large horizontal motions as they have moved from where they are initially accreted to the main site of erosion at the forearc high (Brandon, 2004).

Another aspect that highly influences fluxes within a wedge is the polarity of subduction. Despite the inherent doubly-vergent nature of a subduction wedge, the polarity determines the main direction of growth, or, in other words, the main direction of tectonic transport within the wedge. Because of the asymmetry involved in the process of subduction (the subducted plate is consumed while the upper plate remains in place and mostly deforms), most of the accretionary flux is carried into the pro-side, and then this is where most of the deformation is absorbed.

The dominance of pro-side accretion creates a strong tendency for all material in the wedge to move laterally from the pro-side towards the retro-side (Willett et al., 1993; Brandon, 2004; Fig. 5, Fig. 6, Fig. 9 and Fig. 10). The asymmetry in the amount of tectonic shortening accommodated by the wedge is thus another distinctive character. As aforementioned, pro-sides are usually characterized by fold-and-thrust belts that absorb most of the convergence below the orogen (Fig. 10A, Fig. 10B, and Fig. 10D) whilst retro-sides are characterized by backfolds (Fig. 10C and Fig. 10D) or by fold-and-thrust belts with a minor absorbed shortening (Fig. 10B). Note in Figure 5, Figure 6 and Figure 9, how horizontal velocities are the highest along the pro-side of the wedge. Towards the rear in the area of maximum thickening, lower, sub-vertical velocities become more important (Fig. 9).

The horizontal motions within the subduction wedge can be highly influenced by the effects of erosion on wedge topography (Willett et al. 1993; Willett, 1999; Malavieille, 2010). Consider a situation in which orographic precipitation is affecting more the pro-side of the subduction wedge. Analogue and numerical experiments illustrate the influence of pro-side erosion, showing how the continuous removal of material from the pro-side surface enhances the localization of deformation and the generation of antiformal stacks in presence of detachments (Malavieille, 2010; Fig. 11). When erosion is focalized in the retro-side, horizontal motions are enhanced at a maximum and a diffused pattern of deformation is generated (Willett, 1999).

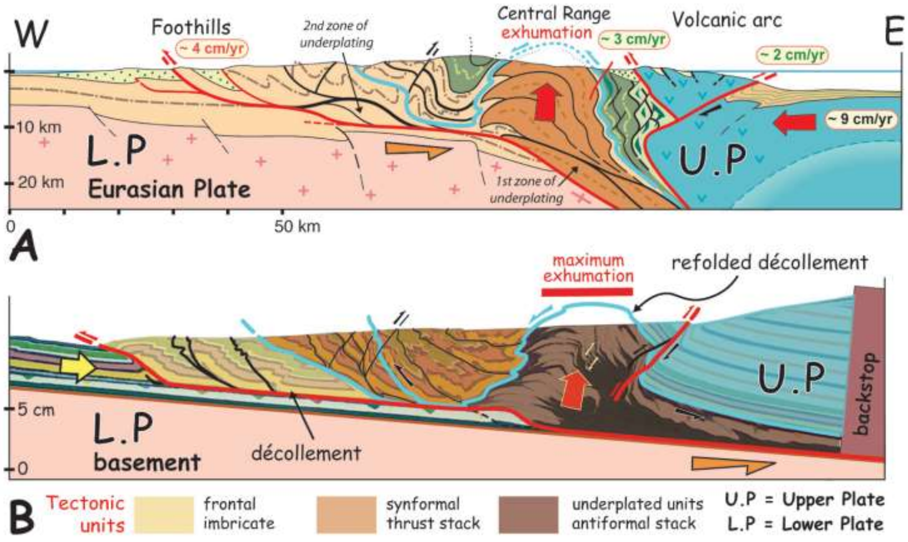

Figure 11 A) Interpretative geological section of Taiwan (same as in Figure 5A), inspired by **B)** analogue experiment involving a décollement and erosion. Note the antiformal stack of the Central Range. In the upper plate, or retro side, no erosion was applied. Modified from Malavieille (2010).

3.5. Important aspects in the growth of a subduction wedge and modes of accretion

In the aforementioned analogue and numerical approaches, it is illustrated how the accommodation of mass by accretion will be balanced by the asymmetric lateral expansion and an increase in crustal thickness within a doubly vergent subduction wedge (Fig. 4 and Fig. 5). Following critical taper theory, this overall growth will tend to be in self similar fashion, at a constant, critical taper, and at the verge of failure everywhere (accommodation of shortening induces deformation everywhere in the wedge). Accordingly, in the case of doubly-vergent wedges, thrusting must be synchronous at both sides. Storti et al. (2000) showed how displacements within model doubly-vergent sand wedges are synchronous within all faults. In that particular work, retro-vergent thrusting dominates at the early stages of convergence, whilst pro-vergent thrusting dominates most of the experimental run. Figure 4 shows the basic thrusting sequence of deformation in a model doubly vergent wedge (Malavieille, 1984). As convergence must be distributed within the entire wedge, fault displacements diminish towards advanced stages of convergence and wedge growth.

Similar results were obtained in this work for the faultless wedge model, showing how shearing in all bands was synchronous throughout. Synchronous shearing was characterized by the crisscross pattern of shear band and a "pulsating" history of deformation (stick-slip). Figure 6 shows how displacements are occurring within all shear bands developed in the wedge. There is a more focused deformation at the rear of the wedge, particularly concentrated at the retro shear. The results shown in Chapter 3 is thus illustrative of how growing wedges composed of cohesionless granular materials are at the verge of failure everywhere and throughout, strongly consistent with critical taper theory. The details on the growth sequence registered in these experiments have been described in the previous section 2.2. and are as well addressed in Chapter 3.

A common aspect of doubly vergent wedges is the asymmetry of their growth. Expansion of the opposite sides of the subduction wedge occur at different rates. Pro sides expand at a rate close to the subduction rate (~ 1 to 1 relationship) whilst retro sides expand at a rate close to 1/5 of the subduction rate (Naylor et al., 2005; Herrera et al., in prep). Whilst growth of the pro side of an accretionary wedge has been well studied in previous work (e.g., Davis et al., 1983; Malavieille, 2010; Konstantinovskaya and Malavieille, 2011), some important aspects of the growth of the retro side have received less attention.

For example, accommodation of material at the rear and below the fold-and-thrust belt produces a passive rearward displacement of the structural lid in the retro plate (e.g., Brandon, 2004). It has been observed in numerical and analogue experiments (e.g., Willett et al., 1993 and Herrera et al., in prep, respectively) that with increased convergence, there is a detachment of the retro side from its base (Fig. 12). Note that in the numerical experiments of Willett et al. (1993), this is characterized by the generation of a break-in-slope of the retro side topography (Fig. 5B). When this detachment occurs, the material below the retro shear and retro side also moves rearwards (Fig. 12), inducing tectonic shortening beyond the limits of the wedge within the upper plate. These results are particularly important as they illustrate for the first time in analogue experiments out-of-the-wedge deformation affecting the upper plate.

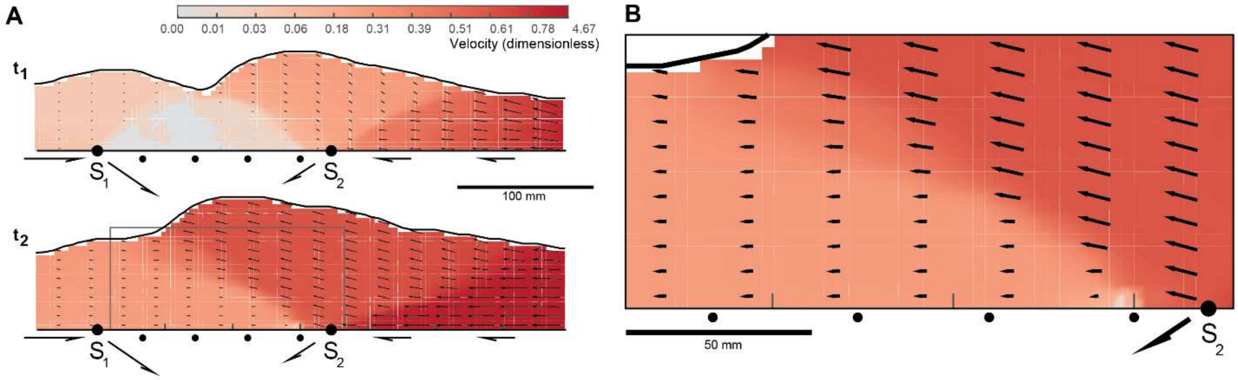

Figure 12. Displacement fields (instantaneous velocity fields) in a doubly vergent coalescent wedges (adapted from Herrera et al., in prep). **A.** Shows the development of two, oppositely facing wedges nucleated at S_1 and S_2 in a subduction advance setting. Note that basal pull towards S-points is opposite. Velocity field (red tones) clearly shows the drop in velocities from pro to retro side (t_1). At t_2, the whole area beyond S_2 to the left, and below the retro side of the larger wedge, is involved in the deformation as displacements towards the rear reach this area. **B.** Close-up of the retro side (corresponding to the area of rectangle in A, t_2), showing velocity vectors of the retro side base.

Apart from kinematic boundary conditions, the thermal structure of the lithosphere is perhaps the most important boundary condition in the evolution of a subduction wedge, as the rheology of the crust is a temperature-dependent property. Detachments in the uppermost crust are certainly defined by the presence of weak layers in to-be deformed basins, basement-cover interactions and structural inheritance. Tectonic shortening and subsequent thickening of an orogenic wedge results in deepening of its crustal roots. In a normal non-thickened continental crust, thermal relaxation is expected to occur at depths of c. 15 to 25 km, in the middle and lower crust. It is then expected that the base of an orogenic wedge weakens by thermal effects when thickened.

The nature of analogue modeling and the difficulties in scaling the effects of temperature disable the exploration of the former in physical experiments. It has been shown in numerical experiments how heating of the lower crust combined with the effects of gravity and the lateral gradient of motions induced by traction of the mantle result in crustal thinning, symmetric lateral expansion and ultimate plateau formation (Fig. 5D; Willett et al., 1993; Beaumont et al., 2004). This aspect will be addressed in more detail in experimental limitations elaborated in 4. Discussion.

Despite the simplicity of wedge growth in synthetic models for lithospheric shortening, the growth sequence in natural systems has a much greater complexity and involves different mechanisms in the process of incorporating material by accretion following the initiation of convergence. Basically, tectonic accretion might occur in the form of the following mechanisms. Frontal accretion occurs at the toe of the wedge and it relates to the imbrication of thrust sheets in "piggyback" sequence, or out-of-sequence, depending on the state of equilibrium of the wedge. Basal accretion occurs throughout the base, above the subduction plane and, if doubly-vergent, towards the rear of the accretionary wedge, mainly involving thrust stacking (duplex formation) and retro vergent thrusts. A wide variety of combinations of these modes of accretion describe the kinematics of complex imbrication sequences of natural fold-and-thrust belts (e.g., Beaumont et al. 2000; McQuarrie, 2002). The different possible kinematics of thrust imbrication may be caused by peculiarities of each orogen, or local factors, such as, mechanics of the stratigraphy or localized erosion (e.g., Konstantinovskaya and Malavieille, 2011), convergence obliquity (e.g., McClay et al., 2004), syntectonic erosion and sedimentation (e.g., Storti et al., 2000; Malavieille, 2010; Konstantinovskaya and Malavieille, 2011) and the pre-orogenic structural inheritance and nature of the orogenic crust (e.g., Beaumont et al., 2000). All thrusting modes can be observed in both the pro and retro side of an orogenic wedge at the local scale, but there is some prevalence regarding the main faulting mechanism at the scale of the orogen.

Forward breaking, or "piggyback" thrusting is a common overall feature of pro sides, as great part of the convergence is accommodated within this portion. A few examples have been aforementioned already (Fig. 10), and to mention others, the Subandean Sierras and Eastern Cordillera of the Central Andes have grown due to thrust sheet emplacement in a forward sequence to the east, in response to westward subduction of the Brazilian craton (Fig. 13, e.g., Roeder, 1988; McQuarrie, 2002). Here, frontal accretion occurs by the incorporation of thrust sheets carried from the Chaco foreland at the toe of the orogenic wedge, whilst basal accretion concentrates within the hinterland, resulting in anticlinal stack emplacement that contributes to thickening of the wedge (Fig. 13). Towards the rear, passive tectonic transport of the accreted thrust sheets is facilitated by retrocharriage and backthrusting, which creates the space for more emplacement of material frontally accreted (Fig. 13).

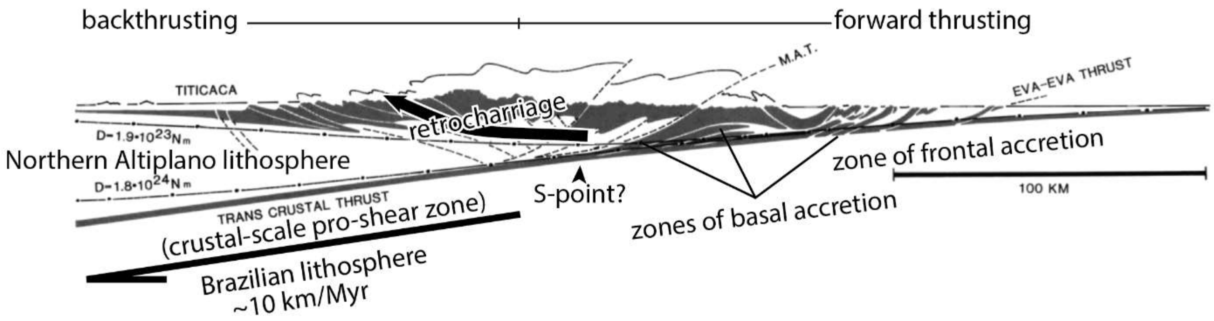

Figure 13. Crustal-scale cross section of the eastern flank of the northern Altiplano (adapted from Roeder, 1988), illustrating modes of accretion within an orogenic wedge. A tentative position of the S-point of the system is indicated for reference.

3.6. Wedge coalescence

While the growth of subduction wedges is a rather continuous process as it is driven by the accumulation of material in the leading edge driven by convergence, this accretion can also be episodic, involving the collision of large lithospheric blocks, called tectonostratigraphic terranes. For example, the early (Paleozoic) growth of western South America has been interpreted as the result of such events, in which autochthonous and allochthonous terranes were accreted to the early margin (Bahlburg and Hervé, 1997; Charrier et al., 2007 and references therein). Regarding modern deforming regions, mechanical models simulating shortening of the lithosphere show that orogen widening may result from the activation of multiple thrusts that reach the mantle lithosphere, and a subsequent growth of orogenic wedges forming above those subduction thrusts (Martinod and Davy, 1994; Martinod et al., 2020). Conditions that may favor such a situation are a mantle soft enough or a lithosphere composed of amalgamated terranes bounded by ancient sutures (Martinod and Davy, 1994; Martinod et al., 2020). If there is available material for accretion and convergence is continuous, lateral growth or expansion of one or both wedges will eventually lead to their coalescence (e.g., Fig. 14).

Along-strike changes in the geology and morphology of an orogen can range reflect the increasing imprint of a subduction process. The Taiwan orogen reflects how an along-strike (northward) increase in continental subduction has led to a greater (northward) expansion of the underlying orogenic wedge. The expansion affects the adjacent forearc basin which is progressively incorporated to the retro side. To demonstrate this hypothesis, Malavielle and Trulenque (2009) ran analogue experiments in which two wedges grew separated by a central topographic basin (Fig. 11 and 14). Their model (Fig. 14) shows how the layers of the basin are incorporated into the retro-side toe (Fig. 14A to Fig. 14C), and with increased convergence, the wedges of the system end up merging with each other (Fig. 14D and Fig. 14E). Then accretion is episodic and leads to the formation of a single, larger wedge (Fig. 14E).

The particular example of Taiwan illustrates how wedge coalescence can lead to rapid orogen widening when another wedge is encountered in one of the expanding sides. In the cross-sectional area of coalescence, the structure of both wedges is overlapped. Cross-cutting of existing structures by the main shear zones of the systems, rooted at the active S-points, is expected to occur (Malavieille and Trulenque, 2009; Fig. 14E). A peculiarity of the Taiwan example is that the orogenic wedges composing the system do not grow at the same time. The location of the active subduction point (slot in the model of Fig. 14) migrates throughout the evolution of the range. At a final stage, both wedges are underlain by the same mantle thrust, and grow together as a single, larger wedge (Fig. 14E).

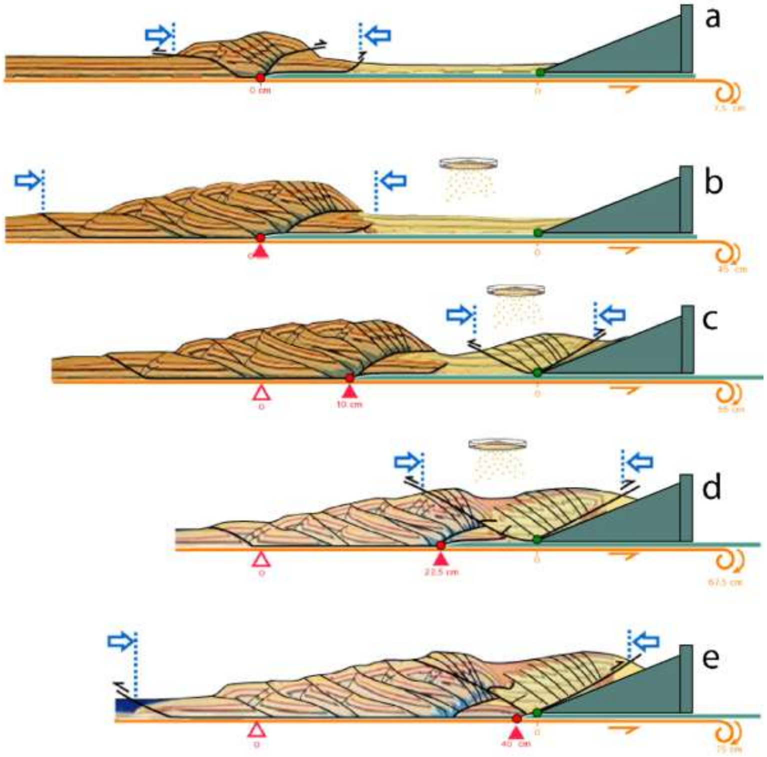

Figure 14. Analogue experiment for the Taiwan orogen, in which two doubly-vergent accretionary wedges are growing adjacent to one another. Red triangles represent the basal velocity discontinuities in which deformation is nucleated to generate each wedge. Blue arrows show the basal sheets that are active at each stage. The first wedge is developed at stages a) and b), whilst the second, smaller wedge is developed at stage c) and d). At stage d) and e), the wedges are merged together, and the entire basal sheet is again active. Compare **e)** to Fig. 8A and Fig. 9. Modified from Malavieille and Trulenque (2009).

An important consequence of growth and coalescence of subduction wedges is that its occurrence can lead to rapid orogenic widening and ultimately, to the formation of large orogens with plateaus (e.g., Martinod et al., 2020). Such large orogens have been considered a consequence of the following situations: (1) if subduction and accretion into an orogenic wedge are sufficient to thicken the wedge, enough so its base becomes hot and ductile (see 2.1.5. Growth sequence of an orogenic wedge above); or (2) by the coalescence of independent wedges above respective subduction thrusts, that grow separately until they encounter each other by lateral expansion.

Beaumont et al. (2006) presented mechanical models for shortening of the lithosphere in which extended subduction beneath an orogenic wedge led to sufficient expansion to generate a plateau-like orogen (similar to Fig. 5D; Willett et al., 1993). The increase in temperature at the base of the wedge leads to the formation of weak and ductile root. Frictional detachments are then restricted to the “colder” areas formed at the margins of the wedge (Fig. 5D), which grow frontally and at their base, progressively outward by accretion. An example of a currently expanding plateau is the Altiplano eastern flank. As aforementioned, accretion in association to westward subduction of the Brazilian shield enables growth of the critically tapered eastern flank, specifically along the Subandean Sierras (Fig. 13; e.g., Roeder, 1988; Baby et al., 1997; McQuarrie, 2002).

The particular case of Taiwan is important for this thesis. The along-strike geological and morphological changes caused by increasing convergence provide a space-for-time representation of the evolution of orogenic topography of this orogen. In a similar way, along-strike changes in the Andes are interpreted in Chapter 3 as the result of increasing convergence along the retro-arc region, and as well provide of a space-for-time representation for Andean evolution. The analogue models presented in this thesis show additional insights to wedge coalescence and allow to propose the application of this concept to the Andean system (see Chapter 3).

The Taiwan case is also relevant to this work as it explored wedge growth and coalescence within a similar geodynamic scenario proposed for the Central Andes by Armijo et al. (2010), followed by Riesner et al., (2017; 2018). I note that the resulting geometries in the experiments of Malavieille and Trulenque (2009) do not correspond the first order Central Andean structure. Figures 14d and 14e show a final state of two coalescing wedges formed by subduction with equal polarity, or synthetic subduction. The wedge formed against the backstop can be seen as analogue to the Main Cordillera of the Central Andes, whilst the wedge formed during stages a and b (Fig. 14) would correspond to the Coastal Cordillera. The wedge representing the Main Cordillera has an opposite structure regarding this natural prototype, with a larger accretionary prism on a western side and a sole oppositely verging retro thrust. Foreland fold-and-thrust belts are a prime-order feature of the Central Andes along the retro arc region, whilst smaller and less deformed thrust systems developed in the inner forearc of Chile, suggesting that synthetic subduction might not be a corresponding tectonic scenario for the Central Andes.

4. EXPANSION AND COALESCENCE OF OROGENIC WEDGES IN THE CENTRAL ANDES

In the previous chapter, a review of physical and numerical models for shortening of the lithosphere was presented to provide of the reader of the basis for understanding the basis of the analogue model carried out in the context of this thesis. In this chapter, the details on the analogue model setup, results and implications are provided. The model shows how there is synchronous uplift throughout a doubly-vergent sand wedge, and that there is a detachment of the retro-side of the wedge from its base when shortenings in the pro-side are high. This has a good correspondence with the westward migration of the thrust systems emplaced along the Chilean Precordillera and Western Cordillera during middle to late Miocene times. The results are then compared to the geology of the Western Cordillera of Northern Chile at 19°15’S in the discussion of this text.

Expansion and coalescence of orogenic wedges in the Central Andes

Sebastián Herrera*[1], Mark Brandon[2], Marcelo Farías[1], Keith Ma[2]

[1.] Departamento de Geología, FCFM, Universidad de Chile, Plaza Ercilla 803, Casilla 13518, Correo 21, Santiago, Chile.

[2.] Department of Geology and Geophysics, Yale University. New Haven, CT 06520-8109

* Corresponding author's e-mail: sebherre@ing.uchile.cl

ABSTRACT

The Central Andes are underlain by an active orogenic wedge, formed by accretion from its eastern side, in association with westward subduction of the South American basement. Eastward subduction of the Nazca plate along the subduction zone is paralleled by a well-defined forearc high, corresponding to the Coastal Ranges of Chile. We propose that the remarkable morphostructural transitions of the Andes provide a space-for-time representation of the evolution of its orogenic topography. The Southern Central Andes show an "initial" structural configuration of the margin, in which two orogenic wedges are separated by a tectonically stable Central Valley: the Coastal wedge to the west, formed by Nazca subduction, and the Cordilleran wedge to the east, formed by subduction of South America. The Cordilleran wedge has grown at a faster rate due to the accretion of a thick crustal section from the subducting South American plate. The accretion rate increases northward and accounts for the nortward expansion of the Cordilleran wedge towards the eastern foreland, the westward expansion of the Cordilleran retro side and its coalescence with the Coastal wedge along the Chilean forearc. This hypothesis is demonstrated by the results of sandbox models, in which two doubly-vergent wedges growing at different accretionary fluxes representing a subduction advance setting consistent with the Andean geodynamic scenario. We analyze our results using a Particle Image Velocimetry (PIV) software to provide additional insight into the kinematics of deforming sand within individual and coalescent subduction wedges. Strain rates and kinematic vorticity illustrate a continuum character of deformation in cohesionless sand, characterized by ebb and flow motions of the media, and outward solid body rotations of the retro and pro sides. Horizontal instantaneous velocities dominate the pro sides, whilst a vertical component becomes important towards the core and retro sides. Based on our inferences, we conclude that the locus and rate of orogenic deformation are controlled not by decollement stress (i.e, plate coupling) at the Nazca-South America boundary, but rather by accretionary flux from the east. In segments of the Southern Central Andes in which back arc tectonic shortening exceeds ~100 km, the retro side of the Cordilleran wedge expands towards the west to merge with the Coastal wedge. The Coastal wedge has a fast subduction velocity (~70 km/Ma) with only a very thin accreted section (<0.5 km), so wedge growth is slow there. In contrast, the Cordilleran wedge is underlain by a slowly subducting plate (~4 km/Ma and increasing northward) but a much thicker accreted section (~15 km), so wedge growth is faster there. The example of the Southern Central Andes and of other segments of the range suggest that the expansion and coalescence of the inner Cordilleras of the Andean range seem to be an essential part of the history of this orogen.

Keywords: Southern Central Andes, orogenic wedges, accretionary flux, analogue modeling.

I. Introduction

[1] Orogeny in the Central and Southern Central Andes is product of active subduction below western South America (Fig. 1). Protracted eastward subduction of the Nazca plate at the subduction zone is paralleled by a wedge-shaped subduction complex (Comte et al., 2019) underlying a well-defined forearc high, corresponding to the Coastal Cordillera of Chile (Charrier et al., 2007). To the east, along the Andean retro arc, the high elevations of the range are underlain by another subduction wedge, which has mainly grown by thrust sheet emplacement from the eastern foreland, in response to westward subduction of the South American basement (Bally, 1975; Isacks, 1988; Beck and Zandt, 2002; Ramos et al., 2004).

[2] Simple morphostructural comparisons from south to north show a strong segmentation of the high Andes, which has been ascribed to the distribution of crustal shortening within the continental plate (Fig. 1). A south to north increase of retro arc tectonic shortening and rate of accretion correlate with a northward expansion of the orogenic wedge underlying the inner Cordillera (e.g., Kley and Monaldi, 1998; Kley et al., 1999; Ramos et al., 2004; Fig. 1). By the other hand, along the forearc, westward thrust propagation in the Chilean Andes and the narrowing and disappearance of the Central Valley spatially correlate with segments where shortening and accretion at the retro arc is high (Fig. 1). We propose that these transitions provide a space-for-time representation for the evolution of the orogenic topography in this part of the Andes. The Southern Central Andes show an initial configuration of the margin, with two orogenic wedges separated by a longitudinal Central Valley: an old Coastal wedge to the west, formed by ocean-continent subduction, and a young Cordilleran wedge to the east, formed by intra-continental subduction. Rates of accretion increase northward and account for the westward expansion of the Cordilleran wedge, its coalescence with the Coastal wedge, and the formation of the Central Andes Altiplano in an advance state of orogenesis. Moreover, a westward expansion of the Altiplano western flank during the last 8 Ma correlates with the final emplacement of the Subandean Sierras of the eastern plateau. This suggests that there is close relationship between the flanking morphostructures of the Andean plateau, especially because this westward expansion is most notable at segments where shortenings on the eastern side reach maximums, implying that basement underthrusting mechanically couples both parts of the orogen.

[3] To demonstrate these hypotheses, we have run simple sandbox experiments, in which two doubly-vergent wedges grow with different accretionary fluxes in a subduction advance setting. In such configuration, the overriding plate converges towards the subduction zone: a situation that applies for the entire extent of the Andean range (Fig. 1). Our goals are to provide a simple explanation for the development of the first order structure and orogenic topography of the Central Andes, to establish a relationship between the structural systems east and west of the range, and to explain the sense of overall tectonic transport (vergence) in terms of the evolution of our subduction wedge model. We argue that growth of the inner Cordillera is essentially towards the east and propose that its expansion towards the west is a result of increased *retrocharriage* within the underlying wedge, creating space below the forearc for the accommodation of material in response to accretionary fluxes from the east. We propose that material fluxes entering each subduction wedge of the Andes govern the resulting tectonic transport mechanisms of those accreted materials in each wedge (thin accreting section and low accretionary fluxes in the Coastal Ranges; thick accreting section and higher accretionary fluxes in the inner Cordillera). Our results suggest that the growth, expansion and coalescence of independent subduction wedges appear to be essential in the tectonic evolution of the Andean range as well as in the development of other cordilleran systems.

II. Tectonic framework: observations from the Central and Southern Central Andes

[4] The tectonic scenario of the Central and Southern Central Andes (Fig. 1) involves the Nazca and South American plates in a subduction advance setting (i.e., no retreat of the overriding plate; e.g., Waschbush and Beaumont, 1996). This configuration allows a partition of the convergence rates by considering the entire Andean forearc as one separate plate, below which both Nazca slab and the South American basement subduct (e.g., Brooks et al., 2003; Fig. 1). Global plate kinematics indicate that plates converge at a trench-orthogonal velocity of 75 mm/yr (relative rate, 105º azimuth) at 33.5ºS latitude (Gripp and Gordon 2002). As the South American plate moves towards the subduction zone, significant convergence is accommodated in form of tectonic shortening at the retro arc.

[5] Tectonic shortening estimates along the two segments addressed in this study are a direct measurement of retro arc convergence. Crustal deformation along both sides of the high Andes is characterized by a distinct asymmetry in shortening distribution and structural style (Fig. 1). Along the Chilean side, relatively moderate (and rather constant along-strike) amounts of tectonic shortening (<40 km) have been accommodated by west-vergent thrust systems, rooted at east-dipping crustal-scale detachments and associated with high amounts of surface uplift (e.g., Victor et al., 2004; Farías et al., 2005; 2010; Martínez et al., 2021). Contrastingly, along the retro arc (Bolivian and Argentine Andes), fold-and-thrust belts rooted at west-dipping crustal-scale detachments absorb permanent deformation at high rates that increase monotonically. At ~33.5ºS (Southern Central Andes), an estimate of 84 km of retro arc shortening since 22 Ma yields a minimum rate of ~4 km/Ma (Farías et al., 2010). Subtracting this amount from the total convergence at 33.5ºS, a total of 71 mm/yr can be estimated for subduction of the Nazca plate (Fig. 2B). At ~19°-21°S (Central Andes), shortening estimates of up to 330 km since 40 Ma yield an approximate of 8.25 km/Ma of retro arc convergence since the late Eocene (McQuarrie, 2002). These estimates are consistent with GPS measurements for continental motions along the retro arc in a fixed forearc framework, which indicate velocities of ~11 km/Ma at the Bolivian Orocline (Fig. 1; Brooks et al., 2011) and of ~4 km/Ma at the Southern Central Andes segment (Fig. 1; Brooks et al., 2003).

II. 1 Observations from the Central Andes

[6] The Central Andes is characterized by a major bend along the subduction zone and orogen - the Bolivian Orocline (e.g., Isacks, 1988) -, by several high summits (>6 km a.s.l.) and by the second highest plateau on Earth, the Altiplano (average elevation of 3.5 km a.s.l.). Here, the Andes are also the widest (~700 km), and the crust is the thickest (55 km below the Altiplano to 75-80 km below the Western and Eastern Cordilleras; Yuan et al., 2000; Beck and Zandt, 2002) consistent with high amounts of tectonic shortening along the retro arc (>300 km e.g., McQuarrie, 2002; Anderson et al., 2017). Seven morphostructural units parallel to the subduction trench constitute the Andes at this latitude (Fig. 1).

[7] The Coastal Range of northern Chile is mostly composed of arc rocks of the Mesozoic, with a smooth topography (~1200 m a.s.l.) bordering the Pacific Ocean (e.g., Farías et al., 2005; Charrier et al., 2007). The Coastal Range has developed by the subduction of an oceanic plate and related arc magmatism in central Chile, which have been occurring continuously at the northern and central Chile margin at least since the Triassic (Charrier et al., 2007; Coloma et al., 2017) and even tracked to Paleozoic times (Oliveros et al., 2019). It corresponds to the forearc high of the active wedge associated to subduction of the Nazca plate beneath the leading edge of the continent. To the east, the Coastal Ranges are flanked by the forearc Central Valley, which has remained tectonically stable or slowly uplifting (0 to 500 m of uplift) since the Oligocene (Farías et al., 2005). It is filled with up to 1100 m of synorogenic gravels and ignimbrites of late Eocene to Holocene ages (e.g., Hartley et al., 2000; Hartley and Evenstar, 2010). The northern Central Valley is bounded to the west by the forearc Precordillera; the western Andean front of northern Chile (Fig. 1), characterized by north-south trending, west-vergent monoclines rooted at east-dipping, high-angle thrusts (Muñoz and Charrier, 1996; Victor et al., 2004; Farías et al., 2005). Above these structures, late Oligocene to late Miocene westward-fanning growth strata and coeval ignimbrites record c. 700 m to 2600 m of forearc vertical uplift between 18°S and 21°S (Victor et al. 2004; Farías et al., 2005).

[8] To the east, the Western Cordillera comprises the Present-day magmatic arc. It is structurally bound to the west by the west-vergent monoclines of the Precordillera and to the east, by high-angle, east-vergent thrusts underlying gentle folds towards the western Altiplano, active since the Oligocene and through most of the Miocene until the Present-day (e.g., Charrier et al., 2013; Farías et al., 2005; Cortés et al., 2012; Herrera et al., 2017). Regardless of the mostly Neogene history of orogenic events in of the western Andes at this latitude, at the axis of the Western Cordillera, deformation has been tracked to the late Eocene (Herrera et al., 2017), concomitant to the development of foreland system deposits of a late Paleogene age at the western Altiplano (Horton et al., 2001; Charrier et al., 2013). This evidence suggests a protracted pre-Neogene (late Cretaceous to early Cenozoic) tectonic activity at the margins of the plateau, considering the long-lived thrusting history of the bordering systems at the eastern side (e.g., McQuarrie, 2002; McQuarrie et al., 2005; Barnes and Ehlers, 2009).

[9] The Altiplano is a complex endorheic basin, structured in its western part along northern Chile by east-vergent thrust systems that are possibly connected in depth by the Altiplano low-velocity zone to the west-vergent monoclines of the Precordillera forming together a crustal-scale pop-up structure (Victor et al., 2004; Farías et al., 2005; Charrier et al., 2013). The sedimentology and provenance data of thick Cenozoic continental series outcropping in the Altiplano interiors suggest the presence of high reliefs surrounding the Present-day plateau since mid-Paleocene times, before major uplift of the basin (Horton et al., 2001). The central portion is underlain by a wide syncline detached above long basement structural flats that connect to the east with the thrust systems of the Eastern Cordillera and Interandean Zone (McQuarrie, 2002).

[10] The Eastern Cordillera and Interandean Zone flank the Altiplano to the east and are structured by complex west- and east-vergent thrust systems that involve pre-Cambrian basement with associated thin-skinned thrusts and back thrusts deforming Paleozoic through Cenozoic strata (e.g., Roeder, 1988; Baby et al., 1997; McQuarrie, 2002). To the east, the Subandean Sierras correspond to a mainly in-sequence, thin-skinned wedge detached above lower-Silurian shale (Roeder, 1988; McQuarrie, 2002). It is characterized by large-scale thrust sheets (10-20 km offsets) composed by Paleozoic strata and broad folds covered with up to 6000 m of syntectonic Neogene sedimentary rocks (Baby et al., 1997).

[11] Balanced cross sections show that basement duplexing (Baby et al., 1997; McQuarrie, 2002) and crustal faults (Roeder, 1988; McQuarrie, 2002) are sufficient to explain overall shortening and crustal thickening. Together, the Eastern Cordillera, Interandean and Subandean Zone have accommodated most of the Cenozoic retro-arc shortening, with estimates of 191 km at 15°-18°S to 231 km at 21°-22°S (Baby et al., 1997), 337 km at 22°S (Anderson et al., 2017), 330 km at 19°S (McQuarrie, 2002) and of 210 km at 18°S (Roeder, 1988). It is considered that these eastern morphostructural units are all structurally rooted at the main detachment below which the Brazilian craton subducts towards the west (Roeder, 1988; Isacks, 1988; Baby et al., 1997; Beck and Zandt, 2002; McQuarrie, 2002; McQuarrie et al., 2005). Present-day elevation of the entire Altiplano region and adjacent morphostructural units might have been achieved rapidly in the past 10 Ma, although a slow and steady mode of plateau uplift since the Eocene (~40 Ma) is considered tenable according to a synopsis of available constraints on geodynamic models, balance between tectonic shortening and crustal thickening, incision and exhumation rates (Barnes and Ehlers, 2009).

II. 2. Observations from the Southern Central Andes

[12] In contrast to the Altiplano segment, the Southern Central Andes at central Chile and western central Argentina are a narrow chain (~120 km wide) with lower average elevations and a ~60 km-thick orogenic crust (Ramos et al., 2004; Farias et al., 2010; Giambiagi et al., 2014; Mescua et al., 2016). Here, five morphostructural units parallel the subduction zone. From west to east, these correspond to the Coastal ranges, the longitudinal Central Valley, the inner Main Cordillera, the basement-composed Frontal Cordillera and the Argentine foreland. The segment also includes the transition from flat slab to normal subduction geometry of the downgoing Nazca plate which is ascribed to hinder both the influence of the asthenospheric mantle wedge and occurrence of post-Miocene volcanism. The geological setting of the Southern Central Andes can be summarized as follows.

[13] The Coastal Cordillera of central Chile is mostly constituted by arc-related rocks of the Late Paleozoic-Cretaceous, as well as scarce remnants of subduction accretionary complexes of similar ages. As a morphostructural unit, just like the northern Chile counterpart, it is considered as the emerged portion of the active wedge associated to subduction of the Nazca plate (Comte et al., 2019). The western side of the forearc high in central Chile is mostly composed by late Paleozoic to Triassic igneous and metamorphic complex basement rocks (Rebolledo and Charrier, 1994; Charrier et al., 2007) and, its eastern side, by an east-dipping homocline composed of Jurassic and Cretaceous arc sequences overlaying contemporaneous batholiths (Charrier et al., 2007). The offshore segment is characterized by extensional structures (Farías et al. 2011; Becerra et al., 2016; Comte et al., 2019) and small (5-15 km wide) active accretionary complexes are emplaced near the Nazca trench (Becerra et al., 2016).

[14] To the east, north of 33.5ºS, the Coastal ranges are bounded by Cenozoic arc sequences (late Eocene- Oligocene Abanico Formation) of the Main Cordillera (Charrier et al., 2007; Rodríguez et al., 2018), and south of 33.5ºS by the longitudinal Central Valley (Fig. 1). The Central Valley is a non-subsiding and erosional forearc basin (Farías et al., 2008), filled by a thin section (few hundreds of meters) of Quaternary alluvial deposits, overlying strata of the Abanico Basin (Charrier et al., 2007; Farías et al., 2010). The Central Valley is bounded to the east by active, west-vergent, high angle thrusts of the western flank of the Main Cordillera (Fig. 1; Farías et al., 2008; 2010; Vargas et al., 2014; Ammirati et al., 2019).

[15] Most of the recent structural analyses carried out in the Main Cordillera at 33.5ºS (e.g., Giambiagi and Ramos, 2002; Farías et al., 2010; Giambiagi et al., 2014) identify four main orogenic stages in the history of deformation, which is briefly summarized as follows. The onset of modern orogeny in the Andes began with the tectonic inversion of the Abanico basin during the first stage, from 22 Ma to 16 Ma (Charrier et al., 2007; Farías et al., 2010). This rift basin extended from ~30° S to ~36°S along the present eastern Central Valley and western swath of the Main Cordillera. Initially, tectonic inversion of the basin was mainly accommodated by the bordering rift faults, absorbing 8 to 16 km of horizontal shortening by reverse movements. Deformation migrated to the eastern side after ~16 Ma (Charrier et al., 2007). During a second stage (middle Miocene ~16-8.5 Ma), Mesozoic sedimentary sequences of the marginal Neuquén basin were progressively accreted at the eastern side of the range, during the emplacement of the Aconcagua fold-and-thrust belt, accommodating c. 30 km of backarc convergence (Giambiagi and Ramos, 2002). In a third stage (8.5-4 Ma), Paleozoic-Triassic basement thrust sheets of the Frontal Cordillera were accreted at the leading edge of the fold-and-thrust belt, accommodating c. 32 km of backarc convergence, synchronic to out-of–sequence deformation within the hinterland of the belt. During the latest stage (<4 Ma) deformation reached the Present day foreland region and the Main Cordillera gained most of its current elevation (Giambiagi and Ramos 2002). During this stage, deformed foreland deposits of previous events are incorporated to the tip of the orogenic wedge accommodating c. 6 km of convergence (82 km total; Farías et al., 2010). At the latitudes of the Precordillera (~30ºS-32ºS; Fig. 1), synorogenic deposits have been as well faulted and incorporated into the deformation front suggesting an ongoing forward propagation of the orogenic wedge (Vergés et al., 2007). Active deformation along the eastern front has been recorded at the flanks of basement uplifts of the San Rafael Block south of 33.5ºS (e.g., Sagripanti et al., 2015), and north of 33.5ºS at theSierras Pampeanas (e.g., Alvarado and Ramos, 2011) (Fig. 1).

III. Analogue model setup

[16] By means of a single s-point sandbox experiment we show the long-term evolution (equivalent to millions of years) of two oppositely facing, doubly vergent subduction wedges, growing at different rates of accretion (Fig. 2). The model was repeated 4 times thus validating its reproducibility. Our model setup (Fig. 2) is based on the original subduction slot experiment of Malavieille (1984), with the addition of a second slot and Mylar sheet to match the subduction advance setting. The device consists of a box with glass walls, inside which two Mylar sheets at the base are pulled in opposite directions beneath the modeling surface, carrying a homogeneous sand layer from the hopper to the rest of the box (Fig. 2A). Between the sheets, a narrow (150 mm-long) median plate remains stationary. Therefore, the setting accounts for the subduction of two mobile lower plates at both sides of a narrow and stable upper plate in a three-plate or subduction advance configuration (e.g., Brooks et al., 2003). The left and right sides of the model thus represent the subduction of the Nazca plate beneath the leading edge of the continent and the subduction of the South American basement along the Andean retro arc. The scaling factor used in the experiment is $L^*=10^{-5}$, meaning that 1 cm in the model represents 1 km in nature (cf. McClay et al., 2004).

[17] The quartz sand used in our experiments has a linear Coulomb behavior with an angle of internal friction of 37.8º (friction coefficient of 0.77). Quartz sand mixes have been widely used to simulate the brittle behavior of the upper crust in accretionary wedges and fold and thrust belt experiments (Cowan and Silling, 1978; Malavieille, 1984; Storti et al., 2000; McClay et al., 2004; Konstantinovskaya and Malavieille, 2011). In these experiments, the sand has been assumed to be essentially cohesionless but, in reality, it displays a low apparent cohesive strength due to irregular grain size, surface roughness effects or dense packing (Lohrman et al., 2003; Buiter, 2012). This apparent cohesion results in strain localization, in form of small, fault-like structures developed in most sandbox experiments. In our model setup, cohesion has been removed from the sand layer when carried onto place: a shear band with a normal sense of displacement is generated in the interface between the hopper and the modeling surface (Fig. 2A). In this way, the complete sand layer flows onto place and is brought to failure passing the aforementioned interface before convergence is applied. The sand has therefore already been subject to strain hardening, subsequent softening and decompaction (Lohrman et al., 2003), to remain in a state looser than critical throughout the experiment. Cohesion in the media is then negligible, in full consistency with the critical taper wedge model (Davis et al., 1983) and thus represents the large-scale kinematics of deforming wedges.

[18] Before the initial phase of the model (prior to t_0 in Fig. 3), a thin (15 mm) crust is accreted from the left side at V = 10 mm/step towards s-point S_1 to form the Coastal wedge, while a thick (30 mm) crust will be accreted from the right in the following phases (t_1 and t_2) at V = 5 mm/step towards S_2 to form the Cordilleran wedge (Fig. 3; Video DR1). These values yield accretionary rates of 125 mm^2/step and 150 mm^2/step for the western and eastern sides, respectively, meaning that the Cordilleran wedge will grow 1.2 times faster than the Coastal wedge. At t_1, the left side of the model will be deprived of material to be accreted, so the accretionary flux of the Coastal wedge will become null. In contrast, the Cordilleran wedge will grow at a constant flux throughout. Descriptions of the PIV and strain analysis are provided in Appendix 1. Image treatment steps can be visualized in Video DR2.

IV. Model Results

[19] As the orogenic wedges of the model are grown at different moments of the run for the purposes of the experiment, we first provide a general description of the evolution of the experiment, and second, we describe in detail the growth and deformation of each wedge developed in the model.

[20] Before t_0, an initial Coastal wedge is grown by 266 mm of convergence and accretion of the thin section of the left side of the model, adjacent to a non-deformed region (Fig. 3, Fig. 4, Fig. 5 and Fig. 6, t_0). Immediately after t_0, convergence at the right side initiates at a lower convergence rate but higher accretionary flux regarding the left side and in opposite direction (Fig. 3, Fig. 4, Video DR1). At t_1, a second, larger Cordilleran wedge has grown by 137 mm of convergence and accretion of the thick section on the right side of the model (Fig. 3). Also at t_1, the left side becomes deprived of material available for accretion into the Coastal wedge, analogous to a sediment-starved subduction trench. At t_1, the wedges are separated by a topographic basin and have a similar size despite the lower convergence applied on the right side. At t_2, convergence at the right side is about 4 times greater than in t_1 and the Cordilleran wedge has become about 4 times wider than in the prior stage of the run (t_1). The topographic basin has now been overridden by the Cordilleran wedge retro side, which has expanded far enough to merge with the counterpart of the Coastal wedge (t_2 in Fig. 3). At this moment, the coalescence of the two wedges of t_1 has led to the formation of one larger wedge which deformation is mainly driven by the accretion of material from the right side of the model.

[21] Deformation in each wedge occurs simultaneously in associative compressive flow and is accretion-driven, as depicted by the instantaneous strain rates and velocities (Fig. 3, Fig. 4 and Fig. 5 and Fig. 6, Video DR1). Immediately after convergence is applied, the stress singularities at S_1 and S_2 lead to failure of the respective sand layer and the formation of two pairs of conjugate slip lines, step-ups, or shear bands (Fig. 3, Fig. 4, Fig. 5). As material is accreted from the pro sides, the shear bands rotate outward bounding a central region that becomes uplifted. Accretion at the pro sides occurs simultaneously at the toe and at the base and leads to growth of the wedge by internal deformation to maintain a critical shape. Deformation begins to propagate beyond the initial slip line as the layer begins to shear on multiple detachments developing on the base of the pro sides. When the wedges are distinctively asymmetric, material is flowing from the pro wedges into a central core region that is translated up the hanging walls of the retro shears (Fig. 3, Fig. 4). At this stage, material is accreted at the base of the retro wedges, which also grow at critical taper. The instantaneous strain rates at the pro and retro shear bands have equal magnitudes. However, the cumulative deformation is highly asymmetric because of the accumulation of material at the retro wedge after being transported across the pro side and above the singularity.

[22] The high cumulative strain in the retro shear zones contrasts with the resulting distributed finite strain in the pro wedges and uplifted cores (Fig. 3, Fig. 5). At the retro sides and uplifted cores, material is accommodated by a combination of localized retro-thrusting, uplift and rotations of the wedge core above the retro shear band. The subhorizontal extension directions of the deformation ellipses (Fig. 5) indicate shear stretching at the core of both wedges. On the other hand, subvertical directions dominate the pro and retro sides, indicating shear shortening in association with vertical thickening (Fig. 5). Shear band geometries in our model are equivalent to those estimated analytically and numerically (e.g., Davis et al., 1983; Willett et al., 1993), and are in agreement with a Coulomb rheology.

[23] In the Coastal wedge, strain rates and velocities drop to the lowest values of the experiment when no more material is accreting at its toe (t_1 and t_2 in Fig. 3A, Fig. 4, Fig. 5). This highlights the importance of mass incorporation in the growth and deformation of a subduction wedge. Despite the absence of available material for accretion, the imposed basal traction is still sufficient to maintain the wedge stable at very low strain rates. The model forearc high is thus preserved and the shear band pair of this wedge is still generated at S_1 at low strain rates (Fig. 3A and Fig. 5).

[24] The variations in displacement rates for adjacent increments of shortening (Video DR1) suggest that shearing in the model is stick-slip and occurs simultaneously in all shear bands. Velocity vectors in the model pro-sides are large and almost horizontal during active accretion, with magnitudes consistent with the imposed kinematics and decreasing from pro-side to retro-side (Fig. 3A, Fig. 4A). Towards the rear, horizontal velocities reach minimum values, and an important increase in the vertical component towards the wedge core and retro-side accounts for fast uplift and progressive rearward surface tilting of the retro-wedges (Fig. 3A and Fig. 4A). In the case of the Coastal wedge, where there is no active accretion after t_0, velocities decrease to minimum values and instead of expansion, there is a slow migration of the entire wedge towards its rear. In the case of the Cordilleran wedge, pro side expansion has an approximate rate of ~4.5 mm/step while the retro side expands at an approximate rate of ~0.8 mm/step. This means that the model pro side deformation front expands almost proportional to the convergence rate, and that the retro side does so at a much slower ratio of approximately ~1:5.

[25] At t_2, the retro side of the Cordilleran wedge has expanded far enough to merge with its counterpart of the Coastal wedge. The area of wedge coalescence is characterized by the intersection of the retro shear zones. Strain rates of the retro side of the Coastal wedge are diffuse due to the lack of active accretion at its toe, thus deformation in this moment is mostly localized at the retro shear of the larger Cordilleran wedge (Fig. 3A; Fig. 5). The velocity field in the zone of coalescence denote rearward displacements beneath the Cordilleran retro shear (Fig. 4B); the retro side has in fact detached from the base and is being displaced towards the rear as expected at high accretionary fluxes (e.g., Willett et al., 1993). Strain directions indicate that deformation as well is transferred into the retro side of the Coastal wedge when the Cordilleran wedge detaches from its retro-shear zone, as shown in t_2 (Fig. 3A and Fig. 5; Video DR1).

[26] Another important aspect of wedge deformation is shown by the kinematic vorticity number W_k (Fig. 3B and Fig. 6), also known as the curl of the velocity field. The kinematic vorticity represents a measure of the external vorticity inside the wedges, which is accommodated at the local scale by a combination of rigid-body rotations (or spin) and shear-induced rotations (or internal vorticity; Feehan and Brandon, 2004). W_k is also a measure of the coaxiality involved in the deformation history of the material (Means et al., 1980). In the model, high values of $|W_k|$ (>>1) indicate non-coaxial (simple shear) and pulsating histories of deformation, meaning that material lines being extended at given parts of the wedge may shorten in the following stages. Values of $W_k=0$ represent areas of coaxial deformation (pure shear), which are particularly concentrated in the shear bands (Fig. 3B and Fig. 6). The sense of rotation shown by the kinematic vorticity number is in agreement with a right-hand rule; when tractions are from the left, W_k is positive, and rotations are counterclockwise. On the contrary, clockwise rotations occur in regions of negative values of W_k when basal tractions are from the right. Across the pro sides, shear bands bound small domains of rotations, which shift polarity regarding the sense of rotation of the adjacent domain (Figs. 3B and 6). In the retro sides, the rotations are contrary to the dominant sense of the rotations in the pro-sides.

V. Discussion

V.1. Model interpretations

[27] Critical taper theory (Davis et al., 1983) provides a simple explanation for the main features of our experiments. These include the development of the deformation patterns, strain rate distribution, and overall geometry. The characteristics of the pro and retro wedges result from different mass flux directions with respect to the S-point. Accordingly, the pro wedge grows by frontal accretion at a minimum permissible taper and the retro wedge does so by material added at the back, having a maximum permissible taper or repose angle (Willett et al., 1993). In the case of the model Cordilleran wedge, the incorporation of material at its toe reduces the pro side taper constantly, which causes a lack of bulk strength of the entire wedge to slide above the basal subduction thrust and expand responding to the imposed convergence (stress buildup). Consequently, the wedge deforms internally at high strain rates to thicken and increase its taper and therefore it becomes able to slip above the basal detachment. The model Coastal wedge, in turn, grows in self-similar fashion by accretion at its toe until there is no material input, and, at this point, it evolves as a stable wedge. It is able to slip continuously on its base with very low material velocities and deformation rates, with no major changes in size and shape (Fig. 3; Video DR1). The contrasting strain rates in each side of the model emphasize the dependence on material accretion in deforming subduction wedges (Fig. 4; Video DR2).

[28] The velocity field of the model (Fig. 3A and Fig. 4) yields a similar trend regarding the theoretical solutions for low-Reynolds number flows against a corner with a given angle

(Batchelor, 1967). In our case, the retro-shear band of each wedge act as rigid boundaries for accreting material, above which the sand flows upward and rearward towards the wedge surface (Fig. 4A and Fig. 5). This flow is similar to that observed in the accretionary wedge of Cowan and Silling (1978), with the distinction that there is no predefined backstop in our model. Instead, the shape of the rigid boundary in our model wedges is given by the internal friction of sand defining the retro shear above the flat-lying backstop of the modeling surface. As inertia forces are considered negligible for highly viscous media, and as the motions in the model are induced by traction of the underlying plate, the kinematic and boundary conditions accounted in the approach of Batchelor (1967) are the same as those in our experiment. The pattern of flow in our model can thus be considered analogous to the overall sense of material transport within accretionary prisms and fold-and-thrust belts (Cowan and Silling, 1978; Willett et al., 1993).

[29] The kinematic vorticity number (Figs. 3B and Fig. 6) indicates that external, solid body rotations are ubiquitous in subduction wedges subject to ongoing shear tractions. We highlight the fact that despite the lack of available material for accretion in the model Coastal wedge, the kinematic vorticity number is similar to the larger wedge of the model. This is a relevant aspect for wedges that develop without significant accretion at the toe in erosive margins. Such motions in our model agree with particle trajectories observed in numerical wedges developed in a sediment-starved trench (Van Dinther et al., 2012), and with thermo-mechanical models applied to the Andean margin in which rotations in the forearc high are coupled with the down going motion of the slab (Gerbault et al., 2009).

V.2. Limitations

[30] There are several inherent limitations to the analogue modeling approach that need to be discussed before a comparison with the Andean orogen. The rigid character of the base of our modeling device does not allow simulating the effects of isostatic or flexural compensation due to structural loading. As shown in numerical experiments, isostatic compensation modifies the taper and basal thrust angles of a subduction wedge and leads to the development of flexural basins beyond the wedge margins. Furthermore, isostatic and flexural effects may lead not only to the deepening of the s-point due to wedge thickening, but also, a lateral movement of the entire subduction wedge may be expected. However, the displacements and deformation pattern developed in numerical subduction wedges, with and without the effects of flexure remain rather constant (Willett et al., 1993). Additionally, wedge symmetry (i.e., similarity between the retro and pro wedge) can be influenced by the effects of surface erosion (Willett, 1993), different friction coefficients of the basal detachment of the retro and pro wedge (Buiter, 2012) and obliquity of convergence (McClay et al., 2004). We do not explore the effects of net material influx into the wedge system, which will depend on the amount of material that is subducted versus the material being accreted (Waschbusch and Beaumont, 1996). Our experiments are developed under the assumption that all materials of the upper crust are accreted into the wedge system.

[31] The effects of erosion combined with bed-parallel anisotropies enhance and localize exhumation in analogue (Malavieille, 2010; Konstantinovskaya and Malavieille, 2011) and numerical (Willett et al., 1993) models, with a sense of material transport similar to the observed in our experiments. Sedimentation modifies fault spacing and promotes generation of piggy-back basins in model fold-and-thrust belts, but the first-order structure is still comparable with our model results (e.g., Storti et al., 2000). Other modeling limitations not addressed in our experiments are the presence of asperities or irregularities (promontories, aseismic ridges) in the subducting plate modifying the structural grain generated in the upper plate and, as well, eroding the leading edge of the overlying wedge (e.g., von Heune and Scholl, 1991).

[32] Despite these limitations, our analogue orogenic wedges show similarities in the first order with the wide variety of equivalent wedge models developed in scaled analogue experiment and numerical s-point models applied to different orogens (see Buiter, 2012 and Jamieson and Beaumont, 2013 for reviews). Similar features are the initial symmetric failure subsequent asymmetric development of critically tapered pro and retro sides, and the development of a single retro shear and multiple pro shear zones (Fig. 3., Fig. 4; Fig. 5 and Fig. 6). Strain localization in fault-like and fold-like structures, as seen in analogue experiments are not visualized in our model as deformation is distributed and continuum.

V.3. Model application: the Andean orogenic wedges

[33] Natural doubly-vergent subduction wedges, either subaerial or submarine are considerably more complex than the sandbox models shown in this paper. The inherent limitations of the approach added to the factors outlined in the previous section and their interactions (e.g., tectonic and surface processes interplay) are all likely to increase the complexity of the kinematics, structural architecture and overall evolution of a natural subduction wedge system. Nonetheless, the purpose of our experiments was not to replicate or simulate in detail the structural evolution of the Andean margin, but instead to demonstrate that some general features and processes characterizing this orogen can be developed under a basic geodynamic framework of subduction advance. Previous works have illustrated the affinity of similar natural systems with analogue sand wedges (e.g., European Alps - Malavieille, 2010; Pyrenees – Storti et al., 2000; Mediterranean Ridge – Storti et al., 2000; Taiwan – Malavieille and Trullenque, 2009; Malavieille, 2010). In the following paragraphs, we review the geological and geophysical evidence that supports the application of the subduction wedge concept to the Central and Southern Central Andes.

V.3.1. Coastal Cordillera of Central and Northern Chile

[34] Along northern (Fig. 1 and Fig. 7) and central Chile (Fig. 1 and Fig. 9), the Coastal Cordillera has been developing in response to the subduction of oceanic lithosphere (Phoenix, Chasca, Farallon and Nazca plates; Seton et al., 2012) beneath western South America since the Carboniferous (Oliveros et al., 2019). Crustal-scale cross sections from northern and central Chile (Fig. 8 and Fig. 10) show the first-order structure of the subduction complex, consisting of a well-developed, mostly submerged pro wedge, an emerged axial zone and narrow retro wedge inland. The pro wedge has developed above the subduction mega thrust, or pro shear, which reaches the down-dip limit of frictional detachment at ~60 km of depth (S-point), right below the maximum elevations of the forearc high (Fig. 10A; Comte et al., 2019). A major retro-vergent thrust bounds the wedge to the east, interpreted as the retro shear of the subduction complex in northern (Fig. 8; David et al., 2002; Farías et al., 2005) and central Chile (Fig. 10A; Comte et al., 2019). In the eastern border of the Coastal Cordillera of central Chile, outcrops of late Cretaceous proximal clastic deposits associated with east-vergent, positively inverted, high-angle structures suggest a protracted compressive deformation in this region and the presence of a late Cretaceous-early Cenozoic foreland basin east of the Coastal Cordillera (Boyce, 2015). Above the retro wedge, a regional east-dipping homoclinal backfold is marked by Mesozoic back arc and arc deposits (Fig. 10; Rodriguez et al., 2018; Comte et al., 2019). Large backfolds are a common feature of subduction complexes, such as the Great Valley sequence above the Franciscan metamorphic complex (e.g., Silver and Reed, 1988) or the east-vergent backfold of the Cascadia subduction wedge (Brandon, 2004). Therefore, the Coastal Cordillera have been interpreted as a subduction wedge complex with both basal and frontal accretion expected to occur in the upper plate (Comte et al., 2019).

[35] Compressive focal mechanisms and earthquake distributions below the central Chile Coastal Cordillera suggest that current accretion would be mostly occurring at the base of the subduction complex (Fig. 10A; Comte et al., 2019). Evidence of underthrusting and reverse faulting above the subduction thrust coupled with morphological and stratigraphic evidence along the northern Chile forearc as well support a mechanism of uplift driven by the accretion of material removed by subduction erosion, through subcrustal duplexing beneath the forearc (Fig. 8; Hartley et al., 2000). This mechanism is supported by evidence of sustained coastal uplift and surface normal faulting in central Chile (Fig. 8 and Fig. 10A; Saillard et al., 2009) above the axial zone of the underlying wedge, and by the fact that small modern accretionary prisms are developed in the leading edge of the continental plate with dominant normal faulting. In fact, current frontal accretion at the Coastal ranges is small as indicated by the accretionary flux. Sediment thicknesses in the trench are <0.5 km north of 33.5ºS (Fig. 7 and Fig. 9; Bangs and Cande, 1997) increasing to maximum values of ~2 km to the south (33.5º-45ºS). The convergence velocity of the Nazca plate is of c. 69 km/Myr orthogonal to the subduction trench. These values yield current accretionary fluxes of ~34.5 km^2/Ma and 138 km^2/Ma for both segments assuming that all material in the trench gets accreted to the wedge toe. This means that the Coastal Cordillera in its non-erosive segment (south of 33.5ºS) is growing at similar rates compared to other active ocean-continent subduction complexes (e.g., ~125 km^2/Ma in the Nankai subduction zone; Fuller et al., 2006), but at much slower rates along the erosive segment (north of 33.5ºS). Because precipitations highly influence trench infill, and that current climatic conditions may have precluded modern orogeny in the Andes (e.g., Strecker et al., 2007), we infer that the Coastal Cordillera has grown at similar accretionary fluxes and would have therefore remained stable during most of the Neogene.

[36] The template of our analogue model shows similar structural features, sense of material displacement and rotations as those observed in the Coastal Ranges (Fig. 4; Fig. 5; Fig. 8). According to our model, sustained tilting and accretion at the base of a subduction wedge remain active even in absence of accreting material at its leading edge. Such situation is equivalent to the evolution of the Coastal wedge of our experiment, which evolves stable in absence of material to be accreted during fast growth of the Cordilleran counterpart. The inferred top to the left motions within the subduction complex underlying the Coastal ranges (Comte et al., 2019) agrees with our model results (Fig. 8), with numerical subduction wedge models (Gerbault et al., 2009; Van Dinther et al., 2012) and to the shear sense interpreted for the paleo-accretionary prisms emplaced in the Coastal Ranges of southern-central Chile (e.g., Richter et al., 2007). We therefore suggest that the lack of available sediments for frontal accretion leads to a recycling of materials from the leading edge of the subduction wedge, and to its posterior accretion at its base.

[37] This mechanism has been proposed for the northern Chile forearc by Hartley et al. (2000) and Farías et al. (2005). In this respect, another important aspect, not addressed in our experiments is that the lack of accruable sediments in natural systems usually exposes heterogeneities over the oceanic slab floor, which has been ascribed to cause subduction erosion of the upper plate. This process in fact has been proposed for the Andean margin to have occurred since Jurassic times given a protracted landward arc migration (Rutland, 1970). As described by Comte et al. (2019), this process of material recycling will induce the migration of the S-point towards the retro side (a process not reproduced by our experiment) and might contribute to the coalescence of the Coastal Ranges wedge with the wedge underlying the inner Cordillera. In any case, in lack of incoming accruable sediments above the subducting plate, the state of stress within the Coastal wedge seems to be controlled by spatial variations of the basal mechanical parameters in the down-dip direction of the wedge base, with an influence over adjacent morphostructures reaching only the inner forearc region (Adam and Reuther, 2000), rather than exerting a greater control upon orogenic deformation inland (e.g., Lamb, 2006).

V.3.2. Inner Cordilleras of the Central and Southern Central Andes

[38] The inner Cordilleras of the Central and Southern Central Andes have been formed by westward retro arc convergence of the South American plate (Isacks, 1988; Russo and Silver, 1996) since the Late Cretaceous and throughout most of the Cenozoic (e.g., Horton and DeCelles, 2001; McQuarrie et al., 2005; Bascuñán et al., 2016; Fennell et al., 2017; Henríquez et al., 2019). Well preserved syntectonic deposits, excellent exposures, earthquake distribution, seismic tomography and reflection seismic profiles have allowed the detailed reconstruction and analysis of fault geometries and kinematics within the belt at the latitudes of the Altiplano and Puna (Baby et al., 1997; Kley et al., 1999; McQuarrie, 2002; Victor et al., 2004; Farías et al., 2005; Anderson et al., 2017; Martínez et al., 2015; 2021) and central Chile and Argentina (Ramos et al., 2004; Farías et al., 2010; Giambiagi and Ramos, 2002; Giambiagi et al., 2014; Riesner et al., 2018). The resolution limits and age constraints generally allow detailed reconstruction of thrust displacements through time in both flanks of the inner Cordillera of the Central and Southern Central Andes (e.g., Baby et al., 1997; McQuarrie, 2002; Victor et al., 2004; Farías et al., 2005; McQuarrie et al., 2005; Giambiagi et al., 2014; Riesner et al., 2018; Anderson et al., 2017). The internal architecture of the Central Andes at ~19°S-21°S and Southern Central Andes at 30°S and 33.5°S provide the models that can be compared to our experimental results.

V.3.2.1. Central Andes (~19°S-21°S)

[39] The crustal architecture beneath the Central Andes at ~19°S-21°S (Fig. 7) consists of a large plateau, composed by two, doubly-vergent wedges, distinct laterally at the scale of the orogen (e.g., Martinod et al., 2020). One crustal wedge underlies the Forearc Precordillera, Western Cordillera and western Altiplano (western flank of the Altiplano; Fig. 7 and Fig. 8), whilst a larger crustal wedge underlies the eastern Altiplano, Eastern Cordillera, Interandean zone and Subandean Sierras (eastern flank of the Altiplano; Fig. 7 and Fig. 8). Each wedge underlying the flanks of the Altiplano evolved synchronously during most of the Neogene, although the earlier establishment of fold-and-thrust belts below each flank appears to be diachronic (McQuarrie et al., 2005; Martinod et al., 2020). The main vergence of the wedges is to the east, as they have developed in association with westward subduction of the South American basement. According to our interpretation it is possible to identify the pro and retro side of each wedge in the structural models (Fig. 8).

[40] We point out that the situation described above, in which two orogenic wedges flank the plateau differs from our experimental results (one large wedge represents the inner Cordillera of the Central Andes). However, we do not intend to reproduce the specific tectonic scenario of the Central Andes, but to demonstrate the applicability of a wedge model for the orogen and the influence of accretionary flux upon lateral wedge expansion. We will return to this point further below.

V.3.2.1.1. Western Altiplano wedge

[41] The Altiplano western flank is a doubly-vergent thrust belt formed by convergence between the South American basement and the Andean forearc since, at least, the Late Cretaceous (Horton and DeCelles, 2001; McQuarrie et al., 2005; Horton, 2018). The crustal architecture consists of two, oppositely verging wedges, arranged back-to-back. The retro wedge is narrower and lies upon the South American forearc (Victor et al., 2004; Farías et al., 2005), whilst the pro wedge overlies the subducted South American lithosphere transferred from the east below the Altiplano upper crust (Beck and Zandt, 2002). As in our models, deformation in the retro wedge has focused on a major retro shear corresponding to the West-vergent Thrust System of the Forearc Precordillera (WTS in Fig. 8; Muñoz and Charrier, 1996). The retro wedge has been active through most of the Neogene and after 8 Ma expanded towards the west by progradation of the WTS (Farías et al., 2005), in synchronicity with thrust sheet emplacement at the Subandean Sierras (Baby et al., 1997; McQuarrie, 2002). Monoclinal folds of the WTS have generated westward-fanning growth strata recording up to c. 2,6 km of regional uplift since c. 16 Ma (Victor et al., 2004; Farías et al., 2005). Despite this important uplift, the accommodated tectonic shortenings are moderate, with values of ~2.5 km at ~21°S (Victor et al., 2004) and of less than 7 km at ~18°S (Charrier et al., 2013). Western Altiplano uplift has also been accommodated by westward (counterclockwise) tilting of the forearc (Farías et al., 2005; Riquelme et al., 2007), consistent with retro wedge top-to-left rotations in our experiments (Fig. 3; Fig. 6).

[42] In the pro wedge, similarly to our models, deformation has been distributed on a major pro-verging ramp (Fig. 8). The pro wedge outcrops at the eastern border of the Western Cordillera, where well preserved late Oligocene to late Miocene eastward-fanning growth strata allow detailed structural analysis and reconstruction of an East-vergent Thrust System (Cortés et al., 2012; ETS in Fig. 8), which development was synchronous to tectonic activity within the WTS (Herrera et al., 2017). The ETS corresponds to the internal zone of the pro wedge thrust belt that extends further east below the Altiplano basin infill (McQuarrie, 2002; Horton et al., 2001). Both thrust systems (WTS and ETS, Fig. 8) are thought to be rooted at a mid-crustal main detachment that would correspond to the pro shear of the western Altiplano wedge (Altiplano Low Velocity Zone ALVZ in Fig. 8; Victor et al., 2004; Farías et al., 2005).

[43] Despite the mostly Neogene history of uplift in the Altiplano western flank, less well documented Paleogene and late Cretaceous contractional events suggest a protracted character of thrust belt development in this region. Seismic reflection profiles in the Forearc Precordillera at ~20°S illustrate the synorogenic character of late Cretaceous to middle Miocene sedimentary sequences within buried segments of the west-vergent thrust system (Martínez et al. 2021). In the Atacama basin (~23°S) evidence of exhumation, foredeep and wedge-top sedimentation, associated to the eastward migrating thrust belt has been dated as late Cretaceous (Bascuñán et al., 2016; Henríquez et al., 2019). In the western Altiplano at 19°-21°S, foreland sedimentation was rather continuous during the Paleogene, with peaks of foredeep sediment accumulation accompanied by high subsidence rates in the middle Eocene (Horton et al., 2001; Charrier et al., 2013). Moreover, angular unconformities in the Western Cordillera at ~19°S indicate late Eocene thrusting, prior to Miocene synorogenic sedimentation and volcanism (Herrera et al., 2017). The distribution of shallow seismicity below the WTS suggests that the system is currently active (David et al., 2002; Farías et al., 2005).

[44] The accretionary flux entering the western Altiplano wedge can be estimated using thickness of the accreted sections into the pro wedge and shortening rates as they represent a first approximation for rates of convergence. The west-dipping detachments at which the ETS is rooted reach depths of c. 12 km (Cortes et al., 2012) above the Altiplano Low Velocity Zone (Yuan et al., 2000; Victor et al., 2004; Farías et al., 2005) a value consistent with the estimations of McQuarrie (2002) for the westernmost Altiplano. Considering a total shortening of ~8 km accommodated in the last 30 Myr (Victor et al., 2004; Cortés et al., 2012), the shortening rate, without considering increments or decelerations through time, is of 0.26 km/Ma taking into account the detachment depths outlined above. Consequently, a first approximation to the accretionary flux yields a low value of 3.2 km^2/Ma (96 km^2 added by accretion in 30 Ma). Present crustal area below the Western Cordillera is in the order of 5500 km^2 achieved during most of the Cenozoic (Fig. 8). We note that this low accretionary flux alone cannot account for current thickness of the crust below the Western Cordillera. We suggest that most of the crustal area has been incorporated below the western Altiplano wedge by underplating, or basal accretion associated to westward ductile flow of the South American lithosphere (Isacks, 1988; Farías et al., 2005).

V.3.2.1.2. Eastern Altiplano wedge

[45] The Altiplano eastern flank is a thrust belt formed by convergence between the South American margin and the Brazilian craton since Eocene times (Horton and DeCelles, 2001; McQuarrie, 2002; Horton, 2018). The crustal architecture consists of two oppositely verging wedges arranged back-to-back. The narrower retro wedge lies upon the Altiplano crust and the pro wedge overlies the underthrust Brazilian craton (Fig. 8; Baby et al., 1997; Beck and Zandt, 2002; McQuarrie, 2002). In the same way as in subduction wedge models and in our experiments, retro wedge deformation concentrates on a back-thrust zone (western Eastern Cordillera) whilst deformation of the pro wedge is distributed above a well-developed basal detachment below the external Eastern Cordillera, Interandean Zone and Subandean Ranges (Baby et al., 1997; McQuarrie, 2002; Anderson et al., 2017).

[46] Proposed mechanisms of crustal accretion into the eastern Altiplano wedge mainly include frontal accretion along the Subandean Ranges accompanied by basal accretion focused below the Eastern Cordillera and easternmost Altiplano (Fig. 8; Baby et al., 1997; McQuarrie, 2002; Anderson et al., 2017). The cited structural reconstructions indicate basal accretion in form of anticlinal stacks below the Eastern Cordillera and Interandean Zone. The development of anticlinal stacks near the wedge S-point is not observed in our models but has been illustrated in sandbox experiments with high basal friction and localized erosion on the pro wedge (Malavieille, 2010; Konstantinovskaya and Malavieille, 2011; Malavieille et al., 2019). Balanced cross-sections also suggest that the oppositely-vergent thrust belts of the eastern Altiplano began to develop near the basal velocity discontinuity in middle Eocene times (western edge of the Brazilian shield; McQuarrie et al., 2005), with a symmetrical propagation to the west and east (33-10 Ma) until thrusting became chiefly foreland-ward after 10 Ma (Anderson et al., 2017).

[47] The accretionary flux entering this segment of the Andes is the highest along the strike of the range. Depth to the main detachments beneath the pro wedge toe provide the thickness of the accreted section. The reconstructions of Baby et al. (1997), McQuarrie (2002) and Anderson et al. (2017) all estimate depths of ~15 km for the detachment below the pro wedge tip. Total retro arc convergence accommodated by the eastern Altiplano wedge has been estimated between 200 and 330 km since c. 40 Ma, yielding rates of 5 to 8.25 km/Ma (McQuarrie, 2002; Anderson et al., 2017). Considering the simplification that the depth to detachment of the wedge tip was constant through time, the simple accretionary flux calculation yields minimum and maximum values of

~75 km^2/Ma and ~124 km^2/Ma entering the wedge, respectively. If current GPS velocities of the Brazilian shield are used (i.e., 11 km/Ma; Brooks et al., 2011), the estimate of accretionary flux is of 165 km^2/Ma. These values are high in comparison to accretionary fluxes estimates for other subduction zones: the European Alps have grown at a rate of ~75 km^2/Ma, whilst in the Makran subduction zone (upper boundary for accretionary fluxes at convergent margins), accretionary fluxes reach 210 km^2/Ma (Brandon, 2004).

V.3.2.2. Southern Central Andes (~30°S and ~33.5°S)

[48] In central Chile and Argentina (Fig. 9), the crustal-scale structure beneath the Main Cordillera consists of two, oppositely verging wedges arranged back-to-back: the pro wedge is wider and overlies the subducted South American basement, while the retro wedge lies upon the forearc portion of the South American plate (Fig. 10). As in our models, deformation in the retro wedge is mostly focused on a main retro verging shear. This structure outcrops along the western Andean front at ~33.5°S, corresponding to an east-dipping, seismically active high-angle thrust (San Ramón thrust in Fig. 10B; Armijo et al., 2010; Farías et al., 2010; Vargas et al., 2014; Ammirati et al., 2019). At ~30°S the structure is not exposed, but has been interpreted to intersect the retro shear zone of the Coastal Cordillera subduction complex below the inner forearc (Fig. 10A; Comte et al., 2019). Below the eastern side of the range, a well-developed basal detachment underlies the pro wedge, and corresponds to the main structure above which basement-involved thrust sheets have been accreted. At ~30°S, it involves the La Ramada fold-and-thrust belt, the basement composed Frontal Cordillera and is actively accreting Cambrian to upper Paleozoic sequences in the Precordillera (Brooks et al., 2003; Mescua et al., 2016) with deformation reaching farther inland throughout the Sierras Pampeanas (e.g., Alvarado and Ramos, 2011; Ammirati et al., 2013). At ~33.5°S, a mid-crustal detachment with flat-ramp geometry has been geophysically determined by Farías et al. (2010) (MCD in Fig. 10B). Despite the fact that compressive tectonic events in the inner Cordillera have been tracked to the late Cretaceous at higher latitudes (~34.5°S; Fennell et al., 2017) but the establishment of current fold-and-thrust belt kinematics has been constrained to the early Miocene (Ramos et al., 2000; 2004).

[49] Modern orogenic deformation in this region began in the late Eocene – early Miocene (~22 Ma), with the inversion of the Abanico basin along the western Main Cordillera (Farías et al., 2010; Giambiagi et al., 2014). A similar age has been established for the Chilean Andes at ~30°S (Rodríguez et al., 2018). The structures that bounded the western side of the Abanico basin to the west are part of the same structural system in which the San Ramon thrust has been included (Farías et al., 2010). The inversion of these group of structures limited great part of the westward deformation in the belt and syntectonic sedimentation of the Farellones Formation (21.6-16.6 Ma) developed within the Abanico basin swath. It is thus inferred that the western deformation front and central valley have remained tectonically stable since the onset of inversion of the Abanico basin (22 Ma; Farías et al., 2010). Until c. 16 Ma, the shortening was accommodated by inversion of the Abanico basin under pure shear compressive conditions until it propagated towards the east when simple shear conditions (top to the right) became dominant resulting in fold-and-thrust belt (Farías et al., 2010; Giambiagi et al., 2014). We therefore suggest that the western side of the Andes at these latitudes correspond to the structural lid of the orogenic wedge, this is, the tapered leading edge of the overriding plate that got passively involved in wedge deformation and shouldered aside to the rear of the wedge (e.g., Brandon, 2004).

[50] Within the fold-and-thrust belt of the pro wedge, structures developed in forward sequence, with great influence of Mesozoic rift structures and concomitant to continuous deformation in the western side (Giambiagi and Ramos, 2002; Giambiagi et al., 2014). Depth of the main fold-and-thrust belt ramp detachment is of c. 20 km below the western Main Cordillera and of c. 15-10 km beneath the Argentine side (Farías et al., 2010; Giambiagi et al., 2014). The easternmost Frontal Cordillera is thrusted above a deeper (c. 30 km) detachment at the middle crust (Farías et al., 2010). Synchronous thrusting continues at Present, as shown by recent reverse displacements in the San Ramón thrust (Vargas et al., 2014), lateral displacements with compressive tensors in the arc region (Pardo et al., 2002; Farías et al., 2010; Ammirati et al., 2019) and with most crustal seismic moment being released in the Argentine foreland and Precordillera (Vergés et al., 2007; Alvarado and Ramos, 2011; Ammirati et al., 2013). The crustal geometries outlined above, and timing of deformation suggest that the Aconcagua and La Ramada fold-and-thrust belts correspond to the accretionary complex of the Cordilleran wedge, built by materials carried by the South American basement. As in our models, horizontal motions of accreted materials (in this case, shortening) are greatest in the pro side. Accretion at the base of the wedge focused on the Frontal Cordillera and on the Yeguas Muertas anticlinal stack, and, as well, must be occurring below the western side of the range to accommodate westward subduction (Giambiagi and Ramos, 2002; Farías et al., 2010;

Fig. 10C), whilst frontal accretion is occurring at the orogenic front beneath the wedge toe and proximal foreland.

[51] To obtain an estimation of the accretionary flux entering the Main Cordillera from the eastern foreland, we use the depth to detachments below fold-and-thrust belts and the onset of orogenic deformation constrained by Farías et al. (2010) and Giambiagi et al. (2014). With an overall shortening of 86 km accommodated by the range in the past 22 Myr (resulting in 3.9 km/Ma), and a depth to detachment of c. 15 km, we calculate a rough estimation of the accretionary flux of c. 58 km^2/Ma (~1300 km^2 accreted in 22 Ma). This value varies only slightly if considering the deeper detachment (~30 km) for the emplacement of the Frontal Cordillera during late Miocene times (8.5-4 Ma; Giambiagi and Ramos, 2002). The simple estimation indicates that Andean growth has been similar to that of the Cascadia (52 km^2/Ma; Brandon, 2004) and Taiwan (40 to 60 km^2/Ma; Malavieille et al., 2019) subduction wedges.

V.4. Vergence in the Southern Central Andes

[52] Beyond the objective of our paper is deciphering the vergence of the inner Andean Cordillera of the Southern Central Andes. However, our sandbox model well as other numerical and analogue approaches developed under similar boundary conditions (e.g., Malavieille, 1984; Willett et al., 1993; Beaumont et al., 2000; Storti et al., 2000; McClay et al., 2004) provide additional constraints useful to unravel the specific conundrum of tectonic transport in the region.

[53] A model of west-vergent Andean orogeny has been proposed by Armijo et al. (2010) and Riesner et al., (2018), in which a portion of the forearc is subducting eastwards below the Main Cordillera, synthetic to the Nazca plate. On the other hand, many studies (e.g., Giambiagi and Ramos, 2002; Ramos et al., 2004; Farías et al., 2010; Giambiagi et al., 2014) demonstrate that the polarity of retro arc subduction is westward, as in the Central Andes of northcentral Argentina and eastern Bolivia, with a dominant eastward directed tectonic transport (e.g., Bally et al., 1975; Isacks, 1988; Roeder, 1988; Kley and Monaldi, 1998; McQuarrie, 2002; Beck and Zandt, 2002). We note that models of westward growth of the Andes (Armijo et al., 2010; Riesner et al., 2018) have neglected shortening estimates for the Aconcagua fold-and-thrust belt published in pioneering works (see Fennell et al., 2017) estimations based on crustal balancing as well as the more recent structural reconstructions of Ramos et al. (2000; 2004), Giambiagi and Ramos (2002), Giambiagi et al., (2014). Additionally, Astini and Dávila (2010) offered a thorough summary of evidence contesting the proposal of westward Andean growth.

[54] The importance of a main retro-verging thrust for crustal wedge development has been highlighted in this work and in other models of subduction wedges. Retro wedge thrusting is active during all stages of crustal wedge development as it accommodates the space required for emplacement of material generated by retrocharriage (Malavieille, 1984; Silver and Reed, 1988; Waschbusch and Beaumont, 1996; Storti et al., 2000; Brandon, 2004). The Western Andean Thrust (Fig. 10B) has been subjected to focused deformation throughout modern orogeny since inversion of the Abanico extensional basin (e.g., Farías et al., 2010; Armijo et al., 2010; Riesner et al., 2018). We suggest that the predominant westward vergence of the Main Cordillera's western swath could likely be product of the initial stages of basement subduction. Initial overall vergence of a subduction wedge is downstream the direction of subduction, prior to the predominance of pro wedge distributed thrusting as observed in sandbox experiments (e.g., Storti et al., 2000) and structural reconstructions for other convergent orogens such as the Pyrenees (Beaumont et al., 2000) and in the early stages of growth of the Eastern Cordillera east of the Andean plateau (21°S; Anderson et al., 2017). Indeed, c. 22 km of shortening were accommodated below the western flank of the Main Cordillera at 22 Ma to 15 Ma, with a doubly, yet predominantly westward vergence before eastward-directed thrusting in the Aconcagua fold-and-thrust belt (Farías et al., 2010; Giambiagi et al., 2014).

[55] The hypothesis of an eastward direction of growth of the Main Cordillera is also supported by a large body of data. This evidence seems to fit a subduction wedge model, with a retro wedge facing westwards and a pro wedge facing eastwards. Miocene eastward migration of the Argentine thrust belts (Ramos et al., 2000; 2004; Giambagi et al., 2015), the asymmetry in tectonic shortening along both sides of the range (Ramos et al., 2000; Farías et al., 2010; Giambiagi et al., 2014), a progressive incorporation of synorogenic foreland strata to the toe of the thrust system and an eastward emergence of thrusts in the foreland (Vergés et al., 2007) all support a preferable eastward vergence of the orogenic wedge, with a mantle thrust dipping to the west above the subducting basement. Seismic tomography and earthquake distribution of the forearc defines a geometry favoring a westward direction of subduction below the range (Farías et al., 2010). The current direction and magnitude of the South American crustal velocity field match the convergence rates estimated by structural reconstructions (Brooks et al., 2003). We thereupon suggest that basement subduction in the Main Cordillera is from east to west, below a west-dipping mantle thrust, and with an overall eastward vergence. Considering the aforementioned, we find difficult to conciliate the available geological, geophysical, structural and geodetic data with the west-vergent model of Armijo et al. (2010) and Riesner et al. (2018).

V.5. Westward expansion of the Andean wedges

[56] We have illustrated that stress distribution and material velocity field in our experiments may have a correspondence in the Andean orogen. We therefore propose that the cross-sectional distribution of shortening and first order structure, from subduction trench to Andean foreland, is best explained by a model in which two crustal-scale subduction wedges grow antithetically at different rates of accretion. The Coastal wedge remains close to a steady state and is associated to a low accretionary flux along a starved subduction trench at a fast convergence velocity. On the other hand, accretion of a thick crustal section accounts for the fast lateral expansion of the inner Andean Cordillera. The northward increase in rates of accretion along the retro arc cause a progressive dominant foreland-ward widening of the range from south to north. Widening towards the west is slower given of the composite stress field resulting from the asymmetry in boundary conditions (westward basement subduction) resulting in the asymmetric overall expansion of the orogenic wedge. We propose that tectonic shortening and uplift of the Chilean Andes is strongly influenced by east to west retrocharriage in the orogenic wedge, creating the space for the accommodation of materials accreted into the eastern side. Certainly, orogens developed along advancing subduction zones are characterized by important backthrusting to accommodate material accretion (Silver and Reed, 1988; Waschbusch and Beaumont, 1996; Brandon, 2004).

[57] Our experiments illustrate how retro wedge expansion occurs both by backthrusting of material above the retro shear (Fig. 3) and by the detachment of the retro wedge base away from the singularity when convergence is high (Fig. 5B). Along the Andes, westward expansion of the inner Cordillera is more evident and marked especially in segments where shortenings, and therefore, the accretionary fluxes from the east are high. In the Altiplano segment, the westward progradation of thrusts, associated uplift and westward tilt of the Chilean forearc was synchronous to c. 200 km of westward basement subduction below the Eastern Cordillera and Interandean Zone, during the late Oligocene-middle Miocene (Victor et al., 2004; Farías et al., 2005; Charrier et al., 2013). Uplift and tilting along the West-vergent Thrust System continued during the late Miocene at lower rates, coeval to frontal accretion into the Subandean Sierras (Victor et al., 2004: Farías et al., 2005; Herrera et al., 2017). This synchronicity can be explained by the lateral ductile flow of the lower crust below the Altiplano, triggered by westward subduction of the Brazilian craton below the eastern flank. The ductile westward transfer of the lower crust leads to the accretion of material at the base of the Altiplano western flank, as illustrated by the models of Isacks (1988) and Lamb et al (1997) and demonstrated by the numerical models of Vietor and Oncken (2005).

V.6. Wedge coalescence in the Central and Southern Central Andes

[58] We have shown that distinct crustal wedges underlie the inner cordilleras of the Central and Southern Central Andes, developing parallel to the subduction zone. While the forearc high has been developing continuously since Paleozoic times, the younger wedges have been growing at faster rates since the late Cretaceous and throughout the Cenozoic. Mechanical models suggest that the increased accretion of material into a crustal wedge associated with protracted convergence leads to a transition from a small and cold wedge towards a large and hot wedge with dimensions of an orogenic plateau (e.g., Willett, et al. 1993; Jamieson and Beaumont, 2013). From this point of view, plateaus can indeed originate from one single crustal wedge progressively thickening and expanding laterally. According to Willett et al. (1993), thermally activated nonlinear viscous flow of the wedge dominates the deformational mechanism below the thick portion, whilst frictional Coulomb rheology still controls deformation at the external parts of the plateau.

[59] This type of viscous flow underneath the Altiplano was proposed by Isacks (1988) and ascribed to account for seismologically determined layering of the Altiplano crust (Beck and Zandt, 2002). Vietor and Oncken (2005) highlight the fact that to achieve an Altiplano-like crustal configuration, two S-points are needed at the base of the plateau flanks to account for frictional deformation of the bounding crustal wedges. They analyze tapers of the western and eastern flanks and conclude that they have good correspondence with retro and pro wedge tapers resulting from their modeling. Such scenario can be observed in the Andean crustal architecture summarized in Fig. 8. Pope and Willett (1998) emphasize the role of subduction ablation to drive shortening in the upper crust and to remove and drag down the incoming lower crust from the east, proposing this mechanism as complementary to lower crustal delamination. Of course, our sandbox models cannot fully reproduce orogenic plateau characteristics, yet they do illustrate how protracted and continuous accretion from the "east" accounts for the generation of a large wedge adjacent to a subduction forearc high, with a pro wedge reaching far into the model foreland, similar to the Central Andean configuration. Additionally, retro and pro side tapers of the large wedge are in agreement with the results of Vietor and Oncken (2005). Expansion of the retro wedge of our model (Fig. 3) is also consistent with the westward expansion of the western Altiplano flank in response to Miocene accretion at the Subandean Sierras.

[60] Despite the good fit between a single expanding wedge model and the current crustal-scale configuration of the Central Andes (Isacks, 1988; Pope and Willett, 1998), sedimentary evidence suggests that the Western and Eastern Cordilleras developed as independent crustal wedges prior to Miocene uplift of the Altiplano. Growth of the Eastern Cordillera began during the Eocene (e.g., Lamb et al., 1997; McQuarrie, 2002) concomitant to deformation in the Incaic Range along the current Forearc Precordillera and Western Cordillera of Chile (Charrier et al., 2013; Herrera et al., 2017). Sediment provenance of foreland sequences outcropping inside the Altiplano indicate mid-Paleocene, cratonic sources east of the plateau and persistent late Eocene-Oligocene sources to the west along the current Western Cordillera (Horton et al., 2001). The Neogene sedimentary record as well indicates two reliefs bounding the proto Altiplano. Based on this data, Horton et al. (2001) propose that a mid-Paleocene to Oligocene, east-vergent thrust belt migrated from west to east, along the western margin of the plateau whilst a doubly-vergent thrust belt developed along the eastern margin during the Oligocene-Miocene corresponding to the Eastern Cordillera. This data suggests that Altiplano growth might have resulted from the expansion of the underlying wedges of the Western and Eastern Cordilleras and their coalescence in Miocene times resulting in sufficient thickening of the crust to generate Altiplano uplift (Martinod et al., 2020). Such a process has been ascribed for the generation of the Tibetan plateau, through piecemeal activation of thrusts that reach the mantle and trigger the generation of adjacent crustal wedges growing by accretion (e.g., Tapponier et al., 2001).

[61] The noteworthy morphological transition in the central Chile forearc north and south of 33.5°S (Fig. 9) as well corresponds to a case of orogenic wedge coalescence, although a westward expansion of the Cordilleran wedge is unclear. South of 33.5°S, the wedges are separated by the

Central Valley, tectonically stable since 22 Ma (Farías et al., 2010). North of 33.5°S, the Coastal Ranges and Main Cordillera wedges are merged (Fig. 10A) and rise up northward towards the Puna and Altiplano. The accretionary flux entering the orogen below the foreland increases considerably northwards as suggested by an important increase in shortening rates along the retro arc (Fig. 1, Kley and Monaldi, 1998; Kley et al., 1999; Ramos et al., 2004). The seismology of the central Chile forearc shows how the retro shears of the Coastal and inner Cordilleran wedges intersect c. 15 km below the surface (Fig. 10A, Comte et al., 2019). However, no evidence of westward expansion of the inner Cordillera allows to interpret that this process is certainly responsible for the coalescence of the Coastal and Cordilleran wedges from 33.5°S to 27°S.

[62] Juxtaposition of the orogenic wedges along this region might have resulted by an initial growth of the Cordilleran wedge closer to the Coastal wedge in comparison to the situation south of 33.5°S, this is, an S-point for the Cordilleran wedge initially closer to the ocean-continent subduction zone. Alternatively, Comte et al. (2019) proposed a mechanism of subduction erosion followed by basal accretion of crustal slices scraped off initially from the leading edge of the subduction wedge, provoking a rearward migration of the entire wedge that might have led to wedge coalescence in this region.

VI. Conclusions

[63] The first-order distribution of deformation along the Central and Southern Central Andean morphostructures can be explained using the results of our specific analogue modeling, which well illustrate the large-scale kinematics of orogenic wedges growing at different rates of accretion in a subduction advance setting.

[64] We propose that the Coastal Cordillera is underlain by a subduction wedge formed by protracted subduction of the oceanic plate beneath the continent. Tectonic erosion, recycling of accreted materials by basal accretion and slow top-to-the-left material motions associated with very low accretionary fluxes are the dominant processes within the Coastal subduction complex along the erosive Chilean margin. The Coastal wedge has a fast subduction velocity (~70 km/Ma) but only a very thin section (<0.5-2 km) has been accreted during the Cenozoic, so wedge growth is slow there. On the other hand, the inner Main Cordillera is underlain by another subduction wedge, formed by accretion of the South American upper crust from the east into the inner forearc.

Here, a slowly subducting plate (~4 km/Ma and increasing northward up to ~11 km/Ma) carrying a thick section to be accreted (~12.5-25 km) results in fast growth of the high Andes.

[65] The higher accretionary flux entering the inner Cordilleran wedge accounts for its northward expansion, large horizontal material motions within the wedge and an asymmetric distribution of deformation in the eastern and western Andes. Space for the accommodation of crustal materials entering the subduction wedge from the eastern foreland is created by retrocharriage, accounting for accretion at the base and westward tilting in the inner Andean forearc (Chilean Andes), associated with low rates of horizontal shortening. Contrastingly, distributed deformation throughout fold-and-thrust belts of the eastern Andean slope record ~20 to ~300 km of A-type subduction. The high rates of Cenozoic accretion at the Cordilleran wedge would account for the westward expansion of its retro side.

[66] This latitudinal variation in shortening provides of a space-for-time representation for the evolution of the orogenic topography in the range, in which, from south to north, the high Andes display a transition from a small and cold orogen (Southern Central Andes) to a large and hot orogen (Central Andes). An early state of Andean evolution would thus correspond to a scenario in which two subduction wedges run parallel along-strike, separated by a longitudinal central valley: a Coastal wedge to the west, grown by ocean-continent subduction, and a Cordilleran wedge to the east, grown by accretion from the eastern foreland. Rates of accretion increasing northward account for the northward westward expansion of the Cordilleran wedge. We finally conclude that Andean deformation rates are controlled by the accretionary fluxes entering each subduction wedge, rather than décollement stress (aka plate coupling) at the Chile subduction zone.

VII. Acknowledgments

The authors would like to thank Christopher Fiederlin and William Samela at Yale University for building and assisting us with our modeling device. We thank Lucas M. Fennell (Universidad de Buenos Aires) for fruitful discussions on Andean tectonic evolution at the very beginning of this work. We thank Luisa Pinto, Huber Rivera and Pablo Molina (Universidad de Chile) who kindly reviewed this manuscript and provided helpful comments and recommendations. S. Herrera was supported by a PhD grant from the Ministry of Education of Chile: Beca de Doctorado Nacional Nº 21150639.

VIII. Appendix

VIII. 1. Particle Image Velocimetry (PIV)

A custom PIV software package was created by authors Ma and Brandon which meets the specific requirements of the sandbox modeling (large irregular sand grains, high particle density and a free upper boundary).

Image pre-processing

The software required several image processing steps prior to the PIV analysis: rectification, masking and histogram equalization. In the rectification, the raw images (warped by lens distortion, rotation and perspective) are transformed into a regular Cartesian coordinate system (origin in S_2, Fig. 3) with a fixed square pixel size. Using manually defined control points, a flexible locally-weighted polynomial coordinate transformation was used to map original pixel coordinates to a regular grid in world coordinates. In the masking step, a series of image filters allowed to differentiate sand and background for the purposes of velocity field measurements. Sand and background were reliably differentiated by a combination of minimum and maximum threshold for brightness. The filters yielded a mask that labeled each pixel as sand (1) or background (0). The histogram equalization converted the colored images into grayscale eliminating lightning anomalies caused by spatial gradients and changes between steps. An example of these pre-processing steps can be visualized in Video DR2.

Particle Image Velocimetry (PIV)

The PIV basically consisted in a computation of local offsets between pairs of images by estimating the location of small sample windows extracted from the initial image within a larger interrogation window extracted from the final image. To measure local velocity vectors, the software computes the cross-correlation between the sample and interrogation window, locates the peak in the correlation plane to sub-pixel precision, and adds the peak location to the initial offset between the windows. For the cross-correlation calculation, a masked, normalized method was implemented, which improves performance at the boundaries of the sand. To estimate the location of the peak, two Gaussian models were applied to the neighboring area of the maximum pixel. The first model computes the least-square fit, and the second, more accurate, but slower model interpolates the location of the peak to within a tolerance at a sub-pixel precision (10^{-6} pixel). The location of the computed velocity vectors was always assigned at a mid-point between the initial and final images (i.e., mid-point between the location of the sample window and that of the final location). The measured velocity field is at scattered points because of assigning vector locations at midpoint time and accounting for the sample window centroid. A normalized median test allowed to identify and remove outlier vectors from the velocity field that typically corresponded to vectors assigned to the boundaries of sand. Before the next pass, the velocity field is interpolated from the scattered observation points for interpolation to provide a higher resolution initial estimate for the velocity field, and for strain computation on a regular grid.

The resulting velocity field is either used as in initial estimate for the next (higher resolution) pass or returned as the final result. In this way, the algorithm iteratively improves the resolution and accuracy of the velocity field. The results are stored in a time-indexed netCDF file, along with all the parameters needed to repeat the analysis.

From the PIV, the instantaneous features of the resulting velocity field are visualized for analysis of the experimental results. These features correspond to the velocity field, the principal directions and magnitudes of the strain rates and the vorticity (equal to twice the local rotation rate, or curl of flow).

Velocity field and Strain rate

For the velocity field, the vectors of the velocity field are defined by a location, represented by Eulerian coordinates $\{x_1, x_2, x_3\}$, and Eulerian velocity components $\{v_1, v_2, v_3\}$, which vary as a function of location, and also as a function of time.

The velocity gradient tensor L is equal to the Jacobian of the velocity field, and expressed as

$$\mathbf{L} = L_{ij} = \frac{\partial v_i}{\partial x_j} = \begin{bmatrix} \frac{\partial v_1}{\partial x_1} & \frac{\partial v_1}{\partial x_2} & \frac{\partial v_1}{\partial x_3} \\ \frac{\partial v_2}{\partial x_1} & \frac{\partial v_2}{\partial x_2} & \frac{\partial v_2}{\partial x_3} \\ \frac{\partial v_3}{\partial x_1} & \frac{\partial v_3}{\partial x_2} & \frac{\partial v_3}{\partial x_3} \end{bmatrix} \tag{1}$$

This provides a complete description of the spatial gradients in velocity around a point, which provides a useful way to measure the instantaneous deformation and rotation occurring at a point.

The velocity gradient tensor is decomposed into symmetric and anti-symmetric components, D and W, respectively, so that L = D + W, where

$$\mathbf{D} = D_{ij} = \frac{L_{ij} + L_{ji}}{2} = \begin{bmatrix} \frac{\partial v_1}{\partial x_1} & \frac{1}{2}\left(\frac{\partial v_1}{\partial x_2} + \frac{\partial v_2}{\partial x_1}\right) & \frac{1}{2}\left(\frac{\partial v_1}{\partial x_3} + \frac{\partial v_3}{\partial x_1}\right) \\ \frac{1}{2}\left(\frac{\partial v_1}{\partial x_2} + \frac{\partial v_2}{\partial x_1}\right) & \frac{\partial v_2}{\partial x_2} & \frac{1}{2}\left(\frac{\partial v_2}{\partial x_3} + \frac{\partial v_3}{\partial x_2}\right) \\ \frac{1}{2}\left(\frac{\partial v_1}{\partial x_3} + \frac{\partial v_3}{\partial x_1}\right) & \frac{1}{2}\left(\frac{\partial v_2}{\partial x_3} + \frac{\partial v_3}{\partial x_2}\right) & \frac{\partial v_3}{\partial x_3} \end{bmatrix}, \text{ and} \tag{2}$$

$$\mathbf{W} = W_{ij} = \frac{L_{ij} - L_{ji}}{2} = \begin{bmatrix} 0 & \frac{1}{2}\left(\frac{\partial v_1}{\partial x_2} - \frac{\partial v_2}{\partial x_1}\right) & \frac{1}{2}\left(\frac{\partial v_1}{\partial x_3} - \frac{\partial v_3}{\partial x_1}\right) \\ -\frac{1}{2}\left(\frac{\partial v_1}{\partial x_2} - \frac{\partial v_2}{\partial x_1}\right) & 0 & \frac{1}{2}\left(\frac{\partial v_2}{\partial x_3} - \frac{\partial v_3}{\partial x_2}\right) \\ -\frac{1}{2}\left(\frac{\partial v_1}{\partial x_3} - \frac{\partial v_3}{\partial x_1}\right) & -\frac{1}{2}\left(\frac{\partial v_2}{\partial x_3} - \frac{\partial v_3}{\partial x_2}\right) & 0 \end{bmatrix}. \tag{3}$$

D is called the rate-of-deformation tensor or stretching tensor. The stretching tensor provides information about the orthogonal strain-rates operating around a point. W is called the spin tensor in that it describes the local rotation rate of a material point around its center. The spin can be visualized as the rate of rotation of a paddle wheel immersed in flow at a local point. The tensors L, D and W are everywhere uniquely defined at each point within the velocity field. Thus, they provide a complete description of the stretching and rotation within the velocity field.

The magnitudes and directions of the principal strain rates are determined by doing an eigen-decomposition of D,

$$\mathbf{D} = \mathbf{T} \cdot \Lambda_D \cdot \mathbf{T}^T, \tag{4}$$

where Λ_D is a diagonal tensor containing the magnitude of the principal strain rates along the diagonal, $\Lambda_D = \operatorname{diag}\left\{D_1, D_2, D_3\right\}$, and T is a transform matrix containing the principal directions as column vectors in the same order as the principal values. The eigen-decomposition is usually organized so that principal values are in order of decreasing magnitude $D_1 \geq D_2 \geq D_3$.

Strain rate is defined by $D_i = \frac{\mathrm{d}l}{l\,\mathrm{d}t}$, where *l* is length in the specified direction and *t* is time. A common practice is to show the principal direction for D_1, which would be the first column vector in T. This direction corresponds to the direct with the maximum extension rate.

Kinematic vorticity number

The kinematic vorticity number, W_k was introduced to structural geology by Means et al. (1980). For plane strain, $W_k = 0$ for irrotational flows (also called coaxial deformation, with pure shear as a special case). An absolute value of one indicates simple shear, where the vorticity and stretching rate are the same, and an absolute value greater than one indicates super shear, where the vorticity is greater than the stretching rate.

For a general three-dimensional flow, the kinematic vorticity number is given by

$$W_k = \frac{\left\|2\mathbf{w}\right\|}{\sqrt{2}D_T} = \frac{\left\|2\mathbf{w}\right\|}{\sqrt{2\left(D_1^2 + D_2^2 + D_3^2\right)}} \tag{5}$$

where w is the spin vector and 2w is the vorticity vector. Using the kinematic number for dilation,

$$A_{\mathrm{k}} = \frac{D_{\mathrm{v}}}{\sqrt{2}D_D}.$$

for dilational deformation, it makes more sense to normalize relative to the deviatoric strain rate, giving

$$W_k^* = \frac{\left\|2\mathbf{w}\right\|}{\sqrt{2}D_D}, \text{ and } A_{\mathrm{k}}^* = \frac{D_{\mathrm{v}}}{\sqrt{2}D_{\mathrm{D}}}.$$

This modification ensures that a simple shear deformation combined with dilation will give $W_k^* = 1$.

IX. References Cited

Adam, J., Reuther, C.D., 2000. Crustal dynamics and active fault mechanics during subduction erosion. Application of frictional wedge analysis on to the Northern Chile Forearc. Tectonophysics 321, pp. 297-325.

Alvarado, A., Ramos, V., 2011. Earthquake deformation in the northwestern Sierras Pampeanas of Argentina based on seismic waveform modelling. Journal of Geodynamics 51, 205-208. doi:10.1016/j.jog.2010.08.002

Ammirati, J.B., Alvarado, P., Perarnau, M., Saez, M., & Monsalvo, G., 2013. Crustal structure of the Central Precordillera of San Juan, Argentina (31°S) using teleseismic receiver functions. Journal of South American Earth Sciences, 46, 100–109. doi:10.1016/j.jsames.2013.05.007

Ammirati J.B., Vargas, G., Rebolledo, S., Abrahami, R., Potin, B., Leyton, F., Ruiz, S., 2019. The Crustal Seismicity of the Western Andean Thrust (Central Chile, 33°–34° S): Implications for Regional Tectonics and Seismic Hazard in the Santiago Area. Bulletin of the Seismological Society of America, Vol. 109, No. 5, pp. 1985–1999. doi: 10.1785/0120190082

Anderson, R.B., Long, S.P., Horton, B.K., Calle, A.Z., Ramirez, V., 2017. Shortening and structural architecture of the Andean fold-thrust belt of southern Bolivia (21 degrees S): Implications for kinematic development and crustal thickening of the Central Andes. Geosphere 13, 538–558.

Armijo, R., Rauld, R., Thiele, R., Vargas, G., Campos, J., Lacassin, R., Kausel, E., 2010. The West Andean Thrust, the San Ramon Fault, and the seismic hazard for Santiago, Chile. Tectonics 29 TC2007

Astini, R.A., Davila, F.M., 2010. Comment on “The West Andean Thrust, the San Ramon Fault, and the seismic hazard for Santiago, Chile” by Rolando Armijo et al. Tectonics 29 TC4009

Baby P, Rochat P, Mascle G, Hérail G (1997) Neogene shortening contribution to crustal thickening in the back arc system of the Bolivian Orocline (Central Andes). Geology 25:883–886

Bally, A. W., 1975, A geodynamic scenario for hydrocarbon occurrences: Proc the 9th World Petrol.Congr., Tokyo, v. 2 (Geology), Applied Sci. Pub., Ltd., Essex, England, p. 33-44

Bangs, N.L., Cande, S.C., 1997. Episodic development of a convergent margin inferred from structures and processes along the southern Chile margin. Tectonics 16, 3. pp. 489-503. https://doi.org/10.1029/97TC00494

Barnes J.B., Ehlers T.A., 2009. End member models for Andean Plateau uplift. Earth Sci Rev 97:105–132

Bascuñán, S., Arriagada, C., Le Roux, J., Deckart, K., 2016. Unraveling the Peruvian phase of the Central Andes: stratigraphy, sedimentology and geochronology of the Salar de Atacama Basin (22°30–23°S), northern Chile. Basin Res. 28, 365–392.

Batchelor, G., An Introduction to Fluid Dynamics. 615 pp., Cambridge University Press, New York, 1967.

Beaumont, C., Muñoz, J.A., Hamilton, J., Fullsack, P., 2000. Factors controlling the Alpine evolution of the central Pyrenees inferred from a comparison of observations and geodynamical models: Journal of Geophysical Research, v. 105, p. 8121–8145, doi:10.1029 /1999JB900390.

Becerra, J., Arriagada, C., Contreras-Reyes, E., Bascuñán, S., De Pascale, G.P., Reichert, C., Díaz-Naveas, J., Cornejo, N., 2016. Gravitational deformation and inherited structural control on slope morphology in the subduction zone of north-central Chile (~29–33◦S). Basin Res. https://doi.org/10.1111/bre.12205

Beck, SL, Zandt, G., 2002. The nature of orogenic crust in the central Andes. J Geophys Res 107(B10):2230. doi:10.1029/2000JB000124.

Bellhasen, N., Sebrier, M., Siame, L., 2016. Crustal shortening at the Sierra Pie de Palo (Sierras Pampeanas, Argentina): near-surface basement folding and thrusting. Geol. Mag. 153 (5/6), pp. 992-1012. doi:10.1017/S0016756816000467

Boyce, D., 2015. Modelo de evolución tectónica y paleogeográfica del margen andino en Chile Central durante el cretácico medio - tardío: El registro estructural y sedimentario en la formación Las Chilcas. Unpublished MS. Thesis. Departamento de Geología, Universidad de Chile. Santiago, Chile. 296 p.

Brandon, M.T., 2004. The Cascadia subduction wedge: the role of accretion, uplift, and erosion. In: van der Pluijm, B.A., Marshak, S. (Eds.), Earth Structure, An Introduction to Structural Geology and Tectonics, second ed. W.W. Norton & Company, Inc., New York, pp. 566–574.

Brooks, B.A., Bevis, M., Smalley Jr., R., Kendrick, E., Manceda, R., Lauría, E., Maturana, R., Araujo, M., 2003. Crustal motion in the Southern Andes (26–36 S): Do the Andes behave like a microplate? Geochemistry, Geophysics, Geosystems, 4(10).

Brooks, B.A., Bevis, M., Whipple, K., Arrowsmith, R., Foster, J., Zapata, T., Kendrick, E., Minaya, E., Echalar, A., Blanco, M., Euillades, P., Sandoval., M., Smalley Jr., R.J., 2011. Orogenic-wedge deformation and potential for great earthquakes in the central Andean backarc. Nature Geoscience. doi: 10.1038/ngeo1143.

Buiter, S. 2012. A review of brittle compressional wedge models. Tectonophysics. s 530–531. 1–17. 10.1016/j.tecto.2011.12.018.

Charrier, R., Pinto, L., Rodríguez, M.P., 2007. Tectono-stratigraphic evolution of the Andean orogen in Chile. In: Gibbons W, Moreno T (eds) Geology of Chile, Chapter 3. The Geological Society, London, Special Publication, pp 21–116

Charrier, R., Hérail, G., Pinto, L., García, M., Riquelme, R., Farías, R., Muñoz, N. 2013. Cenozoic tectonic evolution in the Central Andes in northern Chile and west-central Bolivia: Implications for paleogeographic, magmatic and mountain building evolution. Int J Earth Sci (Geol Rundsch) (2013) 102:235–264 DOI 10.1007/s00531-012-0801-4

Coloma, F., Valin, X., Oliveros, V., Vásquez, P., Creixell, C., Salazar, E., Ducea, M.N., 2017. Geochemistry of Permian to Triassic igneous rocks from northern Chile (28º-30º15'S): Implications on the dynamics of the proto-Andean margin. Andean Geology 44 (2): 147-178, doi: 10.5027/andgeoV44n2-a03

Comte, D., Farias, M., Roecker, S., Russo, R., 2019. The nature of the subduction wedge in an erosive margin: Insights from the analysis of aftershocks of the 2015 Mw 8.3 Illapel earthquake beneath the Chilean Coastal Range. Earth Planet. Sci. Lett. 520, 50–62.

Cortés, J., Farías, M., Comte, D., Charrier, R., 2012. Estructuras y depósitos neógenos de la región de Cariquima (Altiplano Chileno): Implicancias en el origen de la Cordillera Occidental a los 19°30'S. Abstract presented at Congreso Geológico Chileno XIII, Antofagasta, Chile.

Cowan, D. S., and Silling, R. M., 1978. A dynamic, scaled model of accretion at trenches and its implications for the tectonic evolution of subduction complexes, J. Geophys. Res., 83(B11), 5389–5396, doi:10.1029/JB083iB11p05389.

David, C., Martinod, J., Comte, D., Hérail, G., Haessler, H., 2002. Intracontinental seismicity and Neogene deformation of the Andean forearc in the region of Arica (18.5°S–19.5°S), paper presented at 5th International Symposium on Andean Geodynamics, Inst. de Rech. pour le Dév., Toulouse, France

Davis, D., Suppe, J, Dahlen, F. 1983. Mechanics of Fold-and-Thrust Belts and Accretionary Wedges. Journal of Geophysical Research. 88. 1153-1172. 10.1029/JB088iB02p01153.

Farias, M., Charrier, R., Comte, D., Martinod, J., Hérail, G., 2005. Late Cenozoic deformation and uplift of the western flank of the Altiplano: evidence from the depositional, tectonic, and geomorphologic evolution and shallow seismic activity (northern Chile at 19 degrees 30' S). Tectonics 24 TC4001.

Farias, M., Comte, D., Charrier, R., Martinod, J., David, C., Tassara, A., Tapia, F., Fock, A., 2010. Crustal-scale structural architecture in Central Chile based on seismicity and surface geology: Implications for Andean mountain building. Tectonics 29 TC3006.

Farias, M., Comte, D., Roecker, S., Carrizo, D., Pardo, M., 2011. Crustal extensional faulting triggered by the 2010 Chilean earthquake: the Pichilemu Seismic Sequence. Tectonics 30 TC6010

Feehan, J., Brandon, M., 1999. Contribution of ductile flow to the exhumation of low-temperature, high pressure metamorphic rocks: San Juan-Cascade nappes, NW Washington State. Journal of Geophysical Research. Vol. 104. No. B5. Pages 10883-19902.

Fennell, L. M., Folguera, A., Naipauer, M., Gianni, G., Rojas Vera, E., Bottesi, G., Ramos, V. A., 2017. Cretaceous deformation of the southern central Andes: Synorogenic growth strata in the Neuquén Group (35°30′–37°S). Basin Research, 29, 51–72.

Fuller, C.W., Willett, S.D., Branton, M.T., 2006. Formation of forearc basins and their influence on subduction zone earthquakes. Geology v.34, n. 2, p.p. 65-68. doi: 10.1130/G21828.1

Gerbault, M., Cembrano, J., Mpodozis, C., Farías, M., Pardo, M., 2009. Continental margin deformation along the Andean subduction zone: Thermo-mechanical models. Physics of the Earth and Planetary Interiors 177: 180-205.

Giambiagi, L., Ramos, V., 2002. Structural evolution of the Andes between 33°30′ and 33°45′ S, above the transition zone between the flat and normal subduction segment, Argentina and Chile, J. South Am. Earth Sci., 15, 101–116, doi:10.1016/S0895-9811(02)00008-1.

Giambiagi, L., Tassara, A., Mescua, J., Alvarez, P., Godoy, E., Hoke, G, Pinto, L. Spagnotto, S., Porras, H., Tapia, F., Jara, P., Bechis, F., Garcia, V., Suriano, J., Pagano, S., 2014. Evolution of shallow and deep structures along the Maipo-Tunuyán transect (33°40'S): From the Pacific coast to the Andean foreland. Geological Society, London, Special Publication 399. http://dx.doi.org/10.1144/SP399.14.

Grier, M. E., Salfity, J. A., Allmendinger, R. W., 1991. Andean reactivation of the Cretaceous Salta rift, northwestern Argentina. Journal of South American Earth Sciences, 4(4), 351–372. doi:10.1016/0895-9811(91)90007-8

Gripp, A. E., Gordon, R., 2002. Young tracks of hotspots and current plate velocities, Geophys. J. Int., 150, 321–361, doi:10.1046/j.1365-246X.2002.01627.x.

Hartley, A.J.; Evenstar, L. 2010. Cenozoic stratigraphic development in the northern Chilean forearc: Implications for basin development and uplift history of the Central Andean margin. Tectonophysics 495: 67-77.

Hartley, A. J., May, G., Chong, G., Turner, P., Kape, S. J., Jolley, E. J., 2000. Development of a continental forearc: A Cenozoic example from the Central Andes, northern Chile. Geology, 28(4), 331. doi:10.1130/0091-7613(2000)28<331:doacfa>2.0.co;2

Henríquez, S., DeCelles, P.G., Carrapa, B., 2019. Cretaceous to middle cenozoic exhumation history of the Cordillera de Domeyko and Salar de Atacama Basin, Northern Chile. Tectonics 38, 395–416.

Herrera, S., Pinto, L., Deckart, K., Cortés, J., & Valenzuela, J., 2017. Cenozoic tectonostratigraphic evolution and architecture of the Central Andes in northern Chile based on the Aquine region, Western Cordillera (19°-19º30’ S). Andean Geology, 44(2), 87. doi:10.5027/andgeov44n2-a01

Horton, B. K., DeCelles, P. G., 2001. Modern and ancient fluvial megafans in the foreland basin system of the central Andes, southern Bolivia: implications for drainage network evolution in fold-thrust belts. Basin Research, 13(1), 43–63. doi:10.1046/j.1365-2117.2001.00137.x

Horton, B. K., Hampton, B. A., Waanders, G. L., 2001. Paleogene synorogenic sedimentation in the Altiplano plateau and implications for initial mountain building in the central Andes. Geological Society of America Bulletin, 113, 1387–1400.

Horton, B.K., 2018. Tectonic Regimes of the Central and Southern Andes: responses to Variations in Plate Coupling during Subduction. Tectonics 37, 402–429.

Isacks, B., 1988. Uplift of the Central Andean Plateau and Bending of the Bolivian Orocline. J. Geophys. Res. Solid Earth Planets 93, 3211–3231.

Jamieson, R. A., Beaumont, C., 2013. On the origin of orogens. Geological Society of America Bulletin, 125(11-12), 1671–1702. doi:10.1130/b30855.1

Kley, J., Monaldi, C.R., 1998. Tectonic shortening and crustal thickness in the Central Andes: how good is the correlation? Geology 26, 723–726

Kley, J., Monaldi, C.R., Salfity, J.A., 1999. Along-strike segmentation of the Andean foreland: causes and consequences. Tectonophysics 301, 75-94

Konstantinovskaya, E., Malavieille, J., 2011. Thrust wedges with decollement levels and syntectonic erosion: a view from analog models. Tectonophysics 502, 336–350.

Lamb, S., Hoke, L., Kennan, L., Dewey, J., 1997. Cenozoic evolution of the Central Andes in Bolivia and northern Chile. Geol. Soc. Lond., Spec. Publ. 121, 237–264

Lamb, S., 2006. Shear stresses on megathrusts: Implications for mountain building behind subduction zones, J. Geophys. Res., 111, B07401, doi:10.1029/2005JB003916

Lohrmann, J., Kukowski, N., Adam, J., Oncken, O. 2003. The impact of analogue material properties on the geometry, kinematics, and dynamics of convergent sand wedges. Journal of Structural Geology, 25(10), 1691–1711. doi:10.1016/s0191-8141(03)00005-1

Malavieille, J., 1984. Modélisation expérimentale des chevauchements imbriqués: application aux chaînes de montagnes. Bull. Soc. Geol. Fr. 26, 129–138.

Malavieille, J., Trullenque, G., 2009. Consequences of continental subduction on forearc basin and accretionary wedge deformation in SE Taiwan. Tectonophysics. 466. 377-394. doi: 10.1016/j.tecto.2007.11.016.

Malavieille, J., 2010. Impact of erosion, sedimentation, and structural heritage on the structure and kinematics of orogenic wedges: Analog models and case studies. GSA Today, v. 20, no. 1, p. 4–10, doi:10.1130/GSATG48A.1.

Malavieille, J., Dominguez, S., Lu, C., Chen, C., Konstantinovskaya, E., 2019 Deformation partitioning in mountain belts: insights from analogue modelling experiments and the Taiwan collisional orogen. Geological Magazine. doi: 10.1017/S0016756819000645

Martínez, F., Fuentes, G., Perroud, S., Bascuñán, S., 2021. Buried thrust belt front of the western Central Andes of northern Chile: Style, age, and relationship with basement heterogeneities. Journal of Structural Geology 147, 104337. doi: 10.1016/j.jsg.2021.104337.

Martinod, J., Gérault, M., Husson, L., Regard, V., 2020. Widening of the Andes: An interplay between subduction dynamics and crustal wedge tectonics. Earth-Science Reviews 204, 103170. https://doi.org/10.1016/j.earscirev.2020.103170.

McClay, K.R., Whitehouse, P.S., Dooley, T., Richards, A., 2004. 3D evolution of fold and thrust belts formed by oblique convergence. Mar. Pet. Geol. 21, 857–877.

McQuarrie, N., 2002. The kinematic history of the central Andean fold-thrust belt, Bolivia: Implications for building a high plateau. Geol. Soc. Am. Bull. 114, 950–963.

McQuarrie, N., Horton, B.K., Zandt, G., Beck, S., DeCelles, P.G., 2005. Lithospheric evolution of the Andean fold-thrust belt, Bolivia, and the origin of the central Andean plateau. Tectonophysics 399, 15–37.

Means, W., Hobbs, B., Lister, G., Williams, P. 1980. Vorticity and non-coaxility in progressive deformation. Journal of Structural Geology. 2. 371-378. doi: 10.1016/0191-8141(80)90024-3.

Mescua, J.F., Giambiagi, L., Barrionuevo, M., Tassara, A., Mardonez, D., Mazzitelli, M., Lossada, A., 2016. Basement composition and basin geometry controls on upper-crustal deformation in the Southern Central Andes (30–36°S). Geological Magazine, 153(5-6), 945–961. doi:10.1017/s0016756816000364.

Muñoz, N., Charrier, R., 1996. Uplift of the western border of the Altiplano on a west-vergent thrust system, Northern Chile. J. S. Am. Earth Sci. 9, 171–181.

Oliveros, V., Vásquez, P., Creixell, C., Lucassen, F., Ducea, M. N., Ciocca, I., González, J., Espinoza, M., Salazar, E., Coloma, F., Kasemann, S. A., 2019. Lithospheric evolution of the Pre- and Early Andean convergent margin, Chile. Gondwana Research. doi:10.1016/j.gr.2019.11.002

Pope, D.C., Willettt, S.D., 1998. Thermal-mechanical model for crustal thickening in the Central Andes driven by ablative subduction. Geology 26, 511–514.

Ramos, V.A., Cristallini, E.O., Perez, D.J., 2002. The Pampean flat-slab of the Central Andes. J. S. Am. Earth Sci. 15, 59–78.

Ramos, V., Zapata, T., Cristallini, E., Introcaso, A. 2004. The Andean thrust system – latitudinal variations in structural styles and orogenic shortening. Thrust Tectonics and hydrocarbon system. Edition: Memoir 82. Publisher: American Association of Petroleum Geologists, Editors: Ken McClay, pp.30-50

Rebolledo, S., Charrier, R.C.A., 1994. Evolución del basamento paleozoico en el área de Punta Claditas, Región de Coquimbo, Chile (31–32S). Rev. Geol. Chile 21 (1), 55–69. https://doi.org/10.5027/andgeoV21n1-a03.

Richter, P.P., Ring, U., Willner, A.P., Leiss, B., 2007. Structural contacts in subduction complexes and their tectonic significance: The Late Paleozoic coastal accretionary wedge of central Chile. Journal of the Geological Society of London 164: 203-214.

Riesner, M., Lacassin, R., Simoes, M., Carrizo, D., Armijo, R., 2018. Revisiting the Crustal Structure and Kinematics of the Central Andes at 33.5°S: Implications for the Mechanics of Andean Mountain Building. Tectonics, 37(5), 1347–1375. doi:10.1002/2017tc004513

Riquelme, R., Hérail, G., Martinod, J., Charrier, R., Darrozes, J., 2007. Late Cenozoic geomorphologic signal of Andean forearc deformation and tilting associated with the uplift and climate changes of the Southern Atacama Desert (26°S–28°S). Geomorphology 86, 283–306.

Rodríguez, M.P., Charrier, R., Brichau, S., Carretier, S., Farías, M., de Parseval, P., Ketcham, R.A., 2018. Latitudinal and Longitudinal patterns of Exhumation in the Andes of North-Central Chile. Tectonics 37, 2863–2886.

Roeder, D., 1988. Andean-age structure of Eastern Cordillera (Province of La Paz, Bolivia). Tectonics, 7(1), 23–39. doi:10.1029/tc007i001p00023

Russo, R.M., Silver, P.G., 1996. Cordillera formation, mantle dynamics, and the Wilson cycle. Geology 24, 511–514.

Rutland, R.W.R., 1971. Andean orogeny and ocean floor spreading. Nature 233 (5317), 252–255. https://doi.org/10.1038/233252a0.

Sagripanti, L., Rojas Vera, E. A., Gianni, G. M., Folguera, A., Harvey, J. E., Farías, M., Ramos, V. A., 2015. Neotectonic reactivation of the western section of the Malargüe fold and thrust belt (Tromen volcanic plateau, Southern Central Andes). Geomorphology, 232, 164-181. doi:10.1016/j.geomorph.2014.12.022

Saillard, M., Hall, S.R., Audin, L., Farber, D.L., Hérail, G., Martinod, J., Regard, V., Finkel, R.C., Bondoux, F., 2009. Non-steady long-term uplift rates and Pleistocene marine terrace development along the Andean margin of Chile (31◦S) inferred from 10Be dating. Earth Planet. Sci. Lett. 277, 50–63. https://doi.org/10.1016/j.epsl.2008.09.039

Seton, M., Müller, R.D., Zahirovic, S., Gaina, C., Torsvik, T. H., Shephard, G., Talsma, A., Gurnis, M., And Turner, M., 2012. Global Continental And Ocean Basin Reconstructions Since 200 Ma, Earth-Science Reviews 113 (3-4), 212-270, doi:10.1016/J.Earscirev.2012.03.002.

Silver, E. A., Reed, D. L., 1988. Backthrusting in accretionary wedges. Journal of Geophysical Research, 93(B4), 3116. doi:10.1029/jb093ib04p03116

Storti, F., Salvini, F., McClay, K., 2000. Synchronous and velocity-partitioned thrusting and thrust polarity reversal in experimentally produced, doubly-vergent thrust wedges: Implications for natural orogens. Tectonics 19(2),378–396, doi:10.1029/1998TC001079.

Strecker, M.R., Alonso, R.N., Bookhagen, B., Carrapa, B., Hilley, G.E., Sobel, E.R., Trauth, M.H., 2007. Tectonics and Climate of the Southern Central Andes Annual Review of Earth and Planetary Sciences 35:1, 747-787

Tapponnier, P., Xu, Z.Q., Roger, F., Meyer, B., Arnaud, N., Wittlinger, G., Yang, J.S., 2001. Geology - Oblique stepwise rise and growth of the Tibet plateau. Science 294, 1671–1677.

Tozer, B., Sandwell, D., Smith, W.H., Olson, C., Beale, J., Wessel, P., 2019. Global bathymetry and topography at 15 arc sec: SRTM15+. Earth and Space Science. 6. https://doi.org/10.1029/ 2019EA000658

Turienzo, M., 2010. Structural style of the Malargüe fold-and-thrust belt at the Diamante River area (34°30′–34°50′S) and its linkage with the Cordillera Frontal, Andes of central Argentina. Journal of South American Earth Sciences 29(3):537-556. doi.: 10.1016/j.sames.2009.12.002

Van Dinther, Y., Morra, G., Funiciello, F., Rossetti, F., Faccenna, C., 2012. Exhumation and subduction erosion in orogenic wedges: insights from numerical models. Geochem. Geophys. Geosyst. 13, Q06003.https://doi.org/10.1029/2011GC004011.

G. Vargas, Y. Klinger, T.K. Rockwell, S.L. Forman, S. Rebolledo, S. Baize, R. Lacassin, R. Armijo; Probing large intraplate earthquakes at the west flank of the Andes. Geology 42 (12): 1083–1086. doi: https://doi.org/10.1130/G35741.1

Vergés, J., Ramos, V. A., Meigs, A., Cristallini, E.,Bettini, F. H., Cortés, J. M., 2007. Crustal wedging triggering recent deformation in the Andean thrust front between 31°S and 33°S: Sierras Pampeanas-Precordillera interaction. J. Geophys. Res., 112, B03S15, doi:10.1029/2006JB004287

Victor, P., Oncken, O., Glodny, J., 2004. Uplift of the western Altiplano plateau: evidence from the Precordillera between 20 degrees and 21 degrees S (northern Chile). Tectonics 23 TC4004.

Vietor, T., Oncken, O., 2005. Controls on the shape and kinematics of the Central Andean plateau flanks: Insights from numerical modeling. Earth and Planetary Science Letters 236, pp. 814– 827.

von Huene, R., Scholl, D.W., 1991. Observations at convergent margins concerning sediment subduction, subduction erosion, and the growth of continental crust. Rev. Geophys. 29, 279–316. https://doi.org/10.1029/91RG00969.

Waschbusch, P., Beaumont, C. 1996. Effect of a retreating subduction zone on deformation in simple regions of plate convergence, J. Geophys. Res., 101(B12), 28133–28148, doi:10.1029/96JB02482.

Willettt, S., Beaumont, C., Fullsack, P., 1993. Mechanical Model for the Tectonics of Doubly Vergent Compressional Orogens. Geology 21, 371–374.

Winocur, D. A., Litvak, V. D., & Ramos, V. A. (2014). Magmatic and tectonic evolution of the Oligocene Valle del Cura basin, main Andes of Argentina and Chile: evidence for generalized extension. Geological Society, London, Special Publications, 399(1), 109-130. doi:10.1144/sp399.2

Yuan, X., Sobolev, S.V., Kind, R., Oncken, O., Bock, G., Asch, G., Schurr, B., Graeber, F., Rudloff, A., Hanka, W., et al., 2000. Subduction and collision processes in the Central Andes constrained by converted seismic phases. Nature 408, 958–961.

X. FIGURE CAPTIONS

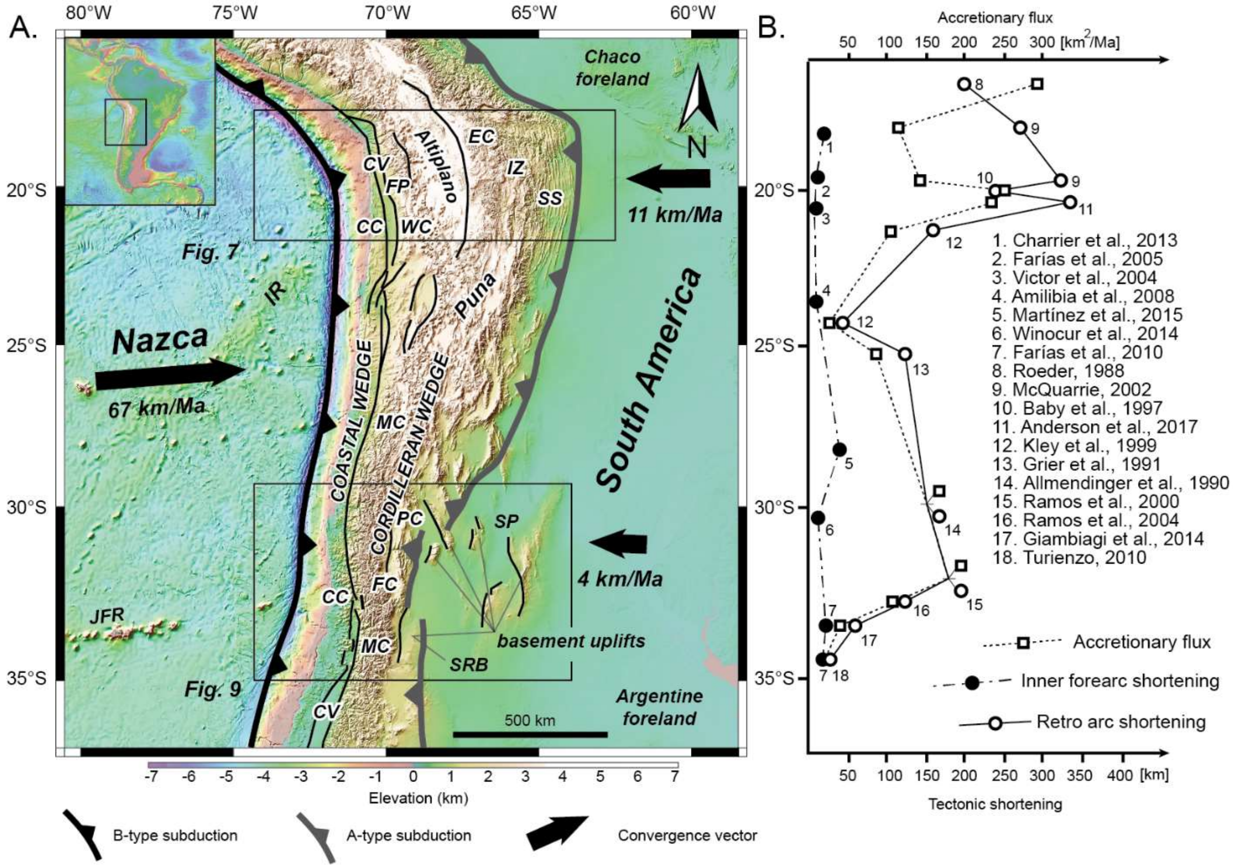

Figure 1. A. Tectonic scenario of western South America above SRTM15+ topography and bathymetry of Tozer et al. (2019) and **B.** Shortening estimates along the western (inner forearc) and eastern (retroarc) sides of the Andes. In A., main morphostructural features and structural boundaries of the Central and Southern Central Andes are shown: CC: Coastal Cordillera; CV: Central Valley; FP: Forearc Precordillera; WC: Western Cordillera; EC: Eastern Cordillera; IZ: Interandean Zone; SS: Subandean Sierras; MC: Main Cordillera; FC: Frontal Cordillera; PC: Precordillera; SP: Sierras Pampeanas; SRB: San Rafael Block; IR: Iquique Ridge; JFR: Juan Fernández Ridge. B- (Benioff) and A- (Ampherer) type subduction boundaries are drawn after Bally (1975). Convergence rates are adjusted to the forearc-fixed reference frame, based on the absolute plate motions of Gripp and Gordon (2002) (Nazca Plate) adjusted to retroarc shortening rates (references in B), in agreement with the continental velocity fields of Brooks et al. (2003; 2011). Estimations of accretionary fluxes in (B) are based on the corresponding shortening rate and depth-to-main detachment of the retroarc thrust system (references in figure).

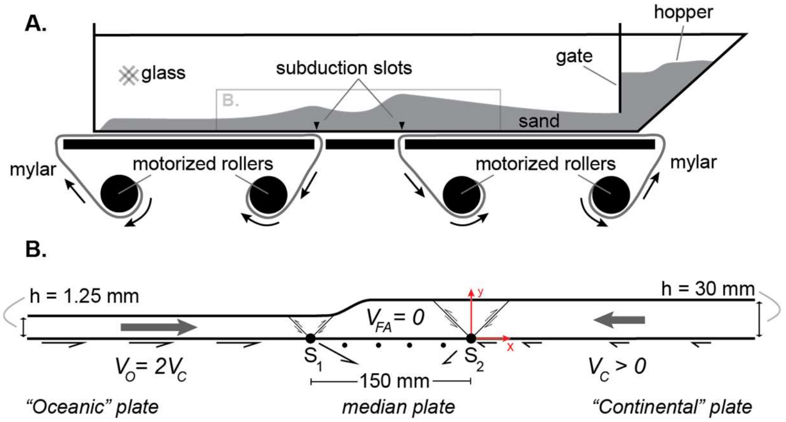

Figure 2. A. Diagram of the experimental setup with two sand wedges formed at each side of the model and **B.** initial conditions for the model. Two layers of different thicknesses are advected towards two respective subduction slots or s-points (S_1 and S_2). Above each s-point, initially, deformation of the sand layer will take place in form of a pair of symmetrical shear band pair. S_2 is the origin of the Cartesian coordinate system used in the PIV software, denoted with red arrows. Above S_1 the thin crust of the left side will be pulled by the Mylar at a displacement increment of ~10 mm/step, to form a Coastal wedge. Above S_2, the thicker crust of the right side will be pulled at a displacement increment of ~5 mm/step to form a Cordilleran wedge. In between the subduction slots, a central portion of the base remains stationary.

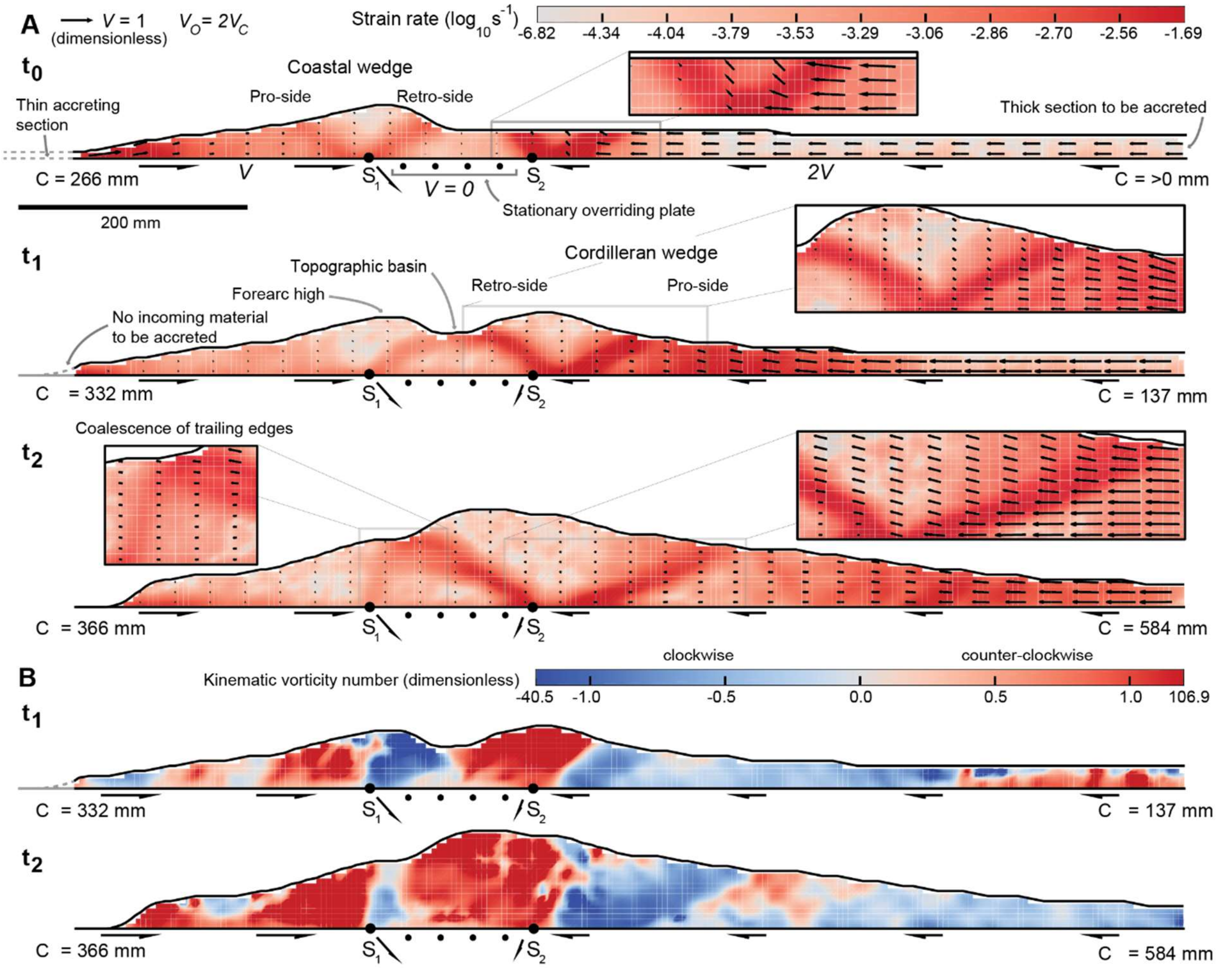

Figure 3. Particle Image Velocimetry (PIV) and numerical strain analysis for the deformation of doubly-vergent sand wedges model, driven by basal traction and material accretion. Color fields show **A)** instantaneous strain rates (second invariant of strain rate tensor) and arrows indicate the instantaneous velocity field; **B)** kinematic vorticity number W_k (external rotation driven by combined particle accommodation and shear induced rotation). **t_0** Initial conditions immediately after the initiation of subduction in the right side of the model, representing a continental margin composed by a forearc high or Coastal Cordillera associated with eastward subduction of an oceanic plate. **t_1** Early stage of Cordilleran wedge development associated with westward subduction of the continental plate and accretion of a thick upper-crustal section along the retro arc region, representing the current configuration of the Chile margin from ~33.5ºS to the south. **t_2** Advanced stage of Cordilleran wedge growth, in which retro wedge expansion has been enough to encounter the trailing edge of the Coastal wedge, leading to coalescence of the two subduction wedges. Here, central valley is absent as it is overridden by the retro-shear zone of the Cordilleran wedge. Deformation is accretion-driven and coaxial throughout, as shown by localizations of the strain rates and kinematic vorticity number at different stages of the model.

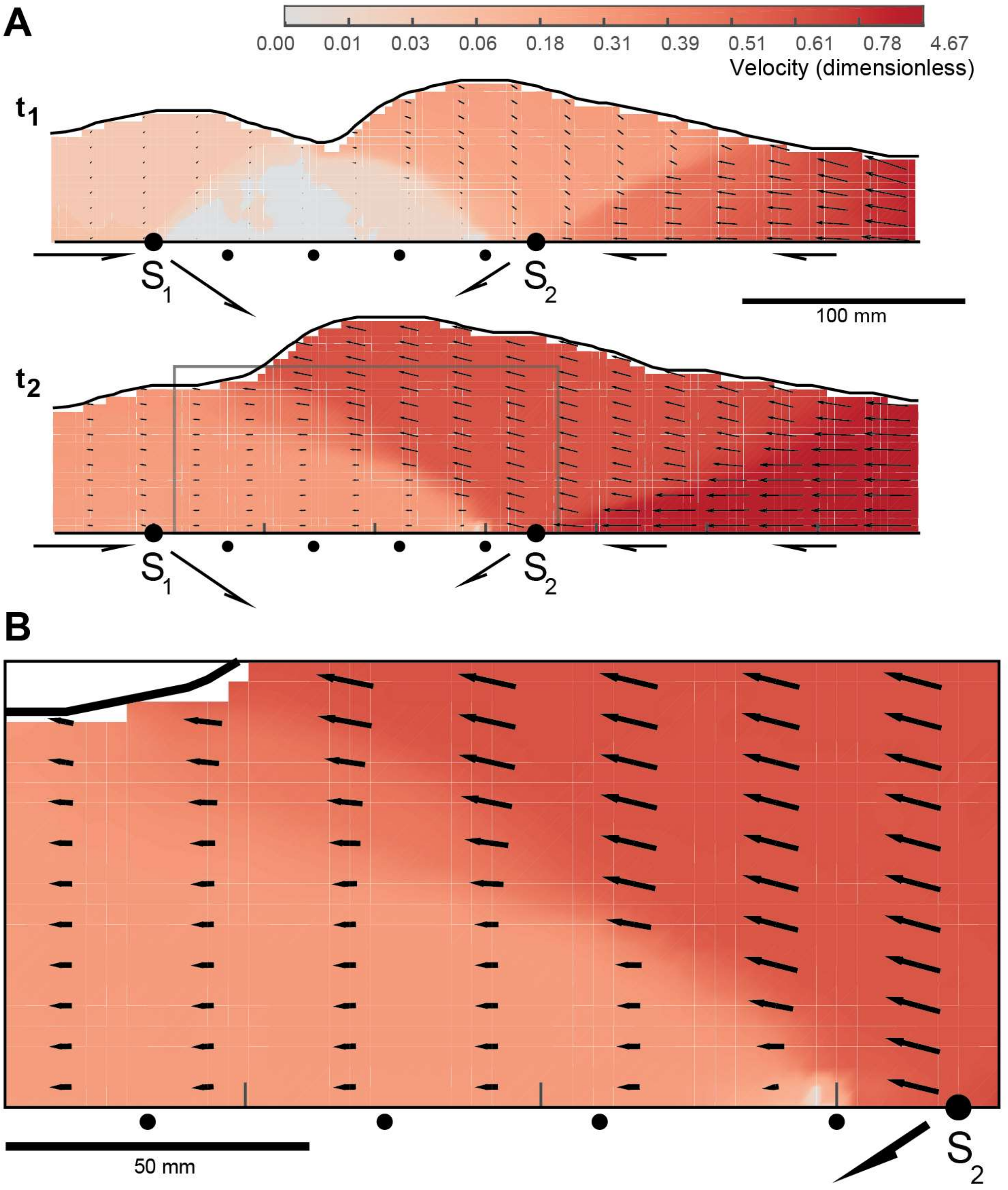

Figure 4. A) Close up of instantaneous velocity field of the model wedges at at t_1 (13.2 cm of convergence from the right) and t_2 (32.9 cm of convergence from the right). **B)** Zoom on the area of wedge coalescence at t_2, showing retro-side expansion of the Cordilleran wedge. Note the sharp variation of the velocity field and the displacements of the retro wedge beyond S_2 showing the detachment of the larger Cordilleran retro side from its base due to increased convergence.

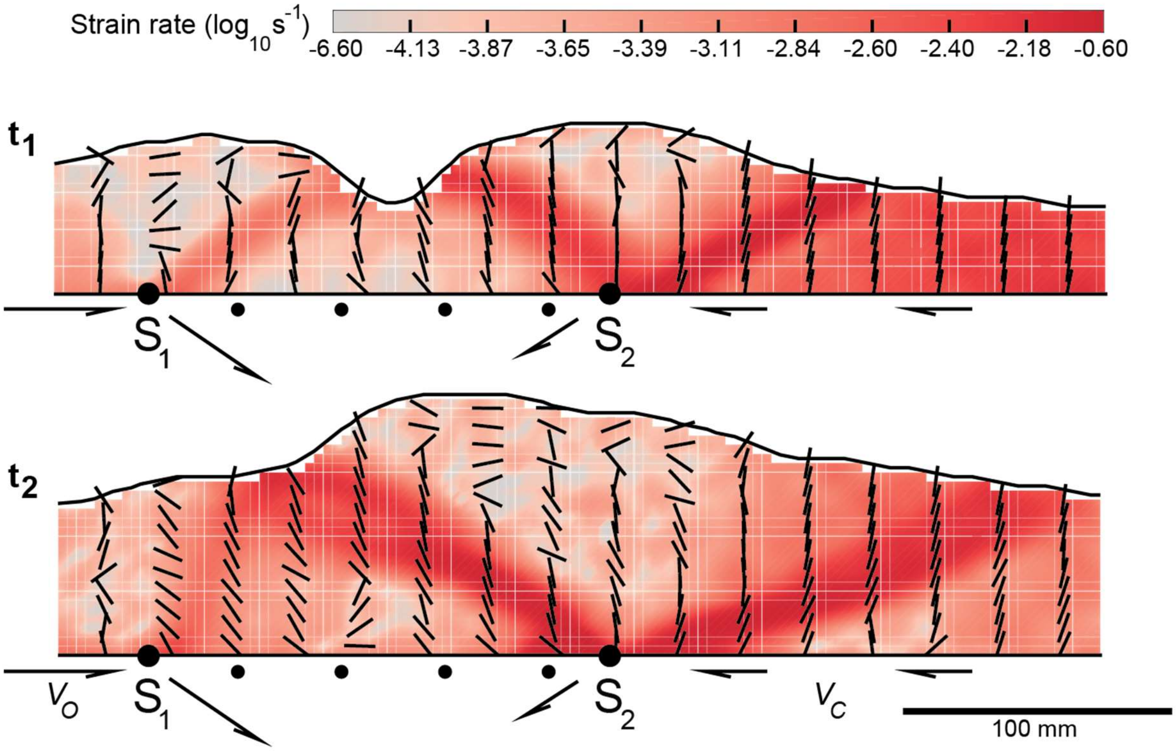

Figure 5. Close up of cross-sectional strain analysis of the model wedges at t_1 (13.2 cm of convergence from the right) and t_2 (32.9 cm of convergence from the right) showing strain rate and superimposed maximum extension directions of the strain ellipses.

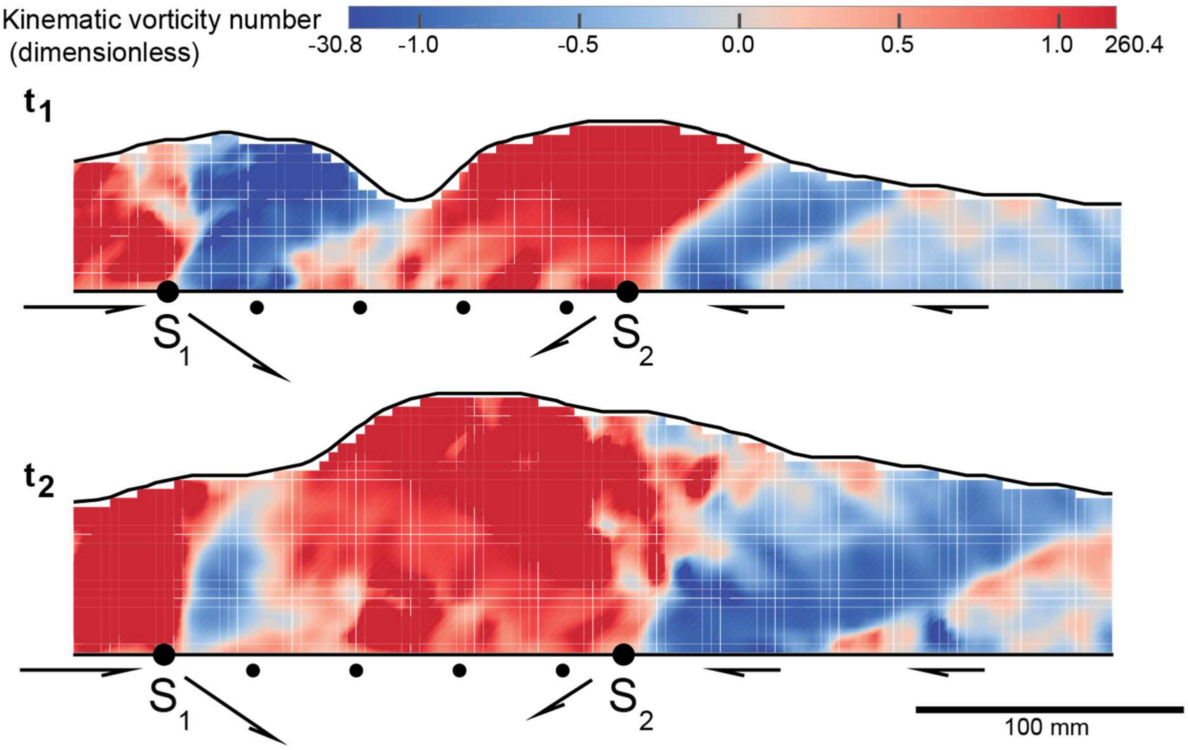

Figure 6. Close up of cross-sectional strain analysis of the model wedges at at t_1 (13,2 cm of convergence from the right) and t_2 (32,9 cm of convergence from the right) showing kinematic vorticity number.

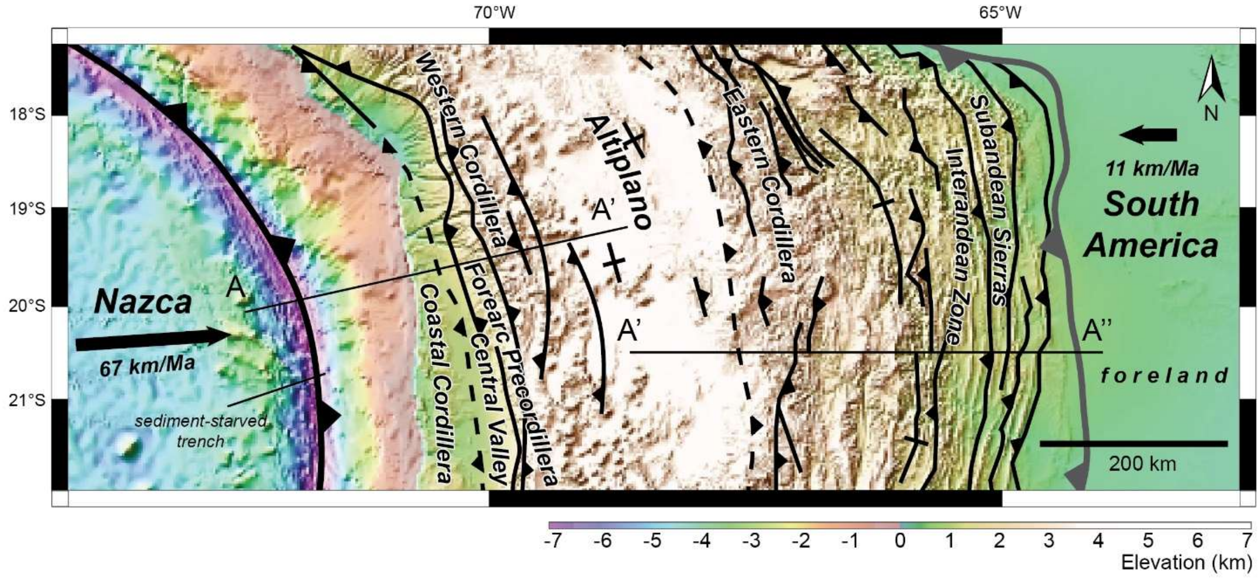

Figure 7. Tectonic setting and morphostructural segmentation of the Central Andes between ~17°S and ~22°S above SRTM15+ topography and bathymetry of Tozer et al. (2019). Convergence rate estimations specified in Figure 1. Cross-sections AA' and A'A'' are integrated in Figure 8.

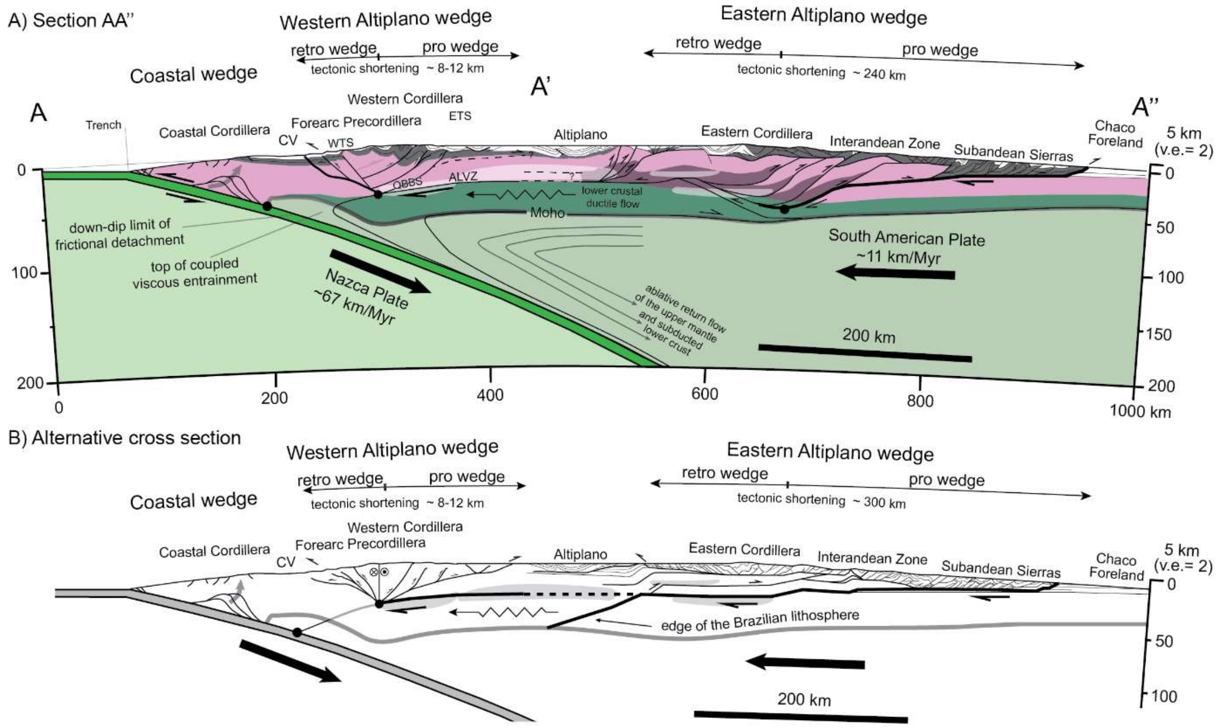

Figure 8. Interpretations for the Central Andean structure between 19°S and 21°S. Location of cross sections is outlined in Figure 7. For both cross-sections, Coastal wedge structure is based on Hartley et al. (2000), David et al. (2002) and Farías et al. (2005). Western Altiplano wedge structure is based on Victor et al. (2004), Farías et al. (2005), Charrier et al. (2013), Herrera et al. (2017) and Cortés et al. (2012). In **A.**, Eastern Altiplano wedge structure is based on Baby et al. (1997) and, in **B.**, is based on McQuarrie (2002). Features shown in the middle-lower crust: ALVZ (Altiplano Low Velocity Zone), from Yuan et al. (2000) and Victor et al. (2004); zone of ductile crustal flow is redrawn after Isacks, (1988) in McQuarrie (2002); shaded gray areas (low velocity zones), Moho and edge of the Brazilian lithosphere are redrawn from Beck and Zandt (2002) in McQuarrie (2002). Abbreviations: CV: Central Valley; WTS: West-vergent Thrust System; ETS: East-vergent Thrust System. Thick solid lines beneath each crustal wedge indicate main detachments in the continental lithosphere. Black dots represent inferred S-points for each crustal wedge. Zones of ablative return flow of the continental mantle and top of coupled viscous entrainment drawn after Pope and Willett (1998).

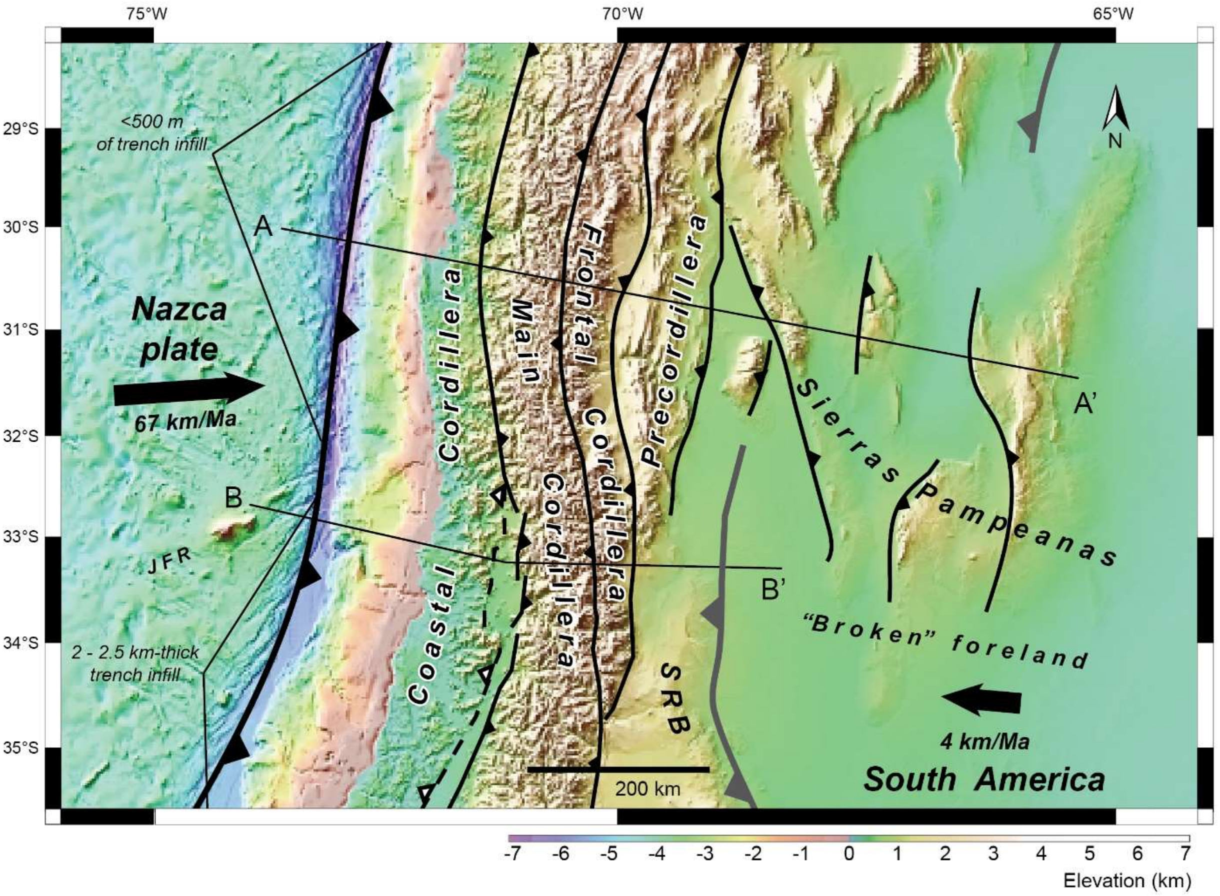

Figure 9. Tectonic setting and morphostructural segmentation of the Southern Central Andes between ~28°S and ~36°S above SRTM15+ topography and bathymetry of Tozer et al. (2019). Convergence rate estimations specified in Figure 1. Cross-sections AA' and BB' are integrated in Figure 10. Note differences in trench infill (from Bangs and Cande, 1997). Abbreviations: SRB: San Rafael Block; JFR: Juan Fernández Ridge.

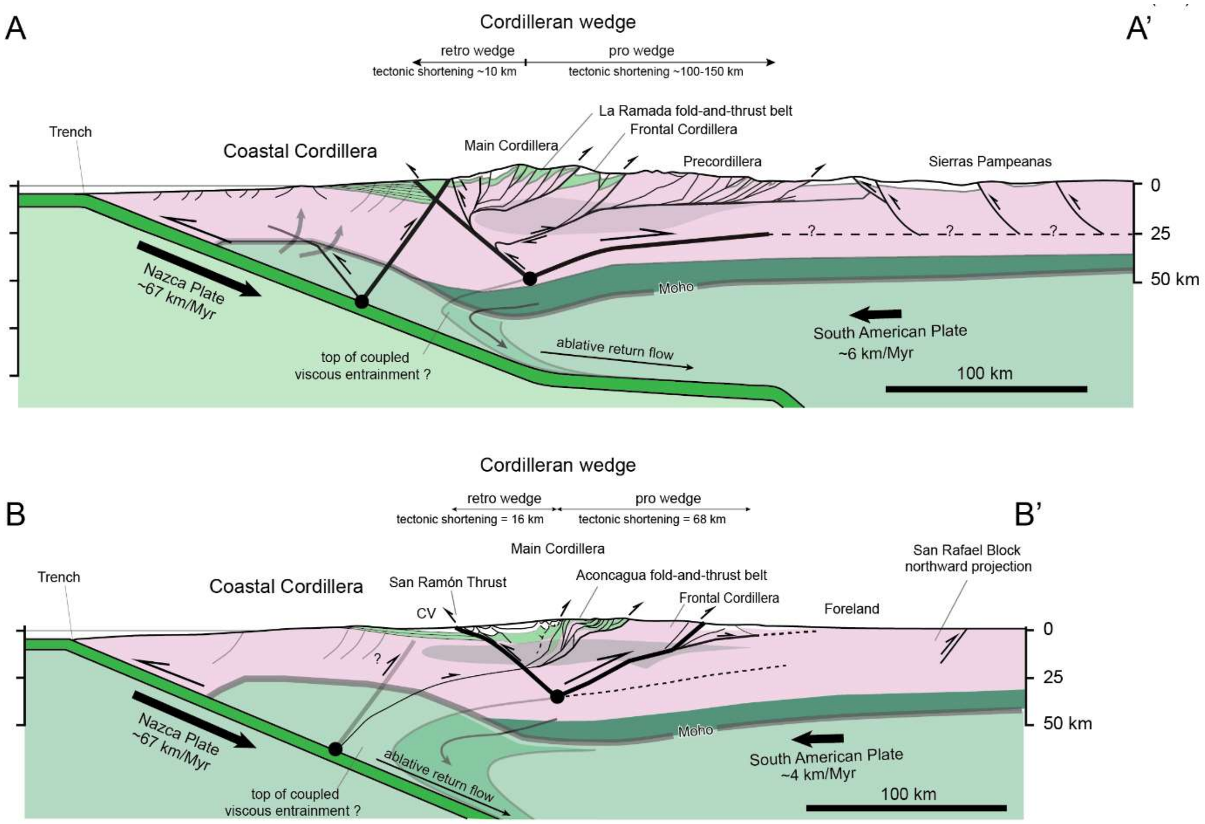

Figure 10. Interpretations for the Southern Central Andean structure at 30°S and 33.5°S. Location of cross sections is outlined in Figure 9. For cross-section AA', Coastal wedge and westernmost Cordilleran wedge structure is based on Comte et al. (2019), Cordilleran wedge structure is based on Ramos et al. (2000), Mescua et al. (2016). Structure underlying Sierras Pampeanas is based on Bellhasen et al. (2016). Moho contour is drawn after Mescua et al. (2016). For cross-section BB', Coastal wedge and Central Valley (CV) structure is based on Farías et al. (2010). Structure of the Cordilleran wedge is based on Farías et al. (2010), Giambiagi et al. (2014) and Mescua et al. (2016). Moho contour and is drawn after Farías et al. (2010). Shaded gray areas correspond to geophysically constrained upper-crustal weak ductile zones (Mescua et al., 2016). Solid black dots represent inferred S-points beneath each crustal wedge. Thick solid lines beneath the Cordilleran wedge indicate main detachments for thrust systems, with MCD corresponding to the Mid-Crustal Detachment of Farías et al. (2010). Zones of ablative return flow of the continental mantle and top of coupled viscous entrainment are hypothetical.

5. DISCUSSION

This section discusses important aspects that were only briefly mentioned in Chapter 3. In a first subsection, limitations of the analogue modeling approach, including Andean geological constraints unexplored in this work are discussed. In the second part, main details on the structural configuration and tectonic evolution of the Western Cordillera of the high Andes of northern Chile are compared and analyzed in terms of a subduction wedge model. Similar aspects of the Andes along other segments (e.g., Southern Central Andes) are shown to find good fit with the model. In a last part, the different segments of the Andes are classified within the context of the main orogenic growth sequence (Temperature-Magnitude framework).

5.1. Experimental Limitations

Physical modeling using analogue materials have extensively offered insight to tectonic processes and structural geometries in simplified tectonic settings. This experimental approach offers several advantages that allow to overcome basic limitations inherent to the study of geodynamic processes in nature (e.g., contraction of large temporal and spatial scales). Furthermore, it allows to investigate the progressive development of a particular geodynamic or geological process from start to finish, providing a complete evolutionary picture of the process under investigation. When properly scaled, the results of the model can be directly applied to the natural prototype. Nevertheless, analogue modeling is commonly carried out in a super-simplified configuration regarding the prototype, and only a few variables are generally tested. Hence, a series of inherent limitations have to be addressed and discussed before comparing results with nature.

In the following paragraphs, the most important variables influencing the modeling of analogue thrust systems as well as the structural development of natural thrust belts are addressed to be considered in this discussion.

Inherent limitations of the modeling approach

The experiments of this work were made above a rigid surface, not allowing any flexural response of the model plates due to tectonic loading (development of flexural basins), or the effects of isostatic compensation below the model to provide a more realistic behavior of the orogenic wedge. The modeling device did not allow the examination of temperature effects. Despite these limitations, the rheology of sand and scaling of the model allows establishing a good analogy with lithospheric deformation driven by plate convergence. Upper-crustal materials behave according to the Mohr-Coulomb failure criterion and the thermal gradient is commonly low (Byerlee, 1978; Burov, 2010). Moreover, numerical experiments with the incorporation of foreland flexure, isostasy and thermal gradient yield results that closely match the ones obtained in sandbox experiments of doubly-vergent wedges (*cf*, Willett et al., 1993; Beaumont et al., 2000; Storti et al., 2000; Jamieson and Beaumont, 2013).

Additional limitations to the models of these work include the impossibility of including fluid pressure within the model sand layer, variations in basal friction, surface erosion and sedimentation. The absence of any pressure within the layer and the relatively high basal friction are able to generate the high-taper wedges of these sand wedges in comparison with natural accretionary wedges (e.g., Byrne et al., 1993). The increase in basal friction was also not considered in the experiments. High friction at the base leads to higher surface slopes, narrower but blunter wedges and, consequently, higher overall taper angles (e.g., Larroque et al., 1995; Naylor et al., 2005). Surface erosion plays a fundamental role in accretionary wedge mechanical evolution. Analogue models that experiment removal of material at the pro side surface illustrate how deformation and exhumation are greatly enhanced and focalized in presence of localized erosion (e.g., Hoth et al., 2004; Bonnet et al., 2007; Konstantinovskaya and Malavieille, 2011; Malavieille, 2010). In doubly vergent wedges, erosion at the retro side will increase the accretionary flux at the rear of the wedge (Willett et al., 1993; Willett, 1999; Brandon, 2004). Sedimentation will hamper the propagation of individual thrusts towards the pro side foreland (Storti et al., 2000).

The layers analogue to the upper crust in Chapter 3 are uniform and the approach does not include heterogeneities in the to-be-deformed stratigraphy, such as weak layers or faults faults generated during previous deformation. It has been shown in analogue experiments that include weak glass micro beads in the model layer (e.g., Bonnet et al., 2007; Konstantinovskaya and Malavieille, 2011; Malavieille, 2010) that the presence of detachments induces accretion at the base of the wedge, in form of duplexes and anticlinal stacks within the pro side. When combined with localized erosion, exhumation is concentrated above this duplex zone, enhancing uplift of deeply buried materials. The role of the basin shape (in 2 and 3D) is a further limitation of the analogue model of Chapter 3. However, shape of the foreland basin can be somewhat uniform in cross section, as in the case of the southern Urals (e.g., Brown et al., 1997). Low-taper wedge geometries are a common feature of sedimentary successions undergoing deformation in active fold-and-thrust belts, as in the Canadian Rockies and the thrust belts of Wyoming and Utah (e.g., Boyer, 1995; DeCelles and Mitra, 1995). In the case of the Andes, as in the European Alps and Pyrenees, the inheritance of pre-orogenic extensional faults and overall shape of the deforming basin defines first order structural styles (e.g., location of duplexes and thrust termination) within the orogenic wedge (e.g., Roeder, 1988; Turienzo et al., 2012; Tapia, 2015; Mescua et al., 2016; discussed in *Local limitations*). It is expected that in a wedge-shaped deforming layer, narrowing towards the foreland, spacing of pro shear band pairs as well as the size of the shears and their spacing decreases (e.g., Davis et al., 1983; Liu et al., 1992).

Local limitations to the modeling approach: key factors modulating Andean thrust belt development

One of the main local limitations, impossible to address by means of our modelling approach is the effect of magmatism, and, of temperature effects in general upon model development. The Main Cordillera of central Chile and the Western Cordillera of northern Chile are both characterized by the occurence of active volcanism and magmatism below the axis of the range. Here, a greater geothermal gradient is to be expected. Main detachments below the Main Cordillera correlate with the 400°C isotherm (Farías et al., 2010) while shallow low velocity zones beneath the Western and Eastern Cordilleras seem to be root of crustal-scale detachments (Beck and Zandt, 2002; Victor et al., 2004). The ocurrence of syn or pre-tectonic magmatic rocks within a sedimentary succession in fact is capable of altering the geometry future thrust propagation, can increase the wavelength of individual thrusts and can locally bend the strike of the deforming thrust belt (Villaroel et al., 2017).

The influence of pre-Andean deformation events exerts a prime role in the current structural configuration of Andean thrust belts. In fact, numerous balanced cross sections for the Southern Central Andes along the inner forearc of Chile and retro arc of western Argentina show how positive tectonic inversion explains most of the structural styles developed within thrust belts at both sides of the range. Particularly, extensional structures in thrust belts of the northern Chile Andes can be observed in the current architecture, as tectonic shortening there has been moderate (Arriagada et al., 2006; Gallardo, 2015; Martínez et al., 2016; Labbé et al., 2018; Fuentes et al., 2018). In the Puna Andes of northwestern Argentina (Allmendinger and Gubbels, 1996; Kley and Monaldi, 2002) as in the Andes of Central Chile and Argentina (Ramos et al., 2002; Giambiagi and Ramos, 2002; Charrier et al., 2002; 2015; Farías et al., 2010; Giambiagi et al., 2014; Mescua et al., 2014; Jara et al., 2014; 2017; Tapia, 2015; Riesner et al., 2017), inversion of extensional basins preceded fold-and-thrust belt emplacement absorbing and geometrically constraining modern Andean deformation in great part.

Basin stratigraphy as well exerts control on structure emplacement. An example can be found in the Malargüe fold-and-thrust belt, Argentine slope of the Southern Central Andes. Here, an eastward thinning of the wedge-shaped pre-orogenic basin involved in fold-and-thrust belt deformation is evidenced by pinch-outs of the Neuquen basin strata (Turienzo, 2010; Turienzo et al., 2012). Particularly, these pinch-outs define thrust ramp terminations which result in localizations for regional anticlines of the Malargüe fold-and-thrust belt. Jara et al. (2014 and 2017) demonstrated how gradients in pre-orogenic extension indeed influence the structural array resulting from posterior tectonic inversion in both cross-section and map view. The results of Jara et al. (2014 and 2017) gave insight into the tentative distribution of the Eocene-early Miocene Abanico Formation along central and southern central Chile, which was inverted in the initial phase of modern Andean orogeny (Charrier et al., 2002; Farías et al., 2010).

The occurrence of basement heterogeneities such as, basin shape, crystalline basement rocks protruding out of the overlying basin infill, or pre-existing basement-involving faults compartmentalizing the sedimentary basin to-be-deformed, all define the future map-view of the deforming region (e.g., Marshak, 2004). For example, Allmendinger and Gubbels (1996) attribute the along-strike morphostructural segmentation of the Central Andean retro arc thrust belt to latitudinal variations in availability of sedimentary succesions to be accreted into the wedge tip. Torres-Carbonell et al. (2016) reproduced thrust belt development in the Argentine Patagonia using analogue models to show the influence of backstop shape in rotation patterns in the map view. In other analogue model, Herrera et al. (2017b) showed how previously developed structures parallel to the convergence vector do not alter the first order main kinematics of a doubly-vergent deforming wedge, but they do define boundaries for compartmentalization of the deformation within the wedge. Strike-slip faulting is also present in such a setting when the convergence vector has a component of rotation.

Geophysically constrained contrasts in basement composition underlying deforming sequences correlate with the localization of crustal detachments for the Precordillera, La Ramada and Aconcagua fold-and-thrust belts of the Southern Central Andes (Mescua et al., 2016). However, these contrasts are subtle and might as well be a product of the inherited pre-Andean basement structure or thermal layering of the crust due to magmatic arc processes. Determinations of the rheological layering of the crust below central Chile show good correspondence with structures constrained palinspastically interpreted as first-order detachments for retro arc thrust belt development (Farías et al., 2010).

5.2. A comparison between the model and the high Andes of northern Chile.

The broad variety of analogical and numerical models on shortening of the lithosphere combined with published first order geological and geophysical data provides insight into the Cenozoic tectonic evolution of the Andes. Because the analogue subduction wedge model presented in this work evolves under boundary conditions matching the Andean geodynamic setting (details in Chapter 3), the model might have a good correspondence with key tectonic features of the Central and Southern Central Andes. There is, in fact, a similarity between model evolution and the first order cross-sectional structure, kinematics and distribution of tectonic shortening in the Andes (details in Chapter 3). This suggests that the orogenic wedges underlying the Andes work in close association with their corresponding rates of crustal accretion entering from the eastern foreland. Wedge mechanics observed in the model offer additional insight into the internal kinematics, strain distribution and material rotations inside the high Andes, and as well for other mountain belts.

The high Andes of northern Chile shows several first order features that allow to frame its structural development and current state in the context of the working models on shortening of the lithosphere presented in this work and available in the scientific literature. Furthermore, Andean segmentation (i.e. the contrast between segments of the range at different latitudes) offer a space-for-time representation for the evolution of the orogenic topography of the range in terms of end members for the growth of a crustal-scale orogenic wedge (*sensu* Jamieson and Beaumont, 2013). Accordingly, in this section, the prime characteristics of the structure and stratigraphy of the high Andes (Western Cordillera along the axis of the volcanic arc), and history of Andean orogeny in northernmost Chile will be briefly discussed in terms of subduction wedge models.

The retro wedge of the Central Andes at 19°-20°S: The forearc Precordillera and Western Cordillera of northern Chile

The Forearc Precordillera and Western Cordillera (active volcanic arc), which, flank together the Altiplano plateau to the west (Figure 1). Here, Andean morphology is remarkably different in comparison to that of the Southern Central Andes, as width of the range reach a maximum (c. 700 km) in consistency with maximum values of tectonic shortening (330 km e.g., McQuarrie, 2002). The range is mainly characterized by the large Altiplano plateau, which is bounded to the west by the aforementioned Forearc Precordillera and Western Cordillera, and to the east by the Eastern Cordillera, Interandean Zone and Subandean Sierras. The large size of the Andes at this latitude has been attributed to the hundreds of kilometers of (essentially Neogene) tectonic shortening at the retro-arc, and subsequent thickening in response to westward subduction of the Brazilian craton (Isacks et al., 1988; Sheffels, 1995; Baby et al., 1997; Beck and Zandt, 2002; McQuarrie, 2002). At the plateau flanks, orogenic thicknesses reach maximum values: the moho is located at depths of 65 to 75 km (Yuan et al., 2000).

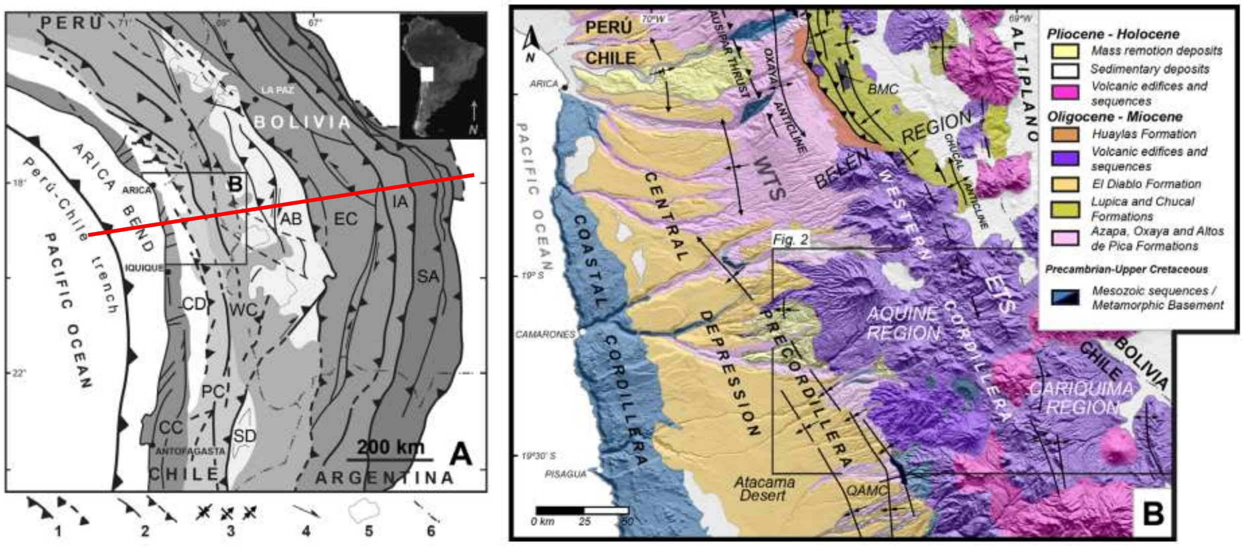

Figure 1. A. Physiography of the Central Andes and thrust systems that define the limits of labeled morphostructural provinces. Red line in **A** corresponds to the location of the cross-section of fig. 3. The Interandean Zone is included as part of the eastern margin of the Eastern Cordillera. **SA:** Subandean ranges; **IA:** Interandean ranges; **EC:** Eastern Cordillera; **AB:** Altiplano Basin; **WC:** Western Cordillera; **PC:** Precordillera; **CD:** Central Depression; **CC:** Coastal Cordillera; **SD:** Salars Depression; (Modified from Charrier *et al*., 2013); **B.** Simplified geological map of northernmost Chile (~18°30'-19°30' S) (Modified from García *et al*., 2004, 2011; Charrier *et al*., 2007, 2013; Cortés *et al*., 2012a). **BMC:** Belén Metamorphic Complex; **QAMC:** Quebrada Aroma Metaturbiditic Complex; **WTS:** West Vergent Thrust System; **ETS:** East Vergent Thrust System. Simbology: **1.** Major thrusts; **2.** Secondary faults and structural alignments; **3.** Syncline, anticline and monocline axis; **4.** Strike-slip direction of displacement; **5.** Major lakes and salars; **6.** International border. Figure adapted from Herrera et al. (2017a).

The structure of the Forearc Precordillera (Figure 1) is characterized by the occurrence of orogen-parallel west-vergent monoclines rooted at east-dipping, high-angle thrusts of the West-vergent Thrust System (Muñoz and Charrier, 1996; García et al., 2004; Victor et al., 2004; Farías et al., 2005 WTS in Fig. 1). The stratigraphy consists of a Paleozoic-Mesozoic substratum above which synorogenic gravels and ignimbrites were deposited in strong angular unconformity, concomitant to development of the WTS (e.g., Muñoz and Charrier, 1996; Pinto et al., 2004; Farías et al., 2005). Above the structures of the system (e.g., Moquella, Aroma, Soga and Cala-Cala monoclines), westward-fanning growth strata in gravels and ignimbrites have been generated synchronic to c. 700 m of vertical fault displacements at ~19.5°S and have allowed to constrain this deformation to the late Oligocene to late Miocene (Pinto et al., 2004; Farías et al., 2005).

Using similar stratigraphic markers, Farías et al. (2005) have measured c. 2 km of modern vertical uplift at 19.5°S. At c. 21°S, the structural reconstructions Victor et al. (2004) indicate ~2.6 km of uplift. In northernmost Chile, at 18.5°S, 1 km of vertical uplift has been ascribed to the WTS according to the balanced cross sections of García (2002). Structures inherited from previous tectonic events (likely the K-T orogenic event or "Incaic" event; Charrier et al., 2013) are currently accommodating tectonic shortening by sub-vertical displacements below the aforementioned monoclines and are thought to have accommodated most of the Cenozoic uplift of the Altiplano western flank (García et al. in prep). The system is considered to be migrating towards the west into the Central Valley since middle Miocene times, as shown by geomorphic and stratigraphic markers (Farías et al., 2005). The westward migration of the thrust belt has been also determined by balanced structural sections (e.g., García, 2002; Victor et al., 2004). Because of the shallow seismicity focalized in the downward prolongation of structures of the WTS, in addition to the active character of forearc seismicity in the region, the system is considered active until Present (David et al., 2002; Farías et al., 2005). An intra-crustal discontinuity defined as a low-velocity zone beneath the Altiplano coincides with the in-depth position of the main detachment of this structural system (Altiplano Low Velocity Zone of Yuan et al., 2000 in Victor et al., 2004; Farías et al., 2005).

Regardless of the important uplift generated by these structures, the WTS has absorbed little tectonic shortening (~2.5 km at 21°S, Victor et al., 2004; <7 km at 18.5°S; García, 2002). A maximum of ~12 km was measured for the Precordillera thrust belt by Gallardo (2015); who also described the inversion of Mesozoic extensional basins as fundamental for structuration of the Altiplano western flank. These values of shortening are in striking contrast with the values measured along the Altiplano eastern flank. There, Andean fold-and-thrust belts have accommodated several hundreds of km of plate convergence during Cenozoic times. These differences in shortening rates from one side of the Andes to the other are key to extrapolate the subduction wedge model to this prototype, as discussed further below.

Within the axis of the Western Cordillera, Upper Cretaceous and Eocene volcanic layers are uplifted above younger Cenozoic sequences by means of high-angle, east-vergent thrusts parallel to the orogen axis (Valenzuela et al., 2014; Herrera et al., 2017a). The Upper Cretaceous rocks are the substratum of late Miocene to Pleistocene and recent volcanoes, which edifices are well preserved due to hyper arid conditions (Valenzuela et al., 2014; Morandé et al., 2015; Herrera et al., 2017a). Recently published updated stratigraphy of the area allows to constrain this deformation as early as Eocene and opens the possibility of important pre-Eocene faulting given angular discordance of Upper Cretaceous strata below Eocene tuffs (Herrera et al., 2017a). This fact greatly extends the span of Andean deformation in the area, which was considered to be essentially Miocene in previous works (e.g., Pinto et al., 2004; Farías et al., 2005). It also allows to relate deformation in the Western Cordillera with pre-Cenozoic (Paleogene) deformation taken place within the Altiplano interiors. There, the sedimentology and provenance of mostly buried foreland sequences suggests the presence of an east-vergent fold-and-thrust belt located at the current Western Cordillera, that provided a >6 km-thick pile of foreland sediments to the adjacent basin during the Paleogene (Horton et al., 2001; 2002; Charrier et al., 2013).

Towards the Altiplano, the predominantly Miocene sequences of the Western Cordillera are gently deformed by a set of ~N-S trending, east-vergent monoclines that compose the East-vergent Thrust System (Charrier et al., 2005; Cortés et al., 2012; ETS in Fig. 1) which bounds the Western Cordillera to the east. The system is superimposed to previous deformation events but share the structural trend and geometry of the thrust involving rocks of Upper Cretaceous and Eocene ages mentioned in the previous paragraph. The ETS (19-3 Ma) is synchronous to the WTS (>25 Ma) (Herrera et al., 2017a) and is geometrically similar: monoclines are developed adjacent to synchronically developed growth strata which in this case, fan towards the east (Cortés, 2011; Cortés et al., 2012). Structural balancing of the ETS shows how the system might be rooted at a detachment located 12 km below surface (Fig. 3, Cortés et al., 2012), and connected in depth with the Altiplano Low Velocity Zone of Yuan et al. (2000), and the Quebrada Blanca Bright Spot (QBBS; Victor et al., 2004) where the WTS is also rooted. Cortés et al. (2012) and Herrera et al. (2017a) connect the ETS with the WTS (Fig. 2), including the structure of the Western Cordillera and proposing a doubly-vergent crustal-scale "pop-up" structural model for the Atiplano western flank. The structure illustrated in Fig. 2 certainly defines a wedge geometry, in which deformation localizes at the western side and propagates towards the east above a crustal-scale fault ramp.

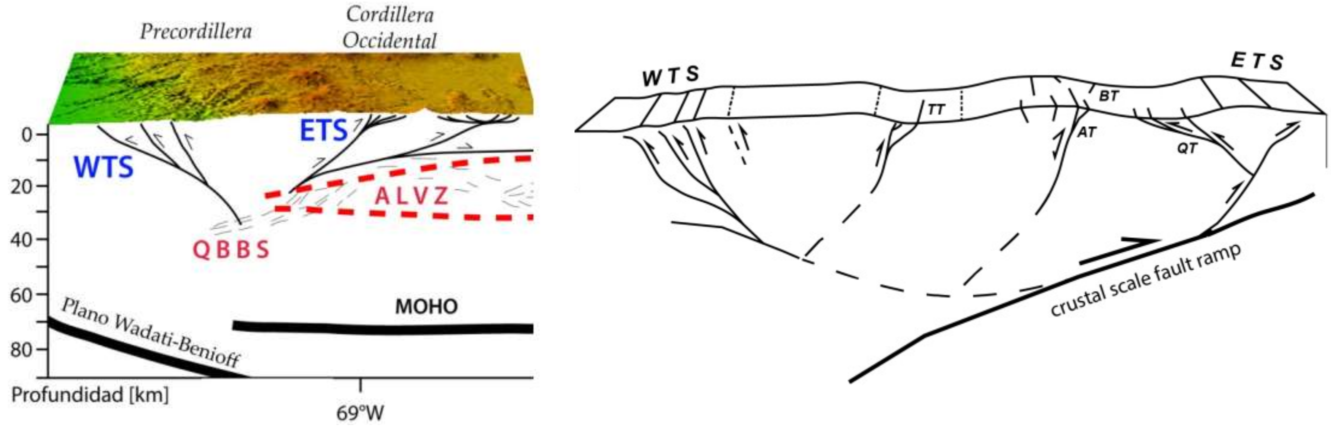

Figure 2. Crustal-scale models for the structure of the Altiplano western flank. Left panel: Cortés et al. (2012). Right model: Herrera et al. (2017a).

If this doubly-vergent system is considered in a broader spatial context, it does terminate towards the west with the western monoclines of the WTS, but, towards the east, the actual termination of the east-vergent structures of the system is obscured by the thick infill of the Altiplano. The scarce outcrops of foreland deposits in the Altiplano interiors suggest that the ETS might be an expression of the recent activity at the hinterland of the hypothetical buried fold-and-thrust belt proposed by Horton et al. (2001; 2002). McQuarrie et al. (2005) indeed proposes that deformation of the Central Andes initiated at the current Western Cordillera considering Paleogene and even late Cretaceous deformation events recorded in the

Salar de Atacama (e.g., Arriagada et al., 2006; Bascuñán et al., 2016). In a recent contribution, Martinod et al. (2020) proposed that initial growth of the Altiplano started with the growth and expansion of one crustal-scale wedge located at the Present-day Western Cordillera during the late Cretaceous and developing continuously during the Paleocene and Eocene. During the late Eocene to Oligocene, a second crustal wedge would have started growing at the eastern Altiplano flank resulting in the current structure of the orogen at this latitude. The combined chronology of deformation and crustal structure of the western flank allows to propose a subduction wedge model for this part of the Andes. Figure 3 summarizes this proposition in the context of the Central Andes. The cross-section runs parallel to the orogen at c. 20°S and offers an alternative structural model for the eastern Altiplano, which is also interpreted in terms of a subduction wedge model in the figure.

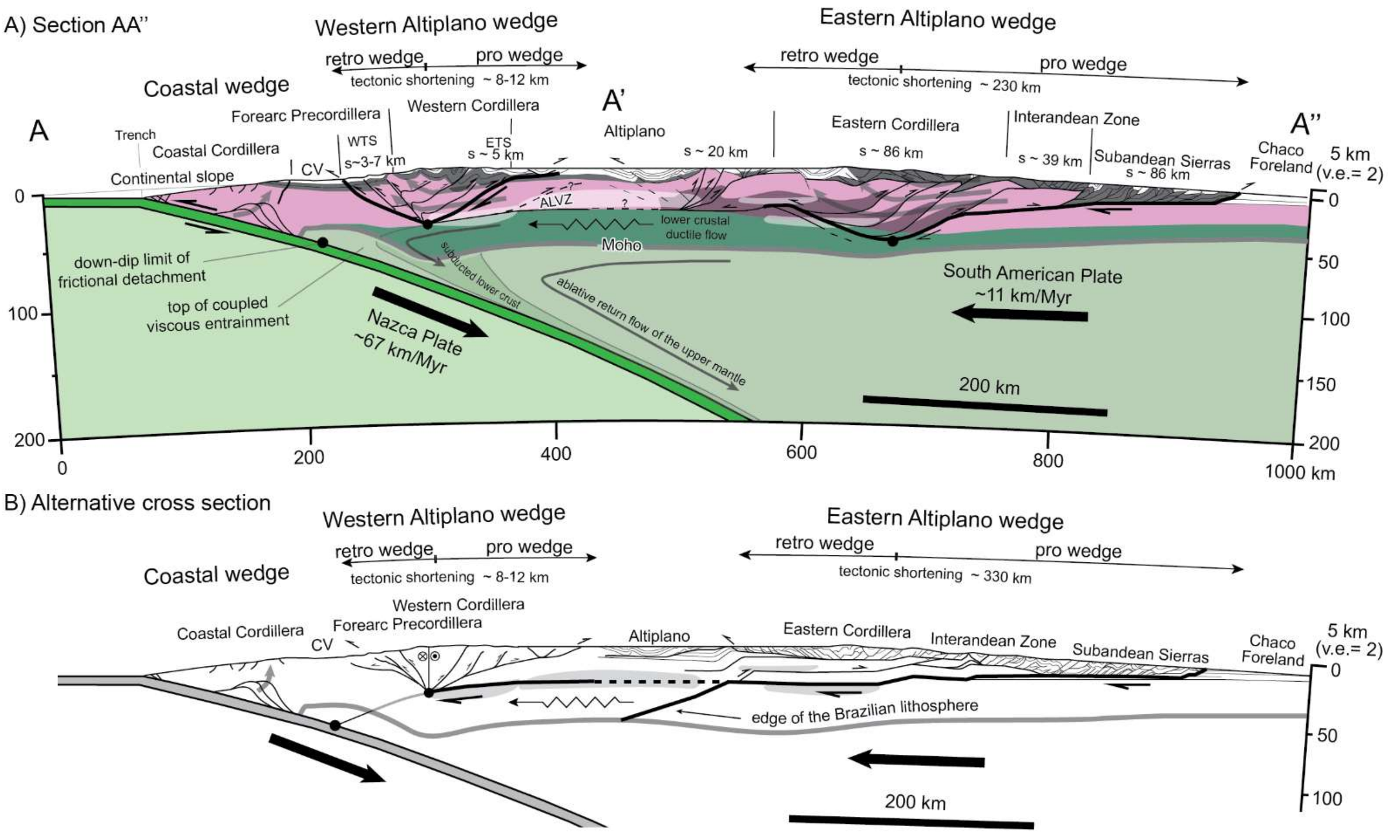

Figure 3. Subduction wedge model for the Central Andean structure between 19°S and 21°S, based on this study and the integration of crustal-scale cross-sections. Location of each cross section is outlined in Figure 7 of Herrera et al. (in prep.). For both cross-sections, Coastal wedge structure is based on Hartley et al. (2000), David et al. (2002) and Farías et al. (2005). Western Altiplano wedge structure is based Farías et al. (2005), Charrier et al. (2013), Herrera et al. (2017) and Cortés et al. (2012) and based on Victor et al. (2004) and Cortés et al. (2012) in B. In **A.**, Eastern Altiplano wedge structure is based on Baby et al. (1997) and, in **B.**, is based on McQuarrie (2002) and Victor et al. (2004). Features shown in the middle-lower crust: ALVZ (Altiplano Low Velocity Zone), from Yuan et al. (2000); zone of ductile crustal flow is redrawn after Isacks, (1988) in McQuarrie (2002); shaded gray areas (low velocity zones), Moho and edge of the Brazilian lithosphere are redrawn from Beck and Zandt (2002) in McQuarrie (2002).

Abbreviations: CV: Central Valley; WTS: West-vergent Thrust System; ETS: East-vergent Thrust System. Thick solid lines beneath each crustal wedge indicate main detachments in the continental lithosphere. Black dots represent inferred S-points for each crustal wedge. The ablative return flow of the continental mantle and locus of coupled viscous entrainment drawn after Pope and Willett (1998).

The WTS would correspond to the retro-shear zone of a crustal-scale subduction wedge, accommodating low tectonic shortening but focusing uplift (analogous to low displacements in the rear of the model wedges of chapters 2 and 3). The WTS is a structural system of a main Neogene activity (>25 Ma; Herrera et al., 2017a), that could as well be as old as the K-T boundary (García et al. in prep.). Changes in the style of deformation concentrated above the structures of the WTS are related to changes in the depth to decollement of the system, which could be explained by a thickening of the wedge, or a deepening of the S-point of the wedge system. This particular geometrical change takes place during the Eocene (García et al., in prep.), roughly coeval to emplacement of the Eastern Cordillera at the eastern Altiplano flank. Topography of the Forearc Precordillera as well is characteristic to that of a retro-side of many mountain belts as shown by Vietor and Oncken (2005). By the other hand, the ETS would correspond to the pro-shear zone of the subduction wedge, right between the uplifting core region and the rest of the pro-side, which, in case of the Altiplano is thought to be buried. In the ETS, little shortening is as well absorbed, and structural vergence is opposite to that of the retro-side.

For the eastern Altiplano wedge, several studies have deciphered in detail structural aspects as well as the history of uplift in this region. Particularly, the model presented in this thesis was based on the works of McQuarrie (2002), and Baby et al. (1997). Applications of a subduction wedge model for this part of the range have can be found in the works of Roeder (1988) and Anderson et al. (2018). The fact that the eastern side of the Andes grows in close relationship with accretionary events, particularly west-directed (crust accretes from the east into the orogen) and dependent on basement underthrusting, allows to conclude that influence of the oceanic plate is restricted to a second order. It could be possible that ocean-continent subduction might stand as a boundary condition for Andean growth, rather than a potential driver for orogenic processes inland. Martinod et al. (2020) proposed that the Nazca plate (and former oceanic plates) is in fact capable of inducing crustal wedge nucleation in the retro arc as a consequence of slab flattening processes affecting mantle flow and the lower crust. Causes for S-point nucleation cannot be addressed in this work as it escapes its scientific scope. However, the scope does allow to stress the fact that Andean deformation might be mainly accretion-driven, and that this mechanism is certainly decoupled from processes acting upon the ocean-continent subduction boundary, such as plate coupling (also known as decollement stresses; e.g., Lamb, 2006).

The analogue model in which Fig. 3 is based as well gives additional insight into the mechanisms of crustal accommodation involved in orogeny of the Central Andes. Frontal accretion is concentrated at the critically-tapered pro-sides of the subduction wedges (e.g., Roeder, 1988; Anderson et al., 2018) and the localization of anticlinal stacks or regional synclines occurs by combined frontal and basal accretion. Pro sides accommodate most of the system's convergence at the eastern Altiplano wedge, whilst this parameter is obscured in the western Altiplano wedge by the presence of the recent Altiplano infill. Accretion at the base occurs in the internal parts of the wedges (retro and pro wedge limits), and below this part is where the S-points of each system are hypothetically located, drawn matching greatest crustal thicknesses and superficial shift of vergence. Towards the west, along the retro-sides, moderate shortenings have been absorbed by the wedge, but there is enhanced uplift by accommodation of materials at the rear from the pro-side. Tectonic transport at the western Eastern Cordillera is indeed directed towards the west along the backthrust zone (e.g., McQuarrie, 2002).

Particularly at the western Altiplano flank, top-to-the-left or westward tilting of the range (e.g., Riquelme et al., 2007) can be explained by the sense of solid body rotations observed in the analogue models of this work (Chapter 2 and Chapter 3). Another key aspect shown in our models is the rearward detachment of the retro wedge from its base when shortening at the pro-side is large. In fact, there is a westward progradation of the WTS since the late-Miocene shown by the westernmost flexures of the structural system. This westward migration of the WTS is coeval to >150 km of shortening absorbed within the Subandean Sierras since 12 to 8 Ma until present. This region is also where maximum accretionary fluxes enter the orogen from the eastern Altiplano flank (Chapter 3). There are two options to explain the rearward expansion of the western Altiplano wedge in relationship with crustal shortening at the eastern Altiplano wedge. The first option is enhanced retrocharriage within the belt generated by high accretionary flux, to create the space to accommodate the material accreted at the Subandean Sierras, and the second option is the basal accretion at the western Altiplano wedge by the westward flow of lower crustal materials from the east, in response to westward underthrusting of the Brazilian craton.

Despite the fact that the Coastal Cordillera is not included in the structural configuration of the Altiplano plateau, the system is fundamental for the processes operating in the plateau's infrastructure. As in the model of Chapter 3, slow growth of the Coastal Cordillera is a result of no accretion at the toe of the subduction wedge. The margin is erosive and there is extension at the submerged continental slope. Details on the modeling of the Coastal wedge are outlined in Chapter 3. A space "problem" regarding the fate of the subducted crust beneath the orogen from the west arises if this material is not removed from the base of the orogen. Several mechanisms have been invoked to explain lower crustal removal, such as delamination subsequent to eclogitization of the subducted crust (e.g., Beck and Zandt, 2002). In fact, Pope and Willett (1998) simulated plateau growth in the Central Andes by a model of ablative subduction. The cited model is capable of reproducing the thermal structure of the orogen but fails to yield a realistic structure for the

Andean margin. The mechanism of ablation consists in the coupled subduction of the oceanic plate with crustal materials of similar density (Tao and O'Connell, 1992). In this case, the lower Andean crust subducting westwards below the forearc from the east would be removed efficiently from the bottom of the Western Cordillera and Forearc by this mechanism, and as well might apply to the entire margin.

The fact that the Central Andes and a subduction wedge model might have a good correspondence opens the possibility of proposing such a model for the Andes in its entire extent. This suggests that the different cordilleras composing the Andes south of the Altiplano and Puna as well are underlain by a subduction wedge, as illustrated in Chapter 4 of this work. At the Southern Central Andes, for example, crustal structure and surface geology of the Coastal Cordillera suggests that the range is underlain by a subduction wedge complex that works in association with the Nazca plate (e.g., Comte et al., 2019). Towards the east, the Main Cordillera is underlain by another subduction wedge, grown by accretion from the eastern foreland, in association with subduction of the South American basement. The rates of retro arc accretion (accretionary flux) increase towards the north, and account for the expansion of the wedge underlying the Main Cordillera, its coalescence with the Coastal Cordillera along central Chile (rearward detachment of the Cordilleran retro wedge), and the formation of the wide Central Andes flanking the Altiplano and Puna.

The latitudinal morphostructural segmentation of the Andes allows to frame the orogen in the context of a main evolutionary growth sequence, as proposed by Jamieson and Beaumont (2013). From the subduction wedge perspective for orogenesis (e.g., Willett et al., 1993), it is known that key factors governing orogenic style are the accumulation of mass from crustal and mantle sources (magnitude, M) and a corresponding increase in temperature (T; Jamieson and Beaumont, 2013). The Andes display the characteristics of end-member states in the Temperature-Magnitude (T-M) framework for the growth of an orogen by crustal accretion. At first, a brief description of the Southern Central Andes is given to show the correspondence of this part of the range with the structure and dimensions of a "small" orogen (Fig. 4). I caution that this comparison is not including temperature and is made for general reference. Finally, the Central Andes are shown in context of the growth sequence as a "large-hot" orogen (Fig. 4).

Along the Southern Central Andes, the high elevations define a narrow, ~120 km-wide, mountain range, which sides are symmetric (~60 km each) and is bounded by asymmetric thrust belts that allow to define pro- (Argentine side) and retro-sides (Chilean side). The retro arc fold-and-thrust belt of this segment has accommodated about 80% of the total shortening absorbed within the orogen. The forearc thrust belt has only accommodated the remaining 20%, with a structural style of basin inversion attained prior to the emplacement of the retro-arc fold-and-thrust belt. The structural system of the Chilean side is thought to have remained stable since the beginning of modern orogeny in this part of the range (e.g., Farías et al., 2008), and thus has remained static throughout, as in a retro side of a subduction wedge model. In turn, the retro arc fold-and-thrust belt has migrated eastward continuously as a pro side of a subduction wedge model. In fact, the fold-and-thrust belt has incorporated basement slices of the Frontal Cordillera since c. 8 Ma, coeval with large uplift of the western side (c. 2 km). There is then a good fit between a subduction wedge model and the orogenic structure of this part of the range (detail of such an extrapolation in Chapter 3). Finally, beyond the scope of this work is the polarity of subduction and main orogenic vergence in this region (~33.5°S). Two models have been proposed to explain crustal-scale structure (Armijo et al., 2010; Farías et al., 2010). The model of Farías et al. (2010) is greatly favored as the proposed structure is constrained seismologically and supported by rheological analyses for the Chilean forearc. The results of this thesis as well favor the model of Farías et al. (2010), as it tests the proposition of such model (orogenic growth in association with westward subduction of the South American basement) finding good fit with the geology and geophysical structure of the range at these latitudes (details in Chapter 3).

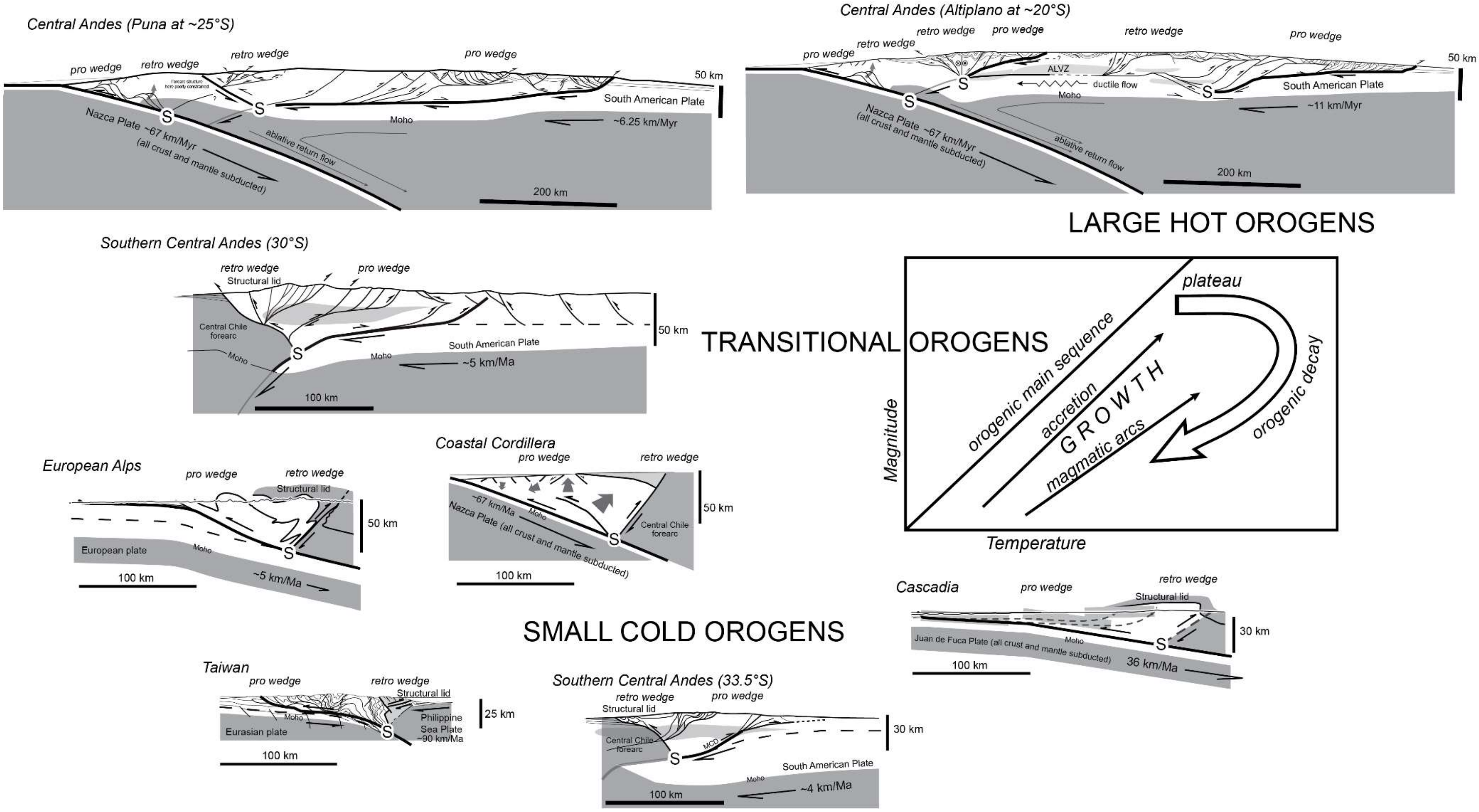

Figure 4. Conceptual orogenic temperature-magnitude (T-M) diagram showing growth from small-cold to large-hot orogens (after Jamieson and Beaumont, 2013). In convergent orogens, increasing magnitude and temperature both result from accretion and thickening of crustal materials.

5.3. Further Research.

To further validate the subduction wedge model proposed in this work, several complementary studies to be carried out in the Central Andes are proposed in this short sub-section.

- The stratigraphy and structure beneath the Forearc Precordillera and westernmost Altiplano should be precisely determined. Despite hyper-arid conditions preserving the geological record, thick sedimentary and volcanic successions have covered most exposures, which are only found in deeply-incised gorges. In fact, recent publications have addressed the subsurface stratigraphy of the Forearc Precordillera of northern Chile at higher latitudes (e.g., Fuentes et al., 2018; Labbé et al., 2018; Martínez et al., 2021), finding buried thrust belts with great influence of previous deformation regimes (extensional structures with an imprint of inversion, accommodating a very subdued shortening). However, there is little availability of seismic reflection profiles and thus it is necessary to constrain subsurface structure using alternative approaches such as geomorphological indicators (e.g., García and Hérail, 2005; Farías et al., 2005) or structural modeling applied to structures exposed in surface (e.g., Victor et al., 2004). Forward modeling of the Precordillera structure has been recently provided in the unpublished work of García et al. (in prep.), offering valuable insight into the pre-Cenozoic structure of the buried thrust belt of the Precordillera at ~19.5°S. The same is suggested for the determination of structure and detailed stratigraphy of the westernmost Altiplano, as there is very little available information for this region (e.g., Horton et al., 2001; 2002; Cortés, 2011; Cortés et al., 2012).

- Numerical mechanical models for shortening of the lithosphere might offer insight not only to the structural evolution of mountain belts, but into the interaction of the main orogenic growth history with the effects of erosion, temperature, rheological layering of the crust, amongst other factors modulating orogenic evolution (e.g., see limitations of the modeling approach at the beginning of this chapter). For example, Willett et al. (1999) provided a wide variety of numerical tectonic models influenced by climatic erosion affecting one side or both sides of the model mountain belt. Different configurations result from the modeling, depending on magnitude and localization of erosion. The underlying theoretical basis of the mechanical model is the same implemented in Willett et al., 1993. In a similar approach, Beaumont et al. (2000) explored combinations of mechanical models of lithospheric shortening with the effects of climatic erosion and influence of previous extensional structure to the Pyrenees, complemented with thermochronology and available balanced cross sections. Works of this same research scope have addressed the evolution of New Zealand, Taiwan, and the European Alps among many others (e.g., Jamieson and Beaumont, 2013). I suggest that this type of approach is ideal for the exploration of the correspondence between a subduction wedge model and Andean structure, as it is cheap, applicable to the Andes in its entire extent (great tectonic and climatic variability), and as it has been tested in many different orogens (small orogens, transitional orogens and plateau orogens) with characteristics matching the Andean prototype, developed in different tectonic settings (Jamieson and Beaumont, 2013).

6. CONCLUSIONS

1. Simple comparisons between mechanical models for shortening and thickening of the lithosphere and the geology of the Central and Southern Central Andes suggest that the cordilleras of this range behave mechanically as doubly-vergent, crustal-scale orogenic wedges, each one in association with a corresponding subduction mega-thrust. The Coastal wedge is an active and long-lived (late Paleozoic) ocean-continent non-accretionary to intermediate-accretionary wedge. The wedge underlying the high elevations of the Central Andes would correspond to another active, fully accretionary orogenic wedge, rapidly growing since late Cretaceous times and throughout the Cenozoic due to westward subduction of the South American craton.
2. Considering boundary conditions of the analogue modeling approach, key aspects of the models are compared to major structural features of the Central Andes. The distributed zone of deformation developed in the pro-side of the model wedge is analogue to the fold-and-thrust belts propagating foreland-ward throughout Argentina and Bolivia. The focused zone of deformation developed in the retro-side of the model is analogue to the west-vergent thrust systems developing along the Western Cordillera. Here, the Miocene propagation of the thrust systems of the western Andean front finds good correspondence with the rearward expansion of the analogue wedges when cumulative subduction and shortening have been high. This suggests that this westward propagation of the Andean front might be in response to the accommodation of material incorporated from the east during the emplacement of the Subandean Sierras.
3. The growth of particular segments of the Central Andes can then be envisioned as a consequence of wedge expansion and coalescence. The southern sector of the Central Andes would represent an initial or early phase of Andean orogenic evolution, with two cordilleras separated by a central valley. The Central Andes at the latitudes of the Altiplano and Puna would represent an advanced state, more evolved, or late phase of Andean orogeny. In between, the region known as *Norte Chico*, where there is no central valley between the cordilleras, would represent a zone where the orogenic wedges underlying the cordilleras coalesce. At different latitudes, the Andes would represent endmembers in the context of the growth of an orogenic wedge (magnitude-temperature framework for orogenesis). The southern sector of the Central Andes corresponds to a “small-warm” orogen. Northwards, the high Andes corresponds to a larger “transitional orogen”. Finally, the Central Andes (at the latitudes of the Altiplano and Puna) corresponds to a “large-hot” orogen.

7. BIBLIOGRAPHY

Allmendinger, R. W., D. Figueroa, D. Snyder, J. Beer, C. Mpodozis, and B. L. Isacks, 1990, Foreland shortening and crustal balancing in the Andes at 30S latitude: Tectonics, v. 9, p. 789–809.

Allmendinger, R.W., Gubbels, T. 1996. Pure and simple shear plateau uplift, Altiplano-Puna, Argentina and Bolivia. Tectonophysics 259, 1–13.

Allmendinger, R. W., Jordan, T. E., Kay, S. M., & Isacks, B. L. 1997. The evolution of the Altiplano-Puna plateau of the Central Andes. Annual Review of Earth and Planetary Sciences, 25(1), 139–174. doi:10.1146/annurev.earth.25.1.139

Anderson, R.B., Long, S.P., Horton, B.K., Calle, A.Z., Ramirez, V., 2017. Shortening and structural architecture of the Andean fold-thrust belt of southern Bolivia (21 degrees S): Implications for kinematic development and crustal thickening of the Central Andes. Geosphere 13, 538–558.

Anderson, R. B., Long, S. P., Horton, B. K., Thomson, S. N., Calle, A. Z., & Stockli, D. F., 2018. Orogenic wedge evolution of the central Andes, Bolivia (21°S): Implications for Cordilleran cyclicity. Tectonics. doi:10.1029/2018tc005132

Argand, E., 1916. Sur l'arc des Alpes occidentales: Ecologae Geologicae Helvetiae, v. 14, p. 145-191

Armijo, R., Rauld, R., Thiele, R., Vargas, G., Campos, J., Lacassin, R., Kausel, E., 2010. The West Andean Thrust, the San Ramon Fault, and the seismic hazard for Santiago, Chile. Tectonics 29 TC2007

Arriagada, C., Cobbold, P.R., Roperch, P., 2006. Salar de Atacama basin: a record of compressional tectonics in the Central Andes since the mid-cretaceous. Tectonics 25.

Arriagada, C., Roperch, P., Mpodozis, C., Cobbold, P.R., 2008. Paleogene building of the Bolivian Orocline: Tectonic restoration of the Central Andes in 2-D map view. Tectonics 27 TC6014.

Baby P, Rochat P, Mascle G, Hérail G. 1997. Neogene shortening contribution to crustal thickening in the back arc system of the Bolivian Orocline (Central Andes). Geology 25:883–886

Babeyko A., Sobolev, S. 2005. Quantifying different modes of the Cenozoic shortening in the Central Andes. Geology v. 33. n. 8. p. 621-624.

Bahlburg, H., & Hervé, F. 1997. Geodynamic evolution and tectonostratigraphic terranes of northwestern Argentina and northern Chile. Geological Society of America Bulletin, 109(7), 869–884. doi:10.1130/0016-7606(1997)109<0869:geatto>2.3.co;2

Bally, A. W., 1975, A geodynamic scenario for hydrocarbon occurrences: Proc the 9th World Petrol.Congr., Tokyo, v. 2 (Geology), Applied Sci. Pub., Ltd., Essex, England, p. 33-44

Bascuñán, S., Arriagada, C., Le Roux, J., Deckart, K., 2016. Unraveling the Peruvian phase of the Central Andes: stratigraphy, sedimentology and geochronology of the Salar de Atacama Basin (22°30–23°S), northern Chile. Basin Res. 28, 365–392

Batchelor, G., 1967. An Introduction to Fluid Dynamics. 615 pp., Cambridge University Press, New York.

Barnes J.B., Ehlers T.A., 2009. End member models for Andean Plateau uplift. Earth Sci Rev 97:105–132

Beaumont, C., Kamp, P. J. J., Hamilton, J., & Fullsack, P. 1996. The continental collision zone, South Island, New Zealand: Comparison of geodynamical models and observations. Journal of Geophysical Research: Solid Earth, 101(B2), 3333–3359. doi:10.1029/95jb02401

Beaumont, C., Muñoz, J.A., Hamilton, J., Fullsack, P. 2000. Factors controlling the Alpine evolution of the central Pyrenees inferred from a comparison of observations and geodynamical models: Journal of Geophysical Research, v. 105, p. 8121–8145, doi:10.1029 /1999JB900390.

Beaumont, C., Jamieson, R.A., Nguyen, M.H., Medvedev, S. 2004. Crustal channel flows: 1. Numerical models with applications to the tectonics of the Himalayan-Tibetan orogen. J. Geophys. Res. 109

Beck, SL, Zandt, G., 2002. The nature of orogenic crust in the central Andes. J Geophys Res 107(B10):2230. doi:10.1029/2000JB000124.

Brandon, M.T., 2004. The Cascadia subduction wedge: the role of accretion, uplift, and erosion. In: van der Pluijm, B.A., Marshak, S. (Eds.), Earth Structure, An Introduction to Structural Geology and Tectonics, second ed. W.W. Norton & Company, Inc., New York, pp. 566–574.

Brooks, B.A., Bevis, M., Smalley Jr., R., Kendrick, E., Manceda, R., Lauría, E., Maturana, R., Araujo, M., 2003. Crustal motion in the Southern Andes (26–36 S): Do the Andes behave like a microplate? Geochemistry, Geophysics, Geosystems, 4(10).

Brooks, B.A., Bevis, M., Whipple, K., Arrowsmith, R., Foster, J., Zapata, T., Kendrick, E., Minaya, E., Echalar, A., Blanco, M., Euillades, P., Sandoval., M., Smalley Jr., R.J., 2011. Orogenic-wedge deformation and potential for great earthquakes in the central Andean backarc. Nature Geoscience. doi: 10.1038/ngeo1143

Brovarone, A.V., Agard, P., Monie, P., Chauvet, A., Rabaute, A. 2018. Tectonic and Metamorphic Architecture of the HP Belt of New Caledonia. Earth-Science Reviews. v.178, p. 47-67

Brown D., Alvarez-Marron J., Perez-Estaun A., Gorozhanina Y., Baryshev V., Puchkov V. 1997. Geometric and kinematic evolution of the foreland thrust and fold belt in the southern Urals. Tectonics 16:551–562

Bonnet, C., Malavieille, J., & Mosar, J., 2007. Interactions between tectonics, erosion, and sedimentation during the recent evolution of the Alpine orogen: Analogue modeling insights. Tectonics, 26(6), n/a–n/a. doi:10.1029/2006tc002048

Boyce, D., Charrier, R., Farías, M. 2019. The First Andean Compressive Tectonic Phase: Sedimentologic and Structural Analysis of Mid-Cretaceous Deposits in the Coastal Cordillera, Central Chile (32°50′S). Tectonics, v. 39, Issue 2. doi:10.1029/2019TC005825

Boyer, S. E. 1995. Sedimentary basin taper as a factor controlling the geometry and advance of thrust belts. American Journal of Science 295,122&1254.

Buiter, S. 2012. A review of brittle compressional wedge models. Tectonophysics, 530-531, 1–17. doi:10.1016/j.tecto.2011.12.018

Burov, E. B., 2010. "Plate Rheology and Mechanics". In Watts, Anthony B. (ed.). Crust and Lithosphere Dynamics: Treatise on Geophysics. Elsevier. p. 100. ISBN 9780444535726.

Byerlee, J. D., 1978. Friction of Rocks. Pure and Applied Geophysics. 116 (4–5): 615–626. doi:10.1007/BF00876528

Byrne, D., Wang, W. and Davis, D. 1993. Mechanical role of backstops in the growth of forearcs. Tectonics 12, 1233144.

Chapple, W. M. 1978. Mechanics of thin-skinned fold-and-thrust belts. Geological Society of America Bulletin, 89(8), 1189. doi:10.1130/0016-7606(1978)89<1189:motfb>2.0.co;2

Chase, C. G., Sussman, A. J., & Coblentz, D. D. 2009. Curved Andes: Geoid, forebulge, and flexure. Lithosphere, 1(6), 358–363. doi:10.1130/l67.1

Charrier, R., Baeza, O., Elgueta, S., Flynn, J.J., Gans, P., Kay, S.M., Muñoz, N., Wyss, A.R., Zurita, E., 2002. Evidence for Cenozoic extensional basin development and tectonic inversion south of the flat-slab segment, southern Central Andes, Chile (33 degrees-36 degrees SL). J. S. Am. Earth Sci. 15, 117–139

Charrier, R.; Chávez, A.; Elgueta, S.; Hérail, G.; Flynn, J.; Croft, D.; Wyss, A.; Riquelme, R.; García, M. 2005. Rapid tectonic and paleogeographic evolution associated with the development of the Chucal anticline and the Chucal-Lauca Basin in the Altiplano of Arica, northern Chile. Journal of South American Earth Sciences 19: 35-54

Charrier, R., Pinto, L., Rodríguez, M.P., 2007. Tectono-stratigraphic evolution of the Andean orogen in Chile. In: Gibbons W, Moreno T (eds) Geology of Chile, Chapter 3. The Geological Society, London, Special Publication, pp 21–116

Charrier, R., Hérail, G., Pinto, L., García, M., Riquelme, R., Farías, R., Muñoz, N. 2013. Cenozoic tectonic evolution in the Central Andes in northern Chile and west-central Bolivia: Implications for paleogeographic, magmatic and mountain building evolution. Int J Earth Sci (Geol Rundsch) (2013) 102:235–264 DOI 10.1007/s00531-012-0801-4

Charrier, R., Ramos, V.A., Tapia, F., Sagripanti, L., 2015. Tectono-stratigraphic evolution of the Andean Orogen between 31 and 37°S (Chile and Western Argentina). Geol. Soc. Lond., Spec. Publ. 399, 13–61.

Comte, D., Carrizo, D., Roecker, S., Ortega-Culaciati, F., & Peyrat, S., 2016. Three-dimensional elastic wave speeds in the northern Chile subduction zone: variations in hydration in the supraslab mantle. Geophysical Journal International, 207(2), 1080–1105. doi:10.1093/gji/ggw318

Comte, D., Farias, M., Roecker, S., Russo, R., 2019. The nature of the subduction wedge in an erosive margin: Insights from the analysis of aftershocks of the 2015 Mw 8.3 Illapel earthquake beneath the Chilean Coastal Range. Earth Planet. Sci. Lett. 520, 50–62.

Cortés, J., Farías, M., Comte, D., Charrier, R., 2012. Estructuras y depósitos neógenos de la región de Cariquima (Altiplano Chileno): Implicancias en el origen de la Cordillera Occidental a los 19°30'S. Abstract presented at Congreso Geológico Chileno XIII, Antofagasta, Chile.

Cortés, J. 2011. Evolución depositacional y tectónica neógena del Altiplano Chileno entre los 19°22'S y 19°42'S. Thesis. Unpublished. Universidad de Chile. Santiago, Chile.

Cowan, D. S., and Silling, R. M., 1978. A dynamic, scaled model of accretion at trenches and its implications for the tectonic evolution of subduction complexes, J. Geophys. Res., 83(B11), 5389–5396, doi:10.1029/JB083iB11p05389

Dahlen, F. A., 1984. Noncohesive critical Coulomb wedges: An exact solution. Journal of Geophysical Research: Solid Earth, 89(B12), 10125–10133. doi:10.1029/jb089ib12p10125

Dahlen, F.A., and Suppe, J., 1988, Mechanics, growth, and erosion of mountain belts, *in* Clark, S.P., et al., eds., Processes in continental lithospheric deformation: Geological Society of America Special Paper 218, p. 161–178

Davis, D., Suppe, J, Dahlen, F. 1983. Mechanics of Fold-and-Thrust Belts and Accretionary Wedges. Journal of Geophysical Research. 88. 1153-1172. 10.1029/JB088iB02p01153.

David, C., Martinod, J., Comte, D., Hérail, G., Haessler, H., 2002. Intracontinental seismicity and Neogene deformation of the Andean forearc in the region of Arica (18.5°S–19.5°S), paper presented at 5th International Symposium on Andean Geodynamics, Inst. de Rech. pour le Dév., Toulouse, France.

DeCelles, P. G. and Mitra, G. (1995) History of the Sevier orogenic wedge in terms of critical taper models, northeast Utah and southwest Wyoming. Bulletin of the Geological Society of America 107, 454-462.

DeCelles, P.G., Horton, B.K., 2003. Early to middle Tertiary foreland basin development and the history of Andean crustal shortening in Bolivia. Geol. Soc. Am. Bull. 115, 58–77.

DeCelles, P. G., Zandt, G., Beck, S. L., Currie, C. A., Ducea, M. N., Kapp, P., …Schoenbohm, L. M. 2014. Cyclical orogenic processes in the Cenozoic central Andes. Geodynamics of a Cordilleran Orogenic System: The Central Andes of Argentina and Northern Chile, 459–490. doi:10.1130/2015.1212(22)

Escher, A., Beaumont, C., 1997. Formation, burial and exhumation of basement nappes at crustal scale: a geometric model based on the Western Swiss-Italian Alps. J. Struct. Geol. 19, 955–974.

Farias, M., Charrier, R., Comte, D., Martinod, J., Hérail, G., 2005. Late Cenozoic deformation and uplift of the western flank of the Altiplano: evidence from the depositional, tectonic, and geomorphologic evolution and shallow seismic activity (northern Chile at 19 degrees 30' S). Tectonics 24 TC4001.

Feehan, J., Brandon, M., 1999. Contribution of ductile flow to the exhumation of low-temperature, high pressure metamorphic rocks: San Juan-Cascade nappes, NW Washington State. Journal of Geophysical Research. Vol. 104. No. B5. Pages 10883-19902.

Farias, M., Charrier, R., Comte, D., Martinod, J., Hérail, G., 2005. Late Cenozoic deformation and uplift of the western flank of the Altiplano: evidence from the depositional, tectonic, and geomorphologic evolution and shallow seismic activity (northern Chile at 19 degrees 30' S). Tectonics 24 TC4001.

Farías, M., R. Charrier, S. Carretier, J. Martinod, A. Fock, D. Campbell, J. Cáceres, and D. Comte, 2008, Late Miocene high and rapid surface uplift and its erosional response in the Andes of central Chile (33°–35°S), Tectonics, 27, TC1005, doi:10.1029/2006TC002046.

Farias, M., Comte, D., Charrier, R., Martinod, J., David, C., Tassara, A., Tapia, F., Fock, A., 2010. Crustal-scale structural architecture in Central Chile based on seismicity and surface geology: Implications for Andean mountain building. Tectonics 29 TC3006.

Fuentes, G., Martínez, F., Bascuñan, S., Arriagada, C., & Muñoz, R. 2018. Tectonic architecture of the Tarapacá Basin in the northern Central Andes: New constraints from field and 2D seismic data. Geosphere, 14(6), 2430–2446. doi:10.1130/ges01697.1

Gallardo, F. 2015. Geología y estructura de la Precordillera Altiplánica entre 19°45'S y 20°00'S, Región de Tarapacá, Chile. Thesis, Unpublished. Universidad de Chile. Santiago, Chile.

García, M. 2002. Évolution oligo-néogene del'Altiplano Occidental (Arc et Avant-Arc du Nord du Chili, Arica): Tectonique, volcanisme, sédimentation, géomorphologie et bilan érosion-sédimentation. Tesis de Doctorado (Unpublished), Université Joseph Fourier, Grenoble: 117 p. France.

García, M.; Hérail, G. 2005. Fault-related folding, drainage network evolution and valley incision during the Neogene in the Andean Precordillera of Northern Chile. Geomorphology 65: 279-300.

García, M., Riquelme, F., Pinto, L., Charrier, R., Herrera, S., Hérail, G. In preparation. Episodic and focused shortening since 100 Ma in the western border of the Andes (northern Chile): Geological evidence and forward structural modeling. Submitted to Tectonics (2019).

Giambiagi, L., Ramos, V., 2002. Structural evolution of the Andes between 33°30′ and 33°45′ S, above the transition zone between the flat and normal subduction segment, Argentina and Chile, J. South Am. Earth Sci., 15, 101–116, doi:10.1016/S0895-9811(02)00008-1.

Giambiagi, L., Tassara, A., Mescua, J., Alvarez, P., Godoy, E., Hoke, G, Pinto, L. Spagnotto, S., Porras, H., Tapia, F., Jara, P., Bechis, F., Garcia, V., Suriano, J., Pagano, S., 2014. Evolution of shallow and deep structures along the Maipo-Tunuyán transect (33°40'S): From the Pacific coast to the Andean foreland. Geological Society, London, Special Publication 399. http://dx.doi.org/10.1144/SP399.14

Graveleau, F., Malavieille, J., & Dominguez, S. (2012). Experimental modelling of orogenic wedges: A review. Tectonophysics, 538-540, 1–66. doi:10.1016/j.tecto.2012.01.027

Gripp, A. E., & Gordon, R. G. 2002.Young tracks of hotspots and current plate velocities. Geophysical Journal International, 150(2), 321–361. doi:10.1046/j.1365-246x.2002.01627.x

Hartley, A. J., May, G., Chong, G., Turner, P., Kape, S. J., Jolley, E. J., 2000. Development of a continental forearc: A Cenozoic example from the Central Andes, northern Chile. Geology, 28(4), 331. doi:10.1130/0091-7613(2000)28<331:doacfa>2.0.co;2

Herrera, S., Pinto, L., Deckart, K., Cortés, J., & Valenzuela, J., 2017. Cenozoic tectonostratigraphic evolution and architecture of the Central Andes in northern Chile based on the Aquine region, Western Cordillera (19°-19º30' S). Andean Geology, 44(2), 87. doi:10.5027/andgeov44n2-a01

Horton, B. K., Hampton, B. A., Waanders, G. L., 2001. Paleogene synorogenic sedimentation in the Altiplano plateau and implications for initial mountain building in the central Andes. Geological Society of America Bulletin, 113, 1387–1400.

Horton, B.K.; Hampton, B.A.; Lareau, B.N.; Baldellón, E. 2002. Tertiary provenance history of the northern and central Altiplano (Central Andes, Bolivia): A detrital record of plateau-margin tectonics. Journal of Sedimentary Research 72 (5): 711-726

Hoth, S., et al. 2004, Influence of erosion on the kinematics of bivergent orogens: Results from scaled sandbox-simulations, Spec. Pap. Geol. Soc. Am., 398, 201 – 225.

Isacks, B., 1988. Uplift of the Central Andean Plateau and Bending of the Bolivian Orocline. J. Geophys. Res. Solid Earth Planets 93, 3211–3231.

Jamieson, R. A., Beaumont, C., 2013. On the origin of orogens. Geological Society of America Bulletin, 125(11-12), 1671–1702. doi:10.1130/b30855.1

Jara, P., Likerman, J., Winocur, D., Ghiglione, M.C., Cristallini, E.O., Pinto, L., Charrier, R., 2015. Role of basin width variation in tectonic inversion: insight from analogue modelling and implications for the tectonic inversion of the Abanico Basin, 32–34 S, Central Andes. Geological Society, London, Special Publications, 399(1), 83-107.

Jara, P., Likerman, J., Charrier, R., Herrera, S., Pinto, L., Villarroel, M., Winocur, D., 2018. Closure type effects on the structural pattern of an inverted extensional basin of variable width: Results from analogue models. Journal of South American Earth Sciences, 87: 157- 173.

Kay, S. M., & Coira, B. L. 2009. Shallowing and steepening subduction zones, continental lithospheric loss, magmatism, and crustal flow under the Central Andean Altiplano-Puna Plateau. Geological Society of America Memoirs, 204(0), 229–259. doi:10.1130/2009.1204(11)

Kley, J., Monaldi, C.R., 1998. Tectonic shortening and crustal thickness in the Central Andes: how good is the correlation? Geology 26, 723–726

Kley, J., Monaldi, C.R., Salfity, J.A., 1999. Along-strike segmentation of the Andean foreland: causes and consequences. Tectonophysics 301, 75-94

Kley, J.,Monaldi, C.R., 2002, Tectonic inversion in the Santa Barbara System of the central Andean foreland thrust belt, northwestern Argentina: Tectonics, v. 21, no. 6, doi:10.1029 /2002TC902003.

Koons, P. O. 1990. Two-sided orogen: Collision and erosion from the sandbox to the Southern Alps, New Zealand. Geology, 18(8), 679. doi:10.1130/0091-7613(1990)018<0679:tsocae>2.3.co;2

Konstantinovskaya, E., Malavieille, J., 2011. Thrust wedges with decollement levels and syntectonic erosion: a view from analog models. Tectonophysics 502, 336–350.

Labbé, N., García, M., Simicic, Y., Contreras-Reyes, E., Charrier, R., De Pascale, G., & Arriagada, C. 2018. Sediment fill geometry and structural control of the Pampa del Tamarugal basin, northern Chile. GSA Bulletin, 131(1-2), 155–174. doi:10.1130/b31722.1

Lamb, S., 2006. Shear stresses on megathrusts: Implications for mountain building behind subduction zones, J. Geophys. Res., 111, B07401, doi:10.1029/2005JB003916

Larroque, C., Calassou, S., Malavieille, J., & Chanier, F. 1995. Experimental modelling of forearc basin development during accretionary wedge growth. Basin Research, 7(3), 255–268. doi:10.1111/j.1365-2117.1995.tb00109.x

Liu, H., et al. (1992), Physical models of thrust wedges, in Thrust Tectonics, edited by K. R. McClay, pp. 71 – 81, CRC Press, Boca Raton, Fla.

Lossada, A. C., Giambiagi, L., Hoke, G. D., Fitzgerald, P. G., Creixell, C., Murillo, I., Suriano, J. (2017). Thermochronologic Evidence for Late Eocene Andean Mountain Building at 30°S. Tectonics, 36(11), 2693–2713. doi:10.1002/2017tc004674

Malavieille, J., 1984. Modélisation expérimentale des chevauchements imbriqués: application aux chaînes de montagnes. Bull. Soc. Geol. Fr. 26, 129–138.

Malavieille, J., Trullenque, G., 2009. Consequences of continental subduction on forearc basin and accretionary wedge deformation in SE Taiwan. Tectonophysics. 466. 377-394. doi: 10.1016/j.tecto.2007.11.016.

Malavieille, J., 2010. Impact of erosion, sedimentation, and structural heritage on the structure and kinematics of orogenic wedges: Analog models and case studies. GSA Today, v. 20, no. 1, p. 4–10, doi:10.1130/GSATG48A.1.

Malavieille, J., Dominguez, S., Lu, C., Chen, C., Konstantinovskaya, E., 2019 Deformation partitioning in mountain belts: insights from analogue modelling experiments and the Taiwan collisional orogen. Geological Magazine. doi: 10.1017/S0016756819000645

Marshak, S., 2004. Salients, recesses, arcs, oroclines, and syntaxes - A review of ideas concerning the formation of map-view curves in fold-thrust belts. In K. R. McClay (ed.), Thrust tectonics and hydrocarbon systems: AAPG Memoir, 82, 131-156.

Martínez, F., Arriagada, C., Peña, M., Deckart, K., & Charrier, R. 2016. Tectonic styles and crustal shortening of the Central Andes "Pampean" flat-slab segment in northern Chile (27–29°S). Tectonophysics, 667, 144–162. doi:10.1016/j.tecto.2015.11.019

Martínez, F., Fuentes, G., Perroud, S., Bascuñán, S., 2021. Buried thrust belt front of the western Central Andes of northern Chile: Style, age, and relationship with basement heterogeneities. Journal of Structural Geology 147, 104337. doi: 10.1016/j.jsg.2021.104337.

Martinod, J., Davy, P., 1994. Periodic instabilities during compression of the lithosphere. 2. Analog experiments. J. Geophys. Res.-Solid Earth 99, 12057–12069

Martinod, J., Gérault, M., Husson, L., Regard, V., 2020. Widening of the Andes: An interplay between subduction dynamics and crustal wedge tectonics. Earth-Science Reviews 204, 103170. https://doi.org/10.1016/j.earscirev.2020.103170.

McClay, K.R., Whitehouse, P.S., Dooley, T., Richards, A., 2004. 3D evolution of fold and thrust belts formed by oblique convergence. Mar. Pet. Geol. 21, 857–877.

McQuarrie, N., 2002. The kinematic history of the central Andean fold-thrust belt, Bolivia: Implications for building a high plateau. Geol. Soc. Am. Bull. 114, 950–963.

McQuarrie, N., Horton, B.K., Zandt, G., Beck, S., DeCelles, P.G., 2005. Lithospheric evolution of the Andean fold-thrust belt, Bolivia, and the origin of the central Andean plateau. Tectonophysics 399, 15–37.

Means, W., Hobbs, B., Lister, G., Williams, P. 1980. Vorticity and non-coaxility in progressive deformation. Journal of Structural Geology. 2. 371-378. doi: 10.1016/0191-8141(80)90024-3.

Mescua, J. F., & Giambiagi, L. B. 2012. Fault inversion vs. new thrust generation: A case study in the Malargüe fold-and-thrust belt, Andes of Argentina. Journal of Structural Geology, 35, 51–63. doi:10.1016/j.jsg.2011.11.011

Mescua, J.F., Giambiagi, L.B., Tassara, A., Gimenez, M., Ramos, V.A., 2014. Influence of pre-Andean history over Cenozoic foreland deformation: structural styles in the Malargüe fold- and-thrust belt at 35 S, Andes of Argentina. Geosphere, 10(3), 585-609.

Mescua, J.F., Giambiagi, L., Barrionuevo, M., Tassara, A., Mardonez, D., Mazzitelli, M., Lossada, A., 2016. Basement composition and basin geometry controls on upper-crustal deformation in the Southern Central Andes (30–36°S). Geological Magazine, 153(5-6), 945–961. doi:10.1017/s0016756816000364.

Metcalf, K., & Kapp, P. 2015. Along-strike variations in crustal seismicity and modern lithospheric structure of the central Andean forearc. Geological Society of America Memoirs. doi:10.1130/2015.1212(04)

Morandé, J.; Gallardo, F.; Farías, M. 2015. Carta Guaviña, Región de Tarapacá. Servicio Nacional de Geología y Minería, Carta Geológica de Chile, Serie Geología Básica 177. 1 mapa escala 1:100.000.

Mpdozis, C., & Ramos, V. 1989. The Andes of Chile and Argentina. In: Geology of the Andes and its Relation to Hydrocarbon and Mineral Resources. Houston, TX., Circum-Pacific Council for Energy and Mineral Resources. Earth Science series, v. 11.

Muñoz, N., Charrier, R., 1996. Uplift of the western border of the Altiplano on a west-vergent thrust system, Northern Chile. J. S. Am. Earth Sci. 9, 171–181.

Muñoz, M., Farías, M., Charrier, R., Fanning, C. M., Polvé, M., & Deckart, K. 2013. Isotopic shifts in the Cenozoic Andean arc of central Chile: Records of an evolving basement throughout cordilleran arc mountain building. Geology, 41(8), 931–934. doi:10.1130/g34178.1

Naylor, M., Sinclair, H. D., Willettt, S., Cowie, P. A. 2005. A discrete element model for orogenesis and accretionary wedge growth. Journal of Geophysical Research, 110(B12). doi:10.1029/2003jb002940

Nemčok, M., Mora, A., & Cosgrove, J. 2013. Thick-skin-dominated orogens; from initial inversion to full accretion: an introduction. Geological Society, London, Special Publications, 377(1), 1–17. doi:10.1144/sp377.17

Oliveros, V., Vásquez, P., Creixell, C., Lucassen, F., Ducea, M. N., Ciocca, I., González, J., Espinoza, M., Salazar, E., Coloma, F., Kasemann, S. A., 2019. Lithospheric evolution of the Pre- and Early Andean convergent margin, Chile. Gondwana Research. doi:10.1016/j.gr.2019.11.002

Pearson, D. M., Kapp, P., DeCelles, P. G., Reiners, P. W., Gehrels, G. E., Ducea, M. N., & Pullen, A. (2013). Influence of pre-Andean crustal structure on Cenozoic thrust belt kinematics and shortening magnitude: Northwestern Argentina. Geosphere, 9(6), 1766–1782. doi:10.1130/ges00923.1

Pinto, L.; Hérail, G.; Charrier, R. 2004. Sedimentación sintectónica asociada a las estructuras Neógenas en la Precordillera de la zona de Moquella (19°15'S, norte de Chile). Revista Geológica de Chile 31 (1): 19-44. doi: 10.5027/andgeoV31n1-a02

Pope, D.C., Willettt, S.D., 1998. Thermal-mechanical model for crustal thickening in the Central Andes driven by ablative subduction. Geology 26, 511–514.

Ramos, V.A., Cristallini, E.O., Perez, D.J., 2002. The Pampean flat-slab of the Central Andes. J. S. Am. Earth Sci. 15, 59–78.

Ramos, V., Zapata, T., Cristallini, E., Introcaso, A. 2004. The Andean thrust system – latitudinal variations in structural styles and orogenic shortening. Thrust Tectonics and hydrocarbon system. Edition: Memoir 82. Publisher: American Association of Petroleum Geologists, Editors: Ken McClay, pp.30-50

Riesner, M., Lacassin, R., Simoes, M., Carrizo, D., Armijo, R., 2018. Revisiting the Crustal Structure and Kinematics of the Central Andes at 33.5°S: Implications for the Mechanics of Andean Mountain Building. Tectonics, 37(5), 1347–1375. doi:10.1002/2017tc004513

Riquelme, R., Hérail, G., Martinod, J., Charrier, R., Darrozes, J., 2007. Late Cenozoic geomorphologic signal of Andean forearc deformation and tilting associated with the uplift and climate changes of the Southern Atacama Desert (26°S–28°S). Geomorphology 86, 283–306.

Rodríguez, M.P., Charrier, R., Brichau, S., Carretier, S., Farías, M., de Parseval, P., Ketcham, R.A., 2018. Latitudinal and Longitudinal patterns of Exhumation in the Andes of North-Central Chile. Tectonics 37, 2863–2886.

Roeder, D., 1988. Andean-age structure of Eastern Cordillera (Province of La Paz, Bolivia). Tectonics, 7(1), 23–39. doi:10.1029/tc007i001p00023

Russo, R.M., Silver, P.G. 1996. Cordillera formation, mantle dynamics, and the Wilson cycle. Geology 24, 511–514

Sempere, T., Hérail, G., Oller, J., and Bonhomme, M. 1990. Late Oligocene–early Miocene major tectonic crisis and related basins in Bolivia: Geology, v. 18, p. 946–949

Sheffels, B., 1990, Lower bound on the amount of crustal shortening in the central Bolivian Andes: Geology, v. 18, p. 812–815

Sheffels, B.M., 1995, Is the bend in the Bolivian Andes an orocline?, in Tankard, A.J., Suarez, R., and Welsink, H.J., eds., Petroleum basins of South America: American Association of Petroleum Geologists Memoir 62, p. 511–522

Silver, E. A., Reed, D. L., 1988. Backthrusting in accretionary wedges. Journal of Geophysical Research, 93(B4), 3116. doi:10.1029/jb093ib04p03116

Sobolev, S. V., & Babeyko, A. Y. 2005. What drives orogeny in the Andes? Geology, 33(8), 617. doi:10.1130/g21557.1

Springer, M., & Förster, A. 1998. Heat-flow density across the Central Andean subduction zone. Tectonophysics, 291(1-4), 123–139. doi:10.1016/s0040-1951(98)00035-3

Storti, F., Salvini, F., McClay, K., 2000. Synchronous and velocity-partitioned thrusting and thrust polarity reversal in experimentally produced, doubly-vergent thrust wedges: Implications for natural orogens. Tectonics 19(2),378–396, doi:10.1029/1998TC001079

Tao, W. C., and O'Connell, R. J., 1992, Ablative subduction: A two-sided alternative to the conventional subduction model: Journal of Geophysical Research, v. 97, p. 8877–8904

Tapia, F. 2015. Evolución tectónica y configuración actual de los Andes Centrales del sur (34°45'- 35°30' S). PhD Thesis. Universidad de Chile. Unpublished. 306 p.

Tassara, A., Götze, H.-J., Schmidt, S., & Hackney, R., 2006. Three-dimensional density model of the Nazca plate and the Andean continental margin. Journal of Geophysical Research, 111(B9). doi:10.1029/2005jb003976

Tassara, A., & Echaurren, A., 2012. Anatomy of the Andean subduction zone: three-dimensional density model upgraded and compared against global-scale models. Geophysical Journal International, 189(1), 161–168. doi:10.1111/j.1365-246x.2012.05397.x

Torres Carbonell, P.J., Guzmán, C., Yagupsky, D., Dimieri, L.V., 2016. Tectonic models for the Patagonian orogenic curve (southernmost Andes): An appraisal based on analog experiments from the Fuegian thrust–fold belt. Tectonophysics, 671, 76-94.

Turienzo, M., 2010. Structural style of the Malargüe fold-and-thrust belt at the Diamante River area (34°30′–34°50′S) and its linkage with the Cordillera Frontal, Andes of central Argentina. Journal of South American Earth Sciences 29(3):537-556. doi.: 10.1016/j.sames.2009.12.002

Turienzo, M., Dimieri, L., Frisicale, C., Araujo, V., Sánchez, N. 2012. Cenozoic structural evolution of the Argentinean Andes at 34°40'S: a close relationship between thick- and thin-skinned deformation. Andean Geology v. 39 (2): 317-357.

Valenzuela, J.I.; Herrera, S.; Pinto, L; Del Real, I. 2014. Carta Camiña, regiones de Arica-Parinacota y Tarapacá. Servicio Nacional de Geología y Minería, Carta Geológica de Chile, Serie Geología Básica 170: 97 p., 1 mapa escala 1:100.000.

Victor, P., Oncken, O., Glodny, J., 2004. Uplift of the western Altiplano plateau: evidence from the Precordillera between 20 degrees and 21 degrees S (northern Chile). Tectonics 23 TC4004.

Vietor, T., Oncken, O., 2005. Controls on the shape and kinematics of the Central Andean plateau flanks: Insights from numerical modeling. Earth and Planetary Science Letters 236, pp. 814– 827.

Villarroel, M., Jara, P., Herrera, S., & Charrier, R., 2020. Influence of the orientation of cohesive blocks upon the structural grain of fold-and-thrust belts: An appraisal by means of analogue modeling. Journal of South American Earth Sciences, 102725. doi:10.1016/j.jsames.2020.102725

Waschbusch, P., Beaumont, C. 1996. Effect of a retreating subduction zone on deformation in simple regions of plate convergence, J. Geophys. Res., 101(B12), 28133–28148, doi:10.1029/96JB02482

Wigger, P. J., and 10 others, 1994, Variation in the crustal structure of the southern Central Andes deduced from seismic refraction investigations, *in* Reutter, K. J., Scheuber, E., and Wigger, P. J., eds., Tectonics of the southern Central Andes: Berlin, Springer-Verlag, p. 23–48

Willettt, S., Beaumont, C., Fullsack, P., 1993. Mechanical Model for the Tectonics of Doubly Vergent Compressional Orogens. Geology 21, 371–374

Willettt, S., 1999, Orogeny and orography: The effects of erosion on the structure of mountain belts: Journal of Geophysical Research, v. 104, p. 28,957–28,981, doi:10.1029/1999JB900248.

Willettt, S. D., & Brandon, M. T. (2002). On steady states in mountain belts. Geology, 30(2), 175. doi:10.1130/0091-7613(2002)030<0175:ossimb>2.0.co;2

Yuan, X., Sobolev, S.V., Kind, R., Oncken, O., Bock, G., Asch, G., Schurr, B., Graeber, F., Rudloff, A., Hanka, W., et al., 2000. Subduction and collision processes in the Central Andes constrained by converted seismic phases. Nature 408, 958–961